



Jacobson, Ben (2023) *Acoustic cavitation characterisation in viscous deep eutectic solvents for optimisation of sonoprocessing of technology critical materials*. PhD thesis.

<http://theses.gla.ac.uk/84020/>

Copyright and moral rights for this work are retained by the author

A copy can be downloaded for personal non-commercial research or study, without prior permission or charge

This work cannot be reproduced or quoted extensively from without first obtaining permission in writing from the author

The content must not be changed in any way or sold commercially in any format or medium without the formal permission of the author

When referring to this work, full bibliographic details including the author, title, awarding institution and date of the thesis must be given

Enlighten: Theses

<https://theses.gla.ac.uk/>  
[research-enlighten@glasgow.ac.uk](mailto:research-enlighten@glasgow.ac.uk)



University  
of Glasgow

**Acoustic Cavitation Characterisation in Viscous  
Deep Eutectic Solvents for Optimisation of  
Sonoprocessing of Technology Critical Materials**

**Ben Jacobson**

**Submitted in fulfilment of the requirements for the degree of  
Doctor of Philosophy**

**College of Science and Engineering**

**University of Glasgow**

**September 2023**

## **Abstract**

The UK alone produced a total of 1.6 Mt of electronic waste in 2019, containing approximately 380,000 kg of technology critical metals worth \$148 M per annum.

Within this, printed circuit boards (PCBs) are the largest source of metals from electronic waste, containing up to 30-40 wt.% of technology critical metals. Traditional recycling techniques lack selectivity and have significant environmental and health impact. Ionometallurgy is a promising new technique for recovering metals from electronic waste using deep eutectic solvents (DESs). These solvents offer distinct advantage over traditional techniques, including much lower temperature requirements, avoidance of toxic reagents and reduced water consumption. DESs are cheap, readily available and can be adapted for selectivity. Despite these advantages, DESs are limited by slow dissolution kinetics primarily due to slow mass transport associated with their high viscosities. Power ultrasonics presents a useful solution to these issues. Sonication in DES is hypothesised to increase mass transport, remove passivating surface layers and promote cavitation-mediated effects. However, study into the cavitation activity in solutions other than water are limited. For efficient processing, cavitation generated at the tip of a sonotrode as a function of input power is required.

This work is the first comprehensive investigation of cavitation in DESs, for process optimisation to enhance precious metal recycling. Detailed characterisation of the cavitation generated by two sonotrodes in a number of DESs of varying viscosity and water is performed. High-speed imaging (HSI) and acoustic detection from a novel in-house constructed cavitation detector, characterised and validated against a commercially available cavitation sensor (NPL CaviSensor<sup>TM</sup>), identifies potentially optimal sonication parameters in each liquid. Detailed characterisation of each DES combining synchronised acoustic detection and HSI reveals generation of specific cavitation dynamics and associated cavitation structure, often characterised by a densely packed bulbous cavitation cloud,

generating multi-fronted shockwaves. The sonotrode is deployed in DES for the delamination of technology critical metals from waste PCBs. Sonication was observed to delaminate the metals from the PCB at a rate over thirty times faster than in silent conditions. Furthermore, an optimally identified lower power sonication was shown to delaminate a greater quantity of metals from the PCB compared to a higher power sonication, over the same duration. The sonotrode is also deployed to investigate delamination of alternative technology critical resources; lithium-ion batteries and photovoltaics, as well as for rate enhancement of electrodisolution of copper. Further collaborative studies investigate single-bubble dynamics for validation of modelling in the audible frequency range, with interesting potential applications.

The results of the studies in this thesis demonstrate the utility and validity of proper cavitation characterisation in solutions intended for sonoprocessing. This characterisation can be performed simply, using bespoke, cheap passive cavitation detectors to gather acoustic measurements at sufficiently fine incremental input powers. Identification of optimal powers of any ultrasonic system for maximum cavitation efficiency is of relevance to many potential processes. In particular, the need for green technologies for electronic waste recycling, could present an ideal problem that can be tackled by ultrasonically enhanced ionometallurgy.

# Table of Contents

Abstract .....	i
List of figures .....	ix
List of tables .....	xix
Acknowledgements .....	xx
Declaration .....	xxii
List of Abbreviations.....	xxiii
List of Symbols .....	xxiv
Thesis Overview & Dissemination .....	1
1 Overview of cavitation.....	7
1.1 An introduction to cavitation.....	7
1.2 Acoustic cavitation .....	9
1.3 Single-bubble dynamics .....	12
1.3.1 Bubble-collapse shockwaves .....	12
1.3.2 Shape distortion and fragmentation .....	13
1.3.3 Jetting .....	14
1.4 Multi-bubble dynamics.....	17
1.5 Monitoring cavitation .....	19
1.5.1 Chemical detection.....	19
1.5.2 High-speed imaging (HSI).....	20
1.5.3 Mechanical detection .....	21
1.5.4 Acoustic detection.....	22
1.6 Monitoring of sonoprocessing using a sonotrode.....	27
2 Electronic Waste Recycling.....	34
2.1 Scope of electronic waste generation .....	34
2.2 Printed Circuit Boards .....	37
2.3 Printed Circuit Board recycling.....	39
2.3.1 Pyrometallurgy .....	41

2.3.2	Hydrometallurgy .....	41
2.3.3	Biometallurgy.....	44
2.4	Deep Eutectic Solvents.....	45
2.4.1	Classification of deep eutectic solvents .....	45
2.4.2	Methods of preparation and Physicochemical properties of DESs.....	47
2.4.3	Applications of DESs.....	50
2.4.4	Current limitations .....	52
3	Primary Materials and Methods.....	56
3.1	Deep Eutectic Solvent (DES) preparation.....	56
3.2	Sonotrodes .....	58
3.3	Sonication tanks .....	59
3.4	High-speed cameras .....	59
3.4.1	Shimadzu High-speed camera.....	59
3.4.2	Photron high-speed camera .....	60
3.4.3	Phantom high-speed camera .....	61
3.5	Illumination sources .....	62
3.5.1	Pulsed laser .....	62
3.5.2	Continuous light.....	64
3.6	Oscilloscope .....	65
3.7	Shockwave passive cavitation detector (swPCD) .....	66
3.8	Manufacturing the swPCD .....	68
3.8.1	Casing design and manufacture .....	68
3.8.2	Active element preparation and bonding .....	69
3.8.3	Backing layer .....	72
3.8.4	Matching layer .....	72
3.8.5	Notable challenges/failure.....	74
3.9	Filters used for acoustic data detected by the swPCD.....	75
4	Performance characterisation of the swPCD and comparison against NPL CaviSensorTM .....	77

4.1	The CaviSensor .....	77
4.2	Requirements of a cavitation detector .....	78
4.3	Characterisation of the cavitation emissions .....	79
4.4	Experimental setup .....	81
4.5	Results and Discussion .....	86
4.5.1	swPCD translation.....	86
4.5.2	CaviSensor Signal .....	88
4.5.3	swPCD comparison with CaviSensor .....	91
4.5.4	Position translation within the CaviSensor .....	95
4.5.5	Shockwave detection under a sonotrode source .....	101
4.6	Conclusions: .....	105
5	Characterisation of the cavitation generated in different Deep Eutectic Solvents and water.....	106
5.1	Introduction .....	106
5.2	Materials and Methods .....	107
5.2.1	Deep Eutectic Solvent preparation.....	107
5.2.2	The experimental setup .....	107
5.2.3	High-speed imaging: .....	108
5.2.4	Acoustic detection and filtering protocol.....	109
5.2.5	Data collection .....	111
5.3	Results .....	112
5.3.1	Bubble cluster shockwave periodicity at selected input powers in water ....	113
5.3.2	Cavitation emission noise spectra at selected input powers in water .....	117
5.3.3	Shockwave content over all measured input powers in water .....	120
5.3.4	Bubble cluster shockwave periodicity at selected input powers in Ethaline	123
5.3.5	Cavitation emission noise spectra at selected input powers in Ethaline .....	134
5.3.6	Shockwave content with the emission signal over all measured input powers in Ethaline.....	136
5.3.7	Horn crossover regions .....	138

5.3.8	Cavitation characterisation for crossover regions in water .....	145
5.3.9	Cavitation characterisation for crossover regions in Ethaline.....	149
5.4	Discussion .....	152
5.5	Conclusion:.....	156
6	A mechanistic study identifying improved technology critical metal delamination from printed circuit boards at lower power sonications in a deep eutectic solvent. ....	157
6.1	Introduction .....	157
6.2	Materials and Methods .....	159
6.2.1	Deep Eutectic Solvent (DES) preparation .....	159
6.2.2	Printed Circuit Board (PCB) samples .....	159
6.2.3	Characterisation of cavitation activity in DES.....	161
6.2.4	The experimental setup .....	161
6.2.5	Shadowgraphic high-speed imaging .....	163
6.2.6	Dual-perspective high-speed imaging.....	163
6.2.7	Microscopy and profilometry.....	164
6.2.8	Data collection .....	166
6.3	Results .....	167
6.3.1	Characterisation of cavitation activity in DES.....	167
6.3.2	Overview of TCM- delamination performance at 60% and 90% input powers 169	
6.3.3	Dual-perspective HSI of TCM-delamination.....	174
6.4	Discussion .....	192
6.5	Conclusion and Future Investigations .....	195
	Conclusions.....	196
7	Future work and spinout activities.....	200
7.1	Ultrasonically enhanced processing and recycling of additional technology critical materials .....	200
7.1.1	Lithium-ion battery recycling .....	200
7.1.2	Materials and methods .....	208

7.1.3	Results .....	210
7.1.4	Discussion and future work:.....	212
7.1.5	Photovoltaic recycling.....	213
7.1.6	Materials and methods .....	223
7.1.7	Results .....	226
7.1.8	Discussion and future work.....	229
7.2	Using ultrasound to increase metal dissolution and prevent passivation using concentrated ionic fluid. ....	232
7.2.1	Introduction .....	232
7.2.2	Materials and methods .....	234
7.2.3	Results and discussion .....	235
7.2.4	Conclusions .....	238
7.3	Mass and heat transfer in bubble driven by audible sound .....	239
7.3.1	Introduction .....	239
7.3.2	Materials and methods .....	242
7.3.3	Results and Discussion from experimental validation.....	246
7.3.4	Limitations and future work.....	248
Appendix A	.....	251
	Previous research within CavLab .....	251
Appendix B	.....	257
	Principal MATLAB filtering code .....	257
Appendix C	.....	259
C.1	Characterisation of cavitation activity in CaDES and Reline.....	259
C.1.1	Bubble cluster shockwave periodicity at selected input powers in CaDES.....	259
C.1.2	Cavitation emission noise spectra at selected input powers in CaDES .....	263
C.1.3	Shockwave content with the emission signal over all measured input powers in CaDES .....	265
C.1.4	Bubble cluster shockwave periodicity at selected input powers in Reline .....	266
C.1.5	Cavitation emission noise spectra at selected input powers in Reline .....	270

C.1.6 Shockwave content with the emission signal over all measured input powers in Reline .....	272
Appendix D .....	274
Basic Principles of Linear Sweep Voltammetry .....	274
Bibliography.....	277

## List of figures

Fig. 1.1: Phase diagram representation of the transition from liquid to vapour. The diagram presents phase transition through temperature increase (boiling) and through pressure decrease (cavitation). Taken from [2].	7
Fig. 1.2: Schematic representation of the compression and rarefaction cycles of an ultrasonic wave. (a) inertial and (b) stable cavitation. Taken from [10].	11
Fig. 1.3: Spherical BCSW (arrowed yellow) emitted by a single bubble driven at 17.885 kHz and detected by a high-speed camera at 2 million frames per second (Mfps).	13
Fig. 1.4: Time variation of bubble shape oscillation and fragmentation observed from an oscillating bubble driven at 25 kHz. Taken from [26].	14
Fig. 1.5: Bubble dynamics displaying a liquid jet protruding towards a solid interface at 101 $\mu$ s caused by non-symmetrical oscillation. Taken from [20].	15
Fig. 1.6: Observation of bubble dynamics, characterised by shape oscillation, fragmentation, BCSW (arrowed yellow) and jetting. High-speed observations generated at 80 kfps under a 20 kHz, 500 W sonotrode at the initiation of sonication.	16
Fig. 1.7: Schematic representation of (a) acoustic streaming, (b) streamers, taken from [29]. (c) microstreaming, taken from [13]. (d) Image of dendritic structure of streamers forming around a central densely backed cluster of bubbles, taken from [39].	18
Fig. 1.8: Basic schematic of shadowgraphic imaging setup. Taken from [52].	20
Fig. 1.9: Example acoustic spectrum generated by a cleaning bath operating at 40 kHz, measured using a commercially available underwater hydrophone. Taken from [60].	22
Fig. 1.10: Schematic representation of the acoustic emission spectra generated by ultrasonic devices. Categorised into direct field (blue), stable cavitation (yellow) and transient cavitation (red). Taken from [64].	24
Fig. 1.11: Commercially available sonotrode device. Taken from [88].	27
Fig. 1.12: Example cone-like bubble structure (CBS) generated at the tip of a 20.7 kHz sonotrode operating through (a) a 120 mm, (b) 80 mm and (c) 20 mm- $\varnothing$ tip in water. Taken from [93].	29
Fig. 1.13: Mean $V_{rms}$ from five 2 s sonications at each input power, of the signal collected by the swPCD, over twenty-five input powers. Error bars represent the standard deviation within the five data sets. The peak-to-peak tip-vibration amplitude, estimated from the imaging data is also presented. Taken from [55].	32
Fig. 2.1: Common PCB structure containing attached components connected at conducting substrate terminals situated on the non-conducting laminate. Taken from [124].	38

Fig. 2.2: Overview of stages involved in PCB recycling. Adapted from [105, 120, 126, 127]. .....	40
Fig. 2.3: Common HBAs and HBDs used for preparation of DESs. Taken from [153]. ....	46
Fig. 2.4: General phase diagram of a DES consisting of one HBA and one HBD. The eutectic point represents the composition at which the minimum melting temperature is achieved. Taken from [150]......	48
Fig. 2.5: Representative cavitation activity in DES. Frames captured at 5 kfps during a 15 s sonication at 30% input power. (a) initial 50 ms, (b) up to 1 s, (c) ~ 1-1.3 s, and (d) ~ 12-13 s. Red arrows indicate bubble-collapse shockwaves. A schematic representation of fluid flow during each regime is presented alongside the selected frames. Scale provided by the 6 mm-Ø tip.....	54
Fig. 3.1: Colourless, homogenous Ethaline-DES formed after heating at 60°C and stirring. .....	57
Fig. 3.2: Branson (a) and Sonics (b) sonotrode comprising the sonotrode, output tips and control console through which all sonications were initiated.....	58
Fig. 3.3: Image of the Shimadzu high-speed camera [183]. ....	60
Fig. 3.4: Image of the Photron high-speed camera [184].....	61
Fig. 3.5: Image of Phantom high-speed camera [185]......	61
Fig. 3.6: Image of Cavilux Smart UHS comprising control unit, laser module and collimating lens. Taken from [186]......	62
Fig. 3.7: White light source coupled to a liquid light guide and collimating lens. ....	64
Fig. 3.8: Image of digital oscilloscope used for collection of acoustic emission data detected by the cavitation detectors. ....	65
Fig. 3.9: (a) final manufactured swPCD, (b) schematic cross section of the swPCD [69]. .	67
Fig. 3.10: Schematic of swPCD casing.....	69
Fig. 3.11: (a) Circular cutter and (b) 10 mm-Ø PVdF disks. ....	69
Fig. 3.12: Coaxial wire stripped and braided to separate positive and ground electrodes for bonding to PVdF disk. ....	70
Fig. 3.13: Coaxial cable bonded to the PVdF on both the upper and lower surface with silver conductive epoxy. The ground wire and bottom PVdF surface are shown here. ....	71
Fig. 3.14: Steps in manufacturing of swPCD. (a) fixing of braided and separated coaxial cable within the inner guide rail of the casing, allowing the positive electrode to extend above the shelf. (b) PVdF fixed in place with ground electrode on bottom surface and positive electrode visible on the top surface for electrical connection. (c) addition of backing layer after curing. (d) addition of matching layer on front face of swPCD. ...	73

Fig. 3.15: magnitude response for (a) high-pass filter, (b) low pass filter, (c) band pass filter, and (d) band stop filter. Taken from [191]. .....	75
Fig. 4.1: Photo of the NPL CaviSensor.....	78
Fig. 4.2: Schematic representation of the position of (a) and (b) the CaviSensor and (c) the swPCD relative to the LIB induction site. ....	80
Fig. 4.3: Schematic of the experimental configuration used for generating LIBs and detecting BCSWs with the following components: 1. Nd:YAG laser brought to focus by 2. Curved mirror. 3. Shimadzu high-speed camera providing shadowgraphic imaging with illumination provided by 4. collimated lens. 5. swPCD detecting LIB emissions. ....	82
Fig. 4.4: Full swPCD voltage trace with key features of the LIB process arrowed and described in the text. ....	84
Fig. 4.5: Representative high-speed frames of an LIB collapse, BCSW generation and rebound, recorded at $5 \times 10^6$ FPS. BCSW detection time is normalised to the voltage trace BCSW of fig. 4.3. to account for propagation time. ....	84
Fig. 4.6: BCSW voltage trace detected by the swPCD at a distance of 7.5 mm (blue), 10 mm (orange) and 15 mm (green). ....	86
Fig. 4.7: BCSW voltage trace detected by the CaviSensor. Zoom inset shows Full BCSW profile.....	88
Fig. 4.8: Schematic representation of an off-axis LIB where $d_1$ and $d_2$ represent the respective distances the BCSW will travel before striking the CaviSensor. ....	89
Fig. 4.9: Amplitude of the BCSW detected in the voltage trace of five LIBs for the swPCD at distances of 7.5 mm, 10 mm and 15 mm, and the CaviSensor positioned with the LIB induction site in the geometric centre of the sensor. Results presented as mean $\pm$ s.d. ....	91
Fig. 4.10: FWHM of the BCSW detected in the voltage trace of five LIBs for the swPCD at distances of 7.5 mm, 10 mm and 15 mm, and the CaviSensor positioned with the LIB induction site in the geometric centre of the sensor. Results presented as mean $\pm$ s.d. ....	92
Fig. 4.11: Spectra of BCSW for swPCD at 10 mm distance (red) and CaviSensor centrally positioned (blue). ....	94
Fig. 4.12: Normalised amplitude of the BCSW detected in the voltage trace of five LIBs for the CaviSensor positioned with the LIB induction site in the geometric centre of the sensor and translated axially 1 mm, 2 mm and 4 mm. Results presented as mean $\pm$ s.d. ....	96
Fig. 4.13: Normalised FWHM of the BCSW detected in the voltage trace of five LIBs for the CaviSensor positioned with the LIB induction site in the geometric centre of the	

sensor and translated axially 1 mm, 2 mm and 4 mm. Results presented as mean $\pm$ s.d. .....	97
Fig. 4.14: Normalised amplitude of the BCSW detected in the voltage trace of five LIBs for the CaviSensor positioned with the LIB induction site in the geometric centre of the sensor and translated laterally 1 mm, 2 mm and 3 mm. Results presented as mean $\pm$ s.d. .....	98
Fig. 4.15: Normalised FWHM of the BCSW detected in the voltage trace of five LIBs for the CaviSensor positioned with the LIB induction site in the geometric centre of the sensor and translated laterally 1 mm, 2 mm and 3 mm. Results presented as mean $\pm$ s.d. .....	98
Fig. 4.16:(a) large primary bubble cluster generated under sonotrode, (b) multi-fronted shock front generated by sub-cluster collapse within primary cluster. Scale provided by the 6 mm- $\emptyset$ tip.....	101
Fig. 4.17:(a) Representative shockwave emissions from the sonotrode detected by the CaviSensor and (b) the swPCD, with zoom insets providing individual shock-profiles exhibiting the detection of multi-fronted shockwaves.....	104
Fig. 5.1: Schematic representation of the experimental arrangement, featuring the following components: 1. The sonotrode, the tip of which was aligned to a Perspex disk for position registration within a custom-made tank filled with DES/water. 2. Photron high- speed camera used to study cavitation development within the vicinity of the tip, with pulsed laser illumination provided via a collimator lens, 3. 4. swPCD gathering acoustic emissions produced during sonications. ....	108
Fig. 5.2: Filtering protocol implemented on raw acoustic emissions detected by the swPCD (blue) to remove 1. low frequency noise over 50Hz. 2. High frequency system noise above 10MHz and 3. Bandpass filtering to remove contributions from the drive signal ( $f_0$ ) to give the final filtered signal (red). ....	110
Fig. 5.3: swPCD data over (a) 200 ms and (b) 2 ms identified by the dashed oval, sampled approximately 4 s into the sonication at 23% input power in water. Sample HSI extracted from the image sequence, corresponding to the green box of (b). Bubble collapse shockwaves are arrowed in yellow. ....	114
Fig. 5.4: swPCD data over (a) 200 ms and (b) 2 ms identified by the dashed oval, sampled approximately 4 s into the sonication at 27% input power in water. Sample HSI extracted from the image sequence, corresponding to the green box of (b). Bubble collapse shockwaves are arrowed in yellow. ....	115

Fig. 5.5: swPCD data over (a) 200 ms and (b) 2 ms identified by the dashed oval, sampled approximately 4 s into the sonication at 40% input power in water. Sample HSI extracted from the image sequence, corresponding to the green box of (b). Bubble collapse shockwaves are arrowed in yellow. ....	116
Fig. 5.6: Cavitation emission noise spectra for the sampled 200 ms section of signal presented previously in water at (a) 23% input power, (b) 27% input power and (c) 40% input power. ....	118
Fig. 5.7: Mean $\pm$ standard deviation VRMS over five 400 ms sonications at each input power over a twenty-five-input power range in water. ....	120
Fig. 5.8: Mean $\pm$ standard deviation VRMS over five 2 s sonications at each input power over a twenty-five-input power range in water. Taken from [62]. ....	121
Fig. 5.9: Representative high-speed imaging of the cavitation development in Ethaline at 60% input power over a 10 s sonication. Bubble collapse shockwaves captured by the shadowgraphic imaging are arrowed yellow, and scale is provided by the 6.4 mm diameter sonotrode tip. ....	124
Fig. 5.10: swPCD data over (a) 200 ms and (b) 2 ms identified by the dashed oval, sampled approximately 4 s into the sonication at 60% input power in Ethaline. Sample HSI extracted from the image sequence, corresponding to the green box of (b). Bubble collapse shockwaves are arrowed in yellow. ....	126
Fig. 5.11: Representative high-speed imaging of the cavitation development in Ethaline at 70% input power over a 10 s sonication. Bubble collapse shockwaves captured by the shadowgraphic imaging are arrowed yellow, and scale is provided by the 6.4 mm diameter sonotrode tip. ....	128
Fig. 5.12: swPCD data over (a) 200 ms and (b) 2 ms identified by the dashed oval, sampled approximately 4 s into the sonication at 70% input power in Ethaline. Sample HSI extracted from the image sequence, corresponding to the green box of (b). Bubble collapse shockwaves are arrowed in yellow. ....	130
Fig. 5.13: Representative high-speed imaging of the cavitation development in Ethaline at 90% input power over a 10 s sonication. Bubble collapse shockwaves captured by the shadowgraphic imaging are arrowed yellow, and scale is provided by the 6.4 mm diameter sonotrode tip. ....	131
Fig. 5.14: swPCD data over (a) 200 ms and (b) 2 ms identified by the dashed oval, sampled approximately 4 s into the sonication at 90% input power in Ethaline. Sample HSI extracted from the image sequence, corresponding to the green box of (b). Bubble collapse shockwaves are arrowed in yellow. ....	133

Fig. 5.15: Cavitation emission noise spectra for the sampled 200 ms section of signal presented previously in Ethaline at (a) 60% input power, (b) 70% input power and (c) 90% input power. ....	134
Fig. 5.16: Mean $\pm$ standard deviation VRMS over five 400 ms sonications at each input power over a seventeen-input power range in Ethaline. ....	136
Fig. 5.17: Mean $\pm$ standard deviation VRMS over five 400 ms sonications at each input power for both the Branson and Sonics sonotrode in water. Crossover regions are highlighted in red and labelled. ....	139
Fig. 5.18: Mean $\pm$ standard deviation $V_{RMS}$ over five 400 ms sonications at each input power for both the Branson and Sonics sonotrode in CaDES. Crossover regions are highlighted in red and labelled. ....	140
Fig. 5.19: Mean $\pm$ standard deviation VRMS over five 400 ms sonications at each input power for both the Branson and Sonics sonotrode in Reline. Crossover regions are highlighted in red and labelled. ....	141
Fig. 5.20: Mean $\pm$ standard deviation VRMS over five 400 ms sonications at each input power for both the Branson and Sonics sonotrode in Ethaline. Crossover regions are highlighted in red and labelled. ....	142
Fig. 5.21: Sampled swPCD data over a 2 ms duration in water at (a) 65% input power on the Branson sonotrode and (b) 20% input power on the Sonics sonotrode. Cavitation emission noise spectra for the sampled swPCD data is presented for (c) the Branson sonotrode at 65% input power and (d) the Sonics sonotrode at 20% input power. ....	145
Fig. 5.22: Sampled swPCD data over a 2 ms duration in water at (a) 80% input power on the Branson sonotrode and (b) 30% input power on the Sonics sonotrode. Cavitation emission noise spectra for the sampled swPCD data is presented for (c) the Branson sonotrode at 80% input power and (d) the Sonics sonotrode at 30% input power. ....	147
Fig. 5.23: Sampled swPCD data over a 2 ms duration in Ethaline at (a) 80% input power on the Branson sonotrode and (b) 30% input power on the Sonics sonotrode. Cavitation emission noise spectra for the sampled swPCD data is presented for (c) the Branson sonotrode at 80% input power and (d) the Sonics sonotrode at 30% input power. ....	149
Fig. 5.24: Sampled swPCD data over a 2 ms duration in Ethaline at (a) 100% input power on the Branson sonotrode and (b) 40% input power on the Sonics sonotrode. Cavitation emission noise spectra for the sampled swPCD data is presented for (c) the Branson sonotrode at 100% input power and (d) the Sonics sonotrode at 40% input power. ...	151

Fig. 6.1: a) Gold-coated printed circuit board as received from supplier. b) Reflected light image of metal layer profile for all printed features c) Profilometry of (untreated) TCM disk feature, used throughout this study. ....	160
Fig. 6.2: Schematic representation of the experimental setup, featuring the following components: 1. The sonotrode, the tip of which was aligned to a PCB section (inset top-right) within a custom-made tank filled with DES. 2. Photron high-speed camera used to study cavitation development in the vicinity of the tip, with pulsed laser illumination provided via a collimator lens, 3, with FOV depicted (inset bottom-right). 4. Phantom high-speed camera for direct observation of the TCM disk, with objective lens 5, and white light illumination, 6. Typical FOV as depicted (inset top-left). Acoustic detection of cavitation activity was undertaken with a swPCD, denoted by, 7.....	162
Fig. 6.3: Image thresholding operation to segment the TCM from the PCB substrate in ImageJ.....	164
Fig. 6.4: Mean VRMS from five 400 ms sonications at each input power, of the signal detected by the swPCD during sonications in DES.....	168
Fig. 6.5: Surface microscopy of TCM-disks from five PCB samples, taken at one-minute intervals (after $6 \times 10$ s sonications), over a total sonication of five minutes ( $30 \times 10$ s sonications) at 60% input power, demonstrating the accumulated delamination. Scale is provided by the 2mm $\emptyset$ disk.....	170
Fig. 6.6: Surface microscopy of TCM-disks from five PCB samples, taken at one-minute intervals (after $6 \times 10$ s sonications), over a total sonication of five minutes ( $30 \times 10$ s sonications) at 90% input power, demonstrating the accumulated delamination. Scale is provided by the 2mm $\emptyset$ disk.....	171
Fig. 6.7: histogram of percentage TCM removal vs sonication time presented as an average of the 5 samples ( $\pm$ standard deviation) at 60% input power (blue) and 90% input power (orange). Average delamination for samples continuously sonicated for 5 minutes are also presented (dashed).....	172
Fig. 6.8: Profilometry of removal features on the TCM-disk at $20\times$ magnification for (a) sample 3, after the 2 <sup>nd</sup> minute of sonication at 90% power, (b) sample 5 after the 5 <sup>th</sup> minute of sonication at 60% power and (c) sample 4 after the 5 <sup>th</sup> minute of sonication at 90% power. ....	173
Fig. 6.9: (a) Single before and after images of an early stage TCM delamination event from the Phantom camera perspective, occurring during the 41-50 s sonication of the 2 <sup>nd</sup> minute at 60% input power, for sample 4. (b) Combination (i) Phantom and (ii) Photron frames from an HSI sequence of specific delamination events during the 41-50 s	

sonication. A jetting bubble at 36 ms (arrowed orange and zoomed inset) dislodges a TCM fragment (arrowed blue within the zoomed insets at 38.625 and 60 ms). Scale provided by (i) the 2 mm Ø TCM disk, (ii) the 6.4 mm Ø tip.....	176
Fig. 6.10: (a) Single images of the TCM disk from the Phantom camera perspective, before and after each of the 10 s sonications, from the fifth minute at 60% input power for sample 2. (b)-(d) Combination (i) Phantom and (ii) Photron frames from HSI sequences, of specific delamination events at different points during the sonication. Bubble collapse shockwaves are arrowed yellow, TCM fragments within zoomed insets arrowed blue, throughout the Photron imaging. Scale provided by (i) the 2 mm Ø TCM disk, (ii) the 6.4 mm Ø tip. ....	185
Fig. 6.11: (a) Single frame captures of the TCM disk from the Phantom camera perspective, before and after each of the 10 s sonications, from the fifth minute at 90% input power, for sample 1. (b) (i) Phantom frames from a HSI sequence, of specific delamination events during the 21-30 s sonication. (b) (ii) corresponding Photron frames for the HSI sequence of specific delamination event detected by the Phantom. (c) Change in the cavitation structure after ~ 1.2 s, with the bubble activity receding from the PCB over 60 ms. (d) complete transformation of the cavitation activity after the first ~ 1.3 s, beyond which a primary cluster close to the sonotrode tip dominates for the remainder of sonication duration. Bubble collapse shockwaves are arrowed yellow, TCM fragments within zoomed inset arrowed blue, throughout the Photron imaging. Scale provided by (i) the 2 mm Ø TCM disk, (ii) the 6.4 mm Ø tip.....	190
Fig. 7.1: Battery cell types and their arrangement into modules and packs. Taken from [223]. .....	201
Fig. 7.2: Basic schematic of a LiB. Taken from [223]. ....	203
Fig. 7.3: Generalised recycling loop of LiB battery modules with products presented in blue and processes presented in orange. Ultrasonic delamination and selective separation in DES are highlighted red as the most relevant processes reviewed for optimisation in the subsequent section. Adapted from [214, 215, 218, 220]. ....	205
Fig. 7.4: LiB cathode sheet prepared for sonication. ....	208
Fig. 7.5: Representative HSI frames capturing cathode material delamination. A concentric ring of bubbles forms upon sonication initiation (circled yellow) with subsequent fragmentation of the cathode material arrowed yellow. Scale is provided by the 20 mm-Ø tip. ....	210
Fig. 7.6: Cathode sheet before sonication (left) and after 3 s sonication at 30% input power and a tip height of 3 mm (right). ....	211

Fig. 7.7:Schematic representation of (a) a first-generation c-Si PV module and (b) the solar cell layer within the module. Taken from [232].	214
Fig. 7.8:Projected growth of PV capacity from 2000 to 2050, based on International Renewable Energy Agency (IRENA) interpolation of annual growth rate. Taken from [235].	215
Fig. 7.9: Projected increase in cumulative PV module waste, based on International Renewable Energy Agency (IRENA) estimates, projecting both a regular-loss and early-loss scenario. Taken from [230].	216
Fig. 7.10: Generalised recycling loop of PV modules with products presented in blue and processes presented in orange. Specific chemical etching processes are simplified to broadly “hydrometallurgy”. Adapted from [201, 223, 237-239].	219
Fig. 7.11:photograph of whole PV cell from (a) front side and (b) back side. Taken from [206].	223
Fig. 7.12: Extracted frames from a HSI sequence of etching of a silver busbar on the PV sample over initial 400 ms, cavitation activity at the sonotrode tip arrowed yellow. Scale provided by the 6.4 mm-Ø sonotrode tip.	226
Fig. 7.13: Surface 2D microscopy of the silver busbar after 30 s of sonication, characterised by pitting of the silver busbar.	227
Fig. 7.14: (a) 3D microscopy of the PV cell after sonication for two minutes for sample 1. (b) 2D surface microscopy of the PC cell after sonication for two minutes for sample 1.	228
Fig. 7.15:(a) LSV of copper electrode in Ethaline run in silent and ultrasonic conditions. (b) LSV of nickel electrode in Ethaline run in silent and ultrasonic conditions. Taken from [261].	236
Fig. 7.16: High-speed imaging sequence of cavitation onset and development at the electrode surface. Bubble-collapse shockwaves are arrowed yellow and jetting bubbles on electrode surface arrowed blue. Scale provided by the 6 mm-Ø tip. Taken from [258].	238
Fig. 7.17:Schematic representation of the experimental apparatus setup. Taken from [267].	242
Fig. 7.18: Representation of (a) original grayscale image, (b) thresholding operation to segment bubble and (c) detected bubble boundary. Taken from [267].	244
Fig. 7.19: Representative frames from a high-speed shadowgraphic sequence at 4 V, captured at 2 Mfps, over one cycle of bubble oscillation. $t = 0 \mu\text{s}$ is defined by the frame closest to the moment of the first bubble collapse captured, confirmed by the emission	

of a shockwave (arrowed). The successive collapse at 56 $\mu\text{s}$ corresponds to the period of the driving acoustic field. Taken from [262].	246
Fig. 7.20: Comparison between experimental data and simulated models at drive frequency, $f_0 = 17.885 \text{ kHz}$ and $R_0 = 7.5 \mu\text{m}$ . Experimental data taken from dataset represented in fig. 8.5. Taken from [262].	247
Fig. 7.21: Single bubble shape oscillations observed over one acoustic cycle at a range of input voltages. Image sequences recorded at 1 Mfps.	249

## List of tables

Table 1.1: Comparison of some acoustic sensors for characterisation cavitation .....	25
Table 2.1: Composition of metals in various sources of E-waste. Taken from [119]......	36
Table 2.2: Value of metals found in waste PCBs. Taken from [119]. .....	37
Table 2.3: Summary of common hydrometallurgical processing for metal extraction from waste PCBs. ....	43
Table 7.1: Cell materials in a typical LiB. Adapted from [223]. .....	202
Table 7.2: Summary of experimental work on PV recycling.....	220

## Acknowledgements

There are several people that deserve my thanks and acknowledgement during my PhD journey.

Firstly, I would like to thank everyone in the FUSE CDT team who made this PhD process a possibility. The course structure and development implemented by the CDT directors Sandy Cochran, Tony Gachagan and James Windmill have allowed me to learn so much in the field of ultrasonics. The CDT has allowed me opportunities to develop a range of skills that I hope to implement in my future career. I would like to thank all the FUSE CDT staff for making the last four years a smooth, enjoyable and educational experience. The efforts of our Business Development Manager, Kirsten Laing, to grant us with industrial contacts and opportunities for learning is greatly appreciated. Nothing in FUSE would get done without our admin team and I would sincerely like to thank Rhona Nicholson, in particular, for always being on hand to support my research needs.

The CDT has allowed me to work as a cohort, developing interpersonal relationships that a traditional PhD would potentially lack. I'd like to thank all my colleagues from FUSE and CMIU who have always been on hand in the laboratory for advice, inspiration and conversation.

I would like to thank all my colleagues from the University of Leicester, who's relationship through the SONOCAT project has introduced me to the world of Chemistry. The collaboration and research we have developed together has been pivotal on my PhD journey.

I would like to thank my CavLab colleagues Hilde Metzger, Paul Daly, Lukman Yusuf and Shida Li. The advice, discussion and work we have shared together on all things cavitation has been inspirational to me.

I am grateful for the supervisor-like guidance I have received from Andrew Feeney since working on the SONOCAT project. Your insight and discussion over the last few years have

been crucial in advancing my research. I am forever grateful for my supervisor, Paul Prentice. The advice and support given to me from my first day in the lab all the way through paper and thesis writing has been crucial in my development as a researcher.

Finally, I would like to thank my friends, family and partner – Aimee. Who have supported my PhD journey. I'm glad to have your encouragement throughout.

## **Declaration**

All work in this thesis was carried by the author unless explicitly stated otherwise.

## List of Abbreviations

- Bubble Collapse Shockwave (BCSW)
- Cavitation Laboratory (CavLab)
- Centre for Medical and Industrial Ultrasonics (CMIU)
- Cone-like Bubble Structure (CBS)
- Crystalline Silicon (c-Si)
- Deep Eutectic Solvent (DES)
- Electronic Waste (E-waste)
- Field of View (FOV)
- Finite Element Method (FEM)
- Frames Per Second (fps)
- Full Width Half Maximum (FWHM)
- High Intensity Focused Ultrasound (HIFU)
- High-speed Imaging (HSI)
- Hydrogen Bond Acceptor (HBA)
- Hydrogen Bond Donor (HBD)
- International Electrotechnical Commission (IEC)
- Kilohertz (kHz)
- Laser Induced Bubble (LIB)
- Lead Zirconate Titanate (PZT)
- Linear Sweep Voltammetry (LSV)
- Lithium Ion Battery (LiB)
- Megahertz (MHz)
- Multi Bubble Sonoluminescence (MBSL)
- National Physical Laboratory (NPL)
- Optical Breakdown Shockwave (OBSW)
- Passive Cavitation Detector (PCD)
- Periodic Shockwave (PSW)
- Photovoltaic (PV)
- Polyvinylidene Fluoride (PVdF)
- Printed Circuit Board (PCB)
- Shockwave Passive Cavitation Detector (swPCD)
- Single Bubble Sonoluminescence (SBSL)
- Technology Critical Metal (TCM)
- Waste Electrical and Electronic Equipment (WEEE)

## List of Symbols

$f_0$	Frequency of Driving Signal	$\lambda$	Wavelength
$f_c$	Cutoff Frequency	$\Sigma$	Surface Tension
$k$	Boltzmann Constant	$v$	Speed of Sound
$\rho$	Density		
$\kappa$	Polytropic exponent		
$\emptyset$	Diameter		
$P$	Pressure		
$P_a$	Acoustic Pressure		
$P_h$	Hydrostatic Pressure		
$P_v$	Vapour Pressure		
$R$	Radius of average void		
$R_0$	Equilibrium Radius		
$T$	Absolute Temperature		
$T_0$	Period of Source		
$V_{RMS}$	Time average shockwave content		
$Z$	Acoustic Impedance		
$\Delta d$	Separation Distance		
$\Delta t$	Time Difference		

## Thesis Overview & Dissemination

The following section details the outline of this thesis as well as summarising the relevant chapters within. The research was undertaken in the Cavitation Research Laboratory (CavLab), at the Centre for Medical and Industrial Ultrasonics (CMIU). CavLab's primary research topic is driven towards a fundamental understanding of acoustic cavitation, with aims of advancing and improving applications. The laboratory is based on three high-speed cameras, described in *Chapter 3*, for imaging rapid cavitation bubble dynamics at high temporal and spatial resolution. A number of commercially available hydrophones and, for this work, in-house designed and manufactured (described in detail in *Chapters 3 and 4*) Passive Cavitation Detectors (PCDs) are available for synchronous acoustic detection. Previous CavLab research has had a bias on medical therapy applications of cavitation, such as microbubble-cavitation for blood-brain barrier disruption or drug delivery, driven by focused ultrasound at several hundreds of kHz. More recent work has focused on industrial applications of cavitation such as characterising cavitation activity generated by a commercially available ultrasonic horn, and investigation of ultrasonic fixation of Nitrogen gas for industrial sonochemistry applications using focused ultrasound.

This thesis is the first CavLab PhD project to study acoustic cavitation activity for ultrasonically enhanced precious metal recycling from electronic waste. The source of ultrasound for this body of work was an ultrasonic horn, or sonotrode. Specifically, two commercially available ultrasonic horns (described in *Chapter 3*) were used during this study, and were implemented in the results *Chapters 5-8*, introduced below. Furthermore, previous CavLab works have typically been studied in degassed or deionised water, this work uses a combination of many liquids of varying properties, particularly viscosity which has a major effect on cavitation dynamic behaviour. The class of liquids used are coined Deep Eutectic Solvents (DESs) and are a class of green designer solvents showing great potential for leaching of metals in a sustainable and environmentally friendly way, to aid in

reduction of traditional pyro- and hydrometallurgy which have drawbacks of high energy demand and environmental impact, respectively – as discussed in *Chapter 2*.

The review of literature in this thesis can be broadly split into three sections. Firstly, an overview of cavitation and sonochemistry is provided detailing the history of cavitation research, fundamentals of cavitation, and methods of monitoring such processes.

*Chapter 2* describes the scale of electronic waste, with a focus on printed circuit boards, and the value of recycling them. In particular, this chapter details the current methods of recycling critically reviewing their advantages and disadvantages before introducing new green and selective methods. *Chapter 2*, §2.4 introduces the class of green chemicals used in this study – DESs – detailing their discovery, formulation, advantages and current uses in the literature. *Chapter 2* concludes with data from a disseminated journal paper – accepted for publication in *RSC Sustainability*, December 2023 under the SONOCAT project with the paper lead by Dr Rodolfo Marin and a 2nd author contribution. Details below:

*Ultra-fast extraction of metals from a printed circuit board using high power ultrasound in a calcium chloride-based deep eutectic solvent.*

*Rodolfo Marin Rivera<sup>a</sup>, Christopher E. Elgar<sup>a</sup>, Ben Jacobson<sup>b</sup>, Andrew Feeney<sup>b</sup>, Paul Prentice<sup>b</sup>, Karl Ryder<sup>a</sup>, Andrew P. Abbott<sup>a</sup>.*

<sup>a</sup> *School of Chemistry, University of Leicester*

<sup>b</sup> *James Watt School of Engineering, University of Glasgow*

*Chapter 3* describes the technical details of the primary equipment, solutions and key code used throughout the project, as follows:

- Process of making and storing each DES used through the project.
- The experimental tank setup within which the sonications were performed.
- The high-speed cameras and sources of illuminations for each.

- The PCD used and filtering protocol applied to the data.
- An in-depth guide on the manufacturing process of the PCD

*Chapter 4* details an in-depth comparison of the final PCD compared to a commercially manufactured cavitation detector – the CaviSensor, manufactured and on loan from the National Physical Laboratory. This comparison, using a single laser-induced bubble, studies sensor position against sensitivity and other relevant metrics to justify selection of the PCD.

*Chapter 5* describes a detailed characterisation of the cavitation activity in three different DESs of varying viscosity as well as deionised water at the tip of two commercially available ultrasonic horns of different system powers, for varying input vibrational amplitudes sampled at fine increments. Firstly, the periodicity of bubble-cluster collapse and shockwave generation is studied to establish the cavitation behaviour in each solution across both ultrasonic horns in order to investigate crossover regions between the two horns. Secondly, the effects of input power on cavitation activity in DES was studied to optimise input parameters for favourable outcomes in terms of cavitation structure and intensity. The data described in *Chapter 5* has been disseminated at the following international conference, selected for oral presentation:

*17th Meeting of the European Society of Sonochemistry (ESS), Jena, Germany, Aug 28th – Sep 1st, 2022.*

*Characterising cavitation activity generated by an ultrasonic horn in a Deep Eutectic Solvent for efficient precious metal recovery from e-waste.*

*Ben Jacobson<sup>1</sup>, Rodolfo Marín Rivera<sup>2</sup>, Chunhong Lei<sup>2</sup>, Jeff Kettle<sup>1</sup>, Mark Hodnett<sup>3</sup>, Gawen Jenkin<sup>2</sup>, Karl Ryder<sup>2</sup>, Andrew Abbott<sup>2</sup>, Andrew Feeney<sup>1</sup>, Paul Prentice<sup>1</sup>*

<sup>1</sup> *James Watt School of Engineering, University of Glasgow, Glasgow, G12 8QQ, UK*

<sup>2</sup> *School of Chemistry, University of Leicester, Leicester, LE1 7RH, UK*

<sup>3</sup> *National Physical Laboratory, Teddington, TW11 0LW, UK*

And subsequent publication in a journal paper, accepted for submission to *Ultrasonics Sonochemistry*, November 2023:

*A mechanistic study identifying improved technology critical metal delamination from printed circuit boards at lower power sonications in a deep eutectic solvent.*

*Ben Jacobson<sup>a</sup>, Shida Li<sup>a</sup>, Rodolfo Marin Rivera<sup>b</sup>, Paul Daly<sup>a</sup>, Christopher E. Elgar<sup>b</sup>, Daniel Mulvihill<sup>a</sup>, Andrew P. Abbott<sup>b</sup>, Andrew Feeney<sup>a</sup>, Paul Prentice<sup>a</sup>*

<sup>a</sup> *James Watt School of Engineering, University of Glasgow, Glasgow G12 8QQ, UK*

<sup>b</sup> *School of Chemistry, University of Leicester, Leicester, LE1 7RH, UK*

*Chapter 6* investigates a dual-perspective delamination of printed circuit boards (PCBs) in a particular DES for the identification of the specific cavitation phenomena underpinning the enhanced etching rate observed in metal delamination under ultrasound. The setup of this experimental process was defined by the use of two high-speed cameras synchronously imaging both (a) the surface of the PCB for real-time imaging of the etching process combined with (b) high spatial and temporal resolution shadowgraphic imaging of cavitation activity throughout the sonication, with particular focus on cavitation events corresponding to etching of the metal surface. Giving a cutting-edge observation of the ultrasonically assisted etching process, with investigation into the effects of differing power – guided by data and knowledge from that of *Chapter 5* – on the etching process. The data presented in *Chapter 6* has been accepted for publication to *Ultrasonics Sonochemistry*, November 2023.

*A mechanistic study identifying improved technology critical metal delamination from printed circuit boards at lower power sonications in a deep eutectic solvent.*

*Ben Jacobson<sup>a</sup>, Shida Li<sup>a</sup>, Rodolfo Marin Rivera<sup>b</sup>, Paul Daly<sup>a</sup>, Christopher E. Elgar<sup>b</sup>, Daniel Mulvihill<sup>a</sup>, Andrew P. Abbott<sup>b</sup>, Andrew Feeney<sup>a</sup>, Paul Prentice<sup>a</sup>*

<sup>a</sup> *James Watt School of Engineering, University of Glasgow, Glasgow G12 8QQ, UK*

<sup>b</sup> *School of Chemistry, University of Leicester, Leicester, LE1 7RH, UK*

Following the main thesis conclusions, the *Future work and spinout activities* chapter summarises additional early-stage research undertaken for the ultrasonic processing and recycling of additional materials other than PCBs. In summary, two different substrates have been investigated at varying levels of depth:

Lithium Ion Battery (LiB) cathode delamination in water is investigated in collaboration with ongoing research with Dr Chunhong Li at the University of Leicester. Particularly, investigating cavitation under a horn tip to visualise material separation. This process occurs in the order of a few seconds and is significantly easier to delaminate than gold on PCBs. The ease of separation and initial investigations under the horn tip have inspired ongoing research in CavLab to develop a flow-based system of cavitating tube transducers to process shredded LiB material, which is briefly summarised.

Photovoltaic (PV) solar panels which contain a layer of silver on the surface have also been ultrasonically etched in a brine. Investigation into silver etching for PV recycling, again using high-speed imaging alongside an ultrasonic horn, is detailed here with results contributing the following grant proposal:

*A proactive Approach to the Recovery and Recycling of Photovoltaic Modules (APOLLO) funded by the European Commission: Programme – Horizon Europe Framework Programme, Topic – Recycling end of life PV modules (HORIZON-CL5-2022-D3-03-09).*

The *Future work and spinout activities* chapter concludes by summarising two spinout investigations running parallel to the main research within this thesis. Firstly, for the recovery of metals via application of electrochemistry in DES. In summary, application of ultrasound appears to increase mass transport at the surface of materials and, thus, improve the electrochemical process. Contribution to this work involves direct high-speed

observations of the sample surface during the electrochemical process. This work was carried out as a collaboration with the group led by Professor Andy Abbott at the University of Leicester and was submitted as a journal paper to Ultrasonics Sonochemistry, August 2023.

*Using ultrasound to increase metal dissolution and prevent passivation using concentrated ionic fluid.*

*C. E. Elgar<sup>1</sup>, S. Ravenhill<sup>1</sup>, P. Hunt<sup>1</sup>, B. Jacobson<sup>2</sup>, A. Feeney<sup>2</sup>, P. Prentice<sup>2</sup>, K. S. Ryder<sup>1</sup> and A. P. Abbott<sup>1</sup>.*

<sup>1</sup> *University of Leicester, Department of Chemistry*

<sup>2</sup> *University of Glasgow, School of Engineering.*

Secondly, modelling of acoustic cavitation at low driving frequency. In summary, this work investigated the mathematical modelling of mass and heat transfer of an acoustically excited single bubble under low frequency ultrasound. This section describes the experimental apparatus and process of experimentally validating the mathematical model. This research was performed as a collaboration with the group led by Professor Prashant Valluri at the University of Edinburgh with submission to the Royal Society Proceedings A.

*Mass and heat transfer in audible sound driven bubbles.*

*D. Masiello<sup>1</sup>, I. Tudela<sup>1</sup>, S. J. Shaw<sup>2</sup>, P. Prentice<sup>3</sup>, B. Jacobson<sup>3</sup>, P. Valluri<sup>1</sup> and R. Govindarajan<sup>4</sup>.*

<sup>1</sup> *University of Edinburgh, School of Engineering.*

<sup>2</sup> *Xi'an Jiaotong-Liverpool University, School of Mathematics and Physics.*

<sup>3</sup> *University of Glasgow, School of Engineering.*

<sup>4</sup> *International Centre for Theoretical Sciences.*

# 1 Overview of cavitation

## 1.1 An introduction to cavitation

Cavitation is the phenomena of isothermal liquid-vapour phase transition due to a decrease in pressure [1-4]. When the pressure ( $P$ ) decreases below the vapour pressure of the liquid ( $P_v$ ), the tensile stress (effective difference between  $P$  and  $P_v$ ) overcomes the cohesion of the fluid molecules, stretching them apart and creating a void. This void is the cavitation bubble. Fig. 1.1 represents a phase diagram for water. Here, the onset of cavitation can be generated by a decrease in pressure at approximately constant temperatures. From a simplified perspective, *Franc & Pierre* [2] stated that cavitation appears similar to boiling, except the driving mechanism is pressure differential not change in temperature.

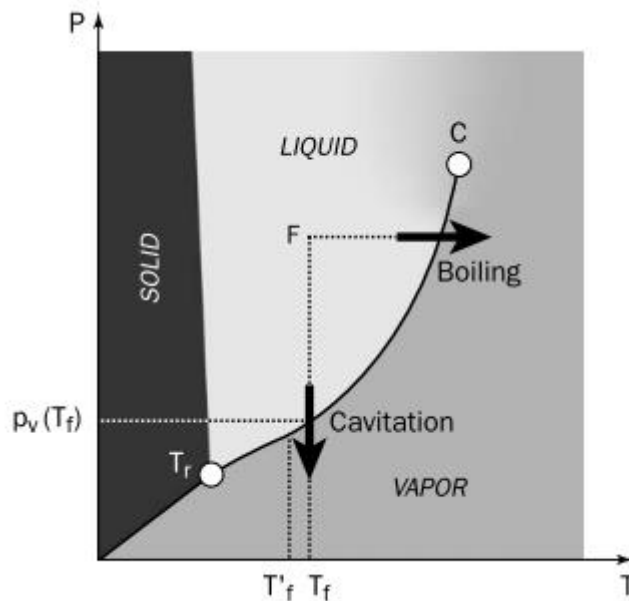


*Fig. 1.1: Phase diagram representation of the transition from liquid to vapour. The diagram presents phase transition through temperature increase (boiling) and through pressure decrease (cavitation). Taken from [2].*

Cavitation bubble nucleation is due to the negative pressure created during rarefaction exceeding the tensile strength of the liquid, causing the liquid molecules to stretch beyond

the critical molecular distance required to hold the liquid intact [3]. Typically, however, this nucleation is inhomogeneous – meaning that this nucleation occurs at pre-existing points of weakness or nucleation sites [3]. Such nucleation sites are often found in solid interfaces where the liquid meets an object or the container within which it is housed. In aqueous systems, pre-existing volumes of non-condensable gas are also found. These nucleation sites typically exist as dissolved gas or gas pockets that are stabilised in crevices of solid surfaces [5].

Cavitation as a phenomenon was first reported in 1895 by Sir John Thornycroft and Sidney Barnaby [6]. This discovery was the result of investigation into the peculiar performance of the newly built British Destroyer, *HMS Daring*. The maximum speed of the ship was observed to be less than its design specifications allowed. This was attributed to the propeller blades, which were not developing sufficient thrust. The problem was identified to be caused by the rapid motion of the blades through water, which was found to tear the water structure apart by their mechanical action. The result of investigation was the identification of what are now called cavitation bubbles. As design and performance of ships improved, the concern for the implications of cavitation bubbles grew. Resultingly, Lord Rayleigh (as commissioned by the Royal Navy) produced his seminal work in cavitation research. Rayleigh confirmed the effect observed on *HMS Daring* were the result of excessive turbulence, heat and pressure produced when cavitation bubbles imploded at the propeller surface. Furthermore, he observed that the cavitation bubbles were the source of noise made when water is heated to boiling point [7]. Rayleigh's seminal work can be thought of as the foundation of cavitation research, with his initial model a single cavitating bubble being the basis for which cavitation modelling has adapted and advanced to become today. This initial reporting of cavitation has expanded into what is now defined as hydrodynamic cavitation, whereby cavitation bubbles are generated by flow conditions and changes in ambient

pressure and is commonly observed around valves and propellers. This thesis, however, will focus on other types of cavitation: acoustic cavitation and laser-induced cavitation.

## 1.2 Acoustic cavitation

As demonstrated previously in Fig. 1.1, a negative pressure must develop to break the cohesion of the liquid molecules and form a cavity. The point of pressure at which this occurs is termed the *cavitation threshold* [4]. Intuitively, for an ultrasonic wave to generate a cavitating bubble in a liquid medium, its acoustic pressure must be greater than the cavitation threshold of the liquid to overcome its tensile strength.

An approximation of the acoustic pressure ( $P_a$ ) required to generate a cavitation bubble of radius  $R_0$  is shown in equation (1.1) [8].

$$P_a \sim P_h + \frac{0.77\sigma}{R_0} \quad (1.1)$$

$\sigma$  is the surface tension of the liquid and  $P_h$  is the hydrostatic pressure (in which approximation to atmospheric pressure is valid under normal conditions). This relationship is valid when  $2\sigma/R_0 \ll P_h$  [9].

However, cavitation can be observed at lower pressure thresholds due to the presence of pre-existing nuclei, discussed previously. Ultrasonic irradiation exists in two cycles: rarefaction and compression. Under rarefaction, a negative pressure is exerted on the medium which effectively pulls the liquid molecules apart. During this cycle, cavities (or bubbles) are formed. The rate at which gas diffuses in and out of the cavity is dependent on pressure differential between bubble and medium. During this rarefaction cycle, the bubble grows due to the pressure within the cavity slightly exceeding the pressure in the medium. Conversely, in the compression phase, liquid molecules are compressed and the pressure within the bubble is slightly less than that of the outside medium. Thus, the bubble oscillates

in size over multiple acoustic cycles. As the number of cycles progresses, the bubble continues to grow during rarefaction through a process called *rectified diffusion* which is defined as the slow growth of an oscillating gas bubble due to an average flow of mass (dissolved gas and solvent vapour) into the cavity as a function of time [8]. Rectified diffusion leads to the growth of the bubble to a resonance size, at which the natural bubble oscillation frequency matches that of the driving ultrasound frequency [8].

Marcel Minnaert in his paper “*On musical air-bubbles and the sounds of running water*” first investigated the sound produced by oscillating bubbles [10]. The resonance frequency ( $f_0$ ) was found to be strongly dependent on the radius of the bubble at equilibrium ( $R_0$ ), as well as ambient pressure ( $P_0$ ) and material properties such as ambient density of the host medium ( $\rho$ ) and the polytropic exponent of the gas within the bubble ( $\kappa$ ). The full Minnaert equation is shown in equation 1.2 [3].

$$f_0 = \frac{1}{2\pi} \sqrt{\frac{3\kappa P_0}{\rho}} \frac{1}{R_0} \quad (1.2)$$

For most gas bubbles oscillating in water at approximately atmospheric pressure and room temperature, the Minnaert equation can be approximated as

$$f_0 \times R_0 \approx 3 \quad (1.3)$$

The size of the cavitation bubble is therefore principally dependent on the frequency of driving ultrasound, with lower frequencies producing larger bubbles and vice-versa. This is, at least partially, because the longer wavelength at lower frequencies allows greater time and space for the bubbles to grow [11]. The bubbles will grow in size until they reach an unstable size and violently collapse, fig. 1.2 [12]. As with growth, lower frequencies will produce

greater cavitation collapse due to the direct relationship between bubble size and implosion energy.

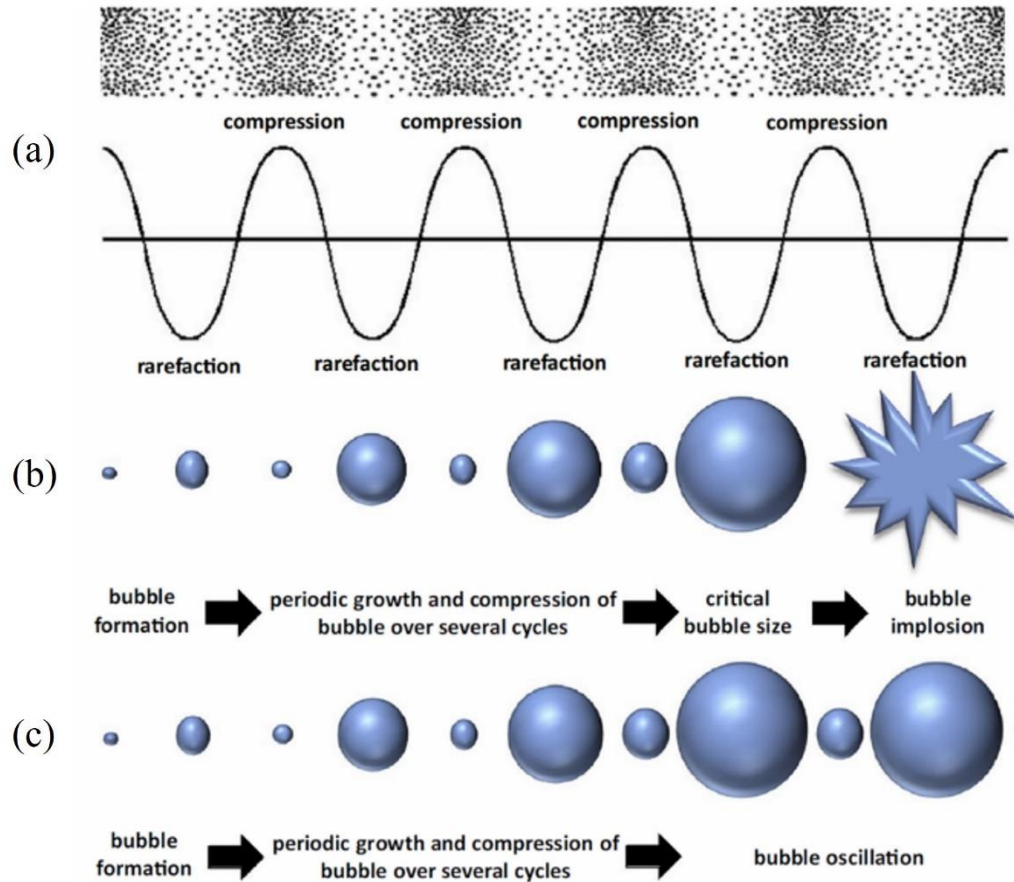


Fig. 1.2: Schematic representation of the compression and rarefaction cycles of an ultrasonic wave. (a) inertial and (b) stable cavitation. Taken from [10].

Two forms of cavitation are typically described in cavitation research, stable and inertial (also referred to as transient). If the bubble generated grows to its resonance size and then becomes unstable, collapsing every cycle or every few cycles, it is termed inertial cavitation (represented in fig. 1.2 (b)). These violent collapses occur with localised transient temperatures and pressures exceeding 15000 K and 1000 atm, respectively [13-15]. Additionally, the collapse is accompanied with a strong release of energy in the form of a bubble-collapse shockwave (BCSW), discussed in §1.3.1. Further effects of inertial cavitation are observed, such as generation of picosecond pulses of light (known as

sonoluminescence) [15-17] and free radicals [13, 18]. In stable cavitation, the ultrasonic driving pressure can alter the bubble size and shape. The bubble oscillates, with stiffness provided by the gas within the cavity and elastic forces provided by the liquid surrounding the bubble, fig. 1.2 (c). Generally, higher acoustic pressures lead to inertial cavitation with lower acoustic pressures resulting in stable cavitation [19].

### **1.3 Single-bubble dynamics**

Single bubbles are an exception in acoustic cavitation, specifically generated as the most basic constituent units for bubble modelling and experimental investigation into bubble dynamics. Although single bubbles have limited efficacy as a representation of the typical multi-bubble configurations, the understanding of specific phenomena arising from cavitating bubbles is often more easily studied with a single bubble.

#### **1.3.1 Bubble-collapse shockwaves**

When an inertially cavitating bubble collapses, a BCSW is radiated [20]. this is observed in fig. 1.3 where the BCSW can be observed at 0  $\mu\text{s}$  and 56  $\mu\text{s}$  (corresponding to the period of driving in this example). Here, the BCSW is observed at collapse of the bubble, when the gas volume reaches maximum compression [21]. The bubble then rebounds and grows to a maximum radius followed by a subsequent collapse at the next compression phase of oscillation. These shock emissions are thought to contribute, at least in part, to destructive action observed during bubble-mediated operations such as acoustic cleaning [20, 22].

Observation of these shockwaves can be performed by use of a high-speed camera with a pulsed-laser illumination (such a camera/illumination setup is employed in this thesis and is described in detail in Chapter 3). With such a configuration, shadowgraphic high-speed imaging (HSI) facilitates direct imaging via refractive index variations imposed by the pressure transient of the propagating shockwave [4, 23-26].

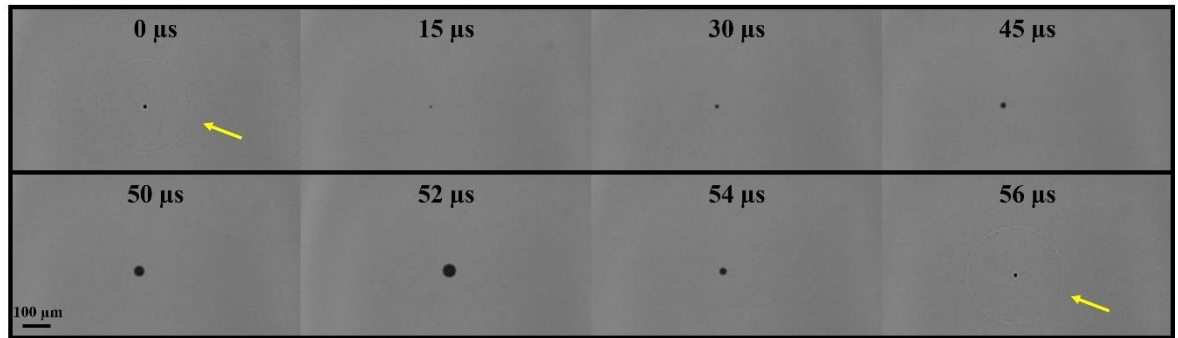


Fig. 1.3: Spherical BCSW (arrowed yellow) emitted by a single bubble driven at 17.885 kHz and detected by a high-speed camera at 2 million frames per seconds (Mfps).

### 1.3.2 Shape distortion and fragmentation

Often, wholly spherical oscillation of bubbles is not observed. Bubbles driven at moderate or high pressures become unstable, which can manifest as shape distortions and fragmentation of the bubble. Fragmentation of an acoustically driven bubble has been both simulated and experimentally observed by *Yamamoto et al* [27]. The cause of fragmentation was determined as an initial non-spherical bubble generation due to pressure distribution directly surrounding the bubble which become amplified during successive oscillations eventually causing the bubble to fragment. Observations of shape distortion and bubble fragmentation is shown in fig. 1.4. The fragmentation of bubbles can be expected to be present in almost all applications of acoustic cavitation and are a continuous source of smaller bubbles that sustain the cavitation process [4]. Small bubbles that fragment from a larger bubble typically do not translate far and will often recombine (or coalesce) with the larger bubble at maximum expansion during rarefaction [4].

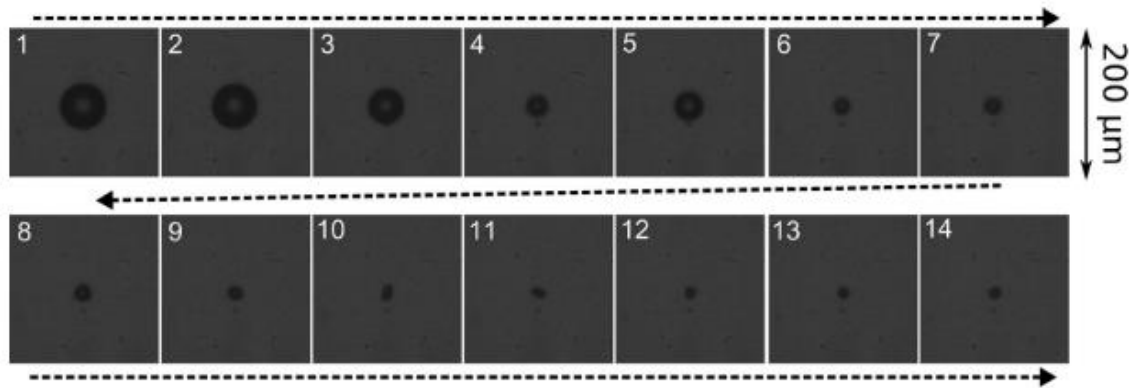
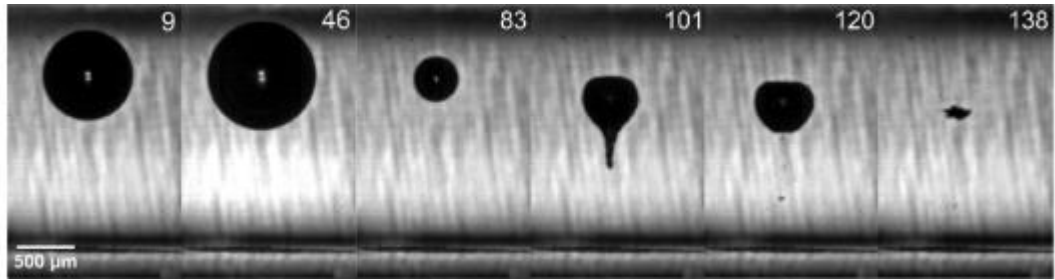


Fig. 1.4: Time variation of bubble shape oscillation and fragmentation observed from an oscillating bubble driven at 25 kHz. Taken from [26].

### 1.3.3 Jetting

When the spherical symmetry of the bubble surrounding is disturbed by a boundary (solid surface or another bubble) or by other means (bubble translation or shockwave), the disturbance causes a liquid jet to pass into and through the bubble. This is observed as the bubble exhibits an involution whereby the upper surface folds into the interior of the bubble, resulting in a high velocity ( $100 - 200 \text{ ms}^{-1}$ ) [14] liquid jet piercing through the bottom hemisphere of the bubble [20, 28]. The effective range of the jet is of the order of bubble size. These jets are known to be a contributor to surface decontamination for cleaning applications [14, 21, 29] as well as contributors to surface erosion through the generation of pitting on the surface of a solid interface [30]. *Reuter & Mettin* [21] demonstrated the generation of jetting from a single laser-induced cavitating bubble as a function of distance from a solid interface, fig. 1.5. Laser-induced bubbles offer an alternative to acoustically generated bubbles with the advantage of more control over bubble positioning and repetition of generation. For this reason, laser-induced bubbles are used and described in Chapter 4.



*Fig. 1.5: Bubble dynamics displaying a liquid jet protruding towards a solid interface at 101  $\mu\text{s}$  caused by non-symmetrical oscillation. Taken from [20].*

The various bubble phenomena exhibited by a cavitating bubble such as BCSWs, shape distortion, fragmentation and jetting, described above, are not mutually exclusive and during a sonication each will be exhibited. Fig. 1.6 demonstrates the initiation of a sonication at 20 kHz with a 500 W high-power sonotrode (used throughout this thesis and described in detail in Chapter 3, §3.2). A single cavitating bubble is observed at 12.5  $\mu\text{s}$ , the bubble is observed to be approximately spherically symmetrical. As the bubble traverses the medium between the sonotrode tip and solid interface shape oscillations are observed (at 25  $\mu\text{s}$ ) with bubble fragmentation observed from 50  $\mu\text{s}$ . A BCSW is observed at 75  $\mu\text{s}$  as the bubble collapses in the free space between the sonotrode and solid interface. As the bubble approaches the solid surface, a liquid jet is exhibited, making contact with the solid interface at 100  $\mu\text{s}$ .

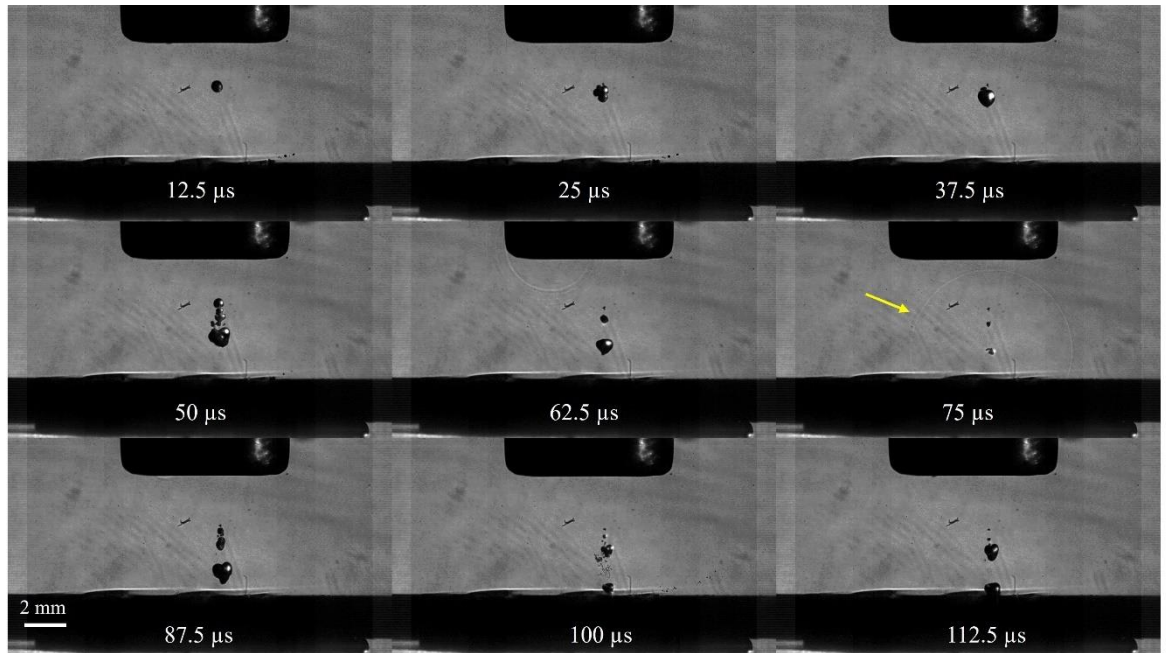


*Fig. 1.6: Observation of bubble dynamics, characterised by shape oscillation, fragmentation, BCSW (arrowed yellow) and jetting. High-speed observations generated at 80 kfps under a 20 kHz, 500 W sonotrode at the initiation of sonication.*

Practically, single bubbles offer an insight into specific cavitation phenomena with more control. However, in reality, large number of bubbles act chaotically and together, with the phenomena observed and discussed above just a part of the overall system.

## 1.4 Multi-bubble dynamics

The interaction of large numbers of bubbles introduces phenomena beyond the already complex oscillations of single bubbles [4, 31]. Bubbles in a sound field generated by an acoustic cleaning bath, for example, form clusters, branches or streamers and a range of patterns associated with the sound field driving [32]. An overall acoustic cavitation structure is composed of an inhomogeneous agglomeration of oscillating bubbles moving at different velocities [33]. These structures, because of their resemblance to electrical discharge patterns, were referred to as an *acoustic Lichtenberg figure* by *Mettin et al* [33]. These structures develop as cavitation nuclei appear at outer regions and migrate inwards to a central point where they agglomerate to form a large cluster. The large bubble cluster forms at pressure antinodes due to primary Bjerknes forces in the system<sup>1</sup>. Around the periphery of this cluster, fainter mists of bubbles are observed. These bubbles move towards the central cluster on preferred paths and appear dendritic in structure, such bubbles are called streamers [35]. The motion of bubble streamers is generated by secondary Bjerknes forces acting between neighbouring oscillating bubbles<sup>2</sup> [36]. This motion is of an order of magnitude faster than the average velocity of the fluid, with bubbles coalescing as they impact each other [14].

The bubble clusters, themselves, generate microstreaming, which is the time-independent circulation of fluid occurring around the vicinity of bubbles stimulated by oscillating pressure fields [14]. Bubble-size oscillation result in the onset of magnitude and direction fluctuations of fluid flow which, in turn, generates strong shear forces [37]. The range of this force is of the order of bubble diameter.

---

<sup>1</sup> Primary Bjerknes forces are caused by an external sound field on bubbles arising from an instantaneous pressure gradient due to the finite wavelength of the sound field [34] K.-m. Quan, "The Bjerknes forces and acoustic radiation energy," in *Energy Aspects of Acoustic Cavitation and Sonochemistry*, 2022, pp. 99-109.

<sup>2</sup> Secondary Bjerknes forces arise from the radiation pressure generated by surrounding cavitating bubbles causing mutual attraction or repulsion between bubbles [34] *ibid*.

Although not directly attributed to cavitation, an ultrasonic pressure wave will cause oscillation in a fluid, generating a back-and-forth motion causing streaming away from the driving source. This is compensated for, typically by inflow from the sides, which causes the phenomenon of acoustic streaming due to liquid flow in the opposite direction [30]. Despite not being directly related to cavitation, acoustic streaming is a crucial phenomenon for improving mass transport [14, 37, 38].

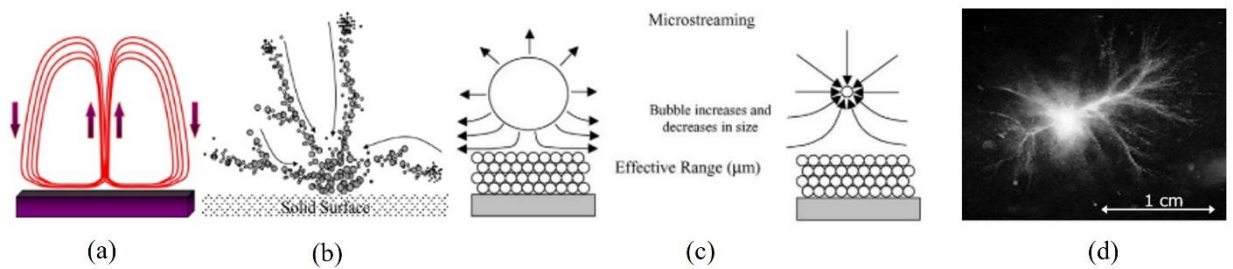


*Fig. 1.7: Schematic representation of (a) acoustic streaming, (b) streamers, taken from [29]. (c) microstreaming, taken from [13]. (d) Image of dendritic structure of streamers forming around a central densely backed cluster of bubbles, taken from [39].*

## 1.5 Monitoring cavitation

Given the large number of bubble-mediated effects that can occur during cavitation, there exists a multitude of methods designed to detect and/or measure them. A particular method may be more favourable in one scenario over another, with the best often a combination of more than one measurement methodology. Such methodologies include:

### 1.5.1 Chemical detection

As briefly mentioned previously, cavitation can result in the induction and acceleration of chemical reactions within the system, known as sonochemistry [40-42]. These chemical reactions occurring during cavitation in a liquid offer a means of measurement within the system. Many studies quantify sonochemistry, with the most common revolving around monitoring of the generation of  $\cdot\text{OH}$  radicals formed on thermolysis of  $\text{H}_2\text{O}$  within the collapsing bubble through reaction equation 1.4 .



Fricke dosimetry [43, 44] involves the addition of an acidified solution of  $\text{Fe}^{2+}$  that, when sonicated, captures the generated  $\cdot\text{OH}$  radicals to form  $\text{Fe}^{3+}$ , the generation of which is detectable using visible spectrometry.

The first reported, and perhaps still the most commonly used, method of sonochemical detection is the Weissler reaction [45]. *Weissler* studied the recombination production of  $\text{H}_2\text{O}_2$  following the generation of  $\cdot\text{OH}$  radicals. Recombined  $\text{H}_2\text{O}_2$  can be observed to oxidise  $\text{I}^-$  ions to  $\text{I}_3^-$  in a solution of potassium iodide under sonication [46, 47]. This reaction is widely used as a study of the efficiency and extent of cavitation, and can be easily monitored by spectrometry or electrochemistry [48]. The number of radicals and chemical species formed during insonation is dependent on several experimental parameters such as frequency

[49], temperature and dissolved gas quantity [50]. Hence, there is a great utility in monitoring sonochemical reaction efficiency and relating this to input parameters.

### 1.5.2 High-speed imaging (HSI)

To study the behaviour of cavitation bubbles in detail, HSI is an often-utilised tool [51]. Imaging in the order of thousands of frames per second (fps) allows for bubble dynamics to be accurately resolved. *Laborde et al* demonstrated observation of bubble clusters in water under sonication driven at 20 kHz using a high-speed camera imaging at 500 fps and a projector light source transmitted through the medium [36]. The resultant figures presented the bubbles as shadows detected by the camera and this imaging technique is referred to as shadowgraphic imaging. An example of the principal setup for shadowgraphic imaging is presented in fig. 1.8.

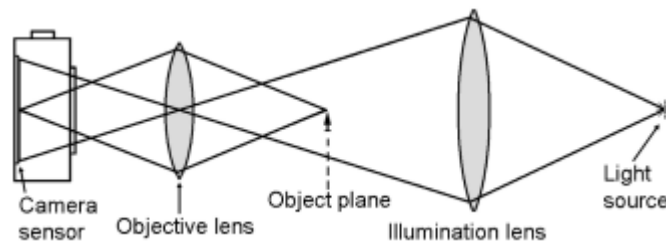


*Fig. 1.8: Basic schematic of shadowgraphic imaging setup. Taken from [52].*

In general terms, shadowgraphic imaging highlights the difference in refractive index at the interface between a body and its medium [52]. With back-illumination, the light that does not interact with the object produces a bright background, whereas the light refracted at the interface is dispersed and thus the interface is dark [52]. Resultingly, shadowgraphic imaging consists of a bright background and the shadows of the interfaces between regions with different refractive indexes. In the case of cavitation monitoring, the object is the cavitation bubble or bubble cloud. Several studies have utilised HSI as a method of direct observation of cavitation dynamics in both single-bubble [21, 28, 53, 54] and multi-bubble systems [32, 55-57]. HSI has also been adopted as a monitoring technique for various sonoprocessing

applications such as exfoliation of graphite [58], fragmentation of free floating metallics for grain refinement [59] and cleaning of fouled membranes [60]. Each study utilising HSI varies in imaging parameters, which are ultimately dictated by desired measurement outcome. Typically, frame rate and record duration require the greatest consideration. In order to assess required frame rate of the HSI system, the relevant timescale of high-speed event must be considered. Cavitation dynamics occur over the range of microseconds and, as such, typically require frame rates in the order of several thousand to resolve the necessary temporal information. However, an increase in frame rate corresponds to a decrease in record length and, thus, often a balance of parameters is required. For example, for monitoring a small number of acoustic cycles, high frame rates in the order of millions of fps are capable of resolving bubble dynamics at precise temporal resolution over a very short duration, often limited to 256 frames [24, 26]. If, however, precise temporal resolution is not required and recording over a period of several seconds is necessary, then lower frame rates facilitate a greater record length. For HSI of cavitation under ultrasound, the frame rate of the imaging should be guided by Nyquist sampling theorem. Whereby frame rate should, at a minimum, be double that of the frequency of the ultrasound [51].

### **1.5.3 Mechanical detection**

Mechanical measurement of the effects of sonication directly on or at a solid interface are often employed as a simple, fast method of assessing the degradative effect of high-power ultrasound on surfaces. For example, the erosion patterns on aluminium foil within an ultrasonic vessel are often monitored for assessment of optimal cavitation zones likely to occur due to standing fields in a cleaning bath [61-63]. Despite downsides including a lack of standardisation, poor repeatability and prolonged use resulting in contamination of the vessel, rendering continued measurements incomparable, the foil erosion test remains amongst the most commonly used mechanical detection methods of cavitation erosion [63]. Advancements on mechanical testing, particularly for a cleaning environment, utilise known

contaminants or “test soils” deposited onto phantoms that mimic narrow gaps, lumen and angled surfaces, representative of typical surgical instruments. Removal of this known test soil can then be quantified by observation and chemical assay [64, 65].

#### 1.5.4 Acoustic detection

Monitoring of the acoustic emissions generated by cavitating bubbles is amongst the most popular, accessible and versatile methods available. The generated acoustic emissions are typically collected by a single element passive cavitation detector (PCD) or hydrophone. A PCD converts an incident pressure signal into a voltage signal. A cavitating fluid exhibits a multitude of acoustic signals, which are observed in their frequency spectra and can be informative of the process in a number of ways [48, 66]. Fig. 1.9 demonstrates a typical acoustic emission spectrum generated in an ultrasonic cleaning bath driven at 40 kHz, detected with a commercially available Reson TC4035 hydrophone.

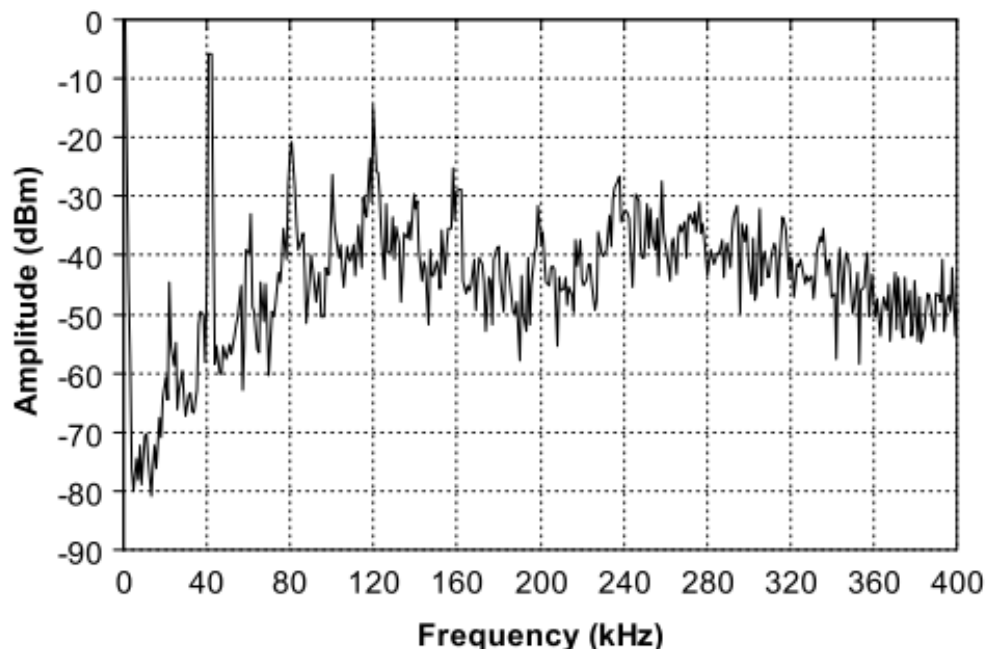


Fig. 1.9: Example acoustic spectrum generated by a cleaning bath operating at 40 kHz, measured using a commercially available underwater hydrophone. Taken from [60].

The main (fundamental) frequency component ( $f_0$ ) corresponds to the drive frequency of 40 kHz. Harmonics of the fundamental frequency component at integer multiples of  $f_0$  are observed ( $nf_0$ ) at 80 kHz and 120 kHz, corresponding to  $2f_0$  and  $3f_0$ , respectively. Harmonics of the fundamental frequency are associated with nonlinear oscillation of the cavitation bubbles [67, 68]. Subharmonics  $f_0/m$ , where  $m$  is an integer, observed in fig. 1.8 at 20 kHz, has been used to define the onset of inertial cavitation and are an important feature in definition of cavitation intensity, with the value of the subharmonic  $m$  increasing through integer values as a function of increased power [55]. This phenomenon is discussed further in Chapter 5. Ultraharmonics at  $nf_0/m$ , where  $m$  and  $n$  are integers and  $m > n$ , are also generated from the same source as subharmonics [67, 68] and are visible at  $3f_0/2$ ,  $5f_0/2$  and  $7f_0/2$ , fig. 1.8. Finally, the broadband emissions detected at all frequencies, generated by the BCSWs originating from bubbles of all sizes, are a common metric analysed to quantify inertial cavitation in a system [68, 69].

Generalisation and a lack of understanding of the complex and highly nonlinear emissions generated by cavitating bubbles can lead to difficulty in interpreting results and comparability amongst studies. The International Electrotechnical Commission (IEC) [70] recently published a technical standard for measuring cavitation noise in ultrasonic baths and reactors. The standard categorised the emission spectra, generated from ultrasonic devices operating at fundamental frequencies between 20 kHz to 150 kHz, into three categories, illustrated in fig. 1.10.

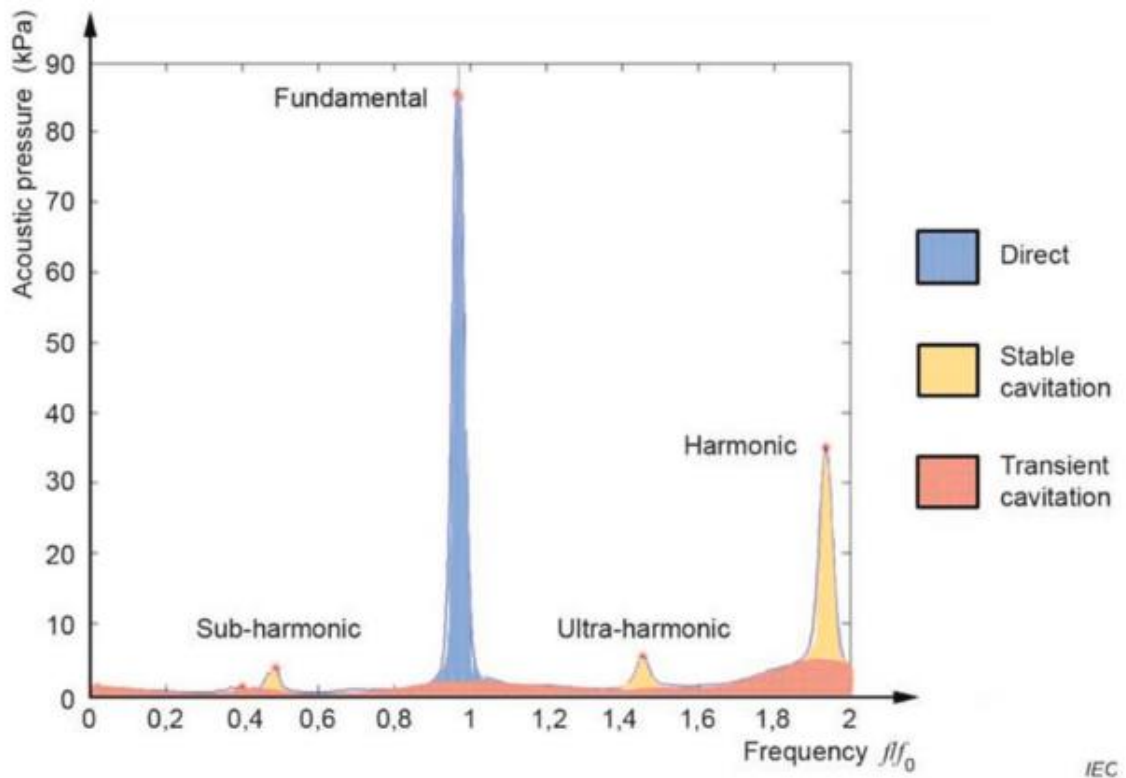


Fig. 1.10: Schematic representation of the acoustic emission spectra generated by ultrasonic devices. Categorized into direct field (blue), stable cavitation (yellow) and transient cavitation (red). Taken from [64].

The IEC document attributed the largest peak in the vicinity to  $f_0$  of the direct field (shown in blue), smaller peaks originating from harmonics, subharmonics and ultraharmonics were attributed to stable cavitation (shown in yellow) and broadband noise sampled between the peaks was attributed to inertial cavitation (red) [69]. However, such a generalisation by this standard may not accurately characterise the cavitation-mediated acoustic emissions observed. Firstly, stable cavitating bubbles can oscillate at  $f_0$  and contribute to the fundamental emission peak [71]. Secondly, in a high intensity acoustic field, waveform distortion in nonlinear wave propagation can also contribute to harmonics [72]. Furthermore, subharmonics have also recently been identified as a resulting from BCSWs from period-doubled collapsing bubbles [55, 73]. Clearly, this generalisation of the emissions generated during cavitation is inadequate and careful considerations of the parameters investigated must be considered. Further reporting on the methods used to generate acoustic data and, as

importantly, the device used to collect the data is crucial for better understanding and comparison of results between studies.

Given the broadband nature of cavitation emissions, the bandwidth of the hydrophone used to measure them becomes an important consideration [25, 48, 74]. The received signals are highly nonlinear and, thus, a sensor with the widest available bandwidth would be preferable. Acoustic measurements are often undertaken with commercially available hydrophones, selected for application and supplied with operating bandwidth [75]. Often, full details surrounding the technical specifications, including active material, of the sensor remain proprietary. Otherwise, generic commercial needle [26, 76] and capsule [77] hydrophones are used, with optional and often expensive calibration data. The most common active material for hydrophones are lead zirconate titanate (PZT) and polyvinylidene fluoride (PVdF). Table 1.1 presents an overview of some reported cavitation sensors and their respective use.

*Table 1.1: Comparison of some acoustic sensors for characterisation cavitation*

Sensor Details	Description	Operating frequency	Drive Frequency	Summary of study	Reference
Bruel & Kjaer 8103	Cylindrical PZT hydrophone	0.1 Hz – 180 kHz	120 kHz	Subharmonic at $f_0/2$ used to characterise onset of inertial cavitation	[78]
Bruel & Kjaer 8103	Cylindrical PZT hydrophone	0.1 Hz – 180 kHz	20 kHz	Subharmonic spectrum used to characterise cavitation intensity	[79]
Cavitometer ICH-3	PZT sensor	20 kHz – 11 MHz	20 kHz	Integration of broadband acoustic	[80]

				emissions up to 10 MHz	
Reson TC4038	Miniature probe hydrophone (active material unknown)	100 kHz – 500 kHz	20 kHz	Pressure measurements across sensor bandwidth with monitoring of subharmonics	[81]
NPL CaviSensor	PVdF hollow ring sensor	20 kHz – 100 MHz	40 kHz	Root Mean Square (RMS) of high-frequency ( $> 1$ MHz) acoustic emissions	[68, 82, 83]
In-house PCD	Cylindrical 15 mm PVdF hydrophone	20 kHz – 5 MHz	20 kHz	RMS of broad frequency signal with $f_0$ removed	[55, 75]

Owing to the broadband scale of acoustic emissions generated by cavitation, there are several reported hydrophones (hence frequencies measured across) reported in the literature. In addition to commercially available PCDs, the use of bespoke in-house are commonly reported [84-87]. Appendix A includes summary of the design and manufacture of an in-house shockwave passive cavitation detector (swPCD) which was the basis for construction of the swPCD manufactured and used in this thesis.

## 1.6 Monitoring of sonoprocessing using a sonotrode

For sonochemical applications, or any application involving power ultrasonics, understanding the efficiency of a device in its operating medium is of utmost importance. In ultrasonics, a transducer covers a wide range of device shapes, powers, operating frequencies and application. Perhaps amongst the most common of these devices are the ultrasonic cleaning bath and the ultrasonic horn (or sonotrode – as referred to in this thesis), shown in Fig. 1.11.



*Fig. 1.11: Commercially available sonotrode device. Taken from [88].*

For best use of these devices, it is important to understand how to optimise the performance of them in the required environment. For example, understanding how to efficiently operate an ultrasonic bath for maximum cleaning efficiency is of importance in several industries. Including, but not limited to, dentistry [88], food processing [89, 90], decontamination of surgical instrumentation [91] and mechanical devices [92]. The same applies for sonotrodes which have equally wide applications ranging from cleaning [29] to sonoprocessing [93]. Understanding of the cavitation generated from these devices may guide selection of parameters for application-specific use. Limited study has been conducted to characterise the cavitation generated by a sonotrode as a function of input power, with *Yusuf et al* [55] providing the single most comprehensive study in water, to date (discussed below and

reviewed in Appendix A). However, with the use of power ultrasonics in a variety of liquids of many different properties [81, 94, 95] and the emergence of ultrasound as a new method of enhancing precious metal delamination – which is the primary focus of this body of work – there is a necessity for a robust method of characterising cavitation under a sonotrode in a variety of liquids.

The sonotrode is one of the most commonly used laboratory-based acoustic devices. Despite this, its process mechanism is poorly understood due to the limited performance characterisation relative to the various parameters available (frequency, input power, tip-diameter, tip geometry). Briefly, a sonotrode operates via mechanical vibrations from a piezoelectric element within the main body of the device. Typical driving frequencies for sonotrodes are in the range of 20 – 40 kHz, with the ultrasound transmitted amplified through a metallic rod such that the tip vibrates at a given displacement amplitude. The amplitude of displacement is dependent on operating parameters. Typically, the smaller the tip diameter, the greater the displacement amplitude. The power of the horn is often reported using the rating power quoted by the manufacturers from which the corresponding intensity is computed by division with the radiating surface area.

For the majority of applications using a sonotrode, the tip of the device is immersed in liquid. In such applications, it is generally accepted that the cavitation in the region surrounding the tip dictate the effect of the sonication [96]. Correspondingly, operating frequency, input power and tip size; which dictate the amplitude of tip displacement; may be expected to significantly influence the characteristics of the cavitation generated. In addition to the ultrasonic parameters, the properties of the liquid such as viscosity and gas content will influence the cavitation [81, 94]. Accordingly, there is research interest in characterising the cavitation activity generated by sonotrodes. As reviewed below, HSI and acoustic detection are often combined facilitate this.

Several studies have documented the generation of a reproducible bubble cloud structure under a sonotrode [79, 97-101]. *Moussatov et al* described this as a cone-like bubble structure (CBS) which developed under sonication at 20.7 kHz through three different horn tip diameters (20, 80 and 120 mm-Ø, respectively), presented below in fig. 1.12 [99].

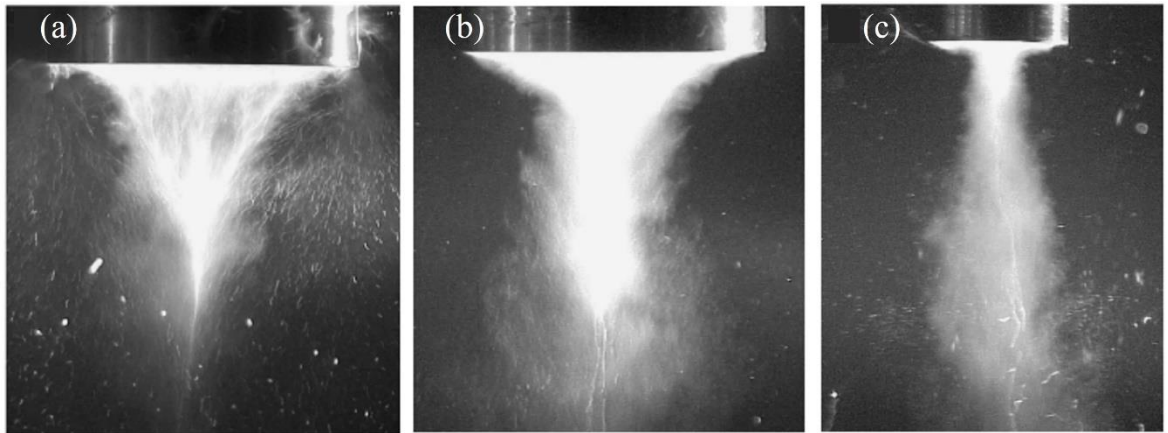


*Fig. 1.12: Example cone-like bubble structure (CBS) generated at the tip of a 20.7 kHz sonotrode operating through (a) a 120 mm, (b) 80 mm and (c) 20 mm-Ø tip in water. Taken from [93].*

The formation of this structure was attributed to the reversal of the primary Bjerknes force at high-pressure regions below the sonotrode tip. Effectively, a repulsive tension region is created which repels the bubbles, causing them to translate through other paths where the pressure is comparatively lower. The effective area of this repulsive tension region decreases with distance from the horn tip which forms the CBS. Furthermore, bubble translation is observed from the sonotrode tip, beyond the main bulk of the CBS, to the tank base. Here, smaller bubble clusters combine via secondary Bjerknes forces to form larger clusters. The formation and structure of the CBS is linked not only to tip diameter but also intensity of the source, with a greater intensity leading to a larger and more stable CBS [99].

Several other studies have attempted to characterise the cavitation activity at the tip of sonotrodes. *Jianhua and Fengjun [97]* investigated cavitation dynamics under sonication at 20 kHz through a 3 mm-Ø tip using both HSI and acoustic pressure measurement for the

purpose of validating a numerical model used to assess cavitation dynamics during surface erosion. The authors concluded that the cavitation erosion pattern was dominated by the cavity behaviour, and that the primary collapse determines the region of erosion. This primary collapse was defined as that which occurred subharmonically, with periodic spikes detected at a frequency of 5 kHz (or  $f_0/4$ ), where  $f_0$  is the driving frequency of the sonotrode.

*Birkin et al* [98] investigated primary cluster collapse via a number of measurement techniques including but not limited to HSI, calorimetry, sonoluminescence and acoustic detection at the tip of a 3 mm- $\emptyset$  sonotrode submerged 15 mm below the surface with a commercially available B & K type 8103 hydrophone. Similarly, the authors reported pressure spikes at subharmonic frequencies of  $f_0/3$  and  $f_0/4$ . This was correlated to the HSI (imaged at 100 kfps using a Phantom V7) with these pressure spikes attributed to subharmonic collapse of the primary bubble cluster. Again, the authors reported correlation of this subharmonic collapse to erosion effects at the surface of a passivated electrode at the base of the test cell.

*Žnidarčič et al* [81] noted pressure spikes, akin to those mentioned in the previous two studies at  $f_0/3$  and  $f_0/4$ . Monitoring methods consisted of HSI (at 100 kfps, Photron Fastcam SA5) and acoustic detection (measured with a Reson TC4038 hydrophone) under a 3.2 mm- $\emptyset$  tip submerged 10 mm below the surface of the water operating at 20 kHz. Crucially, the authors noted that this switch from  $f_0/3$  to  $f_0/4$  subharmonic response was triggered by an increase in driving amplitude of the sonotrode. Between these amplitudes, however, it was noted that the oscillation period of the bubble cluster was inconsistent and regularly switched between the two subharmonic responses.

*Kozmus et al* [101] reported on characterisation of cavitation under a 750 W sonotrode tip driven at 20 kHz with two tip diameters (3 mm and 4.8 mm) for the purpose of generating a cavitation parameter. Cavitation characterisation was performed with a Photron Fastcam SA-Z (the same as used throughout this thesis and described in chapter 3, §3.4) operating at

200 kfps with pressure monitored by a pressure transducer (ABB 266AST). The authors measured the effects of several parameters including liquid properties, immersion depth and tip diameter. Notably, the main cavitation cloud oscillation frequency decreased with an increase in horn amplitude. The authors noted that the cavitation cloud took longer to grow at higher powers and, consequently, longer to collapse. Resultingly the main subharmonic peaks in the detected spectra were presented at lower frequencies for increasing power.

The immersion depth of the sonotrode is of particular interest, with a recent study by *Bampouli et al* [102] investigating the ultrasound field developed in liquids of various viscosities at two immersion depths of 25 mm and 35 mm sonicated through a 50 W, 30 kHz sonotrode. Through simulation of the displacement of the sonotrode tip and shaft, a region of theorised cavitation activity was surrounding the tip was developed. The results suggested that an immersion depth of 35 mm vastly increased the overall cavitation zone for all viscosities of liquid. Furthermore, a secondary cavitation zone extending along the shaft of the sonotrode, above the tip, developed with deeper immersion. This second cavitation zone was apparent through experimental observation using sonoluminescence and luminol.

Although each of these studies appear consistent in terms of subharmonic collapse behaviour corresponding to pressure spikes in the acoustic emissions. There is a common drawback of these studies with regards to the limited number of input powers measured, giving a lack of information as to the trend in cavitation growth and dynamics over a typical input power range available to most commercial sonotrodes. *Yusuf et al* [55] presented data over the entire sonotrode power range at sufficiently fine incremental powers for the most in-depth analysis of cavitation dynamics under a sonotrode, to date. The authors incorporated monitoring of the acoustic emissions (via an in-house swPCD) in conjunction with dual perspective HSI operating at 2 Mfps over 256 frames and 100 kfps over a full 2 s sonication under the same commercially available 450 W, 20 kHz sonotrode used in this thesis.

*Yusuf et al* monitored the time-averaged shockwave content within the emission signal of the cavitation generated by the sonotrode across a range of twenty-five input powers sufficiently sampled at incremental powers. Fig. 1.13 presents the key figure generated from this study.

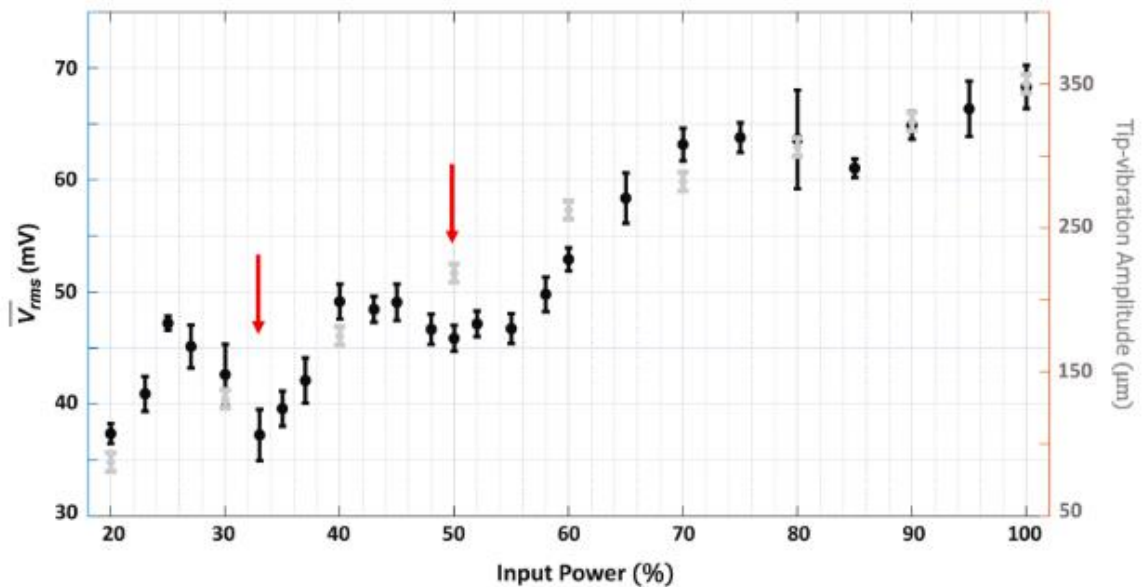


Fig. 1.13: Mean  $V_{rms}$  from five 2 s sonications at each input power, of the signal collected by the swPCD, over twenty-five input powers. Error bars represent the standard deviation within the five data sets. The peak-to-peak tip-vibration amplitude, estimated from the imaging data is also presented. Taken from [55].

It was shown that an increase in input power of the sonotrode did not correspond to a linear increase in cavitation activity, as determined by the average shockwave content in the emission signal (despite near linear increase in vibrational amplitude of the sonotrode). Instead, a series of dips in performance were observed, arrowed in fig. 1.13. Analysis of the emission data and corresponding emission spectra collected by the swPCD, and reinforced by the HSI, identified that as sonotrode input power increased, the primary cavitating cloud under the sonotrode underwent an elevated nonlinear response (discussed in detail in Appendix A, *Song et al, 2016* [73]). The cavitation cloud appeared to progress from  $f_0/2$  emissions through  $f_0/3$ , through  $f_0/4$  eventually exhibiting emissions as high as  $f_0/6$ . However, at intermediary powers where cloud oscillation was neither, for example,  $f_0/2$  or  $f_0/3$  i.e.,

there was a transition to higher order subharmonics, there was a corresponding dip in cavitation activity, despite an increase in input power. These dips in cavitation performance were correlated to the oscillations of the bubble cloud being unable to 'fix' to a single order of subharmonic oscillation. At these so-called 'transitional input powers', a disproportionately high region of non-collapsing bubbles was identified, lowering the shockwave content of cavitation emission, over the duration of sonication.

By analysis of the shockwave content emitted by the primary cavitation cloud, transitional input powers where primary cluster oscillation was inconsistent – such as that observed by [81] – were identified. *Yusuf et al* however, only demonstrated this behaviour for water. The results generated by *Žnidarčič et al* [81] extended to the observation and measurement of cavitation in ethylene glycol and glycerol (which are of the viscosity in the order of 30× and > 1000× greater than water). The authors reported limited influence of viscosity on the emergence and dynamics of the cavitation at the sonotrode tip. However, this was limited to comparison at a single input power. The findings by *Yusuf et al* demonstrate that proper characterisation of an ultrasonic source is beneficial, which would have implications in industrial sonoprocessing in terms of energy efficiency. The fundamental data underpinning the major findings of this study are highlighted in detail in Chapter 5, with comparison to experimental results generated in this thesis for validation of the procedure.

With a vast array of liquids of interest for sonoprocessing applications. Adequate characterisation of the cavitating activity in each of these liquids and with respect to the ultrasonic source, and with attention to the experimental setup parameters such as immersion depth, is essential for process optimisation. Additionally, the utility of high-power ultrasound as a means of extracting materials of value, such as gold, from ores and various waste streams has generated research interest. Resultingly, sonoprocessing of electronic waste is a research focus of industrial relevance.

## 2 Electronic Waste Recycling

### 2.1 Scope of electronic waste generation

Electronic waste (E-waste) refers to all items of electrical and electronic equipment (EEE) and its parts that have been discarded by its owner as waste without the intention of reuse [103]. Owing to this broad definition, the global E-waste monitor (2017) [103] categorises E-waste into six groups: 1) Temperature exchange equipment, 2) Screens & monitors, 3) Lamps, 4) Large equipment, 5) Small equipment, and 6) Small IT and telecommunication equipment. Each group has different lifetimes, waste quantities, economic value and environmental impact. Resultingly, collection and recycling technology differs for each group.

In 2019, approximately 53.6 Mt of E-waste was generated globally, equivalent to 7.3 kg per capita [104]. It is estimated that, by 2030, the global amount of E-waste will exceed 74 Mt, representing a 2 Mt increase per annum [104].

E-waste generation is typically managed in one of four ways [104]:

- (1) E-waste formally collected. This typically falls under national E-waste legislation, in which E-waste is collected by designated organisations, producers and government. The collected E-waste is processed in a specialised E-waste facility where valuable materials are recovered in an environmentally controlled manner and hazardous substances are managed. Residuals are typically incinerated or disposed in landfill.
- (2) E-waste in waste bins. In this scenario, the owner disposes of E-waste in normal waste bins. Resultingly, the disposed E-waste is treated with regular mixed waste and likely incinerated or sent to landfill without material recycling.

- (3) E-waste collected outside of formal systems in countries with a developed E-waste management infrastructure. In countries that have developed waste management laws and infrastructure, E-waste is collected and traded through various channels. Possible destinations for the E-waste include metal and plastic recycling or exportation. However, the hazardous materials in E-waste are often not de-polluted. In this scenario, E-waste is often not treated in a specialised facility.
- (4) E-waste collected outside of formal systems in countries with no developed E-waste management infrastructure. In developing countries, informal door-to-door collection of E-waste is common. With collectors trading and selling the E-waste to be repaired, refurbished or dismantled. Non-reusable components are typically burned, leached and melted to convert into secondary raw materials which has a severe negative impact on the environment and human health.

Reports on recycling rates of E-waste vary, estimated to be between 20-30% being properly collected and reprocessed [104-106]. Additionally, over 70% of all globally produced E-waste is exported to China, Africa and India for reprocessing [105-107]. Once exported, this E-waste is often crudely and illegally processed through dumping, leaching and incineration. Such processes have severe environmental and human health implications associated with release of inorganic (e.g., lead, mercury, chromium, arsenic) and organic (e.g., brominated flame retardants and chlorofluorocarbons) [108-112] into the air, soil and water cycles. E-waste generation is growing at a rate threefold to any other waste source [113] and, as such, to combat increasing demand for responsible and environmentally friendly recycling of E-waste, the EU issued the “Waste Electrical and Electronic Equipment (WEEE)” directive (EC, 2003 [114]; EU, 2012 [115]) forcing EEE producers to take responsibility for the collection and recycling of E-waste [116, 117].

Aside from the environmental impact, E-waste offers an important secondary source of precious metals. In the UK alone, a total of 1.6 Mt of E-waste was produced in 2019. This

waste contained an estimated 380,000 kg of technology critical metals (TCMs) with a value of \$148M per annum [118]. Table 2.1 summarises the weight composition typical metals found in common sources of E-waste.

*Table 2.1: Composition of metals in various sources of E-waste. Taken from [119].*

Type of e-waste	Weight (%)					Weight (ppm)		
	Cu	Fe	Al	Ni	Pb	Ag	Au	Pd
Printed circuit board	20	6	4	1	2.5	1000	250	90
Mobile phone	13	5	1	0.1	0.3	1380	350	210
TV board	10	28	10	0.3	1	280	20	10
Portable audio	21	23	1	0.03	0.14	150	10	4
DVD player	5	62	2	0.05	0.3	115	15	4
Calculator	3	4	5	0.5	0.1	260	50	5

## 2.2 Printed Circuit Boards

Printed circuit boards (PCBs) account for approximately 3% of all E-waste [117, 118]. Despite representing a relatively small fraction, PCBs are the largest source of metals from E-waste [116], with a metal content as high as 40% by weight [105]. Furthermore, the metal content of a PCB is typically 10-100 times greater than that of mined ores [119]. As such, they are a valuable secondary source of base (copper) and precious (gold, silver, palladium and platinum) metals. Table 2.2 demonstrates the value of metals in typical waste PCBs. Despite its very small weight fraction, at a quantity of around 250 g/T [116], gold is the most valuable component of E-waste with estimates for its consumption at over 260 MT per annum [105, 120].

*Table 2.2: Value of metals found in waste PCBs. Taken from [119].*

Metal	Value (\$ g <sup>-1</sup> )	Value in 100 g of PCB (\$)
Au	41	2.06
Cu	0.0075	0.15
Ag	0.53	0.083
Ni	0.017	0.018
Al	0.0024	0.011
Zn	0.0033	0.0066
Fe	0.000066	0.0003

All PCBs consist of three basic parts: 1) a non-conducting substrate or laminate (most commonly fiberglass reinforced epoxy resins), 2) a conducting (typically copper) substrate printed on or inside the laminate, and 3) the components attached to the substrate [105, 111], fig. 2.1. Generally, PCBs contain around 40% metals, around 30% plastics and 30% ceramics [105, 111, 121, 122]. Copper forms the conducting layer for electrical connection and accounts for 10-20% of the PCB. Precious metals, especially gold and palladium, are used as contact materials in joints. Lead and tin solder forms solid joints between PCB and components, and accounts for 4-6% of total PCB weight.

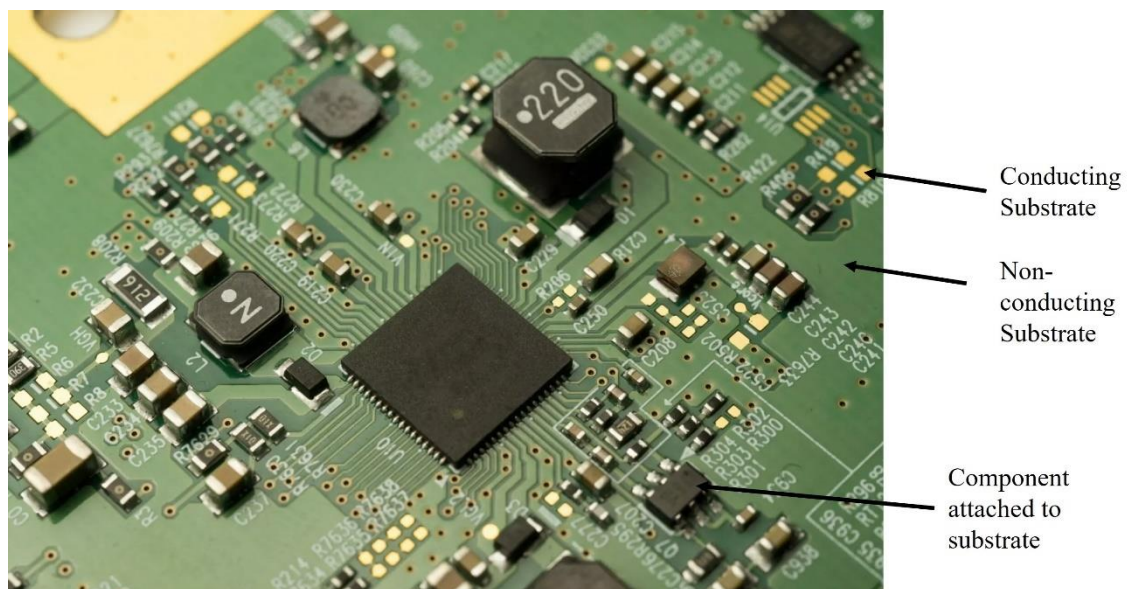


*Fig. 2.1: Common PCB structure containing attached components connected at conducting substrate terminals situated on the non-conducting laminate. Taken from [124].*

### 2.3 Printed Circuit Board recycling

Only 15% of the total discarded PCBs in the UK are subjected to any form of recycling and remaining unprocessed, portions are either dumped in landfill, incinerated or lost in “hidden flow” [111, 123]. The process for recycling this 15% typically involves three stages, each containing individual steps. The first stage involves dismantling of attached components such as microchips, resistors and capacitors for recycling and reprocessing elsewhere. The second stage involves shredding of the PCBs into small sections of approximately 1 cm<sup>2</sup>. The shredded PCBs are then separated into metallic (ferrous and non-ferrous) and non-metallic components. This separation step varies but typically involves at least one of: mechanical crushing followed by gravimetric separation, whereby high shear forces generated by multistep crushers detach the metals from the PCB, subsequent milling to particles sized under 5 mm allow separation of the lighter (non-metallic) and heavier (metallic) constituents. Electrostatic methods separate metallic and non-metallic components based on their electrical conductivity or resistivity. Alternatively, Eddy current separators exploit rare-earth permanent magnets to separate non-ferrous metals [105]. Fig. 2.2 provides an overview of typical and potential stages of PCB recycling.

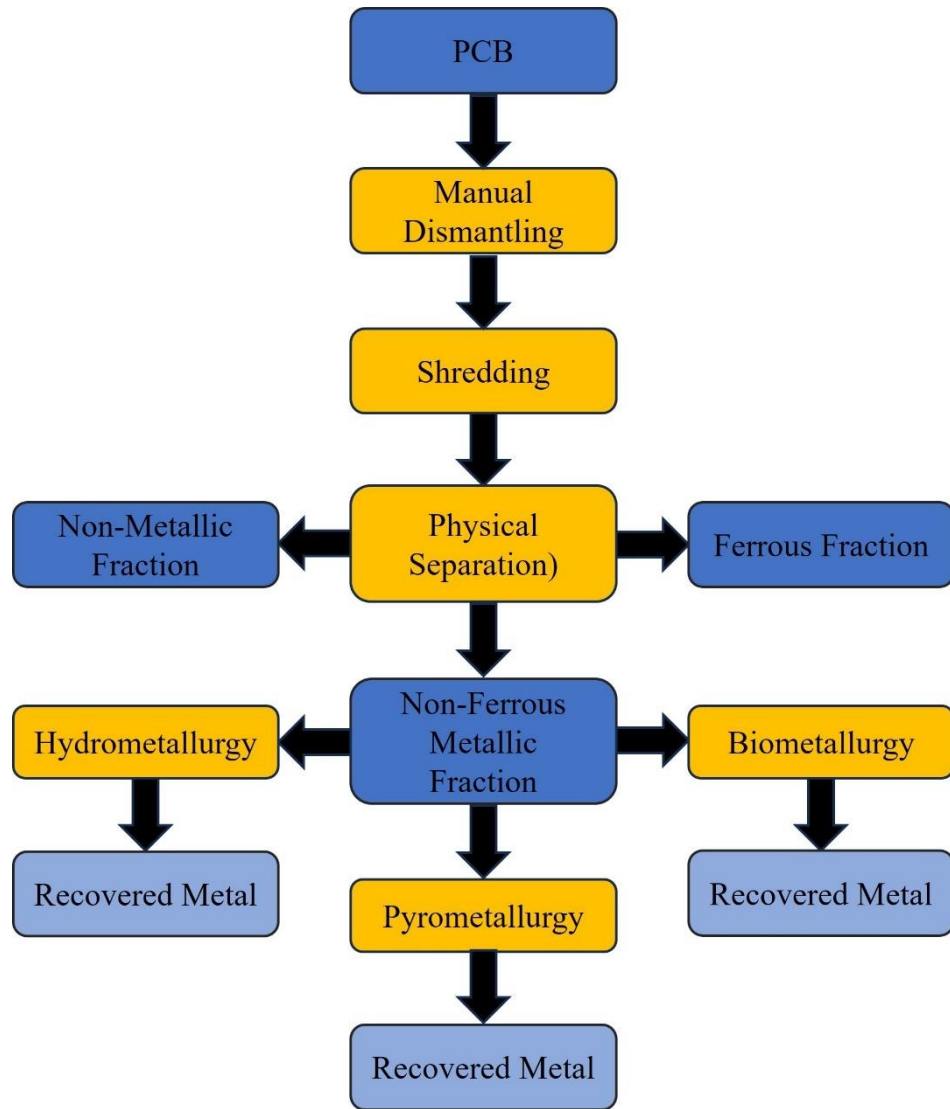


Fig. 2.2: Overview of stages involved in PCB recycling. Adapted from [105, 120, 126, 127].

Following material fraction separation, two typical refining and purification steps can be adopted for the final stage of recycling, pyrometallurgy and hydrometallurgy [117]. In these metallurgical processes, metals can be melted (pyrometallurgy), which is the traditional method of metal recycling of E-waste. In hydrometallurgy, the material is leached in acid, cyanide or caustic solution [117], with subsequent isolation and concentration of the solutions.

### **2.3.1 Pyrometallurgy**

Pyrometallurgy involves incineration, smelting or high-temperature roasting to recover mostly non-ferrous metals [117]. Currently over 70%, of the waste PCBs that are recycled, are smelted as opposed to mechanically or hydrometallurgically processed [119]. This process is primarily chosen for its generalisation – any form of waste can be smelted. Hence, E-waste can be smelted for recovery of particularly copper and gold. Pyrometallurgy, however, generates large amounts of slag, suffers from loss of precious metals due to the presence of large amounts of ceramic and glass within the waste, and is poor at recovering other metals such as iron and aluminium which are lost in the slag [119]. The recovered metal is only partially separated, resulting in limited maintenance of the metal value due to poorer purity. Furthermore, subsequent hydrometallurgical and/or electrochemical processes are required to separate the constituent metals. From an environmental perspective, pyrometallurgy generates heavy metal fumes from constituent materials with low melting point metals such as lead, mercury and cadmium, meaning comprehensive emission control systems are required [119]. It is also a highly energy intensive and expensive process [117].

### **2.3.2 Hydrometallurgy**

Hydrometallurgical processing is more selective towards metal recovery and generally less environmentally hazardous than pyrometallurgy. Maintenance of the base metals without pyrolysis allows for easier leaching and separation of precious metals, with a greater

recovery yield [111]. Several studies have demonstrated hydrometallurgical methods of copper recovery from waste PCBs [124-128] with a variety of acids used as leaching agents such as sulfuric acid, nitric acid, hydrochloric acid and acetic acid. Industrially, sulfuric acid is the most commonly used leaching agent for copper recovery due to its low cost. Recovery of precious metals, particularly gold, is more difficult due to its inert properties and proximity to other metals, with a number of studies exploring the efficacy of different leaching agents. *Sheng and Estell* [129] demonstrated multi-stage leaching of waste PCBs in nitric acid and aqua regia<sup>3</sup> for precipitation of gold. This process is, however, hindered by the need for leaching reactors that can withstand the highly corrosive leaching agents used and the release of toxic gases, which have limited the industrial feasibility of the processes [111]. Cyanide leaching is another method of recovering gold (and silver) that is commonly used in gold mining processing plants [130]. In this process, cyanide acts as a lixiviant<sup>4</sup> to leach gold from the PCBs [131]. The advantage of cyanide leaching is that it can be employed on a large scale. However, the wastewater produced is toxic both to the environment and human health [130, 131]. Thiourea is an organic agent that forms a soluble gold complex when used as a leaching agent for waste PCBs. Research into the efficacy of thiourea has advanced due to its advantage of reduced environmental impact. This is, however, compromised by its reduced selectivity; along with gold dissolution other metals such as copper iron, lead and zinc are also simultaneously dissolved [111]. Halide leaching involves precious metal extraction in fluorine, iodine, chlorine and bromine systems. In halide leaching, the gold complexes with the halide formed from gold dissolution. This process generates improved leaching rates compared to cyanide leaching with reduction on the environmental impact. However, the leaching process can produce toxic gases (most

---

<sup>3</sup> Aqua regia is a mixture of three parts concentrated hydrochloric acid and one part concentrated nitric acid. It is a traditional medium for dissolving gold.

<sup>4</sup> A Lixiviant is a chemical used in hydrometallurgy to extract elements from its ore.

notably chlorine gas) which require specialised reactors. Table 2.3 summaries the most common hydrometallurgical processes reported in the literature.

*Table 2.3: Summary of common hydrometallurgical processing for metal extraction from waste PCBs.*

<b>Authors</b>	<b>Principal Leaching Solution</b>	<b>Metal(s) Recovered</b>	<b>Advantages/Disadvantages</b>
Hsu <i>et al</i> , 2019 [132] Chaurasia <i>et al</i> , 2013 [133]	Nitric Acid	95% Copper, Lead and Tin (solder)	Recovery of high copper percentage Leaching solution cannot be used for electrodeposition of copper
Birloaga <i>et al</i> , 2013 [134] Birgoala <i>et al</i> , 2014 [135] Jha <i>et al</i> , 2014 [136]	Sulfuric Acid	95% Copper	High leaching efficiency Highly corrosive
Bas <i>et al</i> , 2014 [137] Kumar <i>et al</i> , 2014 [138]	Aqua Regia	97% gold and 98% silver	Metal recovery specificity Extremely corrosive, need for strong leaching reactors
Ashiq <i>et al</i> , 2019 [139] Ackil <i>et al</i> , 2015 [140]	Cyanide	90% gold, silver, palladium and platinum	High gold % recovery Slow reaction rate and toxicity of wastewater
Birloaga <i>et al</i> , 2013 [134] Birgoala <i>et al</i> , 2014 [135]	Thiourea	87% gold and 71% silver	Non-toxic and non-corrosive Requires large volumes of leaching solution and high cost of leaching solution
Liu <i>et al</i> , 2021 [141]	Halide	97.5% gold	High metal recovery Leaching of toxic gases

### 2.3.3 Biometallurgy

Biometallurgy has gained interest as a pathway for metal recovery from PCBs at the laboratory scale. All microbes employ metal species for structural and or catalytic functions. These microbes can bind metal ions present in the external environment at the cell surface or to transport them into the cell for various intracellular functions [119]. This metal/microbe interaction provides a possibility for tailoring selective metal recovery. The technique of biometallurgy can be summarised in two main areas: bioleaching and biosorption [142]. Bioleaching can occur in one of two mechanisms: direct action and indirect action. Direct action bioleaching is characterised by microorganisms directly oxidising minerals and solubilizing metals. Indirect action bioleaching utilises ferric iron as an oxidising agent, with the role of the microorganisms to regenerate the iron. Biosorption is a passive physico-chemical interaction between charged surface groups of microorganisms and ions in solution, in which living and dead organisms can be used [119]. Effectively, these microorganisms accumulate heavy and precious metals through both chemical and physical sorption mechanics at the cellular level. Recently, some studies have demonstrated the treatment of waste PCBs using biometallurgy. *Isildar et al* [128] noted copper and gold recovery at efficiency of 98% and 44%, respectively. However, leaching rates were slow, taking two days. Further studies have demonstrated gold leaching from waste PCBs using biometallurgy but are characterised by low recovery efficiency (10-15%) [143, 144]. Biometallurgical processes offer a number of advantages over conventional recycling methods, such as low operating cost, minimisation of the volume of chemical and or biological sludge to be handled and high efficiency in detoxifying effluents [143]. At this stage, however, the drawbacks of the process outweigh the advantages. The influence on toxic components within the PCBs on growth of microorganisms [111], comparably low metal recovery efficiency [132] and very slow reaction rate [111, 117, 119] hinder the scalability of the process for PCB recycling.

## 2.4 Deep Eutectic Solvents

The term deep eutectic solvents (DESs) was coined by Professor Andy Abbott *et al* in 2004 [145], describing mixtures of quaternary ammonium chlorides with a range of carboxylic acids. The general definition for a DES is “*a mixture of Lewis and Brønsted acids and bases which significantly reduce the freezing point compared with those of the components*” [146], although more rigorous classification definitions have been attempted [147]. For generalised purposes, a DES can be considered as an emerging class of green solvent related to ionic liquids (ILs) that are manufactured by the complexation of a compound that acts as a hydrogen bond acceptor (HBA) and a hydrogen bond donor (HBD) [148, 149]. Generally, DESs have found utility in a number of applications (discussed in §2.4.4) due to being cheap, biodegradable, non-toxic and simple to prepare compared to ILs [150].

### 2.4.1 Classification of deep eutectic solvents

DESs can be described by a general formula (2.1).



where  $Cat^+$  is in principle any ammonium, phosphonium, or sulphonium, while  $X$  is a Lewis base, usually a halide ion.  $Y$  represents a Lewis or Brønsted acid and  $z$  is the number of  $Y$  molecules that interact with the corresponding anion [149, 151]. From this general formula, there are four main classifications of DES: *Type I* – a combination of a quaternary ammonium salt and a metal chloride. *Type II* – a combination of a quaternary ammonium salt and a metal chloride hydrate. *Type III* – a combination of a quaternary ammonium salt and a HBD (typically an organic molecular component). *Type IV* – a combination of a metal chloride hydrate and HBD [150]. Typically used HBAs and HBDs are presented in fig. 2.3.

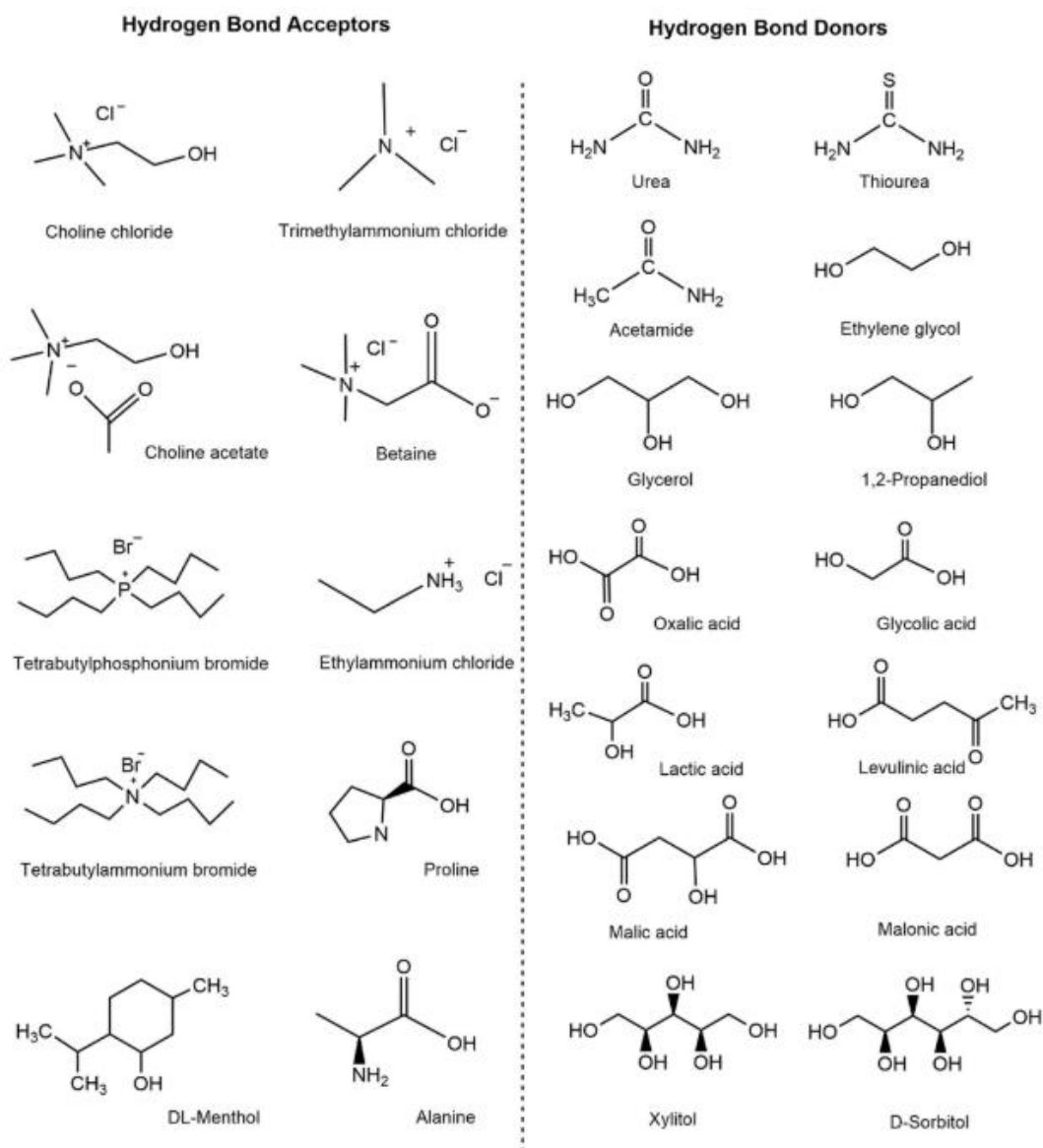


Fig. 2.3: Common HBAs and HBDs used for preparation of DESs. Taken from [153].

Type III DESs are the most studied in the literature and usually based on choline chloride (as the HBA) and various HBDs. Choline chloride has found utility as the predominantly used HBA due to it being cheap, non-toxic, and biodegradable, it is often used as an additive for feedstocks for animals [152]. The HBD are commonly amides, carboxylic acids and alcohols, which make them easily tuneable [148].

## 2.4.2 Methods of preparation and Physicochemical properties of DESs

DESs are easily prepared by simple heating and mixing of the constituent HBA and HBD, under constant stirring, to allow hydrogen bonds to form, generating a homogenous liquid. The heating temperature typically ranges from 50 – 100 °C [145, 153].

The physicochemical properties of DESs are variable and typically characterised by phase behaviour, density, surface tension, ionic conductivity and viscosity. Each property is discussed below:

### Phase Behaviour

The principal defining feature of a DES is the lower melting point of the mixture compared to its pure components. This is exhibited in fig. 2.4. DESs feature large asymmetric ions with low lattice energy leading to the aforementioned low melting point. The difference in freezing point at the eutectic composition of a mixture of HBA + HBD compared to that of a theoretical ideal mixture,  $\Delta T_f$ , is related to the magnitude of the interaction (through hydrogen bonding) between HBA and HBD. The larger the interaction, the larger the  $\Delta T_f$  [149] which is achieved at a given composition of HBA and HBD.

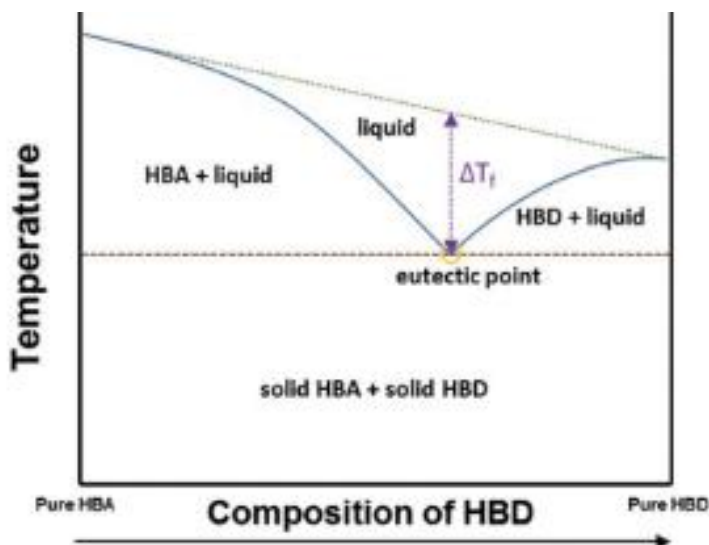


Fig. 2.4: General phase diagram of a DES consisting of one HBA and one HBD. The eutectic point represents the composition at which the minimum melting temperature is achieved. Taken from [150].

Martins *et al* [147] stated the “deep” in DES should only be prescribed to mixtures with a melting point lower than the theoretical ideal eutectic temperature, in order to distinguish them from other mixtures [147, 151]. This was a principal finding in the initial discovery of DESs by Abbott *et al* [154], who observed a significantly lower freezing point (below 100 °C) of a DES composed of choline chloride and urea, compared to the constituent components.

### Density

The density of DESs are typically higher than that of water, and is approximately linearly related to temperature, decreasing with increasing temperature. Furthermore, the density depends on the choice of HBD as the molecular organisation and packing of the mixture is affected by the existence of holes and vacancies within the liquid [155].

**Surface tension**

The surface tension is highly dependent on the intensity of intermolecular forces between the HBD and the HBA. More viscous DESs exhibit higher surface tension. This property can be tailored by altering the selection of quaternary ammonium salt, and linearly decreases with increased temperature [151].

**Ionic conductivity**

Ionic conductivity is mainly dictated by viscosity. Given the relatively high viscosity of DESs, most exhibit poor ionic conductivities at room temperature. Correspondingly, increasing temperature (hence decreasing viscosity) leads to improved ionic conductivity. It can be further tailored through altering the molar ratio of HBA/HBD as well as using different compositions [145, 151, 156].

**Viscosity**

The majority of DESs are highly viscous at room temperature and even the comparably “low” viscosity DESs are of the order of  $30 \times$  more viscous than water [149]. The utility of DESs in some cases has been limited by their increased viscosity and hence reduced ionic conductivity when compared to aqueous electrolytes [149]. The exact viscosities of DESs specific DESs is a contested subject, with different reported values based on preparation method, presence of impurities and viscosity measurement method. However, the main influences of DES viscosity are thought to be related to the extensive hydrogen bonding between HBA and HBD, and the relationship between ion size and void (or hole) spacing within the DES free space [157].

To rationalise the viscosity with respect to motion of ions in DESs, studies have implemented the physical properties in hole theory [149, 158-160]. Broadly, hole theory assumes that, on melting, ionic material contains empty spaces that arise from thermally induced fluctuations in localised density. These holes are of random size and location, and undergo constant flux.

The radius of the average sized hole/void ( $r$ ) is related to the surface tension of the liquid ( $\sigma$ ) by equation 2.2.

$$4\pi r^2 = \frac{3.5kT}{\sigma} \quad (2.2)$$

where  $k$  is the Boltzmann constant and  $T$  is the absolute temperature. At very high temperatures, the average size of the holes are of comparable dimensions to that of the corresponding ion. Resultingly, a small ion can occupy the vacant hole easily and the fluid viscosity is low. However, at lower temperatures, coupled with larger ion size, mobility is difficult. Hence, viscosity is high [149]. Typically the ions in DESs have relatively large radii ( $1.5 - 2 \times$ ) compared to the average radius of the voids [159]. Since the viscosity of the fluid is related to the free volume and the probability of finding holes of sufficient dimensions for the solvent molecules/ions to move into, which is reduced at lower temperatures, the viscosity of DESs is high. Increasing temperature and tailoring of DES composed of smaller quaternary ammonium salts [159] can decrease the viscosity.

### 2.4.3 Applications of DESs

The promising ability to tailor DESs to fit application has led to studies of their efficacy in a number of fields, including: enhancing drug solubility and delivery [161, 162]; separation of gas mixtures [163] and biomass treatment [164]. However, the primary interest and research focus on applications of DESs has come in metallurgy. The high solubility of metal ions exhibited in DESs has made them particularly suitable for metal deposition and metal extraction. The term ionometallurgy has been used to refer to processing using DESs.

#### 2.4.4.1 Metal deposition and electropolishing

The main advantages of DESs for electrodeposition and electropolishing of metals are the ability to control metal redox potentials and deposit morphology, coupled with the ability to process water-sensitive species and deposit alloys [146, 165, 166]. DESs have demonstrated

the ability to deposit wear and corrosion-resistant coatings such as nickel, chromium and cobalt [167-170] at comparable rates to traditional aqueous-based solutions, with improved hardness of due to deposition of different crystal structures. Further deposition of metals such as copper and metal alloys have been demonstrated in DESs for use as electrodes and semiconductors in photovoltaics [171-173]. DESs have also demonstrated utility in electropolishing of stainless steels to reduce surface roughness and improve optical qualities [174].

#### **2.4.4.2 Metal recycling and extraction**

The high solubility of metal ions in DESs has been demonstrated for extraction of metals from a number of sources. *Abbott et al* [175] demonstrated that the use of iodine as an oxidising agent in DES for three separation and extraction experiments: Firstly, the authors demonstrated separation and recovery of zinc and copper powder at a purity of over 99%. Secondly, the authors demonstrated separation and recovery of gallium (Ga) – a precious metal with no primary ore source, and arsenic (As) – a highly toxic element that would usually end up in landfill without proper recycling. These elements were separated and recovered from spent semiconductors, commonly containing GaAs. Finally, the authors demonstrated leaching of gold and silver from ores which could be subsequently recovered. *Jenkin et al* [176] demonstrated the selective leaching of a variety of minerals from ores in a DES with iodine. The extraction of gold as well as tellurium (a rare element sought after for photovoltaics) from ores was demonstrated via leaching at 50 °C with recovery via electrodeposition. The demonstrated recovery using cheap, readily available and easily made DESs demonstrates a significant advantage over traditional pyro-and hydrometallurgical processes. The recovery of gold from ores, for example, typically requires both pyrometallurgical and cyanide-based hydrometallurgical processing. Tellurium is typically not recovered from ores at all and lost as waste [176].

More recently, *Marin Rivera et al* [112] demonstrated the recovery of gold and nickel from waste PCBs in DES using two different oxidising agents. The authors demonstrated the selective dissolution of the bottom copper layer of the PCB, allowing nickel and gold recovery by simple filtration. Through passive etching of the PCBs in the DES-oxidising agent solution at 50 °C, copper was oxidised into the solution and recovered in a post-process involving electrowinning<sup>5</sup>. The leaching of the copper layer allowed the remaining gold and nickel layers to be recovered by filtration as they remained as a solid residue. This study was the first to demonstrate the utility of DESs as a solution capable of recycling E-waste. The advantages of low cost, environmentally friendliness and availability demonstrated potential for DESs as an industrially-scalable alternative to current techniques [112].

#### 2.4.4 Current limitations

DESs are often characterised by their high viscosity, which slows dissolution kinetics. The etching of the waste PCB blocks demonstrated by *Marin Rivera et al* [112] was a slow process, taking up to 8 hours for evidence of delamination of the metals. Although the process enables high selectivity for the separation of metals, the process is mass transfer limited due to the high viscosity of the solvents [177] which is also detrimental to conductivity and diffusion of metal ions.

To overcome the limitations of mass transfer, some studies have demonstrated process intensification using high power ultrasound [178, 179]. Ultrasound-assisted leaching for metal recovery from ores using conventional hydrometallurgical processing in the presence of strong mineral acids and bases has been demonstrated. Copper recovery from ores was demonstrated to be over 70% greater under dual frequency sonication at 20 kHz and 40 kHz [179]. Further studies have demonstrated enhanced copper recovery in DES under sonication [178]. Using a 20 kHz, 180 W sonotrode, the authors demonstrated a 20-fold enhanced rate

---

<sup>5</sup> Electrowinning is **the electrodeposition of metals from their ores that have been put in solution via leaching.**

of copper leaching when sonicating the DES solution compared to silent conditions. Further enhancement to subsequent electrodeposition of the leached copper demonstrated a halving of the deposition time required.

Despite demonstrating utility in enhancing both leaching and electrodeposition, the study of ultrasound for extraction of metals from waste is limited. In a paper submitted to RSC Sustainability, 2023, the utility of high-power ultrasound on extraction of metals from waste PCBs was demonstrated [180].

This study demonstrated that high power ultrasound allowed to overcome the formation of passivating layers leading to the enhancement of copper dissolution at a rate 10,000 times faster than without ultrasound. This significant dissolution rate enhancement resulted in increased leaching rates, showing that metals could be extracted from the PCB much faster ( $7 \mu\text{m min}^{-1}$ ) using ultrasound compared to silent conditions ( $0.6 \mu\text{m min}^{-1}$ ).

This authors major contribution to this paper was through the study of ultrasound-mediated effects generated by the sonotrode source during a sonication. In particular, the acoustic streaming and cavitation behaviour were monitored via high-speed shadowgraphic imaging (discussed and used throughout this thesis). 15 s sonications at the tip of a 500 W sonotrode (described in detail in chapter 3, §3.2) were monitored at a frame rate of 5 kfps. Fig. 2.5 demonstrates sample HSI data taken from [180]. In this study, HSI was performed on a phantom sample comprised of a Perspex disk. Cavitation dynamics are taken as representative of sonications within the DES used for this study.

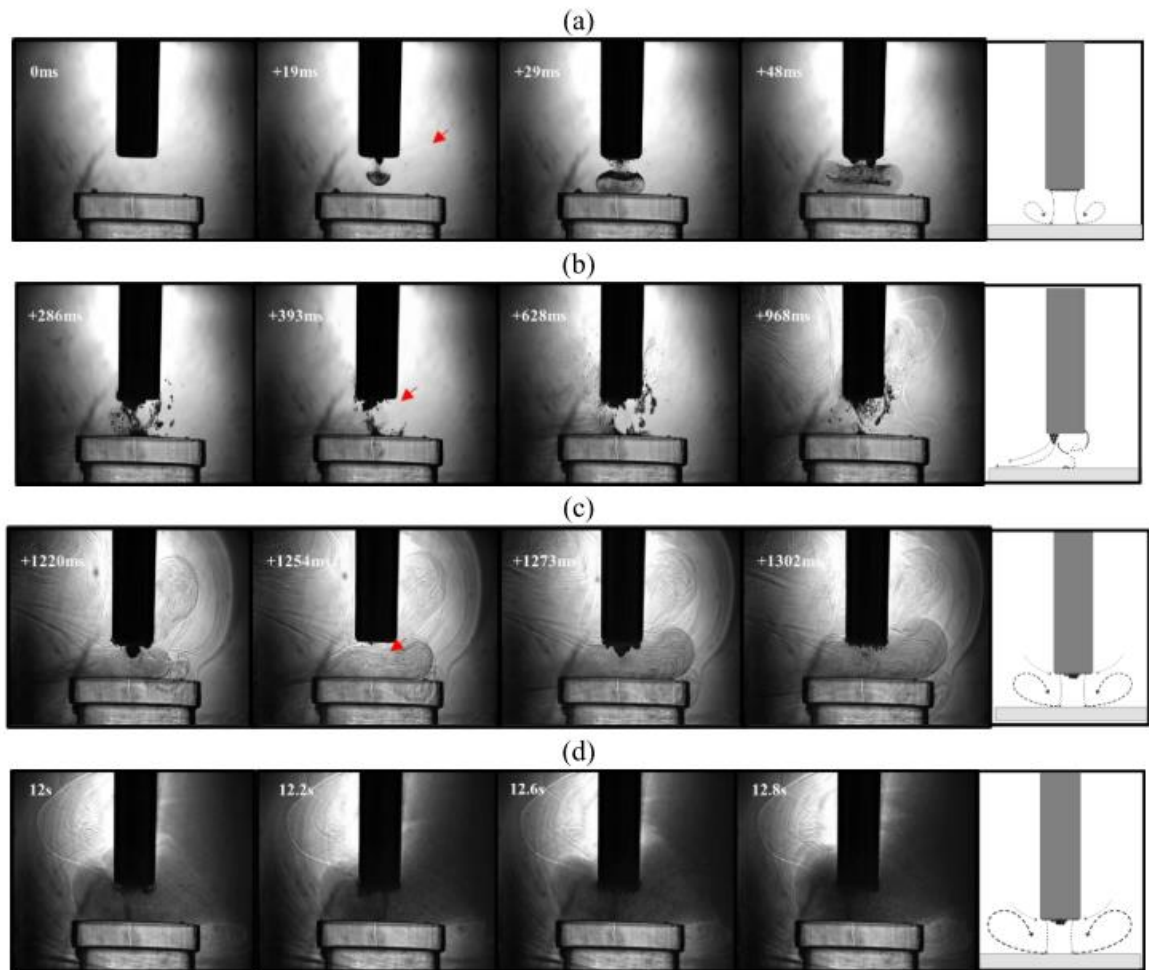


*Fig. 2.5: Representative cavitation activity in DES. Frames captured at 5 kfps during a 15 s sonication at 30% input power. (a) initial 50 ms, (b) up to 1 s, (c) ~ 1-1.3 s, and (d) ~ 12-13 s. Red arrows indicate bubble-collapse shockwaves. A schematic representation of fluid flow during each regime is presented alongside the selected frames. Scale provided by the 6 mm- $\varnothing$  tip.*

Three distinct regimes of activity were identified for the sonication in DES, as represented in Fig. 2.5 (a-c) with Fig. 2.5 (d) exhibiting a continuation of the regime of Fig. 2.5 (c), for the majority of the 15 s sonication duration. The first ~50 ms following sonotrode activation was characterised by a downward stream of bubbles emanating from the centre of the tip, due to primary radiation force-induced translation. The downward stream develops an ‘inverted mushroom’ morphology, attributable to the higher viscosity of ca. 40 mPa s. Once the stream impacts the surface, a densely packed bubbly vortex forms, spreading to

approximately twice the width of the tip-diameter, and sustained for several milliseconds. For the rest of the first second of the sonication (Fig. 2.5 (b)), the vortex evolves into a hemispherical bubble structure extruding from the edge of the tip. A bubble cluster also forms centrally on the surface, which acts to pull streams of bubbles downwards from the hemispherical structure via secondary radiation forces (attractive bubble-bubble interaction), during this dynamic phase of the insonation. From around 1.2 s into the sonication of DES (Fig. 2.5 (c)), the cavitation activity bears a closer resemblance to that generated in water; a 'primary cluster' in contact with the tip surface, oscillating to generate bubble collapse shockwaves at frequencies subharmonic to that of the tip-vibration. The sonication in DES also produces a fine bubble-mist that is sustained by the higher viscosity of the DES, which extends through much of the field-of-view by the end of the sonication period (Fig. 2.5 (d)).

Observation of the cavitation dynamics, coupled with etch rate measurements under sonication, concluded that overall cavitation behaviour contributed to removal of a passivating layer on the PCB surface during copper dissolution. However, any exact cavitation mechanisms that would directly contribute to enhanced delamination were not elucidated. Such phenomena includes bubble jetting and shockwave generation (discussed previously) which would be hypothesised to enhance delamination. Observation of the mechanisms of delamination of metals under sonication is performed in Chapter 6, with corresponding details of journal submission previously provided in Thesis Overview and Dissemination.

### 3 Primary Materials and Methods

This chapter provides brief technical descriptions of the essential experimental apparatus used throughout the results chapters 4-8 and algorithms used to analyse the experimental data reported in this thesis. CavLab has dedicated state-of-the-art devices for research related to cavitation.

The chapter is structured as follows: §3.1 presents a description of the Deep Eutectic Solvents (DESs) used and their preparation. In §3.2, the primary sources of ultrasound, the sonotrodes, are described. §3.3 describes the tank setups used for experimentation. §3.4 presents descriptions of the high-speed cameras used in the research. §3.5 presents the sources of illumination used in correspondence with the high-speed cameras. §3.6 presents the oscilloscope used for displaying and processing of acoustic data. §3.7 presents a brief review of the key features of the bespoke shockwave passive cavitation detector (swPCD) developed in CavLab and discussed previously. Finally, §3.8 details the manufacturing process of the new and adapted swPCD used throughout the results chapters in this thesis.

#### 3.1 Deep Eutectic Solvent (DES) preparation

Throughout the results chapters, a total of three DESs were used. Each DES was comprised of differing chemical constituents and ratios, giving different viscosities. Additionally, a redox catalyst was added for technology critical metal (TCM) delamination at a given concentration (Chapter 6, §6.2.1 ). Below, a description of the three DESs used in this study – Ethaline, CaDES and Reline – is provided with details on the preparation of the DESs.

1. Ethaline is a mixture of Choline Chloride ( $(\text{CH}_3)_3\text{N}(\text{Cl})\text{CH}_2\text{CH}_2\text{OH}$ ), shorthand ChCl (Sigma Aldrich,  $\geq 90\%$ ) and Ethylene Glycol ( $\text{HOCH}_2\text{CH}_2\text{OH}$ ), shorthand EG (Sigma Aldrich, 99 + %) in a 1:2 molar ratio. Ethaline-DES has a viscosity of 37 mPa S. Choline Chloride is most commonly used as an additive in feedstocks,

particularly for chickens. Ethylene Glycol is commonly used as a coolant in, for example, automobiles.

2. CaDES is a mixture of calcium chloride hexahydrate ( $\text{CaCl}_2 \cdot 6\text{H}_2\text{O}$ ) (Sigma Aldrich) and EG in a 1:1 molar ratio. CaDES has a viscosity of 59 mPa s.
3. Reline is a mixture of  $\text{ChCl}$  and Urea ACS-reagent ( $\text{NH}_2\text{CONH}_2$ ) (Sigma Aldrich, 99-100.5%) in a 1:2 molar ratio. Reline has a viscosity of 1750 mPa s.

Preparation of each of the DESs was consistent and involved heating the constituent chemicals on a hot plate at  $60^\circ\text{C}$  and mixing with a magnetic stirrer until a homogenous, colourless liquid was formed (fig. 3.1). Once mixed, DESs were stored in a sealed container out of direct sunlight and allowed to air-cool for 24 hours before use.

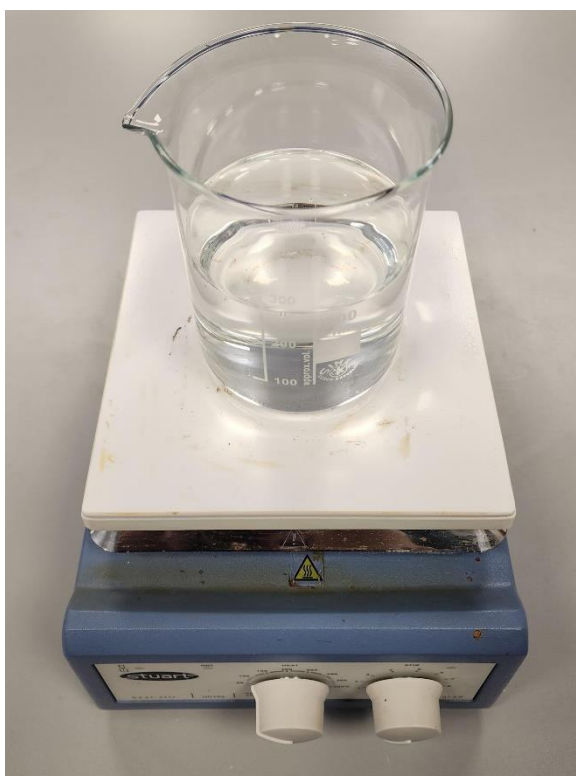


*Fig. 3.1: Colourless, homogenous Ethaline-DES formed after heating at  $60^\circ\text{C}$  and stirring.*

### 3.2 Sonotrodes

The principal sources of ultrasound used in the results chapters are two sonotrodes (fig. 3.2). Firstly, and primarily, a 450 W sonotrode (Digital Sonifier, Branson 450) operating at 20 kHz through a 230 mm long tapered *Ti* probe with a 6.4 mm-diameter ( $\varnothing$ ) tip. Secondly, a 500 W sonotrode (Ultrasonic Processor, Sonics VC-505) operating at 20 kHz through a tapered *Ti* probe with a 6 mm- $\varnothing$  tip. Each sonotrode was manually operated by its respective control console, with power programmable in 1% increments starting at 10%. The Sonics horn has a maximum operating power of 70% with the 6 mm- $\varnothing$  tip.

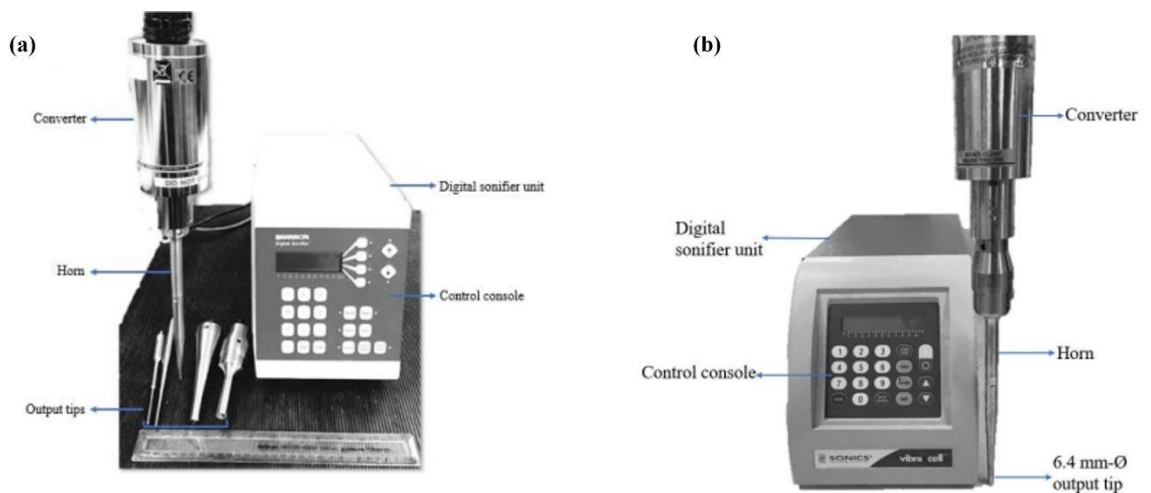


*Fig. 3.2: Branson (a) and Sonics (b) sonotrode comprising the sonotrode, output tips and control console through which all sonications were initiated.*

### 3.3 Sonication tanks

Simple sonication tanks were designed for the cavitation studies to allow for accurate and repeatable positioning of the necessary equipment such as, but not limited to, the swPCD, sonotrode and objective lens. Each tank was designed on computer aided design (CAD) software, Fusion 360, Autodesk, California USA and measured either  $100 \times 50 \times 50 \text{ mm}^3$  or  $200 \times 50 \times 50 \text{ mm}^3$ , with the longer tank required for immersion of the objective lens for dual-perspective imaging (Chapter 5). Each tank was manufactured from 3 mm thickness clear Perspex precisely cut with a laser cutter and bonded with epoxy such that imaging was possible from any coordinate positioning.

### 3.4 High-speed cameras

The choice of high-speed camera is primarily dictated by the required recording length and frame rate required to observe a particular cavitation-related phenomena. The results presented in this thesis are obtained with at least one of, or typically a combination of, two of the three high-speed cameras available in CavLab.

#### 3.4.1 Shimadzu High-speed camera

The Shimadzu HPV-X2 (Shimadzu, Kyoto Japan) (fig. 3.3) camera is capable of acquiring high-speed imaging of up to a maximum frame rate of  $10 \times 10^6$  frames per second (fps) for 256 frames per sequence, each with  $400 \times 250$  pixels. The Shimadzu camera is therefore suited to highly detailed cavitation imaging over shorter durations and was used in this thesis for imaging laser-induced single bubble collapse for swPCD characterisation (Chapter 4); vibrational amplitude assessment of the two sonotrodes at incremental powers (Chapter 5); and imaging detailed single bubble collapse dynamics (Chapter 8).



*Fig. 3.3: Image of the Shimadzu high-speed camera [183].*

### **3.4.2 Photron high-speed camera**

The Photron FASTCAM SA-Z 2100 K (Photron, Bucks UK) (fig. 3.4) high-speed camera has 128 GB of random-access memory (RAM), making it suitable for longer record durations (depending on the selected frame rate and pixel resolution). It is capable of imaging up to a maximum frame rate of  $2.1 \times 10^6$  fps and has a maximum resolution of  $1024 \times 1024$  pixels, with these parameters operating as inverses (as frame rate increases, resolution decreases and vice-versa). The Photron camera gives record lengths in the order of several seconds, allowing for cavitation-related phenomena to be recorded over more meaningful durations relevant to most of the results sections. The Photron camera was the primary camera throughout this thesis, used for shadowgraphic imaging in all results chapters 5-8. Ultimate resolution is determined by the addition of camera lenses, such lens configurations are defined in the materials and methodology sections of the relevant results chapters.



*Fig. 3.4: Image of the Photron high-speed camera [184].*

### **3.4.3 Phantom high-speed camera**

The Phantom v710 (Vision Research, New Jersey USA) (fig. 3.5) has 32 GB of RAM, again making it suitable for longer duration recordings. It has a maximum frame rate of  $1.4 \times 10^6$  fps and a maximum resolution of  $1280 \times 800$  pixels. The one unique advantage of the Phantom high-speed camera over the previously mentioned cameras is that it images in colour as opposed to grayscale. The Phantom camera was used in this thesis for directly imaging the surface of printed circuit boards (PCBs) under sonication (Chapter 6).



*Fig. 3.5: Image of Phantom high-speed camera [185].*

## 3.5 Illumination sources

### 3.5.1 Pulsed laser

The greatest quality imaging from any camera setup is provided by using the pulsed laser illumination. This is provided by synchronous 10 ns collimated laser pulses (632 nm, red) (CAVILUX Smart, Cavitar, Tampere Finland) (fig. 3.6), which both facilitates shadowgraphic imaging and provides effective temporal resolution.



*Fig. 3.6: Image of Cavilux Smart UHS comprising control unit, laser module and collimating lens. Taken from [186].*

These illumination pulses allow direct visualisation of pressure transients (including shockwaves) via refractive index fluctuation imposed to the host medium as the wave propagates, commonly known as shadowgraphic imaging [24-26]. This has been crucial in studying the role of periodic shockwaves within the signals emitted by acoustic cavitation and has been a fundamental data source for research undertaken in CavLab [24-26, 55, 73]. All former research in CavLab has performed shadowgraphic imaging with the Shimadzu high-speed camera, thus limiting record duration to 256 frames.

A key advance in this research is the combination of the pulsed laser illumination with the Photron imaging, allowing for greater resolution of detail and detection of shockwaves over a longer record length. Through synchronising of the 10 ns laser pulses with the Photron camera internal software, the illumination was configured to be on for the duration of imaging by dual synchronisation. Triggering could therefore be initiated from the camera itself, or commonly through an external triggering source from a signal generator (DG4102, Rigol Technologies, Beijing China).

### 3.5.2 Continuous light

Additional illumination, where necessary, was provided by a 150 W halogen lamp (Thorlabs, Ely UK). This high-intensity white light source provided illumination via a coupled liquid light guide and collimating lens (fig. 3.7).



*Fig. 3.7: White light source coupled to a liquid light guide and collimating lens.*

### 3.6 Oscilloscope

The oscilloscope, used for observation and saving of detected acoustic emissions was a Tektronix 5 series (Tektronix, Berkshire, UK) (fig. 3.8), capable of data collection up to 6.25 GS/s and real-time time and frequency domain observations. Data collected on the oscilloscope was stored as .mat files for direct use in MATLAB (Mathworks, MA, USA).

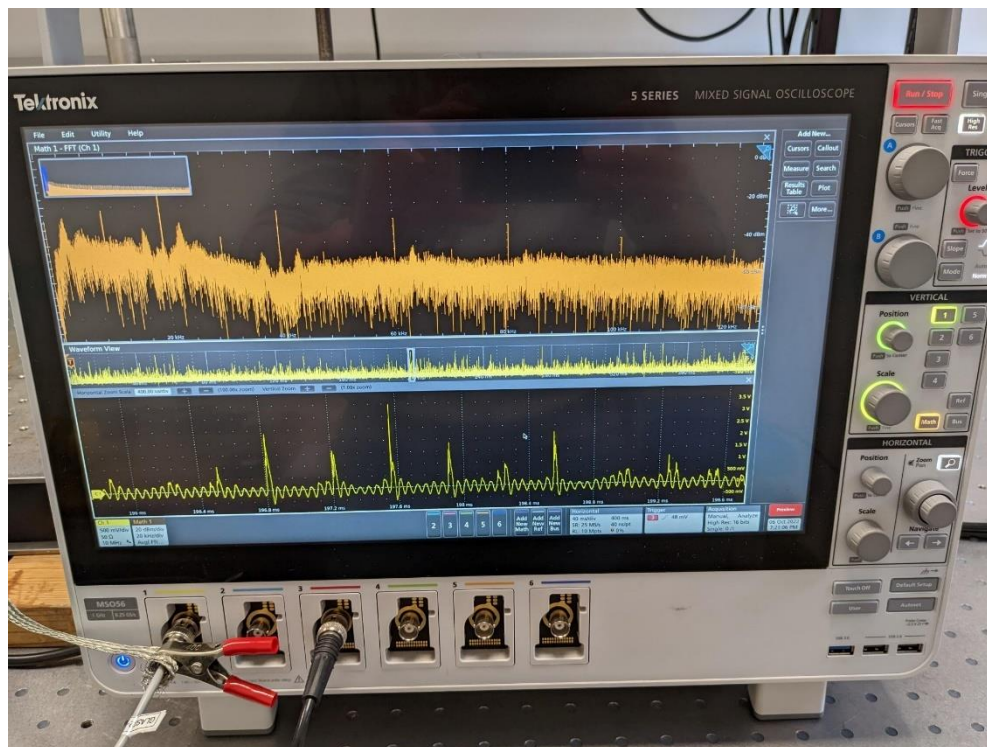


*Fig. 3.8: Image of digital oscilloscope used for collection of acoustic emission data detected by the cavitation detectors.*

### 3.7 Shockwave passive cavitation detector (swPCD)

Since the majority of industrial cavitation-mediated applications require intense cavitation to generate high-intensity shockwaves, most commercially available hydrophones are unsuitable for collecting such acoustic emissions. As the main source of ultrasound used in this thesis was a commercially available high-power sonotrode, acoustic emission data in this thesis was captured using a bespoke adapted version of the in-house 15 mm-Ø swPCD published by *Johansen et al* [75]. The following section reviews the key data with regard to manufacturing of the swPCD.

The swPCD was designed for detection of periodic shockwaves in acoustic emissions. The active material used for construction of the swPCD was 110 µm thick polyvinylidene difluoride (PVdF). The final swPCD has a high acoustic impedance Tungsten-epoxy (> 10 MRayl) backing layer to tailor the resonance of the PVdF (4.56 MRayl) for targeted bandwidth of Megahertz (MHz) and sub-MHz. Furthermore, the swPCD had a single quarter-wavelength matching layer to increase the transmission coefficient [181, 182], with improved sensitivity across the broadband signal. The main drawback of the swPCD related to its large active element area, which inhibits directivity and spatial resolution. Thus, the swPCD used in this study was manufactured to have an active element area 55% smaller than the original.

Fig. 3.9 presents (a) the final manufactured swPCD and (b) the schematic cross-section of the device showing the constituent materials and electrical connection.

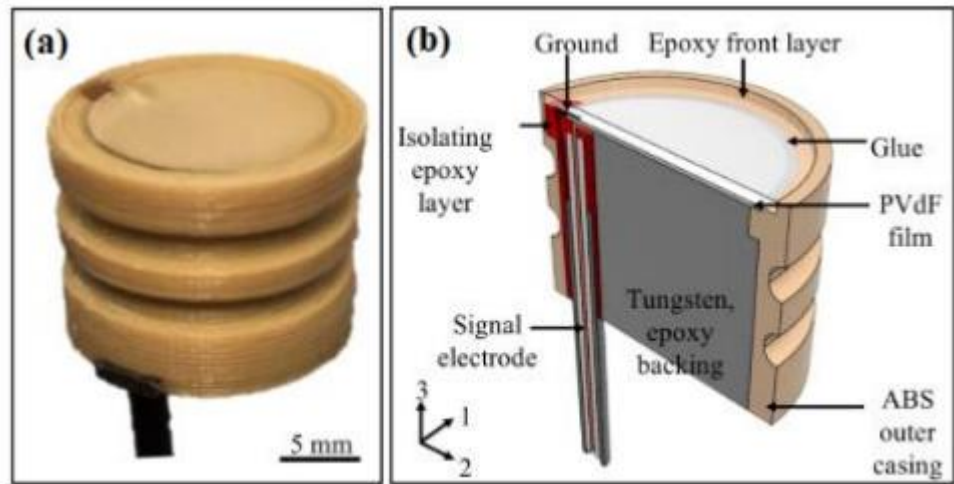


Fig. 3.9: (a) final manufactured swPCD, (b) schematic cross section of the swPCD [69].

### 3.8 Manufacturing the swPCD

The following section details the process of manufacturing the swPCD used for this thesis, who's selection was justified by the characterisation of the previous swPCD [75] and testing of this device against a commercially available sensor, Chapter 4.

The design of the swPCD was composed of five components:

1. 3D printed casing
2. The active element – 110  $\mu\text{m}$  thick PVdF
3. 50  $\Omega$  co-axial cable
4. Backing layer
5. Impedance matching layer

The construction of the swPCD was equivalent to that demonstrated in the schematic, fig. 3.9 (b).

#### 3.8.1 Casing design and manufacture

The casing used to house the key components of the swPCD was designed in Fusion360 (Autodesk, CA, USA) and was defined as a concentric tube, 16 mm in length and with an external diameter 12.5 mm. Within the front-end of the casing, a shelf that protruded 2.5 mm inwards from the external diameter was created to act as a ledge where the active material would sit. This allowed for repeatable positioning of the active material and subsequently the matching and backing layers. Along the length of the casing, a 3 mm diameter cable guide was designed for running the coaxial cable through the internal diameter of the casing. The casing was 3D printed used polylactic acid (PLA) (Makerbot, NY, USA) with a fused deposition modelling (FDM) printed (Makerbot +). Fig. 3.10 shows the design of the casing.

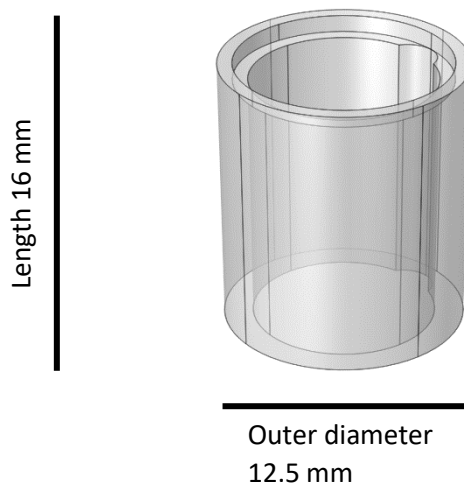


*Fig. 3.10: Schematic of swPCD casing.*

### 3.8.2 Active element preparation and bonding

A 110  $\mu\text{m}$  PVdF sheet (Precision Acoustics Ltd, Dorset, UK) [183] was cut into 10 mm- $\emptyset$  disks using a DSP/AE MT-C Stepless Adjustment Circular Cutter, fig. 3.11.

The co-axial cable used to attach to the PVdF disk was prepared by stripping approximately 1 cm of the wire outer protective layer. The internal ground and positive wires were then independently braided and separated as to not come into contact with each other during attachment to the PVdF disk, fig. 3.12.

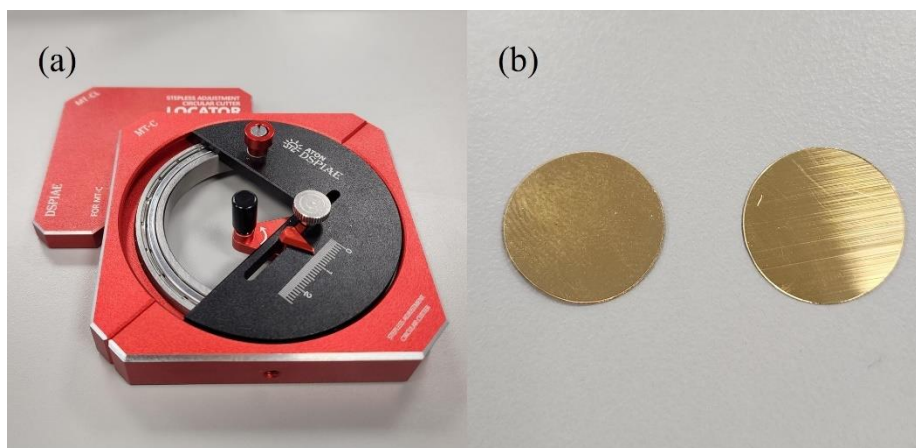


*Fig. 3.11: (a) Circular cutter and (b) 10 mm- $\emptyset$  PVdF disks.*



*Fig. 3.12: Coaxial wire stripped and braided to separate positive and ground electrodes for bonding to PVdF disk.*

Following braiding and separation, the initial protocol developed was to make the electrical connections between the positive electrode and the top PVdF surface, and the ground electrode and the bottom PVdF surface, respectively. Electrical connection was made using conductive silver epoxy (type 8813, MG chemicals). The silver epoxy connection was allowed to cure at room temperature for 24 hours. Fig. 3.13 shows a coaxial cable bonded to the PVdF disk.



*Fig. 3.13: Coaxial cable bonded to the PVdF on both the upper and lower surface with silver conductive epoxy. The ground wire and bottom PVdF surface are shown here.*

However, through trial and error, it was deduced that bonding of the coaxial cable electrodes to the PVdF at this stage was not optimal for integrating it with the casing. Due to the brittleness of the silver epoxy conducting layer, bonding of the cable and PVdF at this stage often resulted in snapping of the connection whilst fitting the active element in the casing.

Subsequent iterations adapted the manufacturing processes to fix the PVdF disk into the casing prior to electrode wiring. This is demonstrated in fig. 3.14 (a) and (b). The PVdF disk was fixed onto the inner ledge of the casing with quick setting glue at spots along the perimeter, allowing space for the positive electrode to be fed through the cable guide. Once the PVdF layer was firmly positioned, electrical connections between the cable electrodes and respective PVdF surface was made with the silver conductive epoxy.

### 3.8.3 Backing layer

The backing layer was manufactured from a combined tungsten epoxy. The epoxy was a two-part Araldite® (CY 221) and hardener (HY 956 E) which was mixed at a 5:1 ratio by weight. High density tungsten powder (Fisher Scientific) was added as a function of epoxy volume at 25% volume fraction.

The tungsten powder was first manually mixed with the Araldite. Once homogenous, the hardener was added and manually stirred for approximately 3 minutes until a viscous, homogenous substance was developed. The mixture was poured into swPCD casing as the backing layer. The swPCD was then cured at 50 °C for 24 hours in an industrial oven (Carbolite Gero, Hope, UK).

### 3.8.4 Matching layer

The matching layer was composed of the same Araldite-hardener epoxy as for the backing layer, without the tungsten epoxy. The mixed epoxy was poured into the front-end of the swPCD casing and cured for 24 hours at 50 °C. Once set, the matching layer was sanded down to be flush with the casing surface. Fig. 3.14 presents the key fabrication steps for the swPCD.

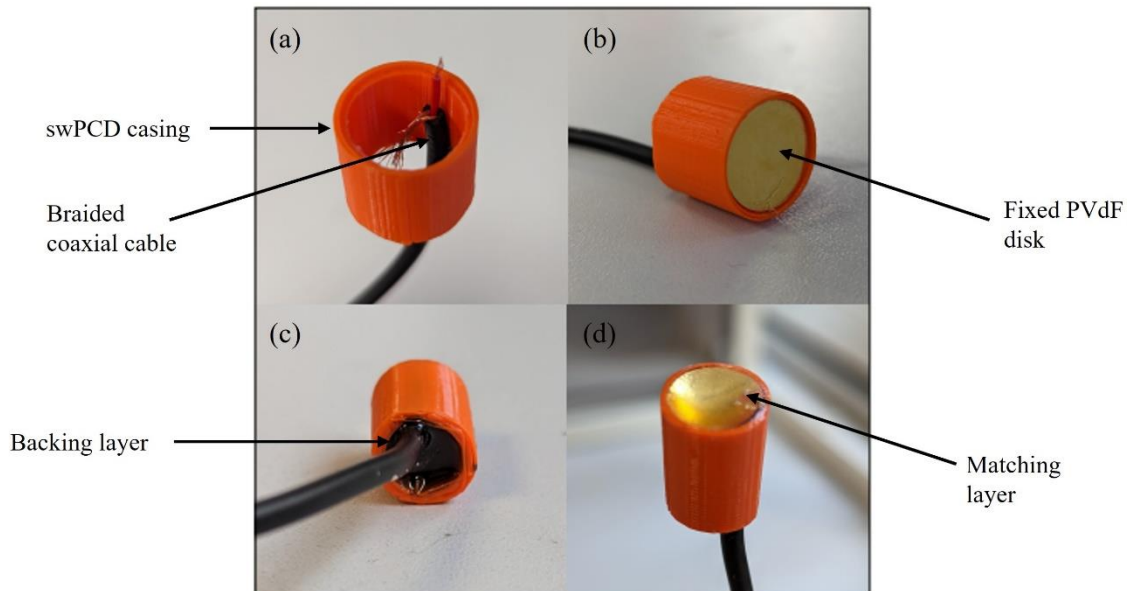


*Fig. 3.14: Steps in manufacturing of swPCD. (a) fixing of braided and separated coaxial cable within the inner guide rail of the casing, allowing the positive electrode to extend above the shelf. (b) PVdF fixed in place with ground electrode on bottom surface and positive electrode visible on the top surface for electrical connection. (c) addition of backing layer after curing. (d) addition of matching layer on front face of swPCD.*

With the swPCD material layers and wiring complete, the termination of the coaxial cable was connected to a BNC for connection to a digital oscilloscope. The swPCD was then tested for detection of BCSWs and comparison to a commercially available cavitation detector (Chapter 4).

### 3.8.5 Notable challenges/failure

The most notable failure of the devices was related to the connection of electrodes to the PVdF surface. Aside from the aforementioned breaking of connections, some swPCDs exhibited no signal after connection to an oscilloscope. This observation was attributed to creation of an open circuit due to inadequate separation of the positive electrode from the ground terminal. The primary source of this issue was identified at the interface with the active layer and casing, where the positive electrode was fed up through the guide rail. Here, a small section of the positive electrode often made contact with the lower surface of the PVdF. Subsequent iterations ensured no open circuit by ensuring the positive electrode was entirely insulated at the region near the PVdF interface, with the conductive connection only made at the end of the positive electrode.

### 3.9 Filters used for acoustic data detected by the swPCD

Filtering is routinely used for signal processing and involves the control of passing or rejecting part of a signal associated with a specific frequency or band of frequencies. Digital filters are commonly used due to their advantage of reduced noise sensitivity, accuracy and high reliability [184]. Fig. 3.15 presents the most common types of digital filters used for processing of an acoustic signal.

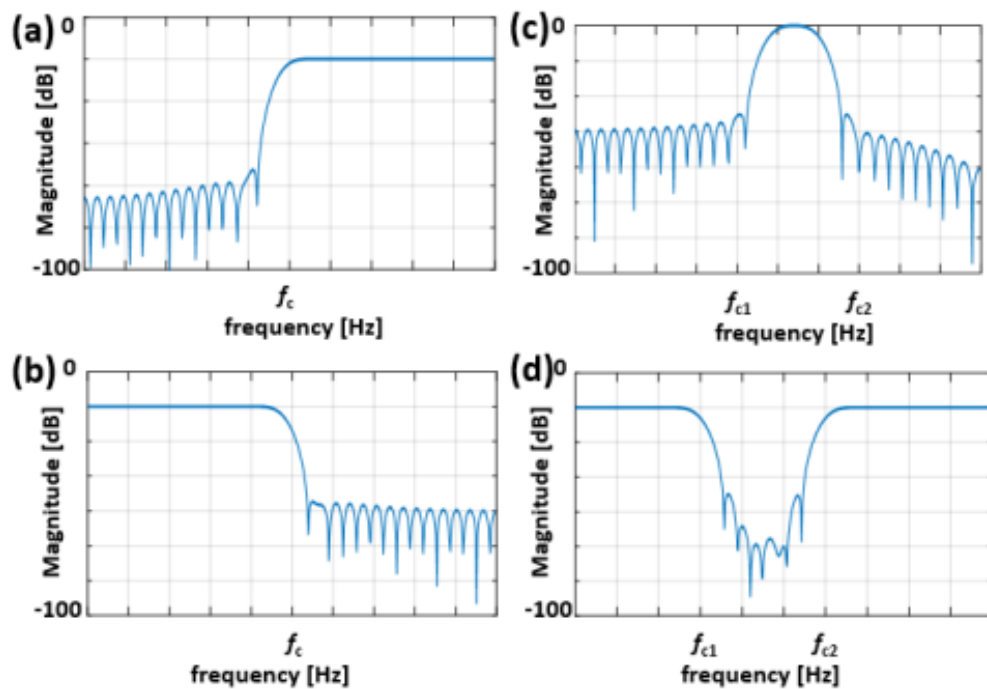


Fig. 3.15: magnitude response for (a) high-pass filter, (b) low pass filter, (c) band pass filter, and (d) band stop filter. Taken from [191].

Briefly, a high pass filter (fig. 3.15 (a)) passes through frequencies above a defined cut-off frequency ( $f_c$ ), cutting off any frequencies below  $f_c$ . Conversely, a low pass filter (fig 3.15 (b)) passes frequencies below  $f_c$  and attenuates those above. A band pass filter (fig. 3.15 (c)) attenuates all frequencies either side of two cut-off frequencies:  $f_{c1}$  and  $f_{c2}$  whilst allowing all frequencies within that range. Intuitively, a band stop filter (fig. 3.15 (d)) attenuates all frequencies within  $f_{c1}$  and  $f_{c2}$  whilst passing all other frequencies.

For this thesis, as was used by predecessors in CavLab, a finite impulse response (FIR) digital filter was used in this due to its stability and ease of use. This filter is an inbuilt function in MATLAB, 2021a, MathWorks and is written as 'fir1'. The basic components of the filter are the filter order ( $N$ ), the  $f_c$ , which must be greater than zero and less than half the sampling frequency ( $f_s$ ) – where half the sampling frequency is referred to as the Nyquist Frequency. This is the limitation imposed on digital systems to inhibit aliasing [184, 185]. The following two steps are used to define the choice of filter.

- Create the filter coefficient using  $h = \text{fir1}(N, f_c, \text{'filter type'})$ . This will return the filter ( $h$ ) with the desired type defined.
- The filter is then convolved with the voltage data collected to obtain the filtered output.

MATLAB filtering code can be found in appendix B.

## 4 Performance characterisation of the swPCD and comparison against NPL CaviSensor™

Ultimately, the swPCD in Chapter 3 was manufactured for implementation in sonoprocessing applications across a range of ultrasound sources. Before implementation, however, the swPCD performance was characterised with additional comparison against a commercially available CaviSensor. The CaviSensor has comparable properties to the swPCD and has demonstrated utility for cavitation monitoring.

This chapter details the process of characterising the swPCD manufactured in Chapter 3. Firstly, §4.1 provides a description of the sensor used for comparison to the swPCD is presented. §4.2 presents a description of the ideal properties of a cavitation detector performance. §4.3 provides an overview and rationale for the characterisation process. §4.4 presents the methodology used to characterise the swPCD with results and discussion presented in §4.5. Finally, a rationale for selecting the swPCD as a viable sensor for future acoustic measurements is provided.

### 4.1 The CaviSensor

The cavitation sensor (CaviSensor) was developed at the National Physical Laboratory<sup>6</sup>(NPL) as a sensor for characterising the acoustic emissions generated by bubbles within a liquid media. The inner surface of the CaviSensor is comprised of a 110µm thick polyvinylidene fluoride (PVDF) active material, coated by a 4mm thick polyurethane-based rubber insulating barrier which acts as a shield to cavitation emissions out with the sensor circumference [83]. The sensor measures 28mm in height with an internal diameter of 30mm (Fig. 4.1).

---

<sup>6</sup> The author is very grateful to Mark Hodnett (NPL) for provision of and guidance on the CaviSensor used in this chapter.

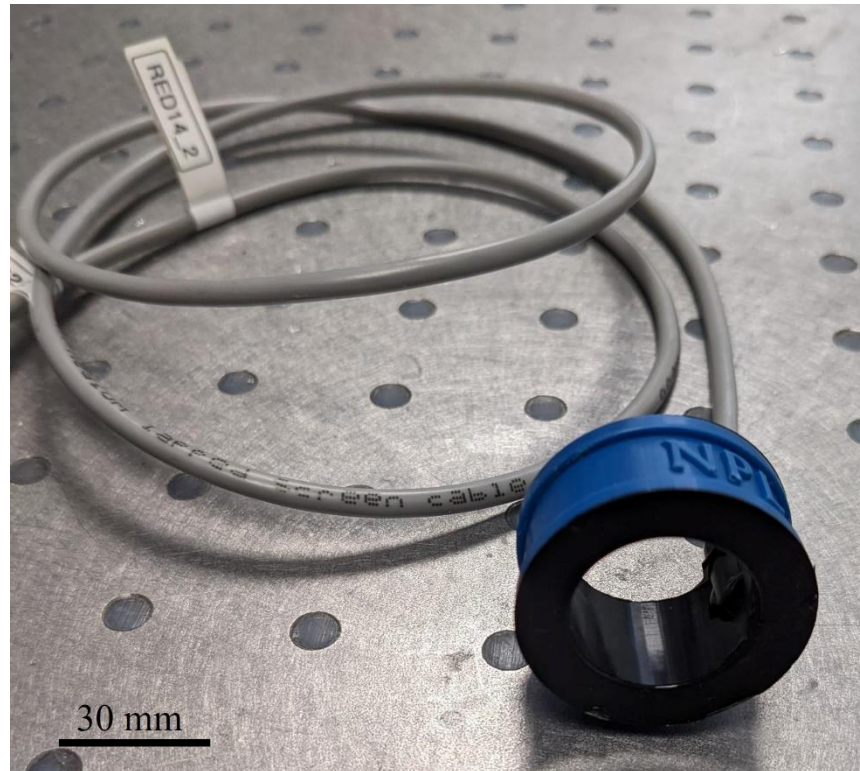


*Fig. 4.1: Photo of the NPL CaviSensor.*

Operation of the CaviSensor involves positioning the sensor parallel to the acoustic source of interest, with the inner diameter accessible to the source of ultrasound. Typical sources investigated with the CaviSensor include ultrasonic cleaning baths and sonotrodes [82, 83, 87, 186] with the advantage that a sonotrode can be directly positioned with the tip of the system within the CaviSensor circumference. The CaviSensor has been previously tested across a range of fundamental frequencies from 20 kHz – 135 kHz and over temperature ranges from 20°C - 60°C. The manufacturers note uses of the sensor for detection of frequencies ranging from subharmonics of the fundamental up to 7 MHz.

## **4.2 Requirements of a cavitation detector**

Ideally, the swPCD should detect the periodic shockwaves emitted from the cavitation cluster with the ability to detect subharmonics, and their ultraharmonics, of the drive signal, but also higher frequency components associated with cavitation such as overharmonics of the drive signal and broadband noise.

### 4.3 Characterisation of the cavitation emissions

The peak positive pressure amplitude of the shockwaves generated by the subharmonic collapse of acoustically driven cavitation clouds are somewhat variable, with clouds of more than a few component bubbles emitting multi-fronted shockwaves [24, 73]. For the purposes of characterising the swPCD, objective testing was undertaken relative to laser-plasma mediated bubble collapse shockwaves (BCSWs), which have a peak positive pressure amplitude of the shockwave proportional to the maximum radius the bubble reaches post-expansion [23, 25], thus giving reproducible shockwaves for each measurement.

The ultimate use of the swPCD is to characterise the acoustic cavitation generated by a sonotrode in a number of fluids including water and various deep eutectic solvents (DES). The newly constructed swPCD presented an apt choice for this application due to its reduced size compared to the previously used and reported swPCD [55, 75].

For comparison, the swPCD was characterised alongside the CaviSensor which also presented a viable choice due to the ability to position the sonotrode within the sensor circumference, ensuring the detected emissions were directly from cavitation at and around the horn tip and reflections from the relatively small chamber walls were limited. The hollow cylindrical geometry of the CaviSensor would be expected to exhibit improved spatial resolution due to the spherical radiating shockwaves impacting the curved geometry as opposed to the planar face of the swPCD. However, these apparent advantages come with the drawback of inhibiting concurrent HSI. Therefore, direct comparison of the newly constructed swPCD was performed against the CaviSensor to determine its efficacy and performance.

For characterisation of the LIB signal detected by the CaviSensor, the sensor was positioned by an x,y,z manipulator with the LIB induction site at the geometric centre of the CaviSensor

(fig. 4.2). This inhibited HSI as the LIB was hidden from the imaging by the CaviSensor circumference.

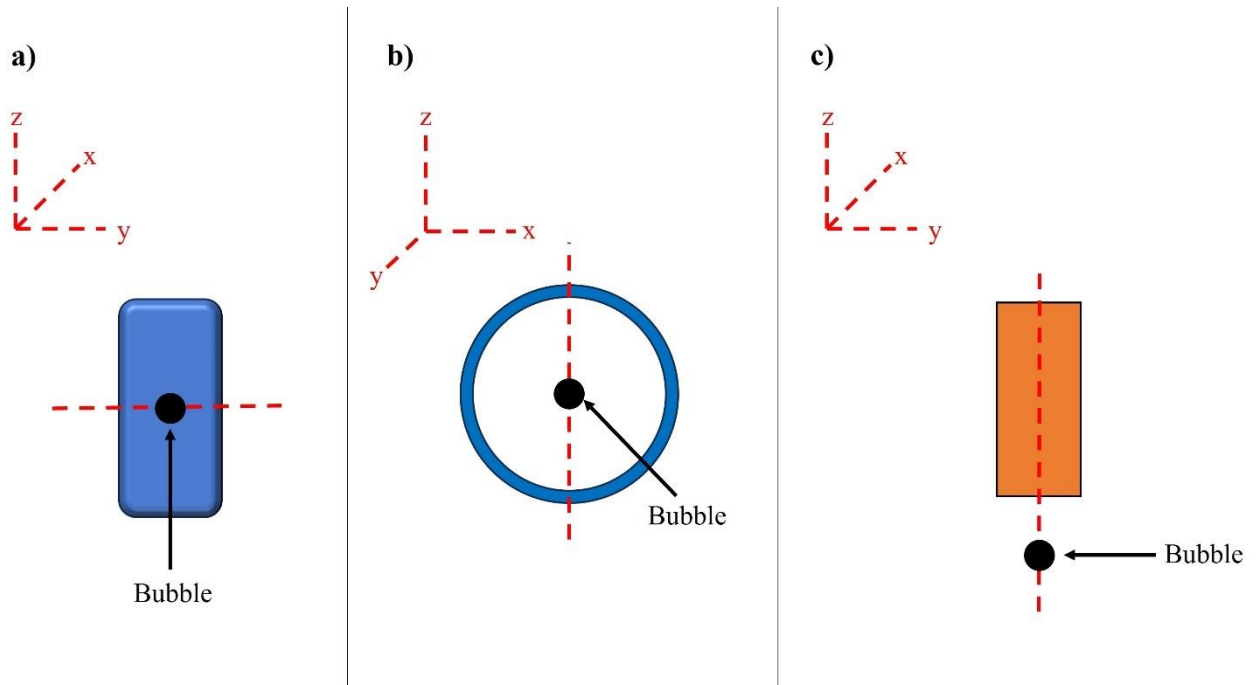


*Fig. 4.2: Schematic representation of the position of (a) and (b) the CaviSensor and (c) the swPCD relative to the LIB induction site.*

#### 4.4 Experimental setup

When a laser pulse of sufficiently high energy to cause optical breakdown is focused into a liquid, a single laser-induced bubble (LIB) is formed. A LIB undergoes an initial expansion phase following the energy deposition of the laser pulse, which the inertia of the host media decelerates eventually causing the bubble to contract and collapse [23, 25]. Acoustic detection of the LIB is characterised by emission of a series of shockwaves. The first shockwave is resultant from the plasma generation on absorption of the laser pulse, called the optical breakdown shockwave (OBSW), with the second emitted during the collapse of the single bubble after the oscillation period of the LIB, termed the BCSW. Figs. 4.4 and 4.5 demonstrate the detectable components of the signal from the LIB process and a HSI sequence of the corresponding BCSW, respectively.

For performance characterisation of the swPCD, LIBs were generated in a custom-built tank, represented in schematic form by fig. 4.3. The tank measured  $420 \times 438 \times 220 \text{ mm}^3$  and was filled with degassed, deionised water.

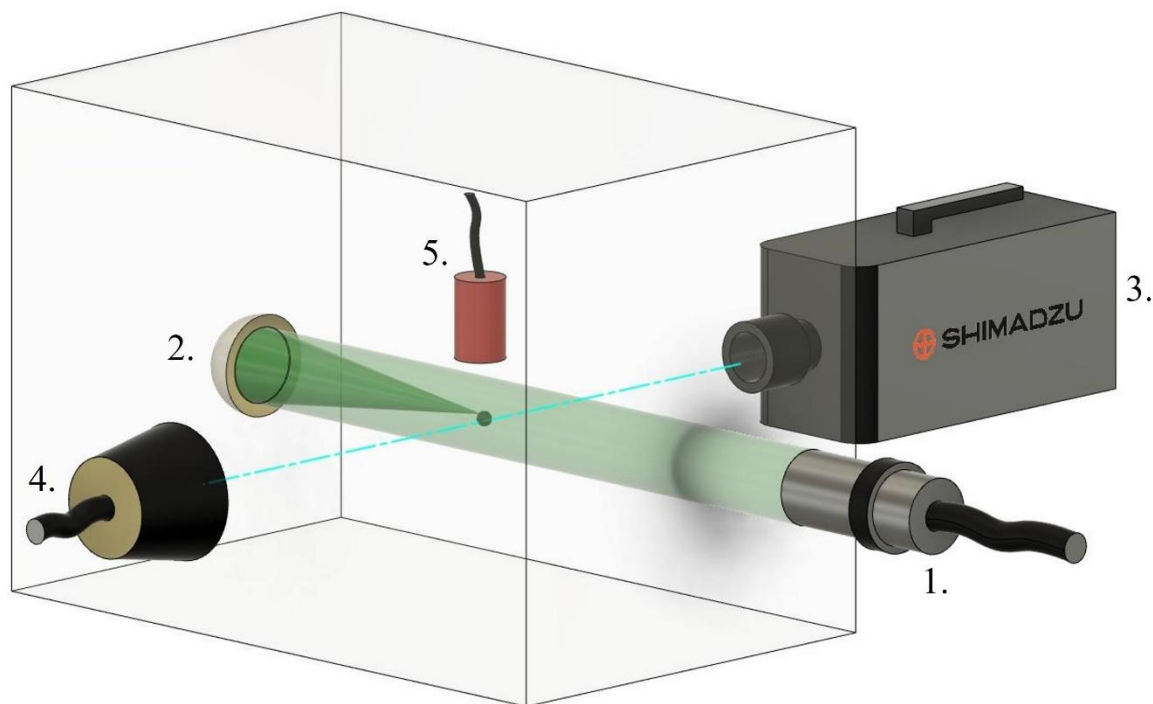


*Fig. 4.3: Schematic of the experimental configuration used for generating LIBs and detecting BCSWs with the following components: 1. Nd:YAG laser brought to focus by 2. Curved mirror. 3. Shimadzu high-speed camera providing shadowgraphic imaging with illumination provided by 4. collimated lens. 5. swPCD detecting LIB emissions.*

A single  $4.0 \pm 0.2$  mJ, 6-8 ns laser pulse (Nano S 130-10 frequency doubled Q-switched Nd:YAG, Litron Lasers, UK) (*component 1*, fig. 4.3) is transmitted through the water tank and brought to focus by reflection from a curved mirror (Thorlabs, Ely, UK) (*component 2*, fig. 4.3) which is mounted on an x,y,z manipulator within the tank. High-speed shadowgraphic imaging of the LIB process is captured at  $5 \times 10^6$  frames per second (fps) (HPV-X2, Shimadzu, Japan) (*component 3*, fig. 4.3). Illumination was provided by synchronous, to frame capture, 10 ns laser pulses (CAVILUX Smart, Cavitar, Finland) coupled to a liquid light guide and collimating lens (*component 4*, fig. 4.3). The Shimadzu offers 256 frames per imaging sequence such that the BCSW can be observed at exceptional temporal resolution. The majority of this type of literature relies on selecting specific frames from a number of HSI sequences, under the assumption that each bubble reaches an equivalent maximum bubble radius and undergoes equivalent collapse [23, 25, 54, 187]. HSI

sequences captured that did not clearly show a BCSW were rejected, and corresponding acoustic detection not considered.

The swPCD (*component 5*, fig. 4.3) was mounted on an x,y,z manipulator and positioned vertically, directly over the induction site of the LIB. Acoustic BCSW measurements were undertaken at distances of 7.5 mm, 10 mm and 15 mm ( $\pm 0.5$  mm), chosen to be comparable to that used by *Yusuf et al* [55] as well as that of the CaviSensor. The swPCD was connected to a digital oscilloscope (Tektronix 5 series, Berkshire, UK) at a sample rate of  $4 \text{ GSs}^{-1}$  and a total of five measurements were taken at each position. As there is an associated propagation delay of the BCSW between the HSI and swPCD, a delay generator (DG535, Stanford Research Systems, USA) was used to provide electronic triggering and synchronisation of each of the instruments.

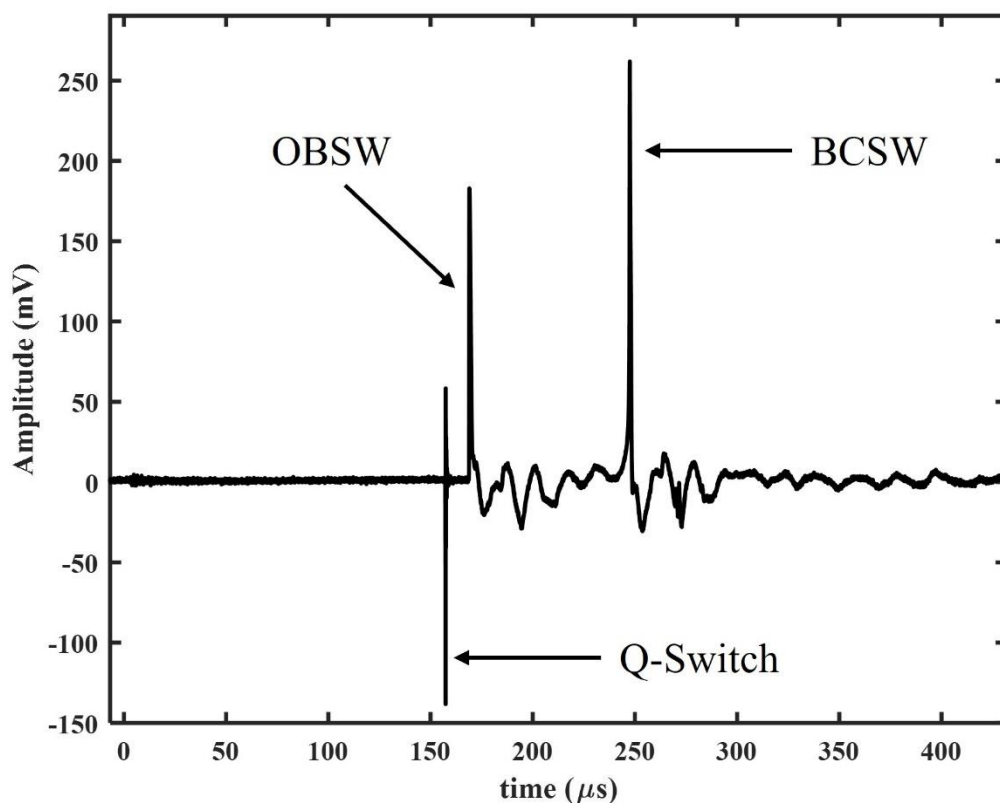


Fig. 4.4: Full swPCD voltage trace with key features of the LIB process arrowed and described in the text.

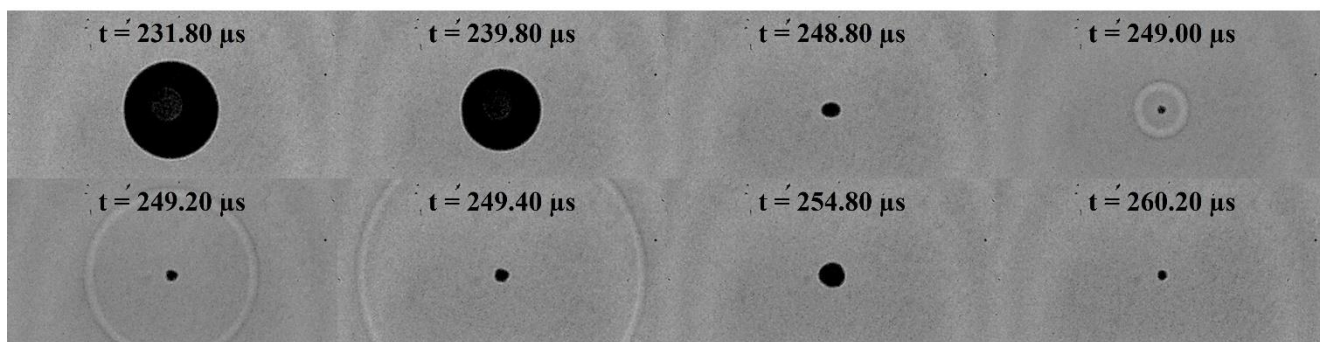


Fig. 4.5: Representative high-speed frames of an LIB collapse, BCSW generation and rebound, recorded at  $5 \times 10^6$  FPS. BCSW detection time is normalised to the voltage trace BCSW of fig. 4.3. to account for propagation time.

As observed in the figures above, shortly after triggering the LIB (labelled Q-Switch), the OBSW is detected. This typically has a slightly steeper more impulse-like rise to peak amplitude with an overall lower amplitude and slightly lower amplitude reverberations. Approximately 80  $\mu$ s later the BCSW is observed with a greater amplitude shockwave than

the OBSW, detected both in the voltage trace (fig. 4.4), and HSI (fig. 4.5). A commonly reported observation for laser induction is the tendency for the bubble to be slightly elliptical in shape due to spherical aberration, during focusing of the laser-pulse [54]. This is typically caused by extension of the LIB focal region through focusing via an objective lens [25]. We observe a similar shape, shown at 248.80  $\mu\text{s}$  (fig 4.5) whilst using a curved mirror to focus the laser rather than objective lens.

## 4.5 Results and Discussion

### 4.5.1 swPCD translation

For the results presented below, BCSWs were measured by the swPCD at each of the three distances and each BCSW dataset was collected from comparable LIBs in terms of single fronted shockwave generation and amplitude of LIB emissions. Accordingly, the BCSWs presented can be considered as representative of the propagation of a single shockwave originating from a bubble of comparable maximum radius [25].

Fig. 4.6 presents an average single BCSW from each of the three swPCD distances measured.

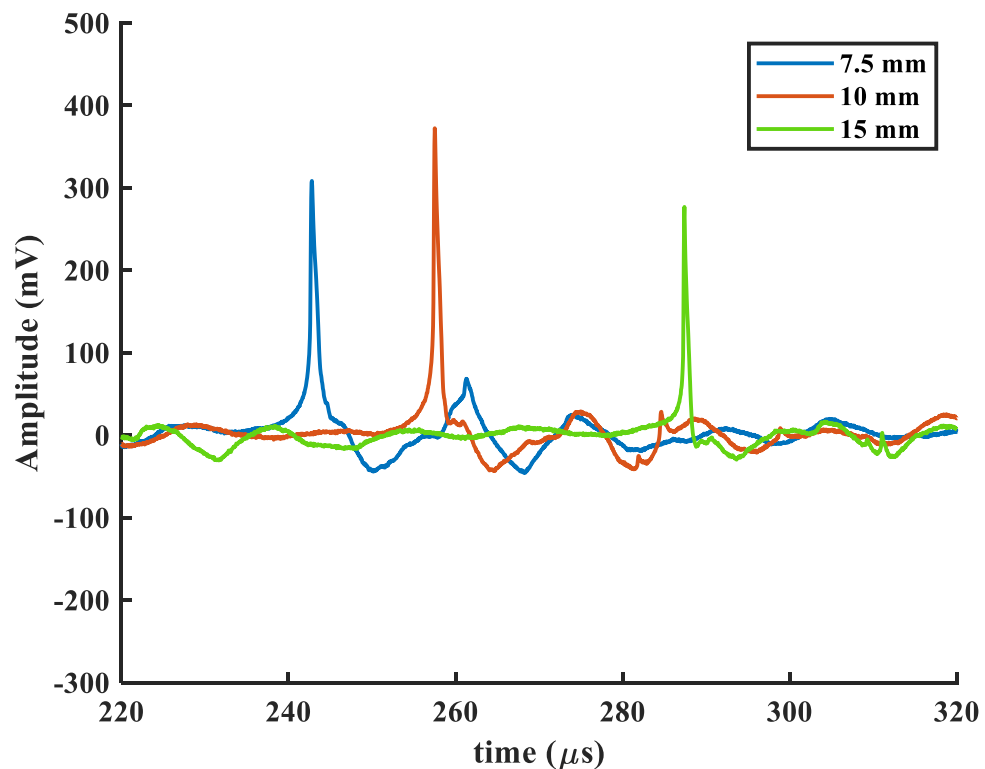


Fig. 4.6: BCSW voltage trace detected by the swPCD at a distance of 7.5 mm (blue), 10 mm (orange) and 15 mm (green).

The most apparent effect of altering swPCD positioning is the change in the amplitude of the voltage signal detected. From fig. 4.6, a distance of 7.5 mm produces an amplitude of approximately 300 mV, increasing the swPCD distance to 10 mm results in further increase to amplitude, to around 350 mV. However, moving the swPCD to a distance of 15 mm slightly reduces the signal amplitude to around 270 mV.

From fig. 4.6, small amplitude peaks can be observed after each respective BCSW. Each BCSW is followed by a short negative phase. This negative phase has previously been reported as a consequence of a tensile phase development, attributed to the host media response following the initial impulse-like compression of the shockwave, in shockwaves for lithotripsy and in detonation, respectively [188, 189]. However, *Johansen et al* reported that, at least for BCSWs in water, this as a detector convolution artefact, rather than a consequence of the bubble oscillation [25].

After the negative phase, each voltage signal exhibits a small, broader peak. Occurring approximately 16  $\mu$ s after the BCSW, these peaks could be related to rebounds of bubble from subsequent oscillatory phases post-BCSW or inherent reverberations of the swPCD active material due to the acoustic impedance mismatch of the media. Notably, the closer the swPCD to the LIB induction site, the higher amplitude of the secondary peak. The design of the swPCD backing and matching layers aid in reducing these reverberations or “ring down”, however, it is apparent that further positioning of the swPCD should be considered when performing experiments incorporating acoustic detection.

### 4.5.2 CaviSensor Signal

The following results present the equivalent BCSW voltage trace detected by the CaviSensor, with the LIB induction site in the geometric centre of the sensor circumference.

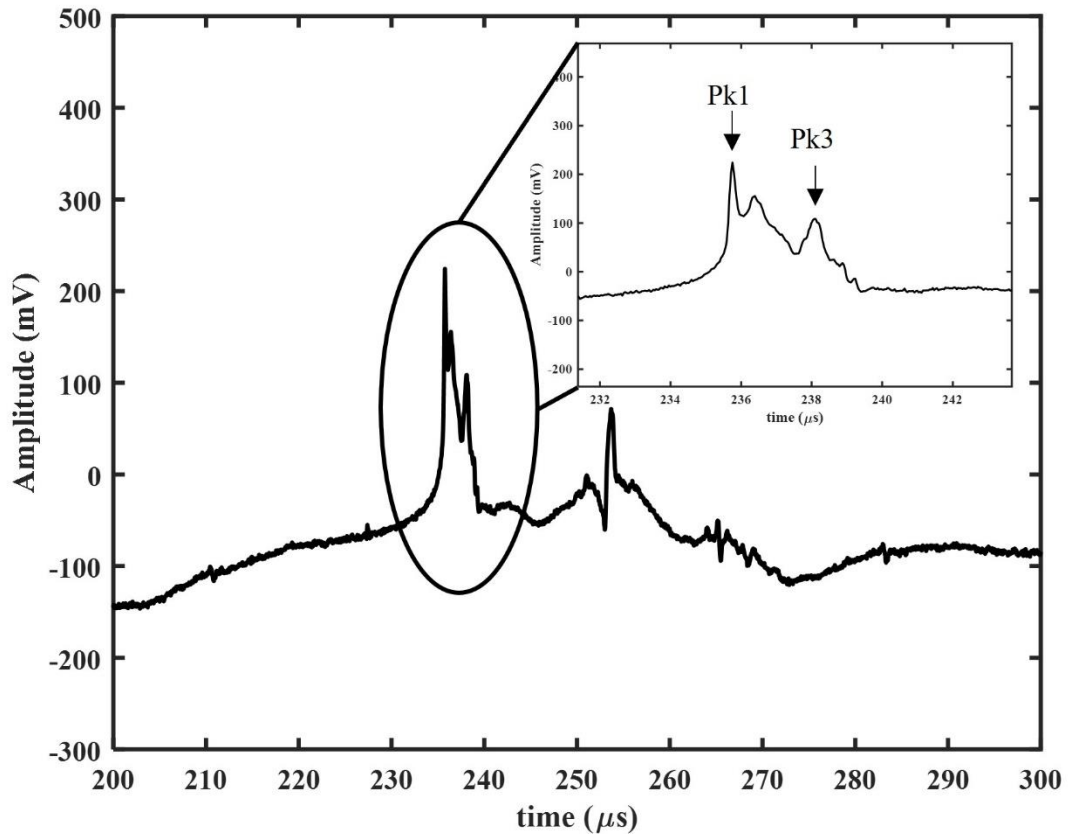


*Fig. 4.7: BCSW voltage trace detected by the CaviSensor. Zoom inset shows Full BCSW profile.*

The voltage trace of the BCSW detected by the CaviSensor is notably different to that of the swPCD. Firstly, the amplitude of the BCSW is approximately 220 mV, a reduction compared to the swPCD at all distances. Furthermore, the secondary peak identified in the swPCD voltage traces is more apparent here, with an amplitude of approximately 70 mV apparent around 17  $\mu$ s after the BCSW. This secondary peak is likely resultant from the same sources as the swPCD. These characteristics of the voltage profile could be down to material properties of the insulating backing layer and/or matching layer of the sensor, which are not known. Additionally, propagation distance in the CaviSensor may be slightly variable

resulting in reduced amplitude peaks when the BCSW strikes the inner circumference. This is due to spatial averaging over the sensor area spreading the BCSW voltage trace (zoom inset, *Fig 4.7*) over a longer duration than that of the swPCD.

From the zoom inset of *fig. 4.7* a 2.1  $\mu\text{s}$  delay ( $\Delta t$ ) between the first and third peak of the BCSW (labelled 'Pk1' and 'Pk3', respectively) is apparent. These sub-peaks are the response of non-uniform BCSW striking points of the inner circumference of the CaviSensor at slightly different times, producing the aforementioned spatial averaging. From this  $\Delta t$ , the separation distance ( $\Delta d$ ) in terms of the BCSW striking each side of the sensor can be calculated from equation 4.1.

$$\Delta d = \Delta t \times v \quad (4.1)$$

where  $v$  is the speed of sound in water (approximated to  $1500 \text{ ms}^{-1}$ ). This gives a  $\Delta d$  of 3.15 mm. Meaning the BCSW has travelled approximately 3.15 mm further in one axial direction than the other. This is represented in schematic form in *fig. 4.8*.

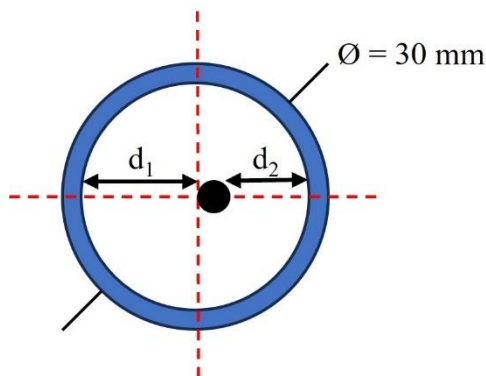


*Fig. 4.8: Schematic representation of an off-axis LIB where  $d_1$  and  $d_2$  represent the respective distances the BCSW will travel before striking the CaviSensor.*

This approximation, however, does not indicate the direction of misalignment. Rather, it can be used as an estimate of lateral offset. *Fig. 4.8* presents a potential offset in schematic form. In practice, this offset could be misaligned on another axis. Nonetheless, a circular geometry will always have an axis of symmetry regardless of bubble position.

A slightly off-axis LIB will result in the BCSW travelling a further propagation distance ( $d_1$ ) on one side compared to the other ( $d_2$ ). Given, the  $\Delta d$  of the BCSW profile was calculated to be 3.15 mm and the diameter of the CaviSensor is 30 mm, the off-axis LIB position can be deduced using simultaneous equations.

$$d_1 + d_2 = 30 \text{ mm} \quad (4.2)$$

$$d_1 - d_2 = 3.15 \text{ mm} \quad (4.3)$$

Thus, the LIB exhibited in fig. 4.7 is calculated as being approximately 1.575 mm off-axis from the CaviSensor centre – a positioning error of 5.25%. Initial positioning of the CaviSensor is therefore subject to human error associated with accurate alignment with the x,y,z manipulator. Results referring to the geometric centre of the CaviSensor can therefore be interpreted as within ~5% positioning error. All future results characterising position changes within the CaviSensor circumference are calibrated relative to this geometric centre and are therefore correct in terms of displacement, however, are subject to the same margin of error generated from the initial positioning.

### 4.5.3 swPCD comparison with CaviSensor

For the results presented below, quantitative comparison of the swPCD against each position and against the CaviSensor is presented, with justification for the importance of selecting and maintaining accurate and consistent sensor positioning during experimental procedures utilising acoustic detection.

Fig. 4.9 plots the mean amplitude of the BCSW  $\pm$  s.d. for five measurements at each position and sensor.

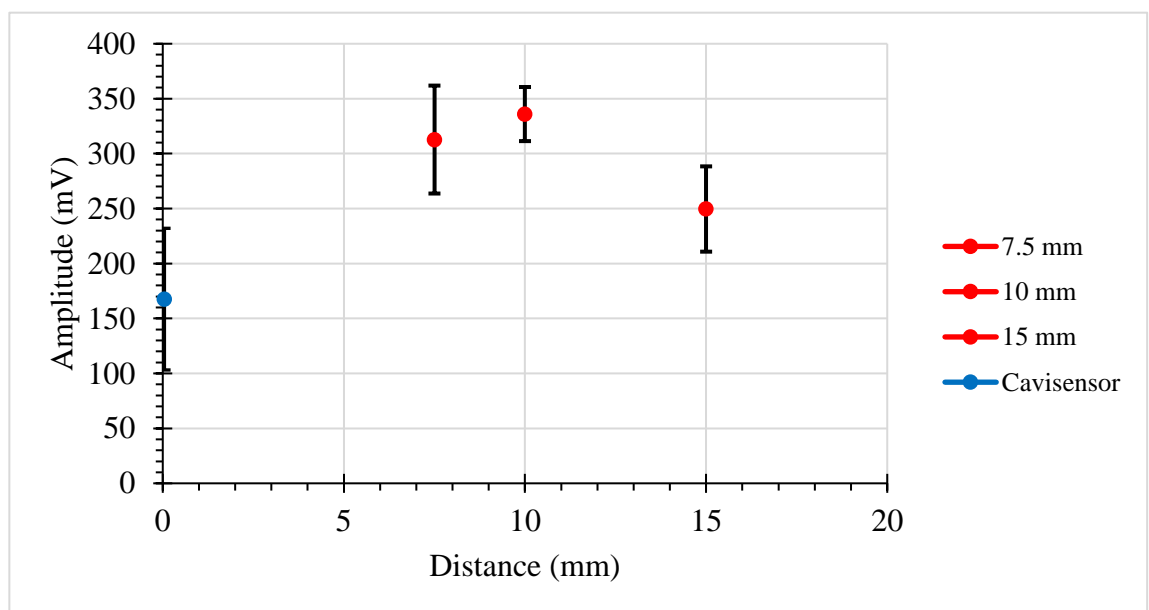


Fig. 4.9: Amplitude of the BCSW detected in the voltage trace of five LIBs for the swPCD at distances of 7.5 mm, 10 mm and 15 mm, and the CaviSensor positioned with the LIB induction site in the geometric centre of the sensor. Results presented as mean  $\pm$  s.d.

The results of fig. 4.9 indicate that the swPCD out-performs the CaviSensor in terms of peak amplitude sensitivity at all distances. At a distance of 10 mm, the swPCD has a greater than 100% increase in peak amplitude compared to the CaviSensor and an over 7% increase compared to the next best amplitude (occurring at 7.5 mm distance). Furthermore, the swPCD exhibits reduced variation in amplitude between signals detected. The CaviSensor presented a greater variability in amplitude compared to the swPCD, resulting in larger error bars in fig 4.9.

Fig. 4.10 plots the mean Full Width Half Maximum (FWHM) of the BCSW detected by the swPCD at each distance and the CaviSensor.

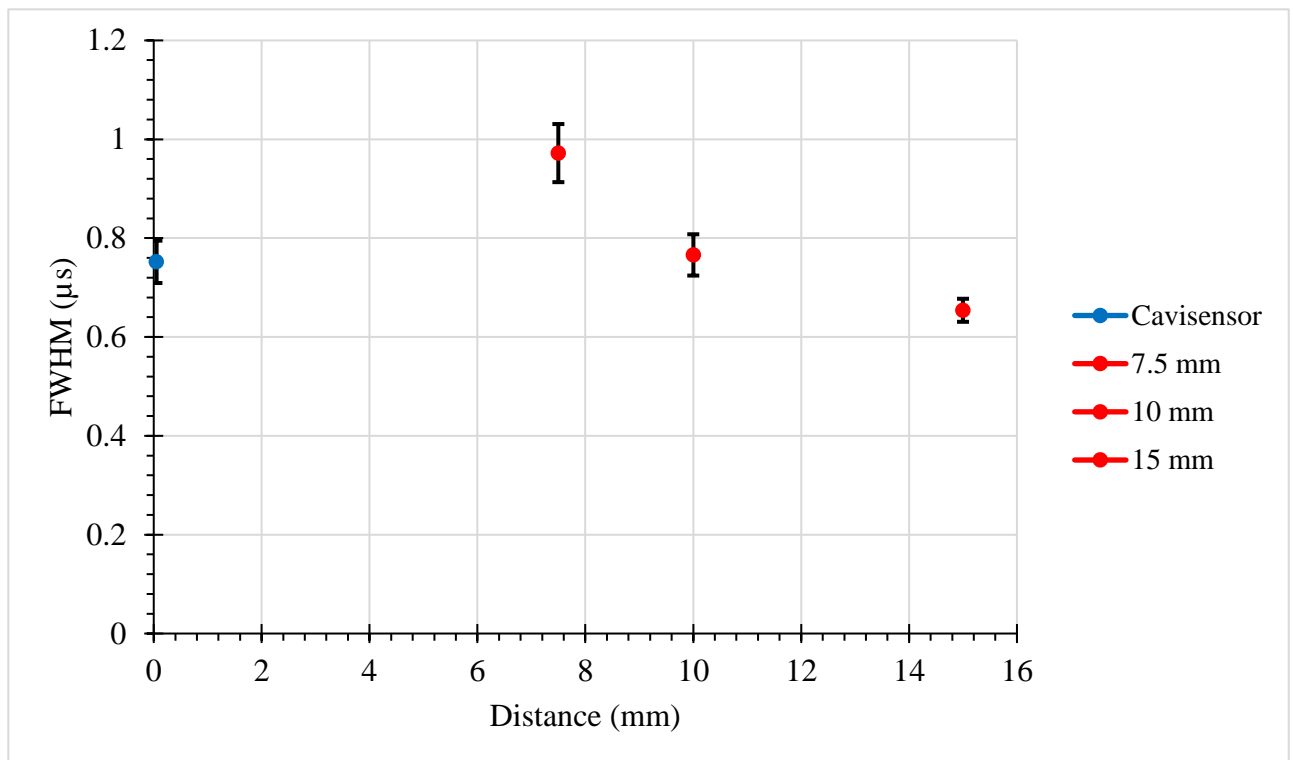


Fig. 4.10: FWHM of the BCSW detected in the voltage trace of five LIBs for the swPCD at distances of 7.5 mm, 10 mm and 15 mm, and the CaviSensor positioned with the LIB induction site in the geometric centre of the sensor. Results presented as mean  $\pm$  s.d.

The results of fig. 4.10 indicate that the FWHM of the swPCD decreases with increased distance from the LIB induction. The maximum FWHM, present at 7.5 mm distance, is reduced by a factor of over 20% and over 32% by moving the swPCD back to 10 mm and 15 mm, respectively. This would be as expected as the further from the LIB induction site, the more the BCSW becomes closer to a planar approximation when striking the swPCD surface. Closer to the LIB, there would be a greater degree of spatial averaging as the spherically diverging shockwave impacts the surface closer, in distance, to its source with the shockwave becoming more planar with distance.

The FWHM for the CaviSensor is slightly improved to that of the swPCD at a distance of 10 mm, outperforming the swPCD positioned at 7.5 mm. As the internal diameter of the CaviSensor is 30 mm, positioning of the LIB induction in the centre should theoretically give a propagation distance equivalent to 15 mm (radius of the sensor) before the shockwave strikes the active material. Spherical propagation of the BCSW, which is apparent for the swPCD high-speed observations (fig. 4.4), would theoretically produce a single shock front on the voltage trace of the CaviSensor. However, the BCSW voltage trace of fig. 4.7 appears to indicate non-uniform striking of the BCSW on the active material, resulting in the features discussed previously. Although the FWHM appears to be comparably narrow to the swPCD, it underrepresents the broader BCSW indicated on the zoom inset of fig. 4.7, occurring due to the BCSW striking the CaviSensor at slightly different points, explained in part as a result of positioning error.

Fig. 4.11 presents the frequency spectra of the BCSW detected by the swPCD optimally positioned at 10 mm distance (voltage trace, fig. 5.6) and the CaviSensor positioned in the centre (voltage trace, fig. 4.7).

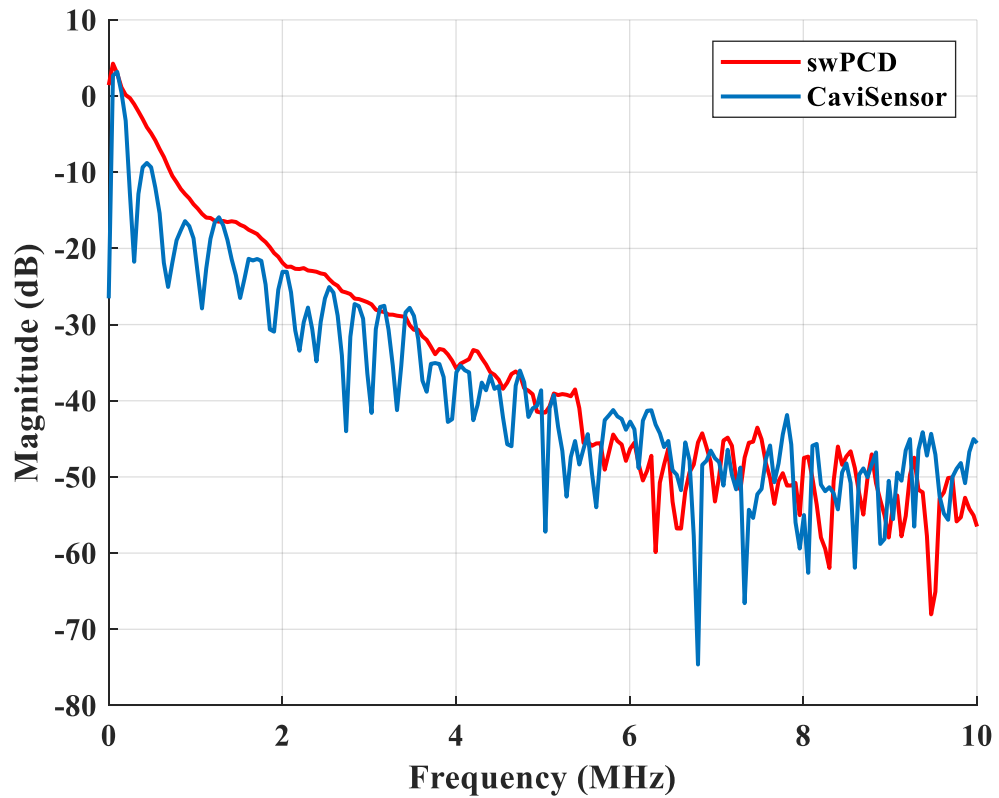


Fig. 4.11: Spectra of BCSW for swPCD at 10 mm distance (red) and CaviSensor centrally positioned (blue).

The swPCD exhibits slightly greater magnitude response across the kHz frequency range (covering all  $f_0$  in this thesis) up to around 5 MHz. Beyond 5 MHz the CaviSensor exhibits a slightly greater magnitude response. As expected from the relatively close amplitudes of the two detectors, both sensors exhibit sensitivity across several MHz, commonly used for cavitation monitoring.

#### 4.5.4 Position translation within the CaviSensor

The following results present quantitative analysis on the effect of directivity on properties of the signal as the LIB is translated both axially (fig. 4.5 (a)) and laterally (fig. 4.5 (b)) from the centre. Results presented below are normalised against the origin, giving the trend in signal quality at corresponding measurement positions.

Fig. 4.12 plots the normalised amplitude of the BCSW detected at the centre of the CavisSensor and further axial translation at 1 mm, 2 mm and 4 mm, bringing the LIB closer to the end on the CaviSensor ring.

As the CaviSensor is translated axially there is an almost exponential decay in BCSW amplitude. With 1 mm of translation, there is an almost 50% drop in signal amplitude and after 4 mm of translation the amplitude of the signal has decreased by over 70%.

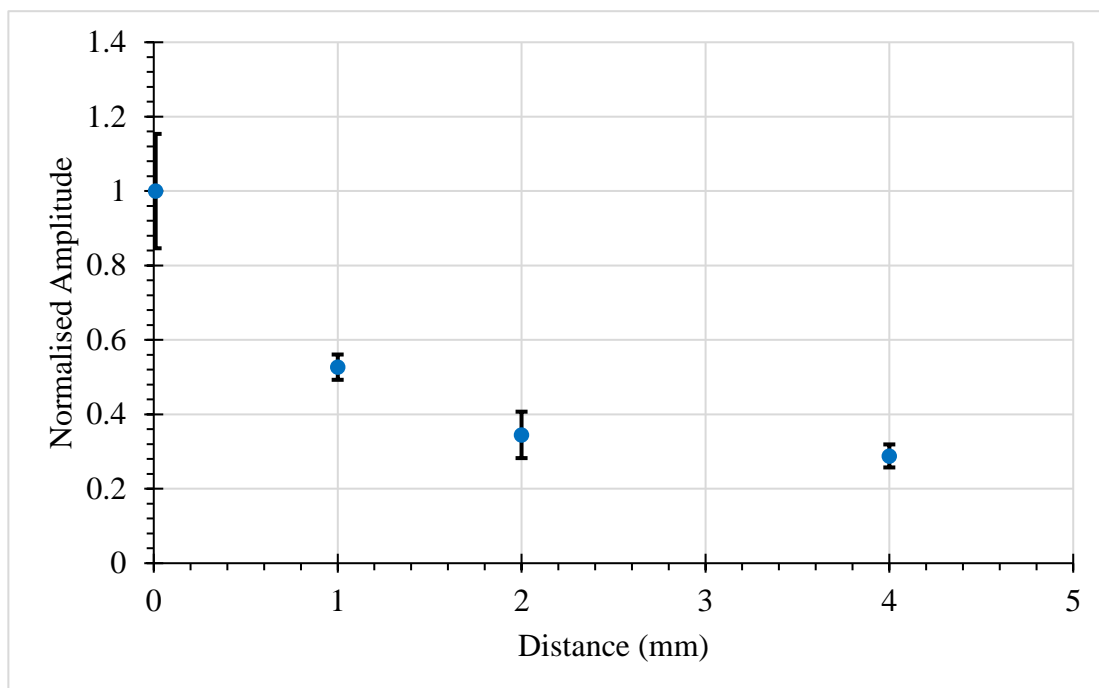


*Fig. 4.12: Normalised amplitude of the BCSW detected in the voltage trace of five LIBs for the CaviSensor positioned with the LIB induction site in the geometric centre of the sensor and translated axially 1 mm, 2 mm and 4 mm. Results presented as mean  $\pm$  s.d.*

Fig. 4.13 presents normalised FWHM of the BCSW corresponding to the same axial translation.

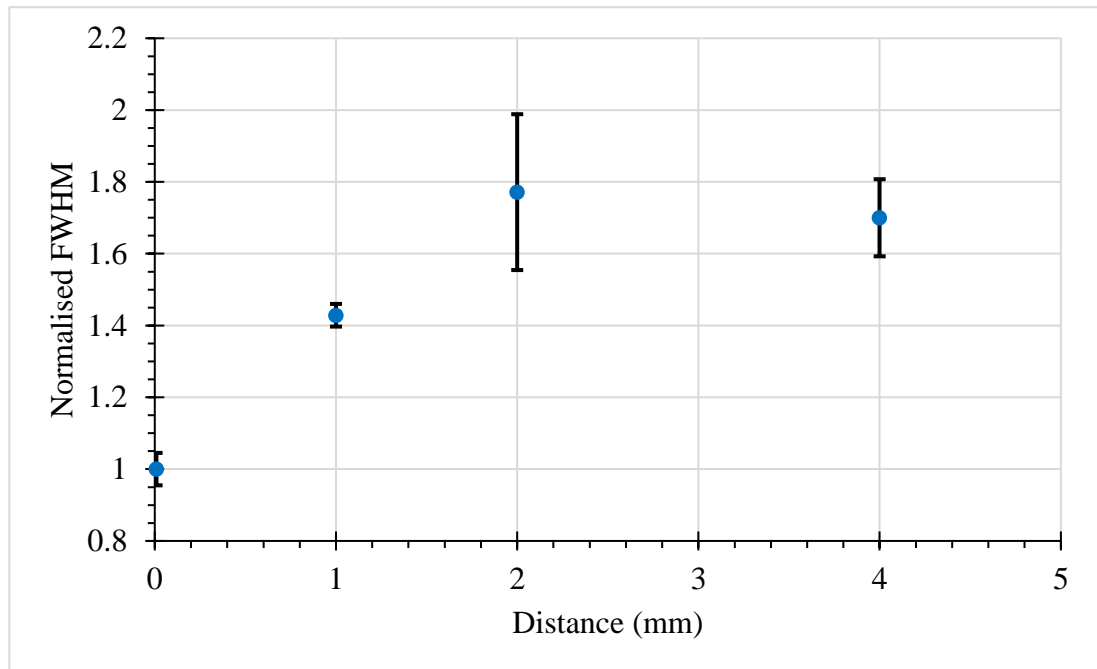


*Fig. 4.13: Normalised FWHM of the BCSW detected in the voltage trace of five LIBs for the CaviSensor positioned with the LIB induction site in the geometric centre of the sensor and translated axially 1 mm, 2 mm and 4 mm. Results presented as mean  $\pm$  s.d.*

As with BCSW amplitude, there is a decaying trend in FWHM as the CaviSensor is translated axially. With 1 mm axial translation, FWHM increases by over 40% and FWHM is over 70% greater at both 2 mm and 4 mm axial translation.

Figs. 4.14 and 4.15 below present the corresponding trend in BCSW amplitude and FWHM, respectively, for 1 mm, 2 mm and 3 mm lateral displacement of the CaviSensor, bringing the LIB closer to the sensor inner diameter on one side.

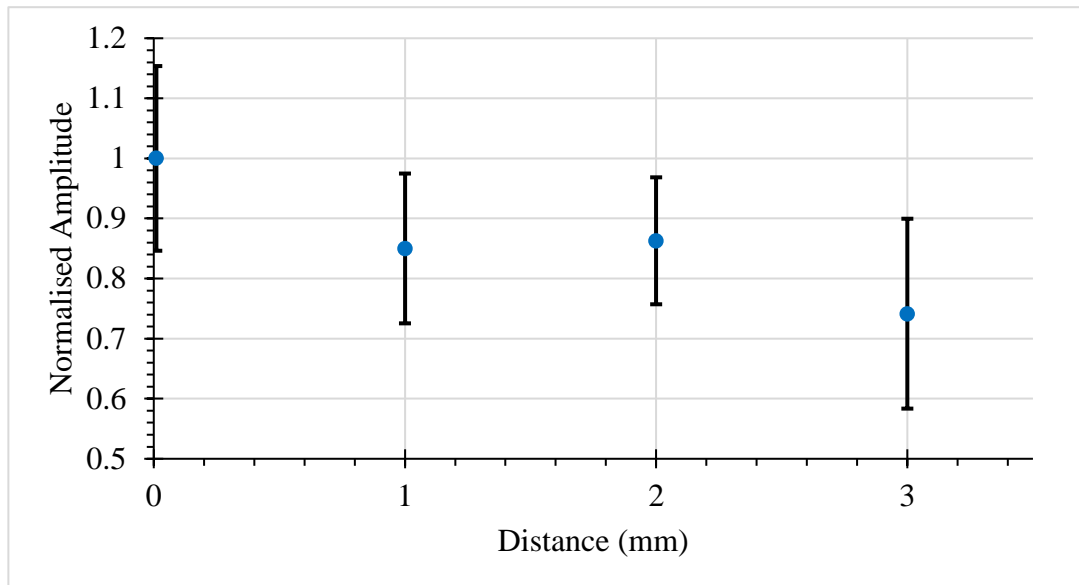


Fig. 4.14: Normalised amplitude of the BCSW detected in the voltage trace of five LIBs for the CaviSensor positioned with the LIB induction site in the geometric centre of the sensor and translated laterally 1 mm, 2 mm and 3 mm. Results presented as mean  $\pm$  s.d.

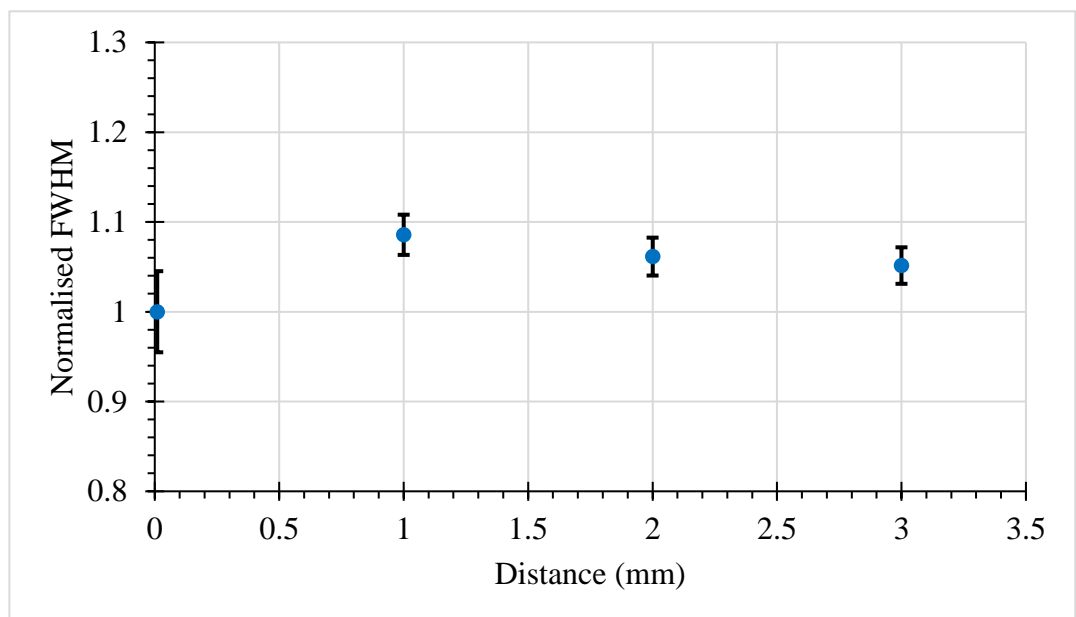


Fig. 4.15: Normalised FWHM of the BCSW detected in the voltage trace of five LIBs for the CaviSensor positioned with the LIB induction site in the geometric centre of the sensor and translated laterally 1 mm, 2 mm and 3 mm. Results presented as mean  $\pm$  s.d.

Figs. 4.14 and 4.15 indicate that lateral translation results in a decay in BCSW amplitude by over 20% for maximum translation, corresponding to a 5% increase in FWHM at maximum translation.

The results presented in the *Results* §4.5.1 - 4.5.4 provide rationale for selection of the swPCD as a viable sensor for acoustic detection of BCSW. Firstly, the CaviSensor offers a promising sensor with the advantage of inhibiting high-frequency noise out with the sensor geometry. Secondly, the CaviSensor provides good temporal resolution of the BCSW, owing to its curved geometry. However, this geometry does lead to the detection of multiple shock-fronts, owing to non-uniform shockwave collision with the sensor. Furthermore, the CaviSensor is shown to be highly sensitive to precise sensor positioning. Sensor performance for BCSW detection was significantly compromised as the LIB source was positioned farther from the centre of the CaviSensor. Lateral positioning had a smaller effect on amplitude and FWHM deterioration (in excess of 20% and 5%, respectively), however does introduce the non-uniform shockwave collision previously discussed. Axial positioning had a greater effect on sensor performance with up to 70% deterioration in amplitude and FWHM at the furthest translation presented. We note that LIBs triggered at the boundary of the CaviSensor were unstable and severely dampened to the point of their exclusion from the main results and LIBs triggered out with the sensor geometry were not detected at all. Clearly, highly accurate sensor positioning is required for meaningful comparison of results and given the error in positioning of the sensor, discussed previously, maintaining consistency and precision of measurements may be more challenging with the CaviSensor.

Conversely, the swPCD presented a clearer signal with reduced reverberations and a greater amplitude sensitivity at all distances measured. Furthermore, at 10 mm and 15 mm distance, the swPCD presented a reduced FWHM to that of the CaviSensor. The results indicate that a swPCD positioned 10 mm from the LIB source was optimal in terms of balancing the greatest amplitude sensitivity, reverberation reduction and FWHM. Both sensors exhibited

sensitivity across a broad frequency range from kHz up to several MHz, with the swPCD providing slightly greater magnitude response up to around 5 MHz, comparable with most commonly reported cavitation research. Finally, the clear advantage of the swPCD is the ability for incorporation of HSI. The ability to both acoustically detect and visually observe the bubble dynamics concurrently is a major advantage for several cavitation applications and research groups with available high-speed cameras.

#### 4.5.5 Shockwave detection under a sonotrode source

The results presented for a laser-induced bubble source allow for detailed characteristics of each sensor to be studied. In practice, however, the swPCD is constructed to be deployed for detection of bubble collapse shockwaves from a sonotrode source. Cavitation under a sonotrode is highly dynamic, with the generation of a large primary bubble cluster and satellite clouds in a cone-like bubble structure (CBS). This dynamic and complex bubble structure will, correspondingly, impact the signal detected with respect to positioning sensitivity. Under a sonotrode, particularly at higher powers, shockwaves can be multi-fronted, consisting of a greater number of component shock fronts. These shock fronts are generated from individual sub-cluster collapses within the primary cluster in the CBS, as shown in fig. 4.16.

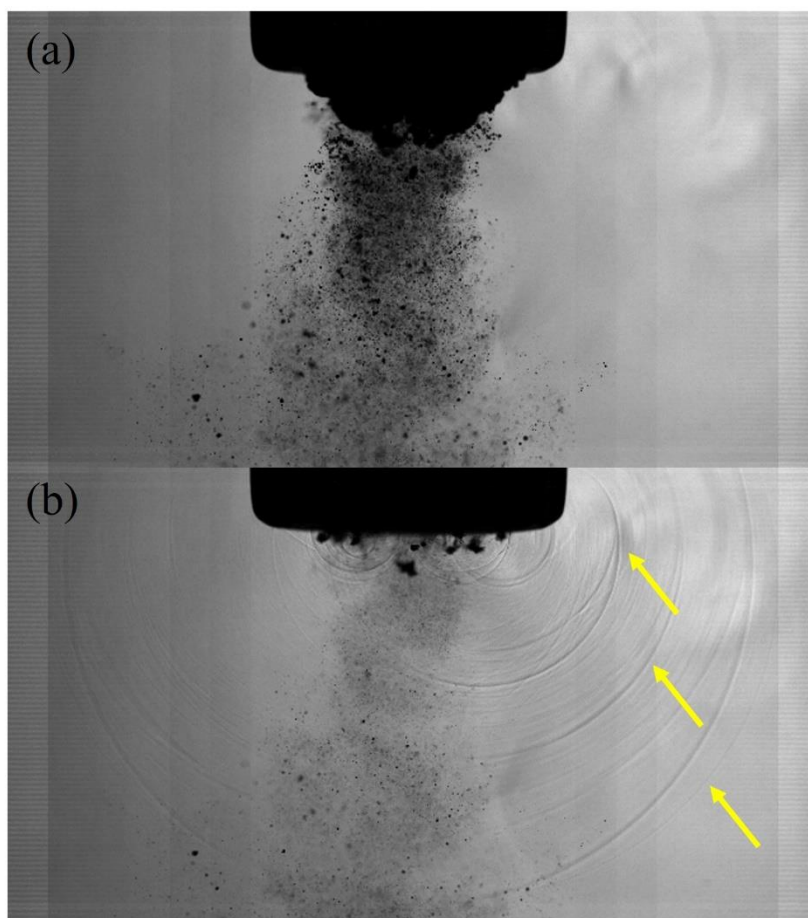


*Fig. 4.16:(a) large primary bubble cluster generated under sonotrode, (b) multi-fronted shock front generated by sub-cluster collapse within primary cluster. Scale provided by the 6 mm-Ø tip.*

The utility of the swPCD and CaviSensor for shockwave detection for the sonotrode source was assessed. The CaviSensor was positioned surrounding the sonotrode tip, such that the sonotrode tip was positioned in the centre of the CaviSensor both vertically and horizontally. The swPCD was positioned 10 mm from the sonotrode tip and aligned such that the centre of the swPCD was in line with the centre of the sonotrode tip. Again, all positioning was performed with an x,y,z manipulator. The swPCD positioning relative to the sonotrode is represented in Chapter 5, fig. 5.1.

Fig 4.17 presents representative acoustic emissions detected by each sensor from the Sonics sonotrode at 30% input power, with emissions over a 400 ms sonication detected and recorded. Shockwave data from the acoustic emissions is generated by the same protocol defined in Chapter 5, §5.2.4.

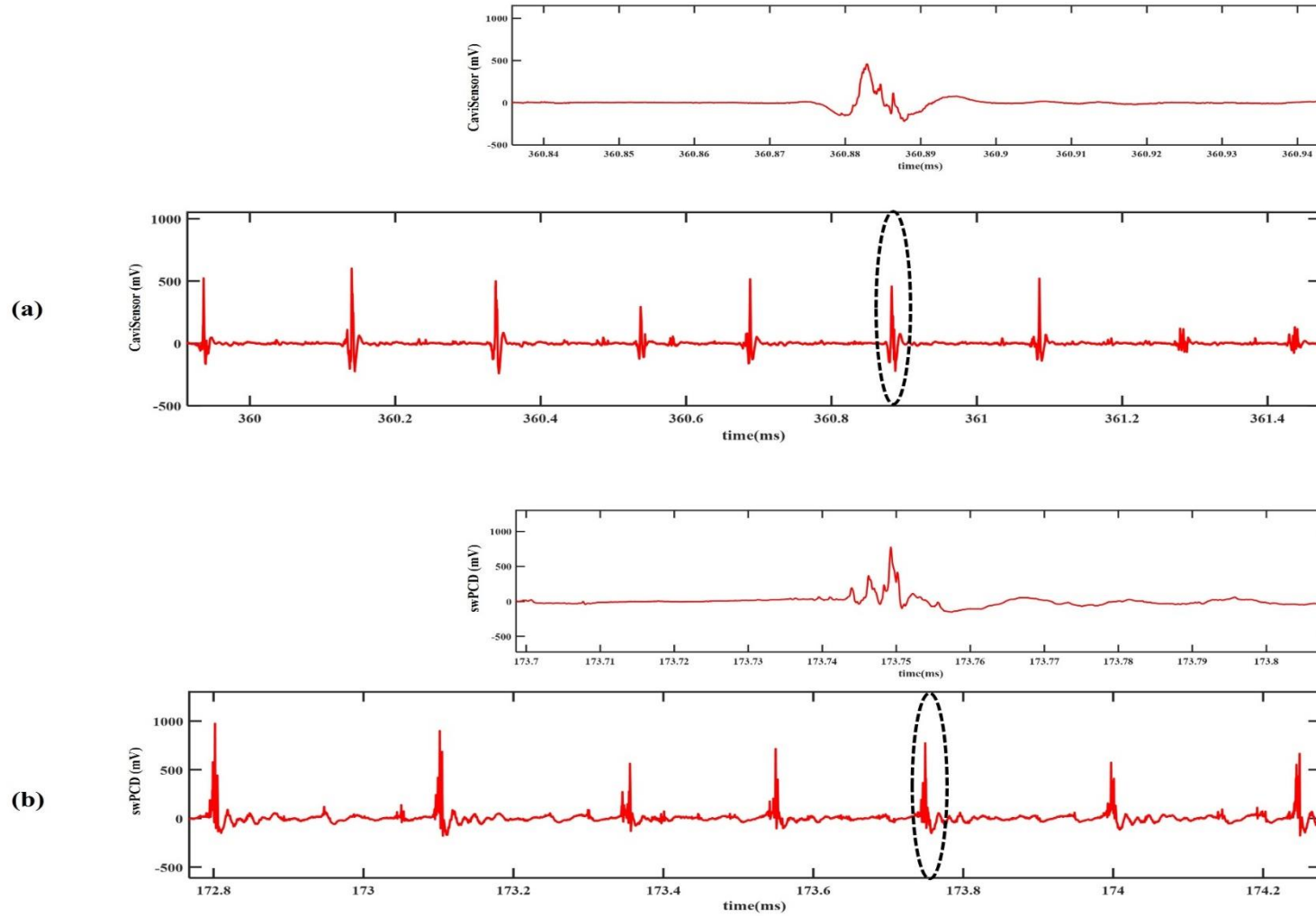


*Fig. 4.17:(a) Representative shockwave emissions from the sonotrode detected by the CaviSensor and (b) the swPCD, with zoom insets providing individual shock-profiles exhibiting the detection of multi-fronted shockwaves.*

Both the CaviSensor and swPCD exhibited detection of the shockwaves emitted by the cavitation at the sonotrode tip. As with the laser-induced shockwave detection (fig. 4.9), the swPCD exhibited a greater than 100% sensitivity to shockwave detection, by measure of average shockwave amplitude over the measured range, compared to the CaviSensor. Both sensors detected the multi-fronted shockwaves generated by the sonotrode (zoom insets, fig. 4.17). Furthermore, the CaviSensor appeared to produce more low amplitude shockwave profiles, detected in fig. 4.17 (a) after 361.2 ms. Here, the periodicity of the shockwave is consistent within the emissions (which is discussed in greater detail in Chapter 5), however the amplitude is greatly reduced. Exhibited previously for laser-induced shockwaves, the CaviSensor is highly sensitive to axial positioning, with sensitivity dramatically reduced as the CaviSensor is translated. The occurrence of low amplitude shockwaves could be related to the origin of the shockwave from the primary bubble cluster, with a shock-front impacting the ends of the CaviSensor inner circumference at the axial ends of the sensor possibly observed as dampened due to poorer sensitivity at these regions.

Both sensors exhibited adequate detection of shockwaves emitted from the primary cluster at the sonotrode tip, where the presence of multi-fronted shockwaves is expected. The swPCD produced greater sensitivity than the CaviSensor and, crucially, allowed for the combination of dual-perspective high-speed imaging, which the CaviSensor geometry inhibits. These distinct advantages rendered the swPCD an attractive option for future acoustic measurements.

## 4.6 Conclusions:

The design and manufacture of a cheap in-house cavitation sensor capable of detection of BCSWs has been demonstrated. The characterisation and comparison of this sensor against a commercially available CaviSensor demonstrate that the swPCD can aptly perform as a cavitation sensor, specifically designed for detection of BCSWs. Precise and consistent positioning of the sensor is required to maximise performance and maintain comparability between results. This is of relevance to studies utilising cavitation detectors of any kind and crucially to the studies presented in this thesis. The results from this chapter guided positioning conditions of the swPCD used in future chapters.

## **5 Characterisation of the cavitation generated in different Deep Eutectic Solvents and water.**

### **5.1 Introduction**

For sonochemical applications, or any application involving power ultrasonics, understanding the efficiency of a device in its operating media is of utmost importance. Recent study has demonstrated [55] that, in water, the notion that simply increasing input power does not necessarily correlate to improved sonochemical yield, for a given application.

Understanding of the cavitation generated from such devices may guide selection of parameters for application-specific use. Limited study has been conducted to characterise the cavitation generated by a sonotrode as a function of input power, with *Yusuf et al* [55] providing the single most comprehensive study in water, to date. However, with the use of power ultrasonics in a variety of liquids of many different properties [81, 94, 95] and the emergence of ultrasound as a new method of enhancing precious metal delamination – which is the primary focus of this body of work – there is a necessity for a robust method of characterising cavitation under a sonotrode in a variety of liquids. This chapter outlines the characterisation of cavitation in four different liquids: water and three deep eutectic solvents (DESs) – Ethaline, CaDES and Reline.

## **5.2 Materials and Methods**

### **5.2.1 Deep Eutectic Solvent preparation**

The three deep eutectic solvents (DESs) used for the investigations in this chapter were Ethaline, CaDES and Reline. Chosen as Ethaline and CaDES are perhaps the most commonly reported DESs and have a viscosity around 39 and 57 MPa S, respectively. Reline is significantly more viscous, quoted at 1750 MPa S in the literature [190, 191]. For each DES, the constituent chemicals were heated on a hot plate at 60°C and mixed with a magnetic stirrer until a clear homogenous liquid was formed. Each DES was stored out of direct sunlight in a sealed bottle for 24 hours to air cool before use.

### **5.2.2 The experimental setup**

The results described below were obtained with two commercially available sonotrodes. Briefly, a Branson 450W sonotrode operating through a 6.4 mm diameter ( $\emptyset$ ) tip and a Sonics 500W sonotrode operating through a 6 mm-  $\emptyset$  tip. Both horns operated at 20 kHz with input power available in 1% increments. Fig. 5.1 schematically presents the experimental arrangement used.

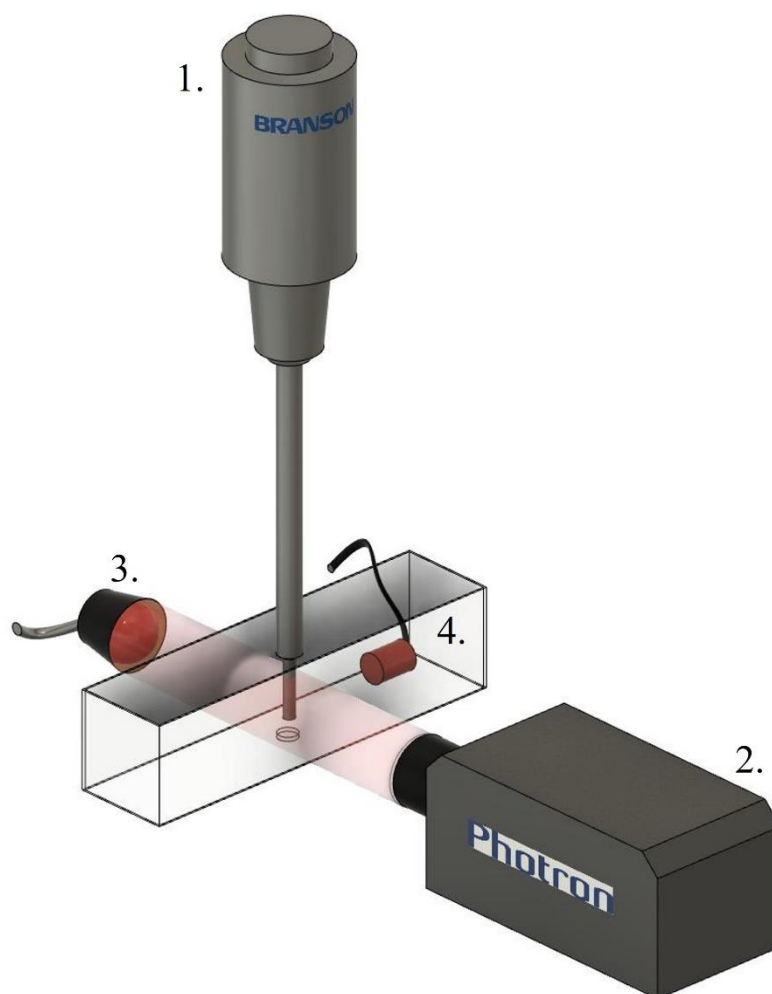


*Fig. 5.1: Schematic representation of the experimental arrangement, featuring the following components: 1. The sonotrode, the tip of which was aligned to a Perspex disk for position registration within a custom-made tank filled with DES/water. 2. Photron high-speed camera used to study cavitation development within the vicinity of the tip, with pulsed laser illumination provided via a collimator lens, 3. 4. swPCD gathering acoustic emissions produced during sonications.*

### **5.2.3 High-speed imaging:**

High-speed imaging (HSI) of the cavitation activity in the vicinity of the sonotrode tip was undertaken with a Fastcam SA-Z 2100 K (Photron, UK) (*component 2*, fig. 5.1). Illumination was provided via synchronous 10 ns laser pulses at 640 nm (CAVILUX Smart, Cavitar, Finland), coupled to a liquid light guide and a collimating lens (*component 3*, fig. 5.1). In addition to setting the effective temporal resolution (the duration of frame capture), this

illumination configuration facilitates shadowgraphic HSI such that bubble-collapse shockwaves may be directly imaged, via refractive index variations imposed by the pressure transient of the propagating shockwave [24-26, 55]. Imaging was undertaken through a macro-lens (Milvus 100 mm f/2M, Zeiss, Oberkochen, Germany), over  $486 \times 324$  pixels, providing a spatial resolution of  $39 \mu\text{m pixel}^{-1}$ , with the field-of-view (FOV). Imaging was obtained at 80 kfps, which is  $4\times$  the driving frequency, thus capable of detailed bubble dynamic observations of several frames per acoustic cycle.

#### 5.2.4 Acoustic detection and filtering protocol

Acoustic detection was performed with the swPCD (described in detail in Chapters 3 and 4). The swPCD was mounted on an x, y, z manipulator for positioning within the tank, fig. 5.1, to detect emissions orthogonally (in the x-direction), with respect to the sonotrode probe (z-direction). The swPCD was connected to an oscilloscope (Tektronix 5 series, Berkshire UK) for data collection at  $25 \times 10^6$  samples/s. For all data presented, the swPCD was positioned  $10 \pm 0.5\text{mm}$  from the tip of the horn, as justified in chapter 4. This positioning allowed for optimal shockwave detection with reduced reflections from the tank boundaries, balancing the potentially poor temporal resolution for detected shockwaves from the cavitation at the sonotrode tip. Through detailed performance characterisation of the swPCD positioning (as previously outlined in chapter 4) both with laser-induced bubbles and the sonotrode, swPCD position had no effect on shock wave periodicity. The positioning of the swPCD was also validated against *Yusuf et al*, where it was positioned directly below the sonotrode tip.

The output voltage signal detected by the swPCD was subjected to a filtering protocol, with the stages of filtering detailed below and demonstrated in fig. 5.2.

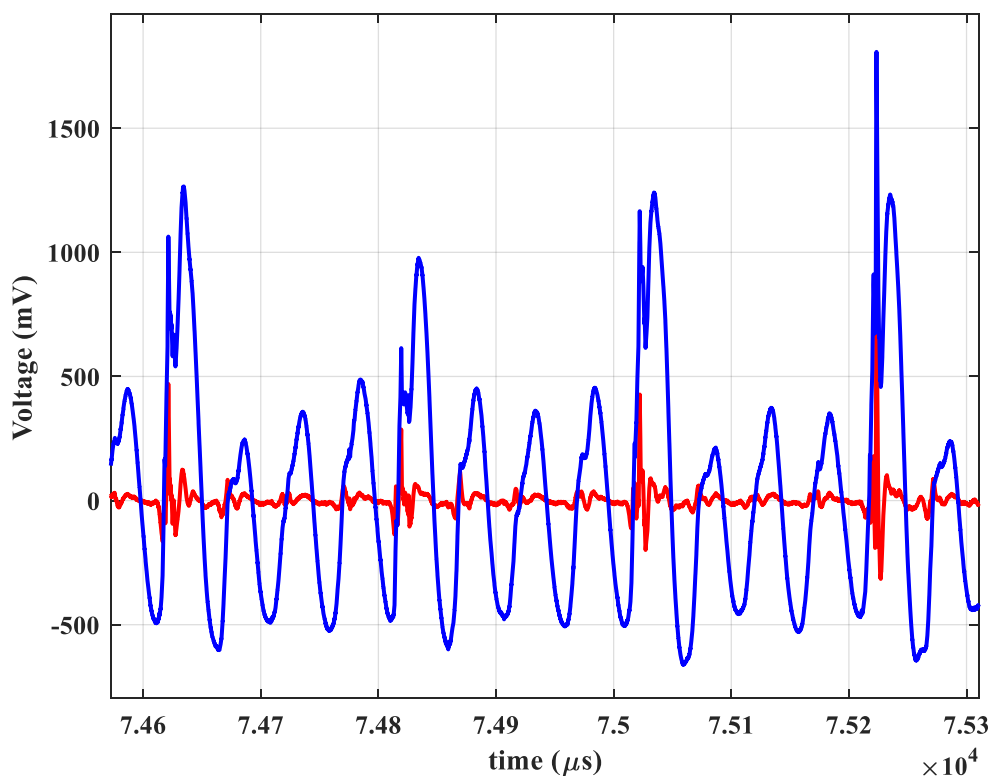


*Fig. 5.2: Filtering protocol implemented on raw acoustic emissions detected by the swPCD (blue) to remove 1. low frequency noise over 50Hz. 2. High frequency system noise above 10MHz and 3. Bandpass filtering to remove contributions from the drive signal ( $f_0$ ) to give the final filtered signal (red).*

As can be observed in fig. 5.2, the shockwaves can broadly be identified in the raw data (blue voltage trace) by the (approximately 2-3 $\times$ ) greater amplitude peaks coupled with the corresponding spike at the start of these peaks. In the example above, taken from a cavitation emission at 35% input power on the Sonics horn in water, these accentuated peaks are observable every fourth acoustic cycle. Thus, the emissions can be described as operating at  $4T_0$  or  $f_0/4$  of the tip driving. Although the shockwaves are broadly observable, filtering the signal to produce purely shockwave-related content is required. The filtering protocol to produce the shockwave emission signal was multi-staged. Firstly, possibly line noise was filtered out using a high-pass filter with cut-off frequency ( $f_c$ ) of 50 Hz. Secondly, system noise was removed with a low-pass filter with an  $f_c$  of 10 MHz. Finally, a bandpass filter with  $f_c$  (20 kHz 4MHz) was implemented to remove contributions from the drive signal with

upper boundary dictated by the sensor sensitivity bandwidth (Chapter 4). Thus, revealing the bubble collapse shockwaves presented in fig. 5.2 (red voltage trace). MATLAB (MathWorks, MA, USA) code for these procedures is provided in Appendix B.

Acoustic emissions for all emission data presented were recorded for a total duration of 400 ms, triggered ~4 s into the sonication. Data is also presented in the frequency domain, via application of a fast Fourier transform and Blackman window over the duration of the time signal. Time-averaged shockwave content is quantified by the root mean square of the voltage ( $V_{\text{RMS}}$ ), over the five 400 ms duration samples per power. Here the mean  $V_{\text{RMS}}$  is presented with the error bars representing the standard deviation, for over 20 input powers in each fluid, as described and presented in the corresponding results.

### **5.2.5 Data collection**

Sonications were initiated manually from the control console of each sonotrode. The remaining instrumentation was synchronised via electronic triggering controlled from a signal generator (DG4102, Rigol Technologies, Beijing, China). Results for the Branson sonotrode are presented from the range of 20 – 100% input power, due to powers below 20% previously being reported to produce inconsistent cavitation [192]. For the Sonics horn, results are presented for the range of 20 – 70% input power due to the manufacturer-imposed limit on power for the system when operating through a microtip.

### 5.3 Results

The results sections below are organised as follows: §5.3.1 presents results comprising representative swPCD data over a 2 ms duration with corresponding HSI. Here, the data is used to describe the differences in cavitation emissions at the selected input powers. §5.3.2 presents the noise spectra of the corresponding emission signal to confirm the differences in oscillation behaviour of the cavitation, presented in §5.3.1, manifest in the acoustic emission signal generated by the cavitation at the respective input power. §5.3.3 presents the average root mean square ( $V_{RMS}$ ) of the swPCD signals collected over five sonications at each input power measured. The results from which are interpreted in relation to the previous sections. These initial results sections present data collected only from the Branson sonotrode at key input powers.

§5.3.5-5.3.6 repeat the data and analysis in the aforementioned sections, but in Ethaline.

Finally, §5.3.7 presents a combination of results presented in §5.3.1-5.3.6 for both sonotrodes in order to establish, by the use of shockwave emission content, regions where both horns operate at equivalent (or closely comparable) levels in terms of cavitation output. In this chapter, results for water and Ethaline are presented as the main liquids of interest in this study. Equivalent data for the other DESs studied, CaDES and Reline, presented in the same format in Appendix C.

### 5.3.1 Bubble cluster shockwave periodicity at selected input powers in water

The results in water, below, present the investigation of bubble collapse periodicity and shockwave emissions across selected key input powers of 23, 30 and 40%. The justification for selecting these powers will be provided in detail in §5.3.3 in the context of all measured input powers. Additionally, this water data is presented in a similar manor to *Yusuf et al* [55], who presented bubble cluster shockwave periodicity with the original swPCD in deionised water with the same Branson sonotrode used in this study [55]. A detailed investigation in water was performed as a comparison to this work with the new swPCD, which was additionally oriented differently to the previous study (perpendicular to sonotrode as opposed to directly underneath), with validation for the new positioning. The results generated in water also provided a comparator to the results generated in the DESs.

Fig. 5.3 is swPCD data over (a) a 200 ms duration and (b) 2 ms duration at an input power of 23%, representative HSI is provided in fig. 5.3 (c) over the shorter duration indicated by the green box, fig. 5.3 (b). Where HSI sequences are presented, a single timing is given in one imaging frame that represents the point of sonication within the green box (fig. 5.3 (b)), all other HSI timings are relative to that identified frame.

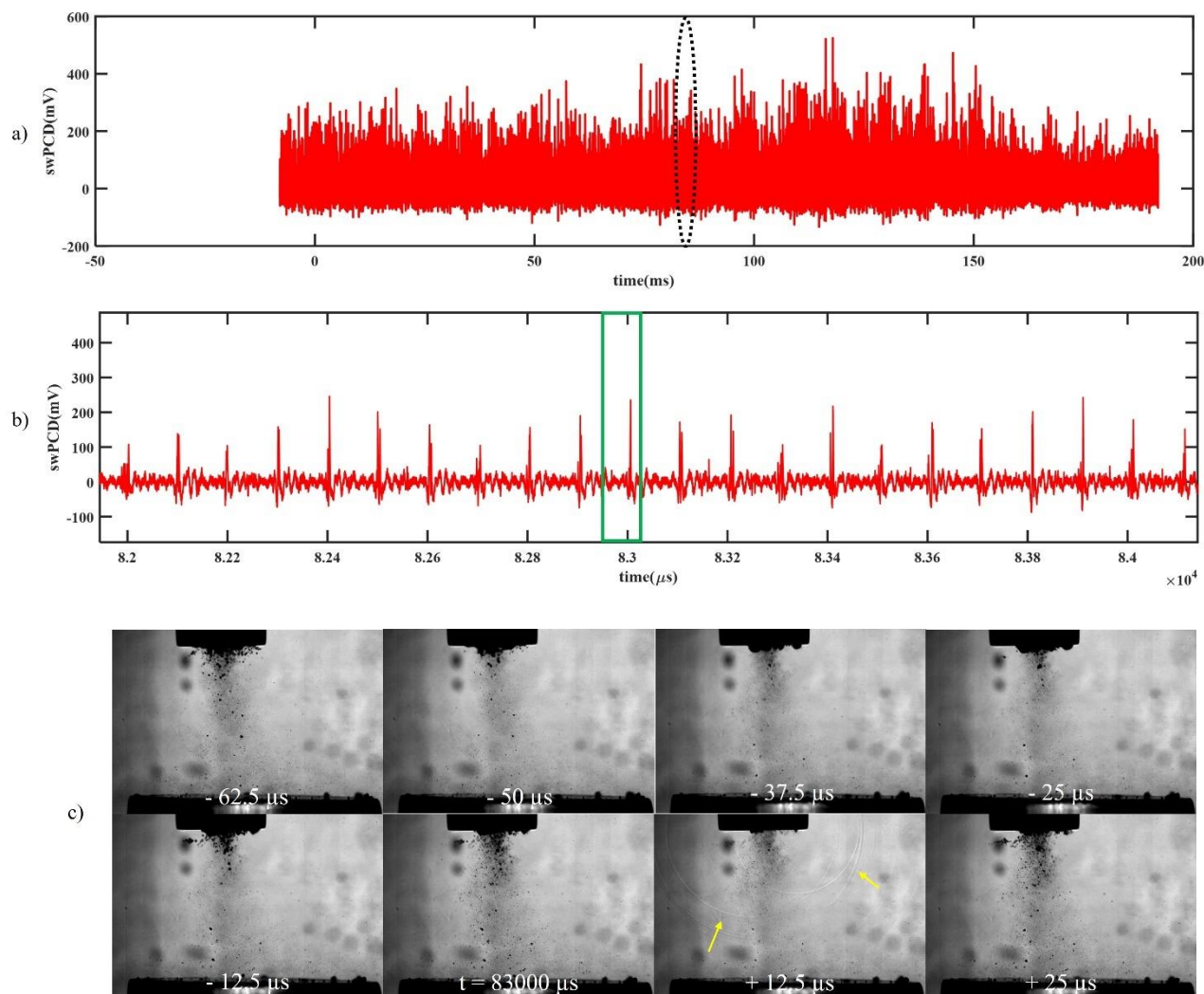


Fig. 5.3: swPCD data over (a) 200 ms and (b) 2 ms identified by the dashed oval, sampled approximately 4 s into the sonication at 23% input power in water. Sample HSI extracted from the image sequence, corresponding to the green box of (b). Bubble collapse shockwaves are arrowed in yellow.

The data of fig. 5.3 reveals primary cluster collapse and shockwave detection at regular periodicity of  $\sim 100 \mu\text{s}$ , or  $2T_0$ . In between each collapse, there is typically a single non-collapsing deflation, captured at  $-37.5 \mu\text{s}$  in fig. 5.3 (c). This is referred to as period doubling. This cavitation activity was similarly observed at powers immediately adjacent to 23% input power, with the difference being shockwave amplitude slightly lower and higher at input powers lower and higher, respectively.

Fig. 5.4 presents data at an input power of 27% in the same format as fig. 5.3, above.

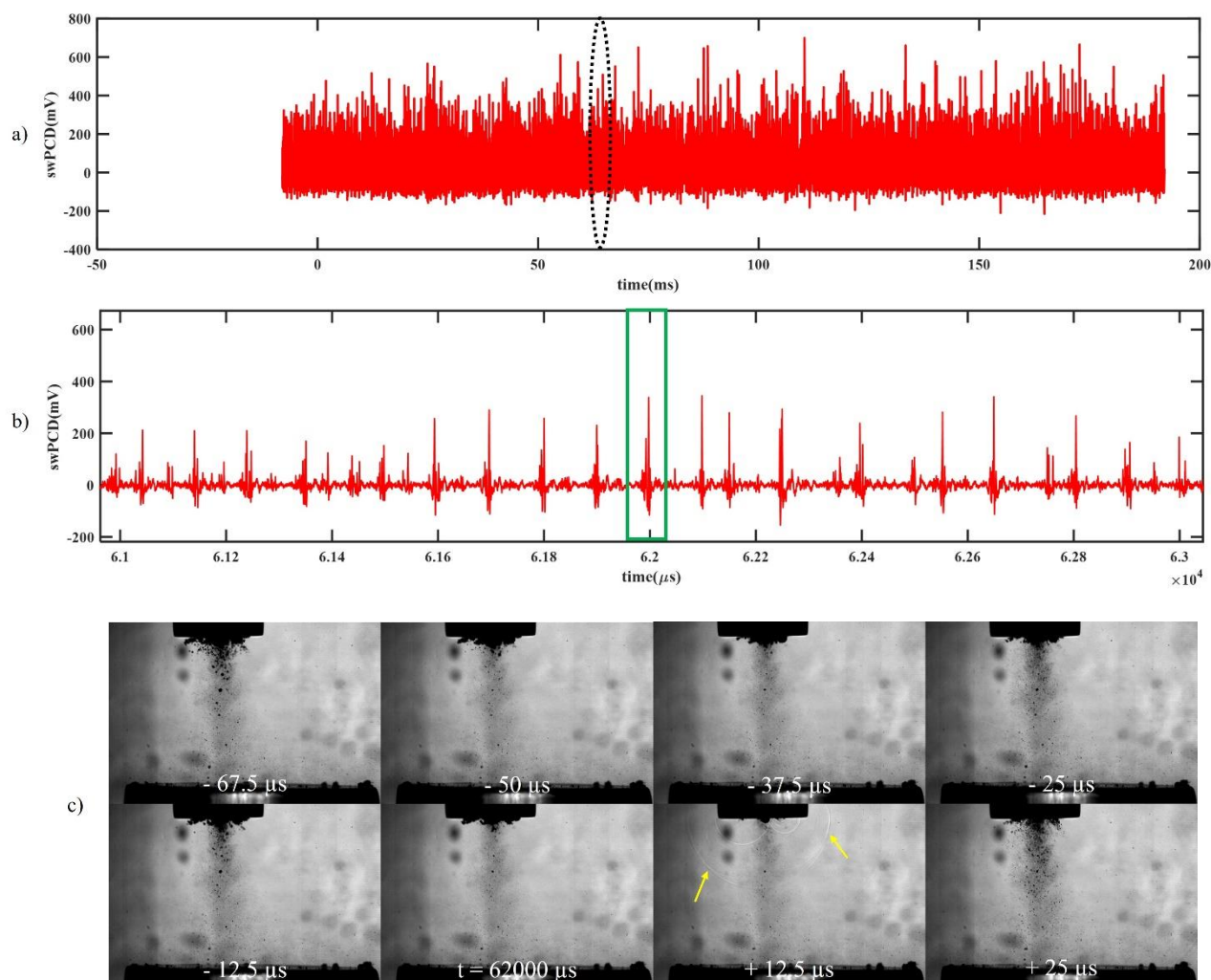


Fig. 5.4: swPCD data over (a) 200 ms and (b) 2 ms identified by the dashed oval, sampled approximately 4 s into the sonication at 27% input power in water. Sample HSI extracted from the image sequence, corresponding to the green box of (b). Bubble collapse shockwaves are arrowed in yellow.

In fig. 5.4, between  $6.1$  and  $6.16 \times 10^4 \mu\text{s}$  there is an apparent extended sequence of signal containing weak or non-collapsing deflations with no prominent shockwave of regular periodicity. Between  $6.2$  and  $6.24 \times 10^4 \mu\text{s}$  there is additional evidence of bubble collapse at periods ranging from  $T_0$  to  $3T_0$ .

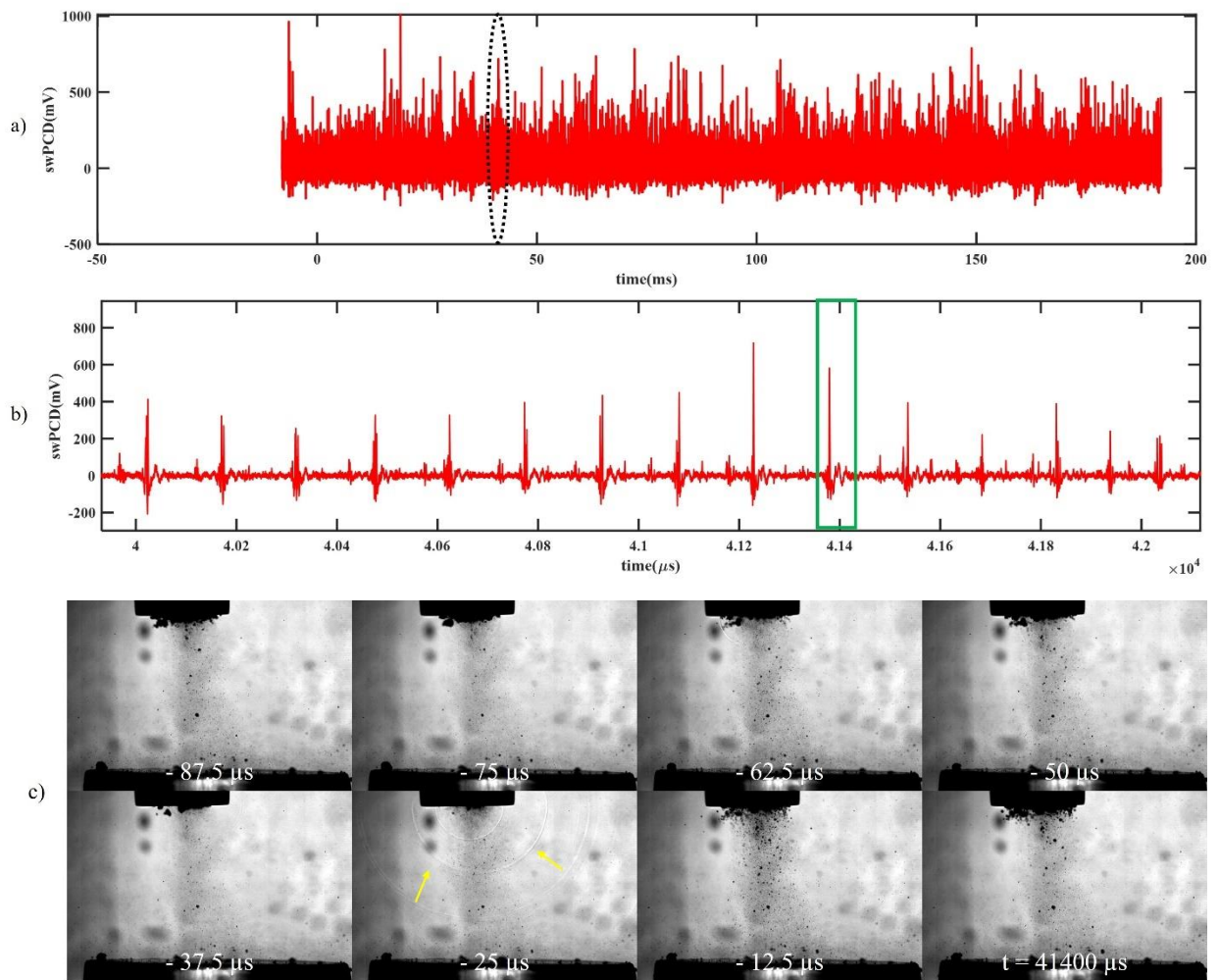


Fig. 5.5: swPCD data over (a) 200 ms and (b) 2 ms identified by the dashed oval, sampled approximately 4 s into the sonication at 40% input power in water. Sample HSI extracted from the image sequence, corresponding to the green box of (b). Bubble collapse shockwaves are arrowed in yellow.

At a higher input power of 40%, fig. 5.5, a larger bubble cluster exhibits regular  $3T_0$  collapse behaviour throughout the represented 2 ms duration. This periodicity is brought about by a cluster collapse - detected by the swPCD and the HSI – followed by subsequent inflation, partial deflation, re-inflation and a final non-collapsing deflation before the next successive detected collapse.

### 5.3.2 Cavitation emission noise spectra at selected input powers in water

The spectra of the swPCD signal were obtained to reveal the frequency content of the corresponding time domain data presented in §5.3.1. In this section, spectra from the swPCD data at 23, 30 and 40% power are presented. *Song et al* provide a model [73] for determining the contribution of periodic bubble-collapse shockwaves to the noise spectrum of the emission signal (summarised in Appendix A). Briefly, the frequency of shockwave emission,  $f_{sw}$ , generates spectral peaks at  $nf_{sw}$ , for all  $n$ . As expressed by *Yusuf et al* [192] and paraphrased here, for shockwaves emitted at subharmonic values the drive frequency,  $f_0$ , spectral peaks are therefore present at  $nf_0/m$ . Scattering of the primary field further contributes to the  $f_0$  and  $nf_0$  peaks in the case of nonlinear propagation.

Figs. 5.6 (a)-(c) provides representative noise spectra from the corresponding 200 ms signals presented in §5.3.1, which has previously been shown to be extensive enough duration for representation of longer sonications [55].

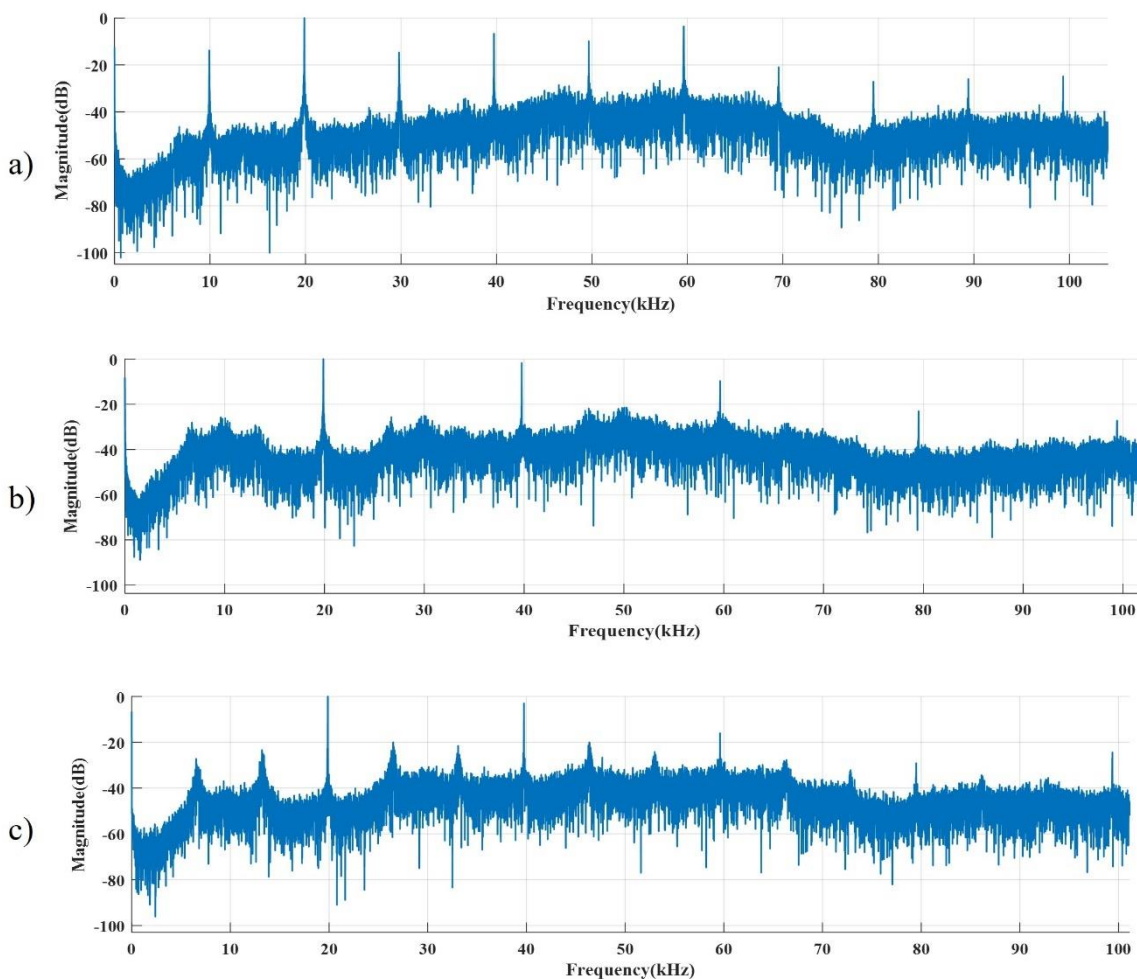


Fig. 5.6: Cavitation emission noise spectra for the sampled 200 ms section of signal presented previously in water at (a) 23% input power, (b) 27% input power and (c) 40% input power.

At 23% input power, the spectrum exhibits clear peaks with  $m = 2$  at  $nf_0/2$ , for all  $n$ . The spectral model of [73] suggests that the  $2T_0$  periodic shockwaves generated by the primary cluster collapse, fig. 5.3, raise these peaks, with additional contributions to  $nf_0$  (with  $n = 2$ , within the presented bandwidth) arising from the primary field.

27% power was previously identified as exhibiting periods of prolonged non-collapsing deflations as well as reduced consistency in periodicity in §5.3.1. This manifests in the spectra of fig. 5.6 (b) with the periodicity of shockwave emission less distinct, resulting in reduced formation of spectral peaks. Minor peaks at  $f_0/3$  are attributed to the development of  $3T_0$  shockwaves with another minor peak at  $f_0/2$ , intuitively, corresponding to  $2T_0$

shockwaves. This inability to fix to a consistent oscillation period at 27% power is coined transitional input power [55] and defines these powers where oscillation period is not clearly defined and appears to lie in between two subharmonic orders of  $m$ .

At the higher power of 40%, the  $3T_0$  shockwaves of fig. 5.5 act to raise the  $nf_0/3$  peaks of fig. 5.6 (c). Here, it can be observed that the transitional phase has ended, and the more defined shockwave periodicity observed in fig. 5.5 is apparent in the definition of peaks above.

This trend repeats for the Branson sonotrode at higher powers with  $m$  transitioning between 3 and 4 around an input power of 47% with  $m = 4$  emerging at 57%. Notably, at higher input powers, any given shockwave periodicity is less dominant, even non-transitioning powers. This behaviour is as expected, having been previously reported by [55]. It was concluded that the increment in values of  $m$  as input power is increased is due to the contribution of the periodic shockwaves and not a shift in bubble resonance at higher powers – as was suggested by [79]. *Song et al* [26] extended the spectral model of periodic shockwaves [73] to demonstrate experimentally that, for contrast agent microbubbles driven to cavitate by focused ultrasound, the spectral floor is determined by variations in the amplitude of shockwaves generated, and the precise timings of shockwave emissions. These variations redistribute power that would otherwise be contained within the frequency peaks to broadband components [192]. This manifests both at transitional amplitudes due to disproportionately large variation in shockwave amplitude (as observed in fig. 5.4) as well as at higher powers, where shockwaves become more multi-fronted due to larger primary clusters generated at higher powers containing more sub-clusters. These sub-clusters, in turn, produce more component shock fronts detected by the swPCD (examples of such can be seen in fig. 4.16). For the noise spectra presented in §5.3.2, the increased variance in shockwave amplitude at transitional input powers and multi-fronted shockwaves generated at higher powers, will both contribute to raising the spectral noise floor. Given that the higher

powers in the Branson sonotrode exhibit this behaviour, it is postulated that the Sonics horn will accordingly produce apparent reduction in shockwave periodicity at much lower powers, given its higher wattage. Data showcasing this is presented later in §5.3.7.

### 5.3.3 Shockwave content over all measured input powers in water

This results section presents swPCD data at 25 input powers ranging between 20 – 100%. The cavitation emission signals collected from five 400 ms sonication are presented at appropriate interval powers. The root mean square of the voltage,  $V_{RMS}$ , of the filtered acoustic emission at each of the input powers was obtained. Data is presented as the mean  $\pm$  standard deviation and provides a quantification to the time-averaged shockwave content of the emissions. Since both the tip-vibrational amplitude of the horn and the sizes of the bubble clusters increases with input power, it is expected that  $V_{RMS}$  should correspondingly increase [55]. Fig. 5.7 presents  $V_{RMS}$  against sonotrode input power.

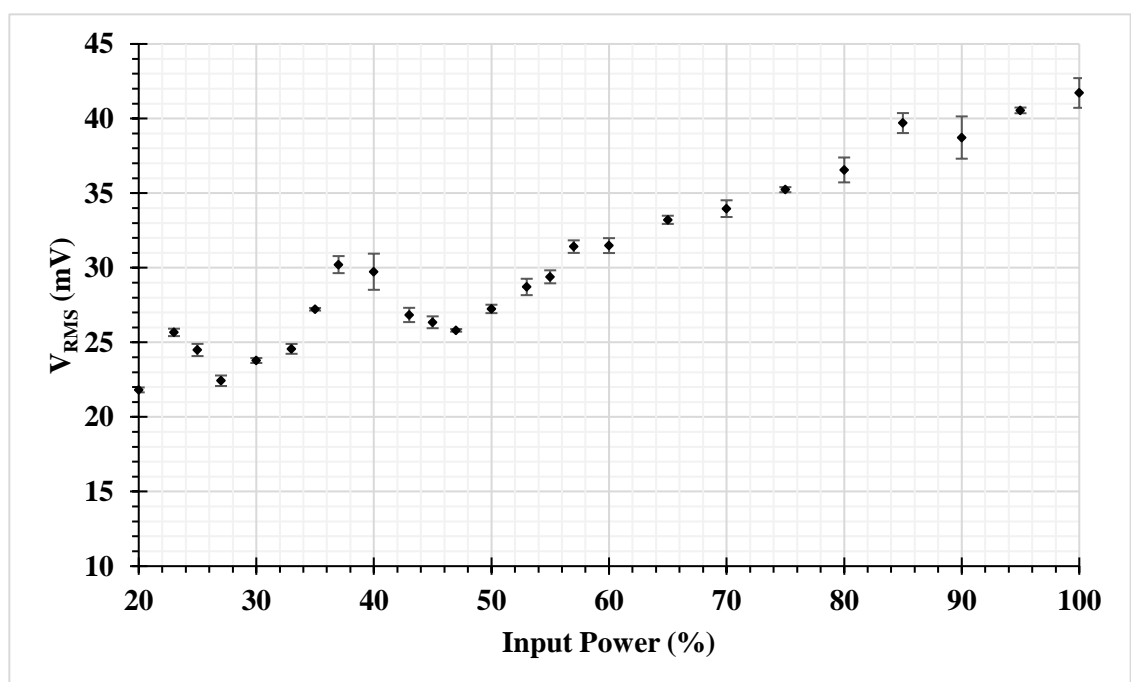


Fig. 5.7: Mean  $\pm$  standard deviation  $V_{RMS}$  over five 400 ms sonications at each input power over a twenty-five-input power range in water.

Fig. 5.7 displays two distinct dips in  $V_{RMS}$ , firstly at 27% input power and secondly at 47% input power. These dips correspond to the previously identified transitional powers presented in §5.3.1 and §5.3.2. At higher input powers, this behaviour is slightly less apparent but nonetheless observable with plateau or minor minima around 70% and 90%, respectively. This corresponds to higher order transition of  $m$  from 4 to 5 and 5 to 6, respectively. The reduced apparence of these dips at higher powers has been attributed to the increased noise of the data (associated with increased translatory speed of bubbles at higher powers) [55]. The dips are attributed to extended durations of non-collapsing deflations, observed in fig. 5.4 which are in direct contrast to the smooth emissions at regular intervals which are observed at powers with a distinct  $m$ .

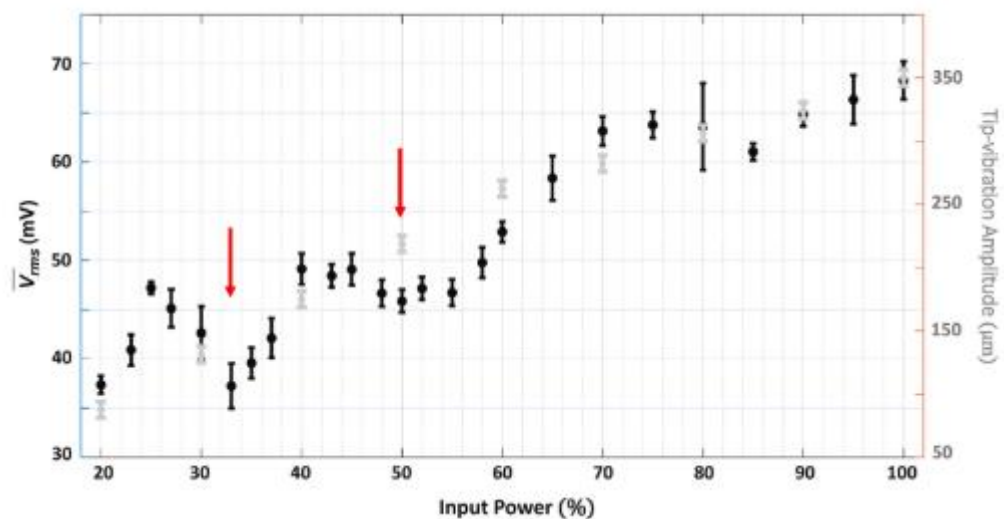


Fig. 5.8: Mean  $\pm$  standard deviation  $V_{RMS}$  over five 2 s sonications at each input power over a twenty-five-input power range in water. Taken from [62].

When comparing the results in water to *Yusuf et al* [55] (fig. 5.8) strong correlation is observed. The trend in  $V_{RMS}$  against input power follows the same trend, with dips in performance occurring around the same power ranges. We note minor shifts in transitional amplitude powers which could possibly be related to immersion depth of the horn (30 mm in this study vs 25 mm in [55]). Further adaptations to this study were: the chamber size being significantly smaller in this study to facilitate the smaller volumes of DES available; and the positioning of the swPCD being perpendicular to the sonotrode tip as opposed to directly facing underneath. Nonetheless, the correlation to [55] justifies the utility of this experimental arrangement for further investigation into the acoustic characterisation in different fluids. Finally, a shorter sampling duration of 400 ms (as opposed to 2 s) had no influence on measurement reliability. We also note that vibrational amplitude of the sonotrode increases with input power, approximately linearly, which is distinguished from bubble activity (fig. 5.8).

### **5.3.4 Bubble cluster shockwave periodicity at selected input powers in Ethaline**

The results in Ethaline, below, are presented in the same format as the water, with three key input powers of 60, 70 and 90% showcased. Again, justification for the selection of these input powers is provided by the shockwave content in the emission signal over all powers, §5.3.6. The only difference in this section of results is the increased presentation of HSI over longer duration sonications. Additional HSI is presented as the cavitation activity in Ethaline, presented below, as referred to and utilised in Chapter 6 for the assessment of optimal sonication parameters in Ethaline.

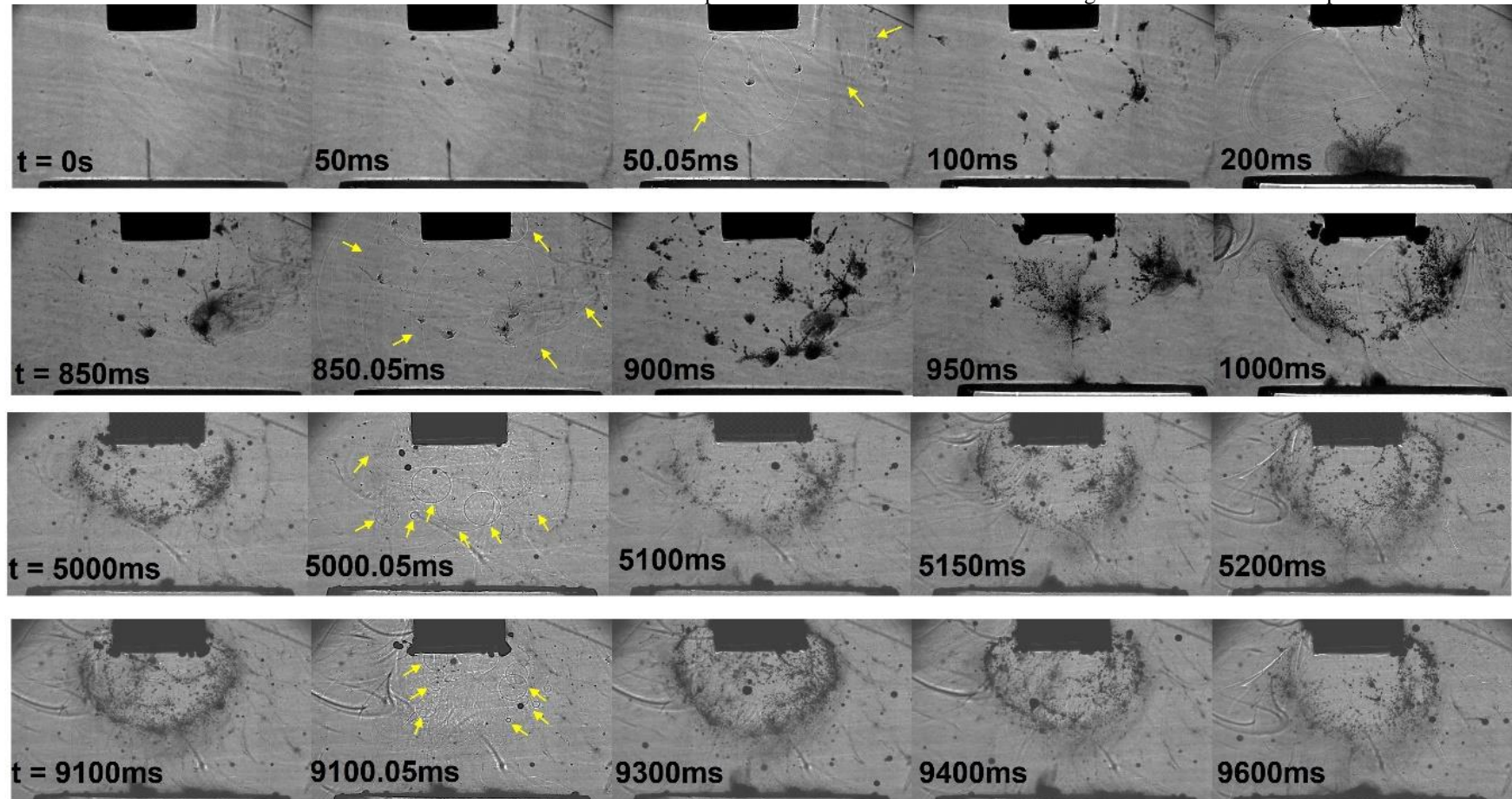
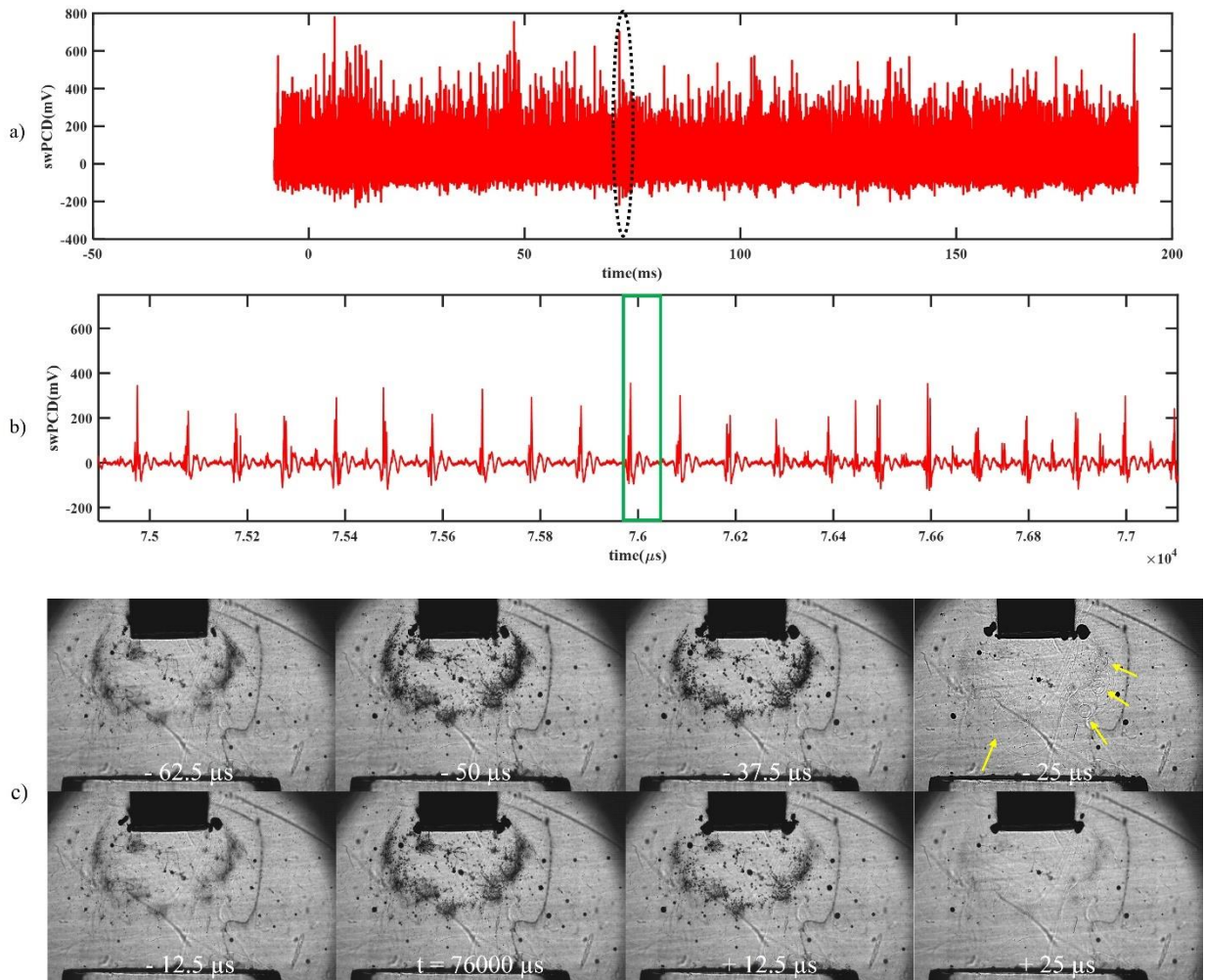


Fig. 5.9: Representative high-speed imaging of the cavitation development in Ethaline at 60% input power over a 10 s sonication. Bubble collapse shockwaves captured by the shadowgraphic imaging are arrowed yellow, and scale is provided by the 6.4 mm diameter sonotrode tip.

Chapter 5: Characterisation of the cavitation generated in different Deep Eutectic Solvents and water. Fig. 5.9 presents extended frames captured at 80 kfps which broadly represent the cavitation structure evolution in the vicinity of the sonotrode tip, operating at 60% input power. The cavitation development is highly complex, particularly over the first 1000 ms of the sonication. Cavitation structures reminiscent of those previously reported in cleaning bath configurations [60, 193] and other ultrasound reactors [194] (central densely packed spherical bubble clouds, with bubble filaments extending radially outwards) are observed towards the end of the first second of the sonication. At 1000 ms, the cavitation has arranged itself into the bulbous structure characteristic of sonotrode sonications in viscous liquids [94, 195, 196]. Notably, this structure is maintained throughout the rest of the 10 s sonication, at this input power.

Chapter 5: Characterisation of the cavitation generated in different Deep Eutectic Solvents and water. Fig. 5.10 presents swPCD data over (a) a 200 ms duration and (b) 2 ms duration collected in accordance with §5.2.4 at an input power of 60% in Ethaline. Fig. 5.10 (c) presents sample HSI extracted from the image sequence, corresponding to the green box of (b).



*Fig. 5.10: swPCD data over (a) 200 ms and (b) 2 ms identified by the dashed oval, sampled approximately 4 s into the sonication at 60% input power in Ethaline. Sample HSI extracted from the image sequence, corresponding to the green box of (b). Bubble collapse shockwaves are arrowed in yellow.*

Chapter 5: Characterisation of the cavitation generated in different Deep Eutectic Solvents and water. The cavitation emissions of fig. 5.10 showcase an oscillation period of  $2T_0$ , similar to that of CaDES (Appendix C) around the same power and to that of water at lower powers, previously reported. This is, again, the result of a single non-collapsing deflation of the primary bubble cluster in between shockwave detections. At 60% power, average shockwave amplitude is  $\sim 300$  mV. As with the previous DESs, shockwave emissions appear to originate from all around the cavitating volume, fig. 5.10 (c).

Figs. 5.11 and 5.12 are equivalent to those described for Ethaline above, but with an input power of 70%. The HSI of fig. 5.11 indicates that the cavitation generated develops with some notable differences to that at 60% input power.

The bulbous structure forms earlier in the sonication and, somewhat counter-intuitively, has a reduced radius of curvature around the tip, although with an apparent greater density of bubble clusters encapsulated. This structure is also accompanied by a fine mist of bubbles that gradually pervades through the Ethaline, forming vortex structures on interacting with the surface of the Perspex disk under the tip at 2000 ms, as shown in fig. 5.11. The bubble mist does not appear to cavitate strongly, and no bubble-collapse shockwaves are generated. It does, however, give an indication of the fluid flow via acoustic streaming within the ethaline, at the slightly higher input power.

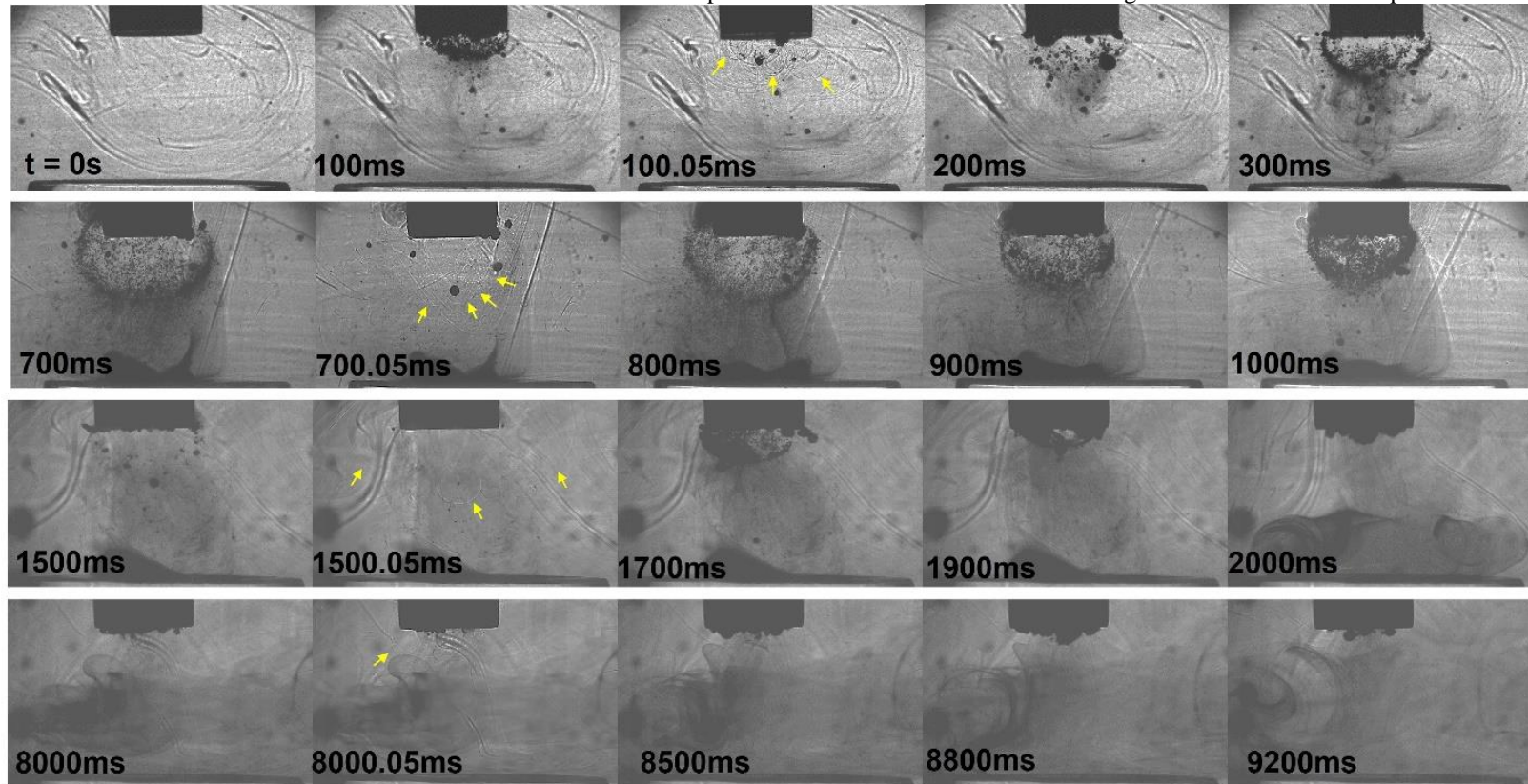


*Fig. 5.11: Representative high-speed imaging of the cavitation development in Ethaline at 70% input power over a 10 s sonication. Bubble collapse shockwaves captured by the shadowgraphic imaging are arrowed yellow, and scale is provided by the 6.4 mm diameter sonotrode tip.*

Chapter 5: Characterisation of the cavitation generated in different Deep Eutectic Solvents and water. The main difference is that, unlike at 60%, the bulbous structure is not maintained throughout the sonication. From around 1500 ms, the main cavitation activity recedes back into contact with the tip surface, where it remains for the rest of the sonication. This phase of the cavitation development bears closer resemblance to sonotrode cavitation in less viscous liquids such as water [81, 95], although the cavitation oscillations are notably suppressed compared to a sonication at a comparable input power, in water. This could suggest that the liquid properties (most importantly and relevantly viscosity) are changing within a few seconds of sonications at higher input powers. Possibly, at least in part, to temperature increase.

The emission signal detected by the swPCD of fig. 5.12 reveals the shockwave detected over the same measurement range as previous.

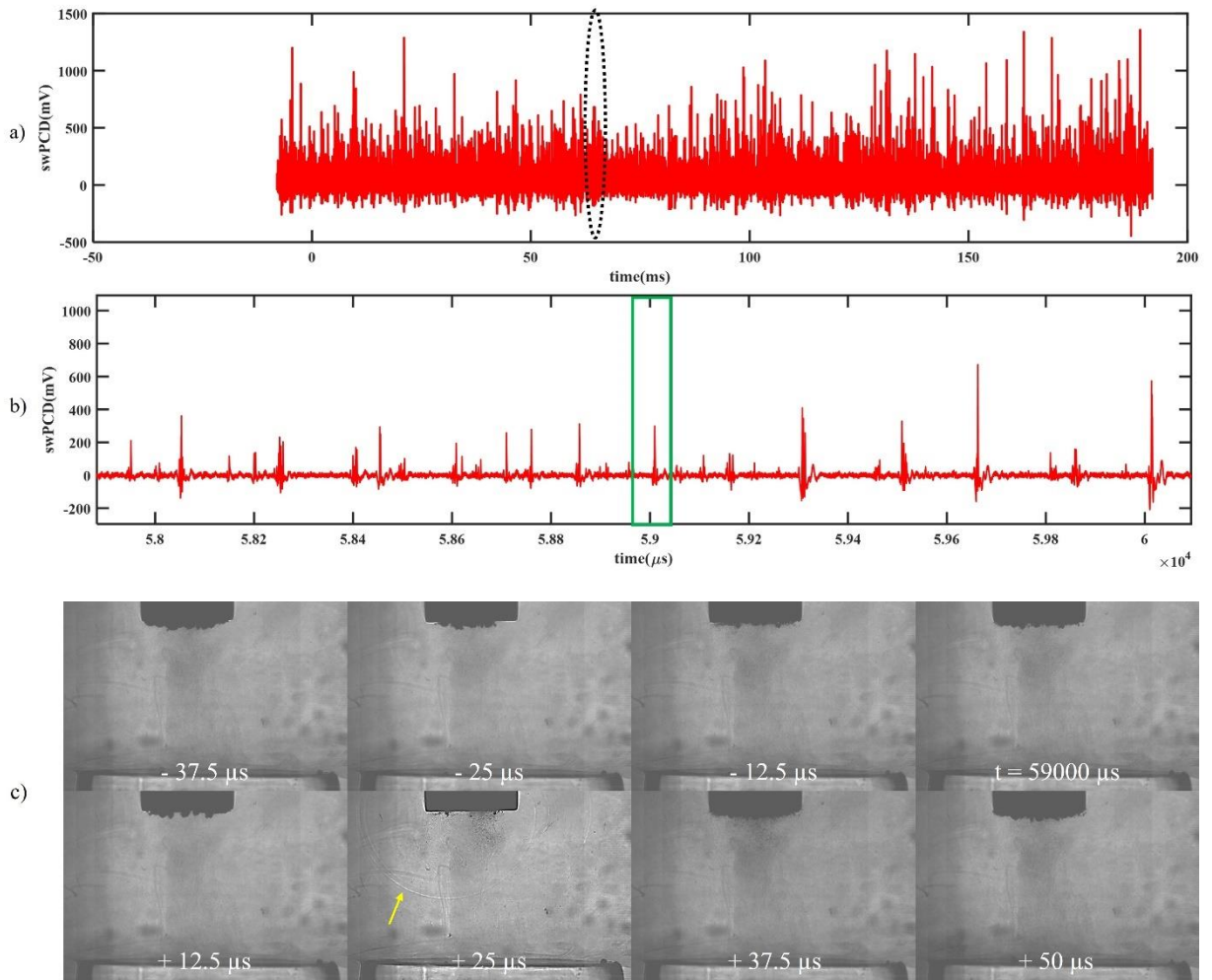


*Fig. 5.12: swPCD data over (a) 200 ms and (b) 2 ms identified by the dashed oval, sampled approximately 4 s into the sonication at 70% input power in Ethaline. Sample HSI extracted from the image sequence, corresponding to the green box of (b). Bubble collapse shockwaves are arrowed in yellow.*

Here, as was the case in each fluid beforehand, the timings of shockwave emissions has changed. Irregular emissions at  $T_0$  and  $3T_0$  are also apparent, with extended durations of weak shockwave detection. Again, suggesting a transition towards period-tripled behaviour, as a higher-order subharmonic response.

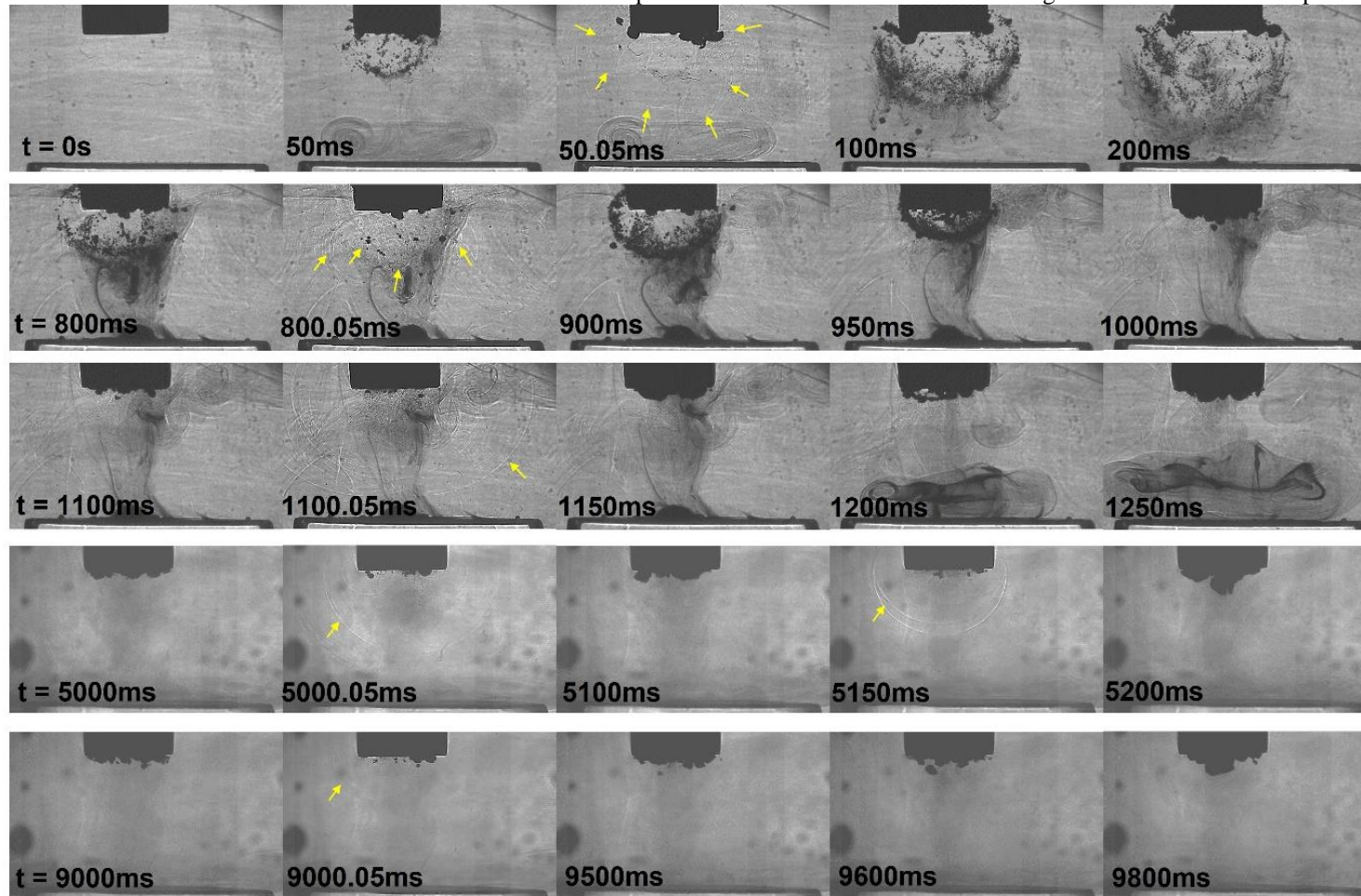
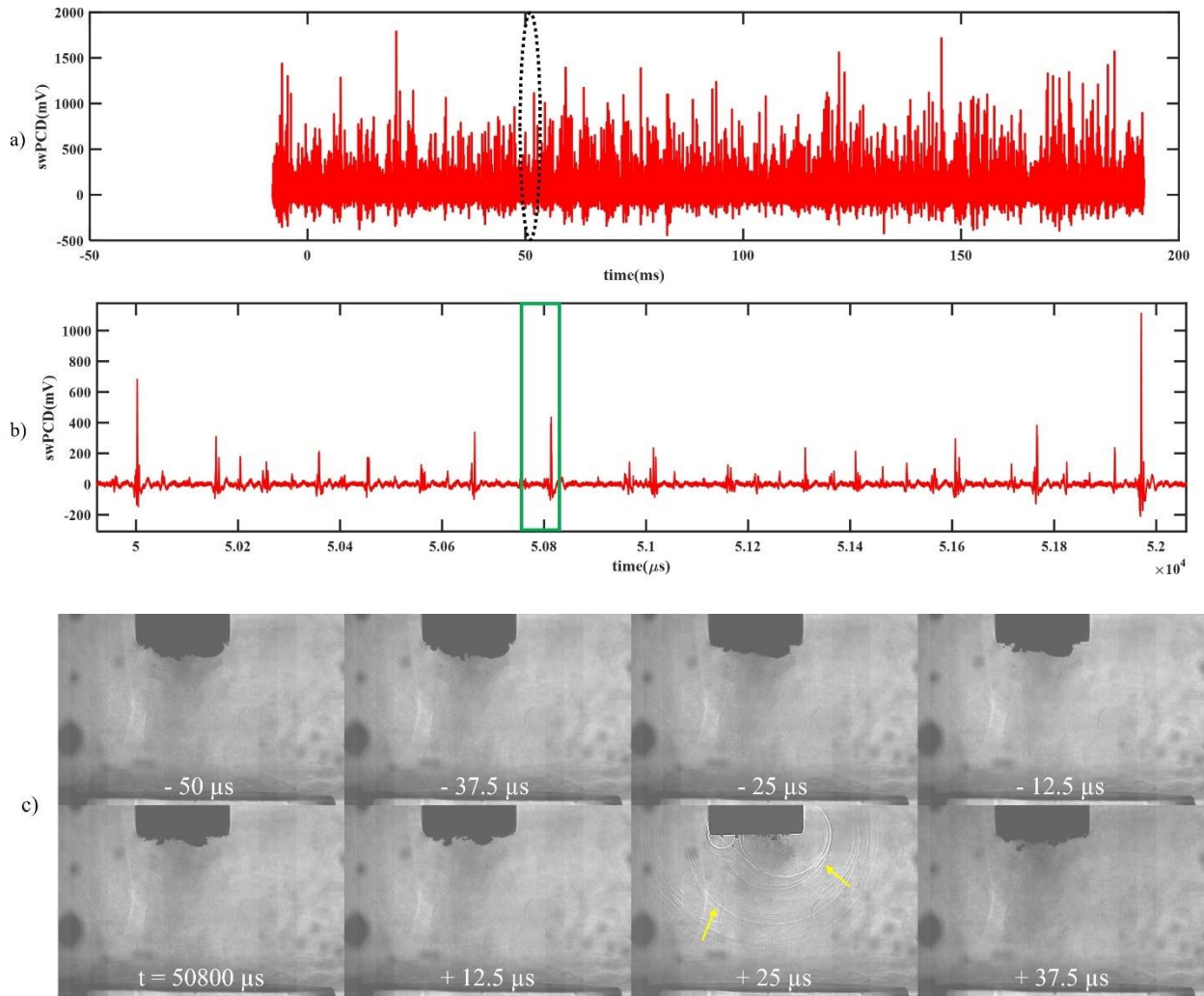


Fig. 5.13: Representative high-speed imaging of the cavitation development in Ethaline at 90% input power over a 10 s sonication. Bubble collapse shockwaves captured by the shadowgraphic imaging are arrowed yellow, and scale is provided by the 6.4 mm diameter sonotrode tip.

Chapter 5: Characterisation of the cavitation generated in different Deep Eutectic Solvents and water. The HSI of fig. 5.13 demonstrates an enhancement in the development trends seen in the imaging data at 70% input power. The bulbous structure develops within the first 100 ms of the sonication, extending down to the surface of the Perspex disk at 200 ms, the receding of the main cavitation activity, back to the horn-tip is also accelerated, to within the first second of sonication. A fine bubble mist again reveals vortex flow at the surface, from 1200 ms. A cavitating bubble cluster is also apparent, intermittently, in contact with the Perspex surface during the first few seconds, however, as with 70%, no bubble-collapse shockwaves were observed emitting from this. After that, the main cavitation is directly under the oscillating tip, and as would be expected, is more prominent than at the lower power of 70%.



*Fig. 5.14: swPCD data over (a) 200 ms and (b) 2 ms identified by the dashed oval, sampled approximately 4 s into the sonication at 90% input power in Ethaline. Sample HSI extracted from the image sequence, corresponding to the green box of (b). Bubble collapse shockwaves are arrowed in yellow.*

As power is increased further, a continuation of non-detection or smaller amplitude (under 100 mV) features occur at  $T_0$ , suggesting sub-clusters within the primary cluster under the tip are collapsing out of phase with others. Most of the higher amplitude shockwaves are, however, detected at  $4T_0$  timings associated with period-quadrupled response.

### 5.3.5 Cavitation emission noise spectra at selected input powers in Ethaline

Fig. 5.15 presents the acoustic emission spectra corresponding to the time domain emission signals detected in Ethaline, above. Presented in the same format as for water (fig. 5.6).

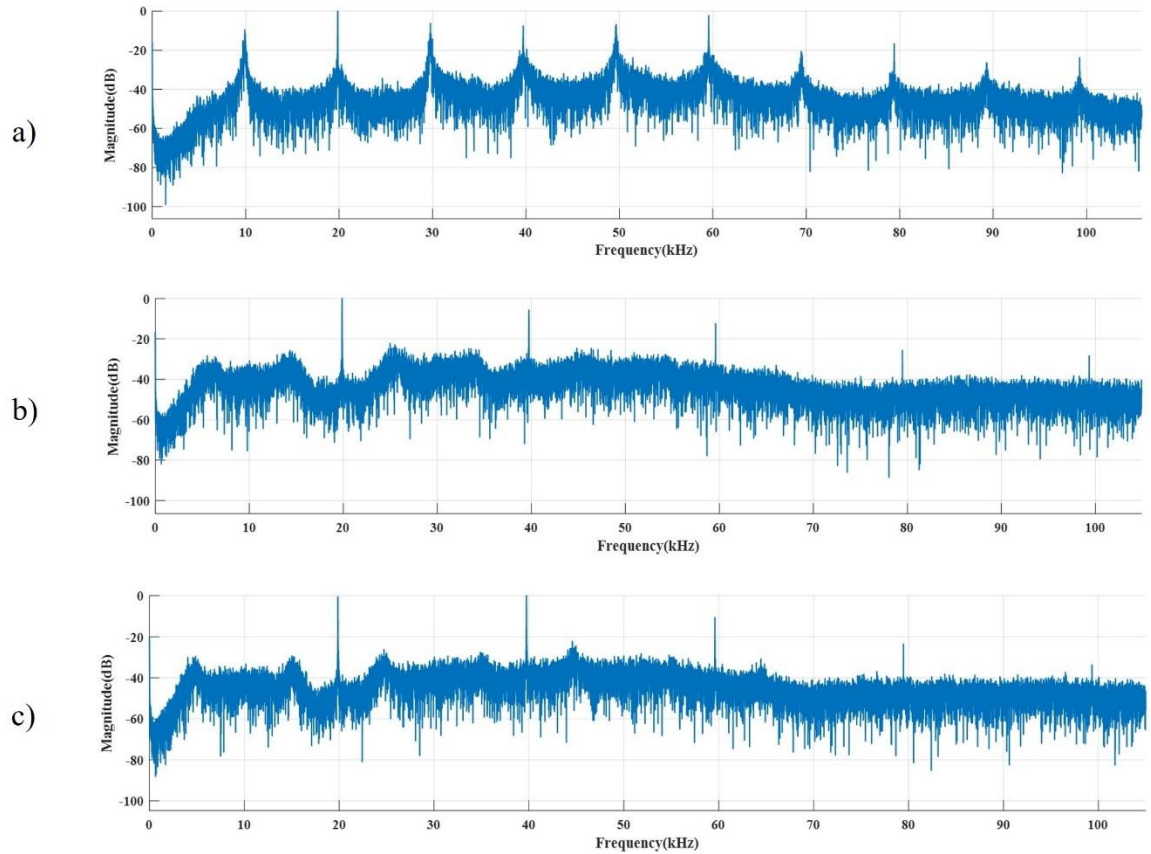


*Fig. 5.15: Cavitation emission noise spectra for the sampled 200 ms section of signal presented previously in Ethaline at (a) 60% input power, (b) 70% input power and (c) 90% input power.*

The acoustic emission presented for Ethaline at 60% power manifest in the spectra with the notable peaks at  $nf_0/m$  where  $m = 2$ , for all  $n$ . This is, again, a result of the almost exclusive period doubling ( $2T_0$ ) oscillations of the bubble cluster.

As expected from the transitional nature of the acoustic emissions at 70% power, with a bias towards  $3T_0$  oscillations, the emission spectra reveals low magnitude, broad peaks at  $nf_0/3$  for all  $n$ . Again, the amplitude variance and multi-fronted shockwaves result in power

Chapter 5: Characterisation of the cavitation generated in different Deep Eutectic Solvents and water. redistribution from the peaks the noise floor. This is observed as beyond 50 kHz the peaks between  $nf_0$  values are not apparent above the spectral floor.

At 90% power there is little definition in the subharmonic spectrum, with barely apparent low amplitude broad peaks visible at  $nf_0/4$  for all  $n$ . Although, for  $n > 60$  kHz, peaks are not apparent above the spectral floor, for the same reason discussed previously.

### 5.3.6 Shockwave content with the emission signal over all measured input powers in Ethaline

This results section presents swPCD data at 17 input powers ranging between 20 – 100%. The cavitation emission signals collected from five 400 ms sonications are presented at appropriate interval powers, as displayed for the previous solutions.

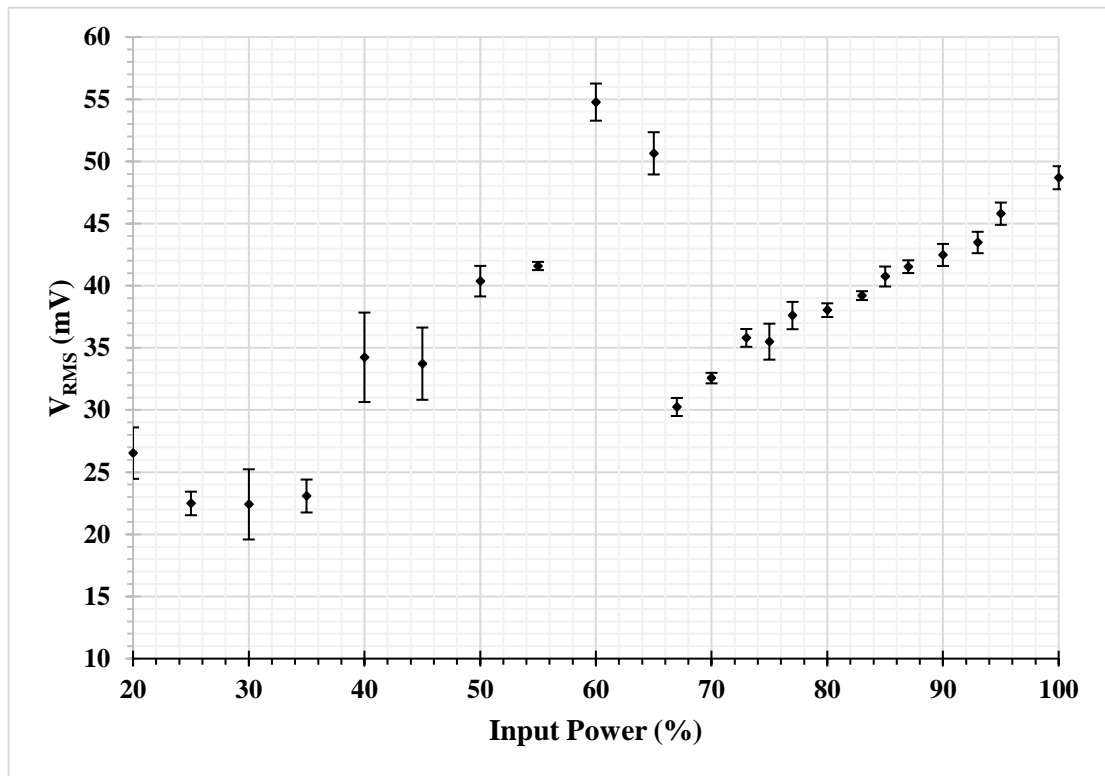


Fig. 5.16: Mean  $\pm$  standard deviation VRMS over five 400 ms sonications at each input power over a seventeen-input power range in Ethaline.

Chapter 5: Characterisation of the cavitation generated in different Deep Eutectic Solvents and water. In fig. 5.16, a general increase in  $V_{RMS}$  is observed until a maximum at 60% input power, which was shown to be the power of most uniform (or synchronous) bubble-cluster oscillation, with periodicity of  $2T_0$ . Beyond 60%, a short drop in cavitation emission is detected, associated with the transitional ( $m$  transitioning for 2 to 3) nature of this power. However, beyond 65% we observe a large drop (over 40%) in  $V_{RMS}$ . This is associated with the greater increased drop in shockwave content detected in the acoustic emissions, associated with vastly increased durations of non-shocking activity (exhibited in fig. 5.12). In conjunction with this shift in bubble collapse oscillation, we also note the characteristic transition of cavitation structure presented over an extended (15 s) duration. From the HSI, it is apparent that the shift in acoustic behaviour and drop-off in  $V_{RMS}$  also corresponds with the recession of bubble activity back to the sonotrode tip, and a smaller overall cavitation zone in each of the DESs (CaDES and Reline outlined in Appendix C).

### 5.3.7 Horn crossover regions

All of the results presented in §5.3 (and Appendix C) were repeated for the higher power Sonics sonotrode. The shockwave content with the emission signal over all measured input powers in each of the four solutions is presented in figs. 5.17 – 5.20. This section also demonstrates the utility of quick and simple  $V_{RMS}$  measurements in any fluid as a method of identifying comparable input powers on different systems of different properties (in this case power and tip diameter) in terms of cavitation output. To demonstrate this, the  $V_{RMS}$  plots for each solution from both sonotrodes are presented, with analysis into the acoustic emissions at key selected powers in water and Ethaline as representative cases.

Figs. 5.17 – 5.20 present the  $V_{RMS}$  plots for each solution with both horns at sufficient interval powers.

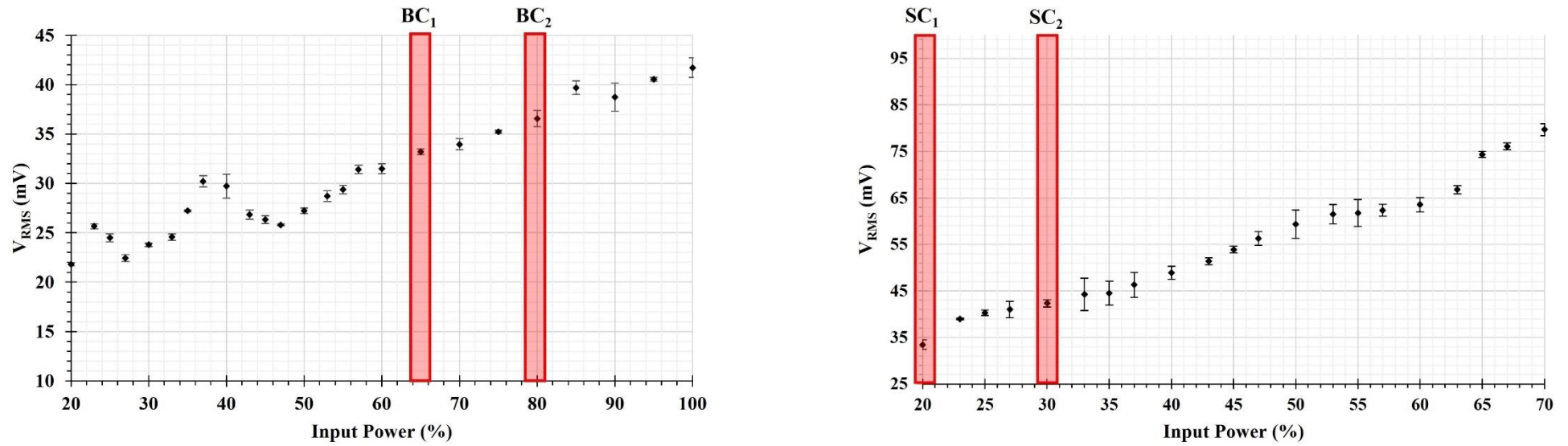


Fig. 5.17: Mean  $\pm$  standard deviation  $V_{RMS}$  over five 400 ms sonications at each input power for both the Branson and Sonics sonotrode in water. Crossover regions are highlighted in red and labelled.

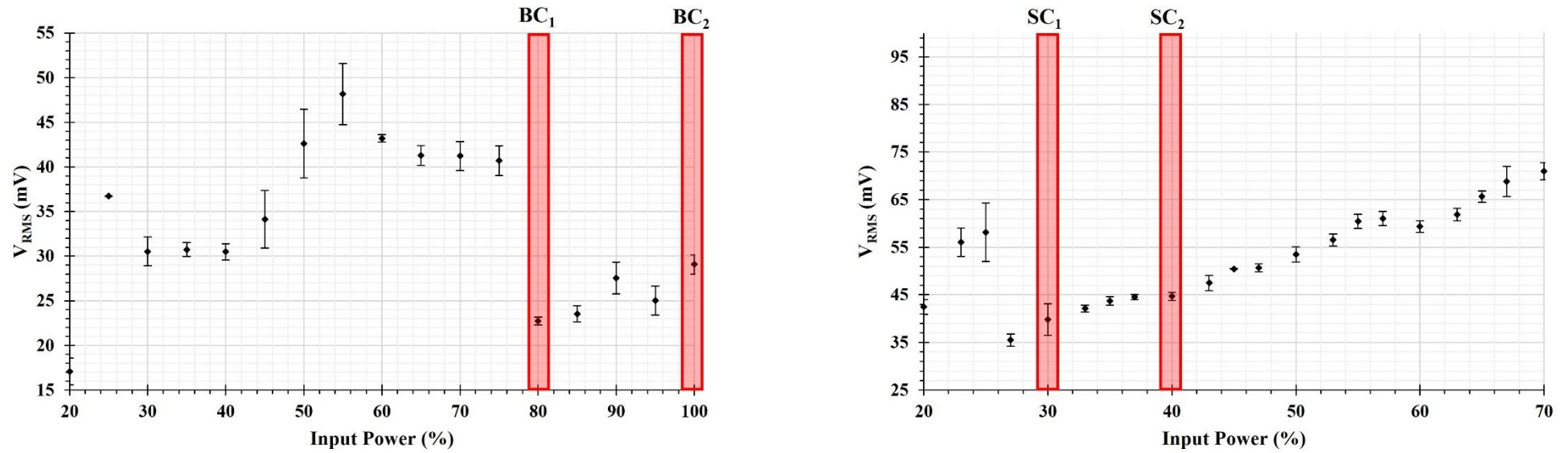


Fig. 5.18: Mean  $\pm$  standard deviation  $V_{RMS}$  over five 400 ms sonications at each input power for both the Branson and Sonics sonotrode in CaDES. Crossover regions are highlighted in red and labelled.

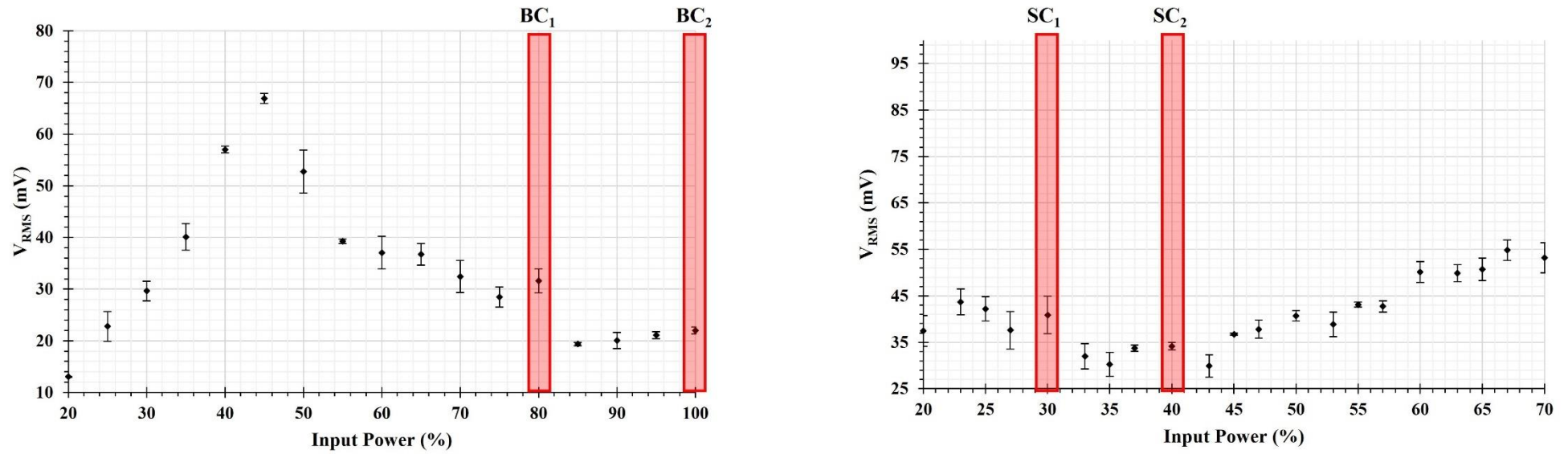


Fig. 5.19: Mean  $\pm$  standard deviation  $V_{RMS}$  over five 400 ms sonications at each input power for both the Branson and Sonics sonotrode in Reline. Crossover regions are highlighted in red and labelled.

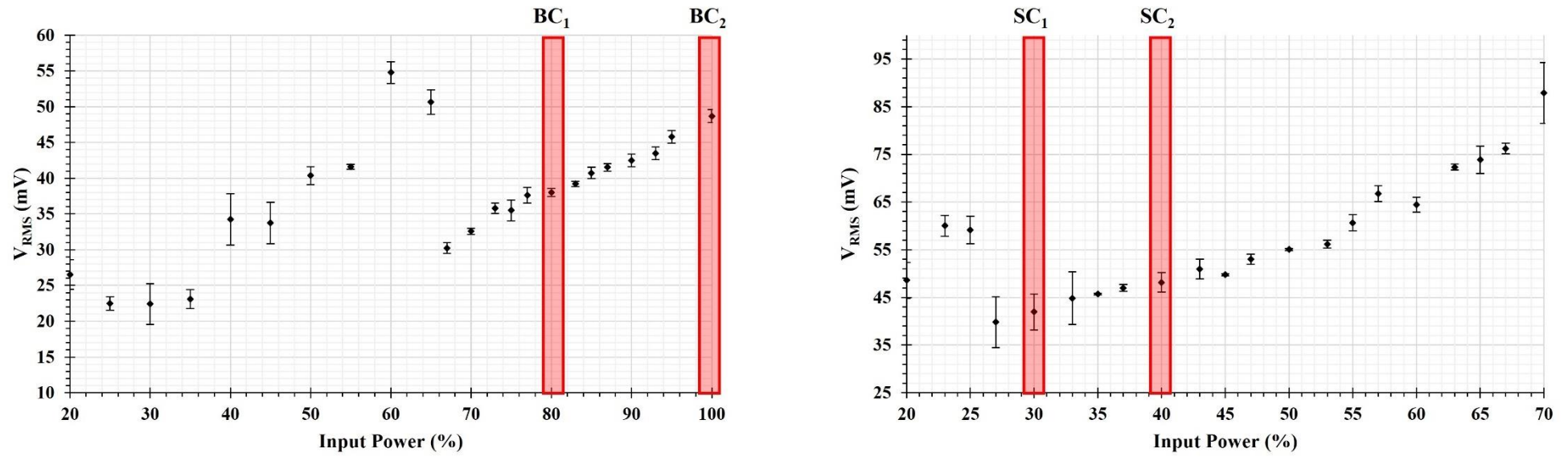


Fig. 5.20: Mean  $\pm$  standard deviation  $V_{RMS}$  over five 400 ms sonications at each input power for both the Branson and Sonics sonotrode in Ethaline. Crossover regions are highlighted in red and labelled.

Firstly, it is shown that, for the higher power Sonics horn in each fluid, the  $V_{RMS}$  plots exhibit notably reduced dips and peaks in comparison to the Branson horn. It is apparent that the Sonics horn, from a lower input power appears to resemble the higher powers of the Branson horn in terms of  $V_{RMS}$  trend. This is expected and explained by the higher power horn producing shockwaves that are more multi-fronted and variable in amplitude. Furthermore, through the distribution of the emission signal from subharmonic peaks to broadband noise at higher powers, the dips are correspondingly dampened (or less apparent) due to the increased noise, which was also associated with increased translatory speed of bubbles at higher powers [55].

From simple observation of the  $V_{RMS}$  plots in each solution, trends are apparent. Particular regions from each horn are highlighted in red and labelled accordingly –  $BC_1$  and  $SC_1$  represent “Branson Crossover 1” and “Sonics Crossover 1”, and these selected powers represent regions of similar  $V_{RMS}$  in terms of magnitude between the two horns. However, the important relevance of these sections is their relative positioning to trend landmarks. For example, in each of the DESs, the crossover region occurs after a dip in the  $V_{RMS}$  signal, with the second identified crossover corresponding to a higher power in each respective horn with a similar trend in growth. It can be observed that highlighted crossover regions are closer in terms of input power difference, in the Sonics horn than the Branson horn – indicating that the Sonics horn is transitioning the cavitation to higher orders over a shorter range of powers. This is as expected with the higher power horn and is also observed in the Branson horn, with transition from  $m = 2$  to  $m = 3$  occurring over a relatively short range of lower input powers.

Furthermore, it is noted that, regardless of fluid, the crossover regions between each sonotrode appear around the same input power. i.e., a crossover region is highlighted at 80% input power for the Branson, and this is matched with a crossover region at 30% input power for the Sonics sonotrode. This suggests that, for this horn-tip setup, the vibrational amplitude

at each respective power is approximately equivalent. From calculation using his to estimate vibrational amplitude in water, this appears to be the case with a vibrational amplitude of  $330 \pm 30 \mu\text{m}$  estimated from the imaging, which is in alignment with the manufacturer's operating manual, as well as [55]. We note, however, that vibrational amplitude is an estimate from the HSI. For precise vibrational amplitude measurements, a laser doppler vibrometer would be recommended. However, such an instrument capable of vibrational measurements in a fluid were not available for this study.

Although, simple observation of the  $V_{RMS}$  trend may give indications as to potential crossover regions between sonotrodes, detailed characterisation of the cavitation activity was performed to generate the highlighted regions shown above. §5.3.8 and §5.3.9 present acoustic emission data for water and Ethaline, respectively, to demonstrate the equivalence in cavitation behaviour at these powers for both sonotrodes.

### 5.3.8 Cavitation characterisation for crossover regions in water

Figs. 5.21 and 5.22 present sampled swPCD data and corresponding acoustic emissions spectra for the four crossover regions identified in §5.3.7, in water.

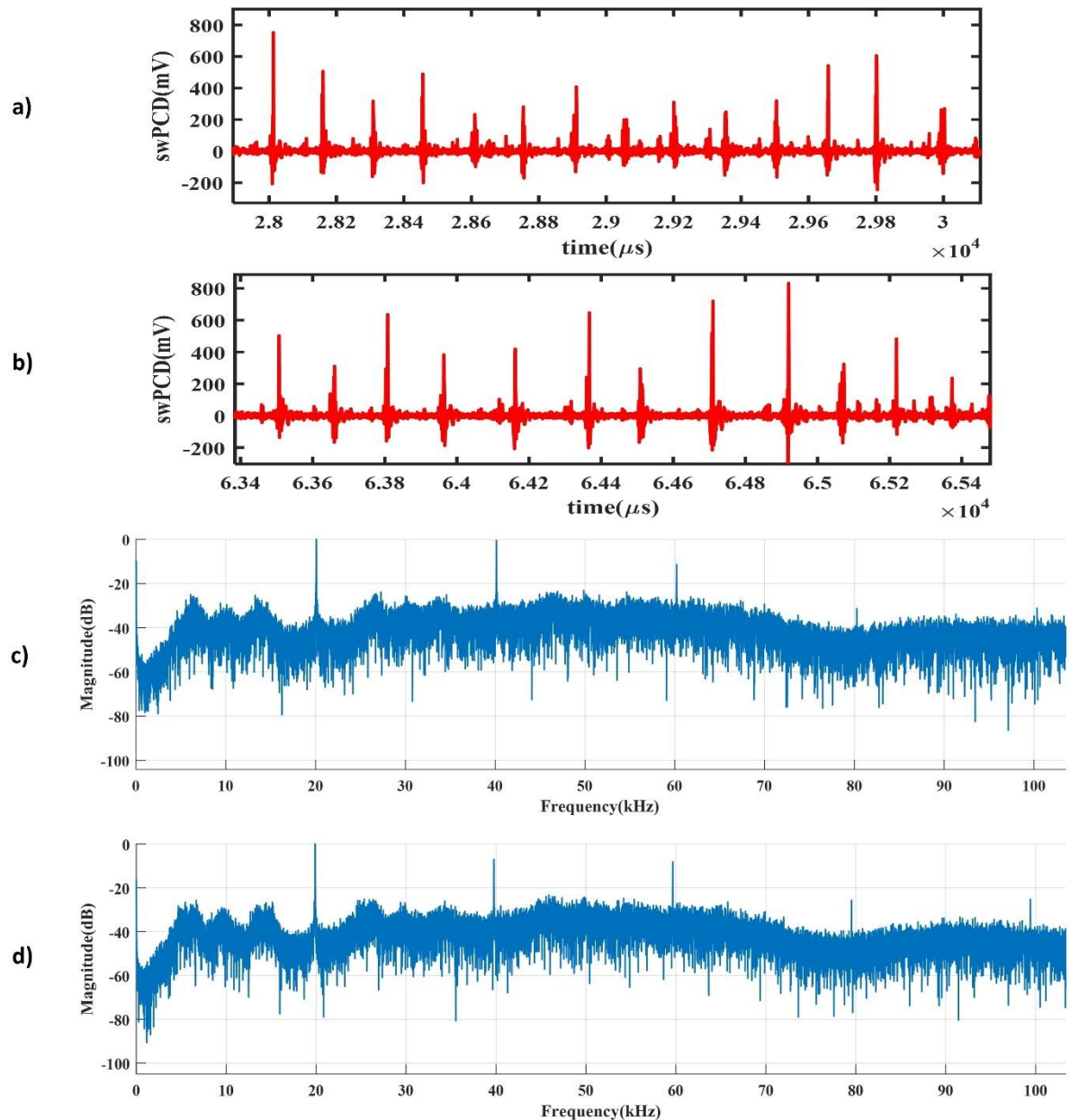


Fig. 5.21: Sampled swPCD data over a 2 ms duration in water at (a) 65% input power on the Branson sonotrode and (b) 20% input power on the Sonics sonotrode. Cavitation emission noise spectra for the sampled swPCD data is presented for (c) the Branson sonotrode at 65% input power and (d) the Sonics sonotrode at 20% input power.

The swPCD data of fig. 5.21 (a) and (b) show that at 65% and 30% input power on the Branson and Sonics sonotrode, respectively, shockwave emissions are detected at both  $3T_0$  and  $4T_0$ , with both traces exhibiting low amplitude  $T_0$  emissions. This manifests in the spectra of the corresponding signals with both sonotrodes producing very similar subharmonic peaks corresponding to mostly  $f_0/4$ , with peaks being relatively low magnitude and broad in signal. The subharmonic spectra is representative of a transition from  $f_0/3$  to  $f_0/4$  which is apparent from the shockwave timings observed in the swPCD data. Additionally, shockwaves are of a comparable average amplitude  $\sim 400$  mV for each sonotrode.

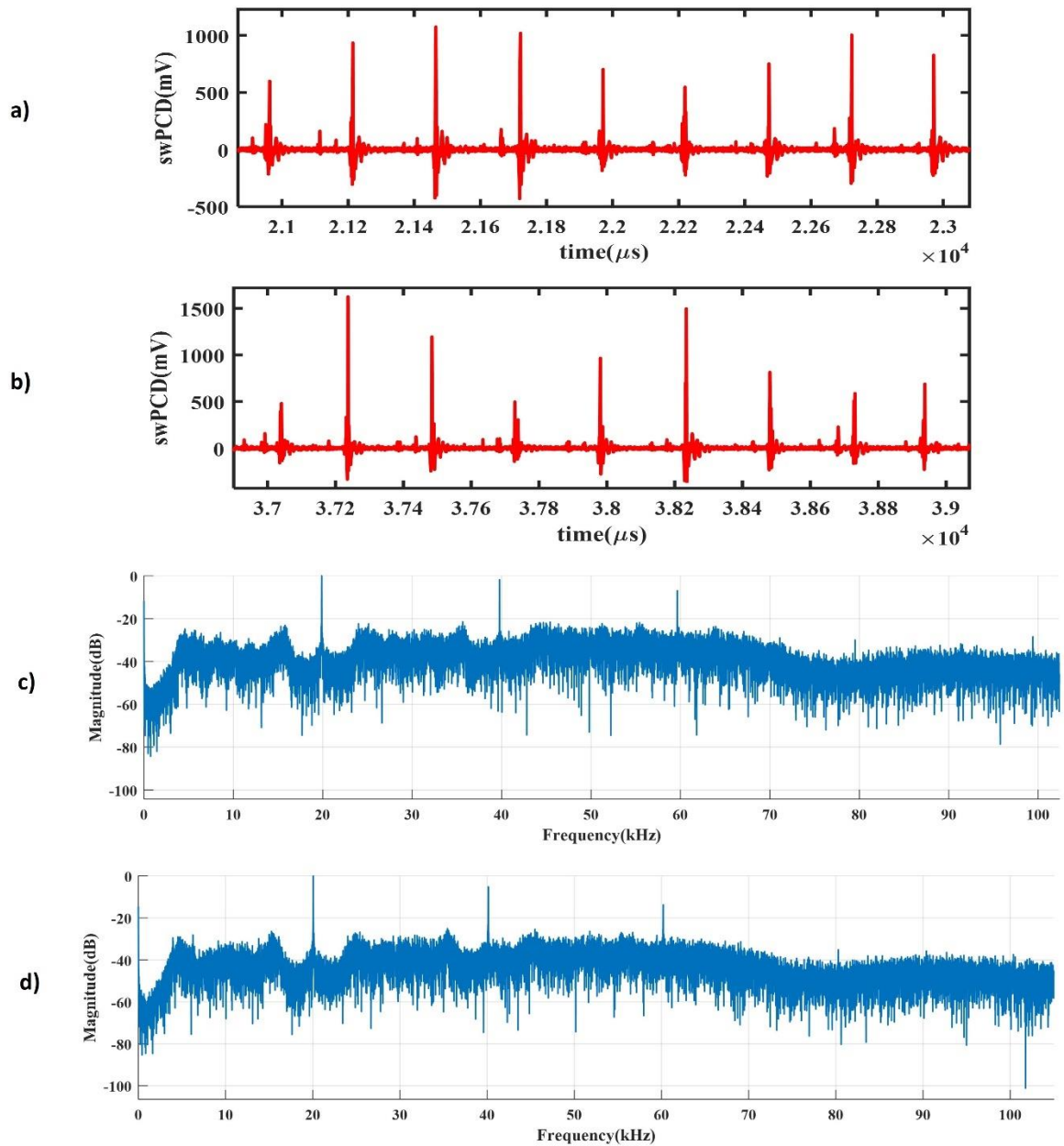


Fig. 5.22: Sampled swPCD data over a 2 ms duration in water at (a) 80% input power on the Branson sonotrode and (b) 30% input power on the Sonics sonotrode. Cavitation emission noise spectra for the sampled swPCD data is presented for (c) the Branson sonotrode at 80% input power and (d) the Sonics sonotrode at 30% input power.

The swPCD data of fig. 5.22 details that shockwave emissions from both horns are mostly comprised of  $5T_0$  timings, with the presence of some  $4T_0$  shockwaves. Again, this manifests in the emissions spectra with the presence of subharmonic peaks most prominent around  $f_0/5$ ,

again these peaks are fairly broad due to power redistribution to the noise floor at higher input powers, with the ultraharmonics falling below the spectral floor beyond 60 kHz.

### 5.3.9 Cavitation characterisation for crossover regions in Ethaline

Figs. 5.23 and 5.24 present sampled swPCD data and corresponding acoustic emissions spectra for the four crossover regions identified in §5.3.7, in Ethaline.

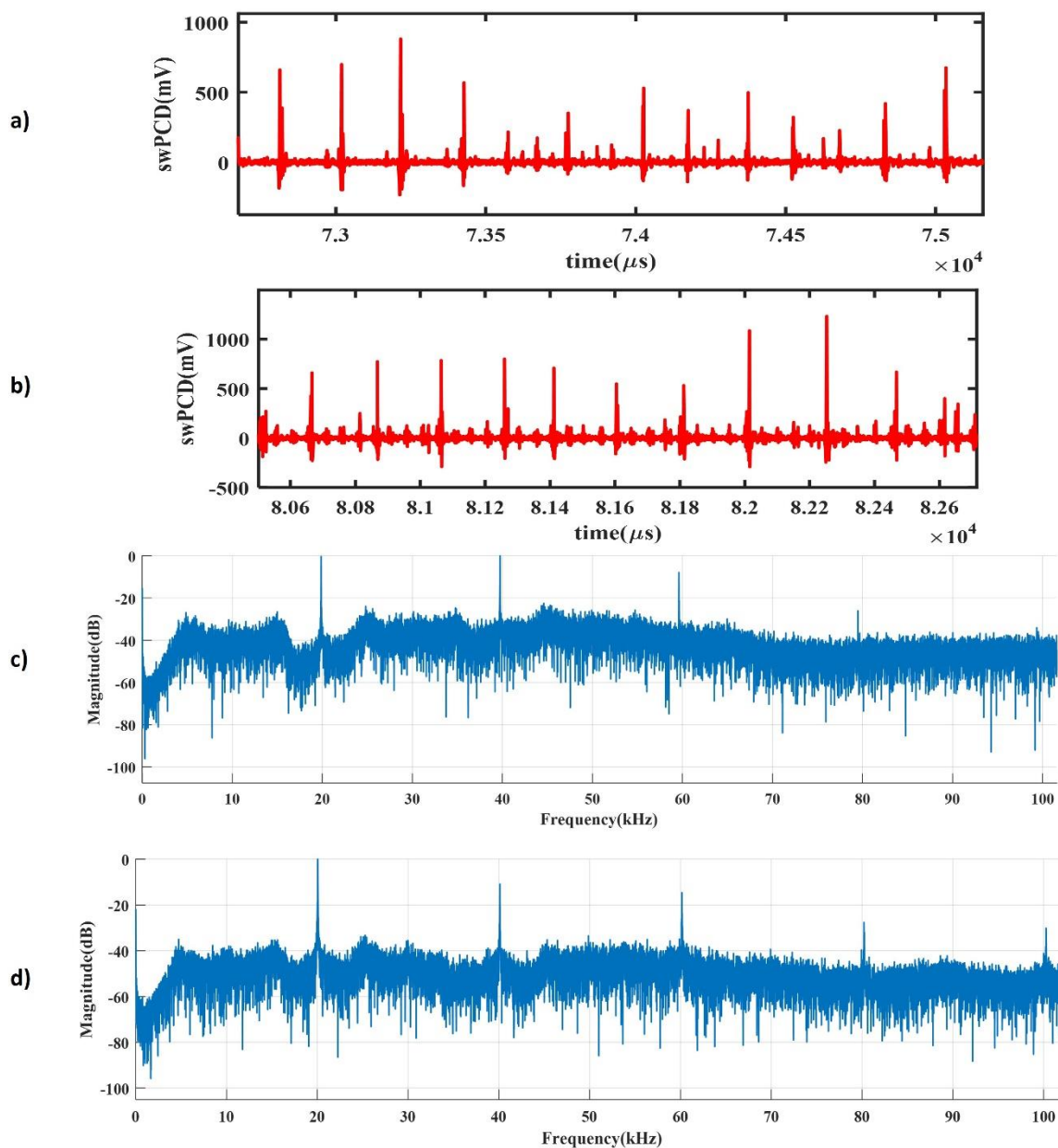


Fig. 5.23: Sampled swPCD data over a 2 ms duration in Ethaline at (a) 80% input power on the Branson sonotrode and (b) 30% input power on the Sonics sonotrode. Cavitation emission noise spectra for the sampled swPCD data is presented for (c) the Branson sonotrode at 80% input power and (d) the Sonics sonotrode at 30% input power.

For both the Branson sonotrode operating at 80% input power and the Sonics sonotrode operating at 30% input power, the emission signal is predominantly dictated by  $4T_0$  shockwaves, with the presence of low amplitude  $T_0$  shockwaves. This again manifests in the spectra of the emissions with broad peaks at  $nf_0/4$  for all  $n$ , with the peaks falling below the spectral floor after around 60 kHz.

Increasing the input power to 100% and 40% on the Branson and Sonics sonotrodes, respectively, results in generation of more uniformly periodic shockwaves at  $5T_0$ , with a small number of  $6T_0$  shockwaves detected. This manifests in the spectra with more clearly defined peaks at  $nf_0/5$  with the subharmonic and corresponding ultraharmonic peaks observed above the spectral floor until around 60 kHz.

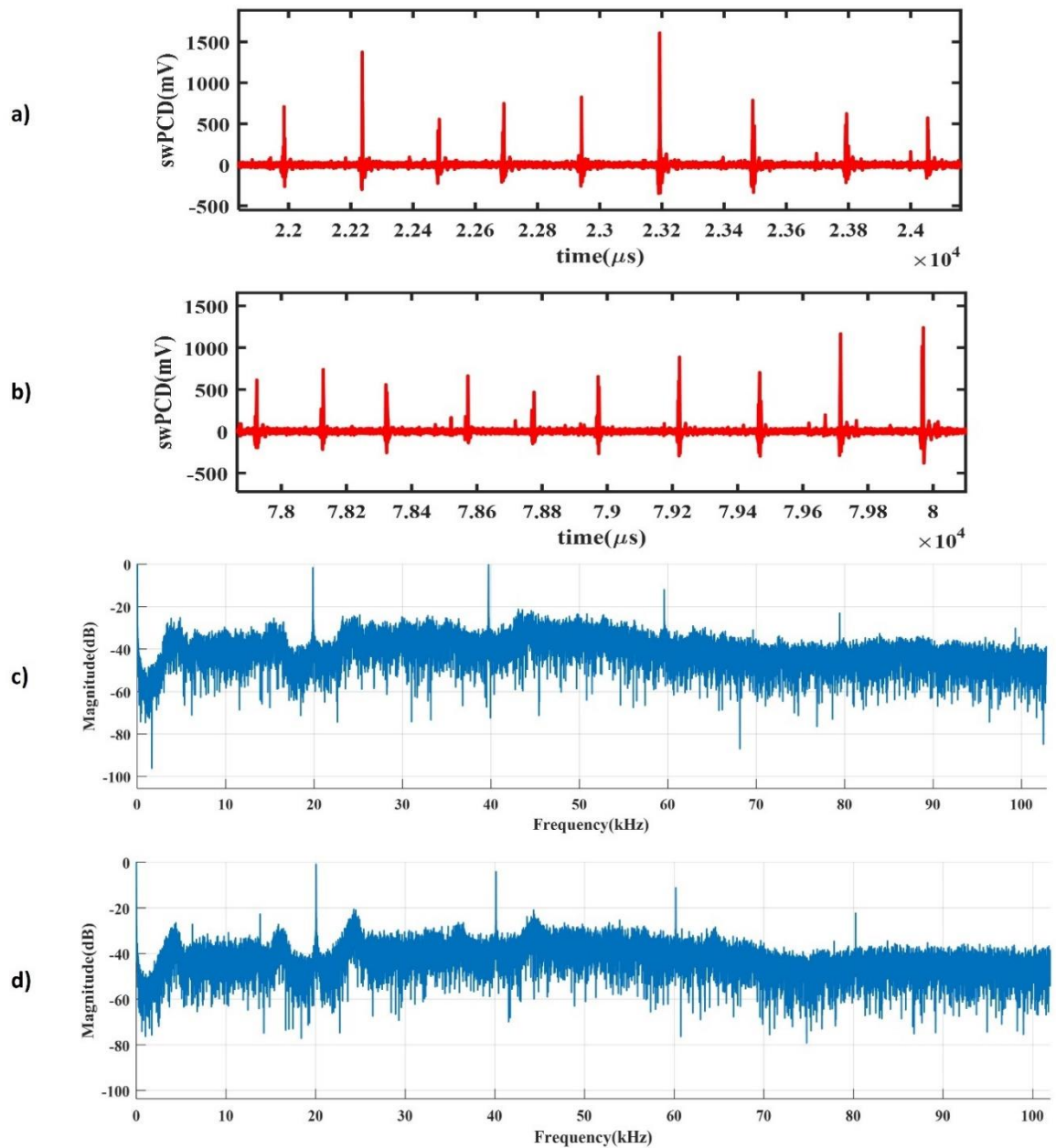


Fig. 5.24: Sampled swPCD data over a 2 ms duration in Ethaline at (a) 100% input power on the Branson sonotrode and (b) 40% input power on the Sonics sonotrode. Cavitation emission noise spectra for the sampled swPCD data is presented for (c) the Branson sonotrode at 100% input power and (d) the Sonics sonotrode at 40% input power.

## 5.4 Discussion

The results presented in this chapter firstly indicate the oscillations of the primary bubble cluster at the tip of a sonotrode advance through orders of subharmonic response, with  $m$  increasing through integer values as the input power (vibrational amplitude) increases. This phenomenon has previously been reported with a 220 kHz focused ultrasound source [24] as well as the same ultrasonic horn used in part of this study, in water [55]. The latter demonstrated the most robust methodology to date in characterising the performance of the sonotrode over a 25-input range of powers, displaying dips in cavitation output as vibrational amplitude (input power) was increased. These dips in power can be related to the transitional amplitudes that are generated as the cavitation switches to higher orders of  $m$  with increased power. At these transitional powers, cavitation is less efficient with an inability to fix to a single order of subharmonic oscillation. This can be observed both in the emission signal and the corresponding spectrum of signal in the subharmonics generated [55, 86]. The combination of HSI and acoustic detection, coupled with the spectral model for periodic shockwaves [26, 73] confirms that the subharmonic emission components are mediated by the shockwaves generated at  $m$ .

Many studies have investigated cavitation under a sonotrode source. Although most studies have only investigated a small number of vibrational amplitudes or power values, there are reports of dips in cavitation performance with an increase in input power. *Žnidarčič et al* reported acoustic emissions, coupled with HSI, at a limited number of input powers of a sonotrode with varied results in output characterised by the oscillatory period of emissions shifting between 3 and 4 cycles and associated ‘irregular cavitation dynamics’ at an intermediate power [81]. This behaviour was linked to transitional amplitudes identified by *Yusuf et al* [55].

Further studies of acoustic emissions against input power have shown similar drops in measured output with an increase in input power. *Tzanakis et al [80]* reported the use of a novel high-temperature ‘cavitometer’ for measuring cavitation in molten metal. Using  $V_{RMS}$  as an indicator of cavitation measurement, emissions generated from a 15 mm-Ø, 20 kHz sonotrode in water showed a range of local minima analogous to the periodic dips presented in this chapter.

*Hodnett et al [68]*, using the CaviSensor described previously in Chapter 4 and the same Branson sonotrode used in this chapter with a 12.7 mm-Ø tip, presented broadband energy from the spectra of sonications in 10% input power increments. Though not sufficiently sampled at fine increments, they did identify dips in output at higher input powers. Both of these studies identified cavitation shielding as a potential source of this reduction in intensity (whereby bubbles situated between the primary cavitation and detector scatter and attenuate the primary cavitation emissions). However, this was refuted by *Yusuf et al [55]* and the results of this chapter did not appear to indicate shielding as an influence.

The comprehensive study by *Yusuf et al*, which was the basis and comparator for this investigation, concluded that for any given ultrasound source, an increase in power to the transducer does not necessarily relate to increased intensity of cavitation. Furthermore, sampling acoustic measurements at sufficiently fine increments could easily identify input powers through which optimisation of the cavitation activity could be performed. The methodology outlined by *Yusuf et al* was adapted and performed in a variety of DESs with differing viscosities, which are of industrial relevance.

Although the majority of investigations involving acoustic measurements with a sonotrode source are performed in water, some studies have investigated lower and (more relevantly to this study) higher viscosity fluids. *Žnidarčič et al [81]* reported cavitation dynamics in ethylene glycol and glycerol which are close in viscosities to Ethaline & CaDES and Reline, respectively. The authors concluded that viscosity did not have a substantial influence on the

‘emergence and dynamics of the cavitation at the horn tip’. This conclusion is somewhat in agreement with some of the results in this study. In particular, for high powers in the Branson sonotrode and the higher power Sonics sonotrode, we observe that the  $V_{RMS}$  plots in each of the four measured fluids observe similar trends in the general increase in cavitation intensity with input power. Furthermore, cavitation activity identified by the HSI is more similar in each solution at these higher powers. However, the study is limited to only one input power and is therefore not representative of the cavitation phenomena across the full utility of the sonotrode. *Khavari et al [95]* presented comparable acoustic emissions in glycerol with a 24 kHz sonotrode. They noted purely fundamental shockwaves at powers where subharmonics were present in water. They attributed frequency peak suppression to larger energy dissipation caused by viscous forces dominating over surface tension and momentum forces. *Tzanakis et al [94]* reported very similar cavitation structures in glycerine to that observed in the DESs (characterised by the bulbous shape) under a 1 kW, 20 kHz sonotrode operating through a 40 mm-Ø tip. The authors also noted an increase in cavitation intensity with power and the characteristic bulbous cavitation structure was maintained for several (over 40) s. Again, these studies are limited to a couple of input powers and do not depict changes in either the cavitation structure or dynamics over the range available with the sonotrodes.

This study presents the most comprehensive work to date characterising the acoustic cavitation generated in 4 different fluids across the range of powers available on 2 sonotrodes, of high industrial relevance for electronic waste recycling. The results presented in this chapter reinforce the rationale for complete characterisation of any ultrasonic source and the utility of shockwave detection as a metric of this. Through detailed characterisation of each fluid, input powers corresponding to reduced cavitation intensity can be avoided and industrial processes optimised. A key output of this chapter is the identification of crossover regions between ultrasound sources. Through monitoring of shockwave activity, the performance of different systems and sources of ultrasound can be compared by  $V_{RMS}$ . This

is of relevance as a drawback of many cavitation related studies is the ability compare outputs. Several metrics for monitoring acoustic emissions exist with no standardisation of reporting. Through monitoring  $V_{RMS}$  generated by shockwave emissions, equivalent cavitation intensity can be identified. This is confirmed by the comparable emission signal and spectra at these crossover regions and would allow comparison of studies using different sources of ultrasound with variable parameters such as frequency, power and tip size.

Studies investigating process optimisation using a sonotrode tip as a function of tip/sample separation distance are limited, with manufacturers recommending a positioning distance ranging between 0.2 and 15 mm [197]. Some studies have investigated the effect of tip/sample distance on streaming velocity under a sonotrode tip [198]. Suggesting that a distance of over 30 mm exhibits the fastest streaming velocities. Further studies of fragmentation in free-floating intermetallics suggested that initial fragmentation occurred after approximately equivalent sonication durations, as long as the material was positioned within the active cavitation zone, which extended 30 mm below the surface of a 500 W, 20 kHz transducer operating through a 22 mm-Ø tip [59]. Whilst acoustic streaming is beneficial for improving mass transport [14, 38], the effect of direct cavitation effects such as BCSWs, jetting and streamers at this distance would be limited due to reduced bubble activity. Hence, the sonotrode/sample positioning was determined by the direct HSI observation of the cavitation activity under the sonotrode. The HSI sequences in §5.3.4 indicate a cavitation zone extending over 6 mm from the sonotrode surface, with maximum bubble density approximately 4 mm from the sonotrode surface, at least in part of the sonication, at all powers measured e.g., Figs. 5.9, 5.11 and 5.13. Hence a distance of 4 mm was selected for all investigations and kept at a constant height. It should be noted, that, full process optimisation by direct observation of cavitation at a range of tip heights would be of research interest and is a recommended future work both for this study and the general sonochemistry research.

## 5.5 Conclusion:

The cavitation generated by a sonotrode is investigated as a function of input power in four different fluids across two sonotrodes. HSI and acoustic emissions indicate main cluster cavitation subharmonically at  $f_0/m$ , with  $m$  increasing through integer values for increasing input power. Transitional input powers where  $m$  is not well-defined manifest as dips in cavitation intensity and are identified in all solutions. The comparison between each of the fluids suggest that each fluid has a unique characteristic  $V_{RMS}$  plot associated with it, for any given ultrasound source. For sonochemical applications generally, the optimal power at which to drive the ultrasonic sources can be identified via hydrophone/cavitation detector sampled at sufficiently small incremental powers. In all DES, the HSI indicates a collapse and recession of the bulbous cavitation cloud identified at low-mid powers which is accompanied by a drop in cavitation intensity. This phenomenon was exploited for experimental metal delamination in chapter 6. Although HSI is useful in terms of monitoring the cavitation structure development, it is not strictly necessary in guiding selection of optimal powers for sonochemical applications.

## **6 A mechanistic study identifying improved technology critical metal delamination from printed circuit boards at lower power sonications in a deep eutectic solvent.**

### **6.1 Introduction**

Ionometallurgy offers distinct advantages over the traditional recycling techniques, including much lower temperature requirements, avoidance of toxic reagents and reduced water consumption [199]. DESs are also cheap, readily available and can be adapted for selectivity of target metals [112]. Despite these advantages, current ionometallurgy approaches using DESs are limited by slow dissolution kinetics, with a recent study reporting that TCM removal from PCBs required immersion in DES for several hours [112]. The addition of redox catalysts can aid in addressing this issue and has shown utility in selectively separating metals from PCB and photovoltaic substrates [112, 200, 201], however this purely chemical-based enhancement is still limited by mass transport. DESs are characterised by high viscosity (ca 40 mPa s) [177] which is detrimental to conductivity and diffusion of metal ions.

One approach to overcoming mass transport limitations which is now demonstrating potential, is via the introduction of power ultrasonics for mechanical and chemical acceleration of ionometallurgical processes. Sonication of DESs is postulated to increase mass transport, remove passivating surface layers and promote radical formation via cavitation-mediated phenomena [14, 202-204]. Previous research has demonstrated ultrasonically-enhanced leaching of metals from ores using strong mineral acids [179] as well as in Ethaline-DES for electrochemical leaching and re-deposition of copper [178, 205]. Despite the clear potential of ultrasonically enhanced ionometallurgy, little is understood of the mechanisms underpinning accelerated TCM delamination, and optimisation in terms of ultrasonic parameters has yet to be explored.

The principal objective for this chapter is the mechanistic investigation of TCM delamination from PCBs submerged in sonicated DES. The delivery of this objective is critical to progress industrially scalable recovery technology. To achieve this, selected results from chapter 6 characterising the cavitation activity in Ethaline-DES at over 20 input powers guided selection of two input powers for use in meeting the objective of observing ultrasonically enhanced TCM delamination from PCBs. For this, a second high-speed camera was introduced to monitor the TCM surface on the PCB, during each sonication. Surface microscopy and profilometry was undertaken at regular intervals within the total sonication, to assess for TCM-layer delamination, as demonstrated in *Results*, §6.3.2. Selected dual-perspective HSI data of significant delamination events at both input powers are presented in *Results*, §6.3.3.

For assessing the degree of ultrasonic enhancement in the current work, the results presented below can be compared to those of Rivera *et al* [112], where passive immersion was used to reclaim TCMs from similar PCB samples. This study investigated the rate of TCM removal for the same DES as is used here, at two different concentrations of anhydrous Iron (III) Chloride oxidising agent, which chemically stimulates removal; specifically, 10 times higher and lower than the concentrations used here. The authors reported passive immersion for 8 hours resulting in ~80% TCM removal, by area, from the PCB structure.

## 6.2 Materials and Methods

### 6.2.1 Deep Eutectic Solvent (DES) preparation

The DES used throughout this chapter was Ethaline – a mixture of Choline Chloride (ChCl) and Ethylene Glycol (EG) in a 1:2 ratio. The DES was prepared by mixing the components at 60°C until a colourless homogenous liquid was formed. To the Ethaline-DES, a redox catalyst of anhydrous iron (III) chloride ( $\text{FeCl}_3$ ) was added at a ratio of 0.1 M/dm<sup>3</sup>. This concentration is 10× lower and higher than those used by Rivera *et al*, for passive immersion [112]. This concentration was selected to maximise chemical stimulation but reduce the opacity of the DES sufficiently, to allow HSI of cavitation development during sonication.

### 6.2.2 Printed Circuit Board (PCB) samples

PCB sections were diced from a larger board, as received from the supplier (Atotech UK Ltd), fig. 6.1, into uniform sections, each containing a single 2 mm Ø TCM disk. Each TCM disk has the same size and metal profile, fig. 6.1. The PCB was then fixed onto a Perspex disk within the centre of tank for repeatable positioning (fig. 6.2 inset top right, and also visible in the Photron field-of-view, bottom right).

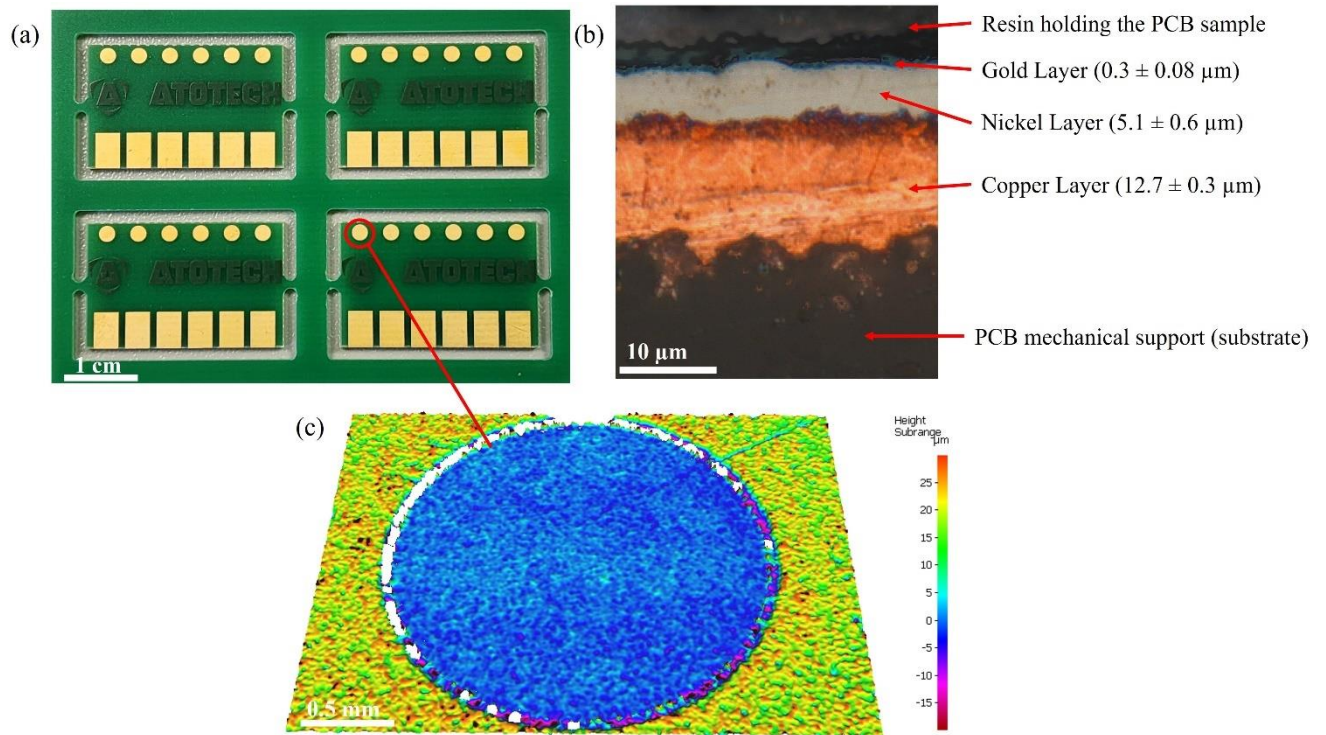


Fig. 6.1: a) Gold-coated printed circuit board as received from supplier. b) Reflected light image of metal layer profile for all printed features c) Profilometry of (untreated) TCM disk feature, used throughout this study.

### 6.2.3 Characterisation of cavitation activity in DES

For the summary of results characterising cavitation in DES as a function of input power, *Results* §6.3.1, shadowgraphic HSI and acoustic emission data was collected from five 400 ms sonications, sampling input power in 5% increments, or less. These methodology and results are presented and discussed in detail in chapter 6 with the relevant data summarised in this chapter.

#### 6.2.3.1 Passive cavitation detection

Acoustic detection of cavitation emissions was again undertaken with the swPCD which was mounted on an x, y, z manipulator for positioning within the tank, fig. 6.2, to detect emissions orthogonally (in the *x-direction*), with respect to the sonotrode probe (*z-direction*). Acoustic emissions were detected in accordance with the methodology outlined in Chapter 5 with the purpose of acoustic detection here being primarily a real-time monitor of cavitation activity with a PCB sample in the tank to ensure consistency with the acoustic emissions presented previously. In this chapter, time-averaged shockwave content is reiterated from chapter 5 in *Results*, §5.3.1 for rationale of the selected sonotrode input powers used in this chapter. Real-time monitoring of the emission spectra during sonication at these selected input powers allowed for collaboration of the shockwave periodicity shown in Chapter 5.

### 6.2.4 The experimental setup

All results presented were obtained with a 450 W sonotrode (Digital Sonifier, Branson 450) operating at 20 kHz through a 230 mm long tapered Ti probe with a 6.4 mm diameter tip (*component 1*, fig 6.2). Input power for the sonotrode is entered as a percentage value on the control console, with a minimum of 10% and programmable in 1% increments. The sonotrode tip was positioned ~4 mm above the PCB, at a consistent immersion depth of ~40 mm.

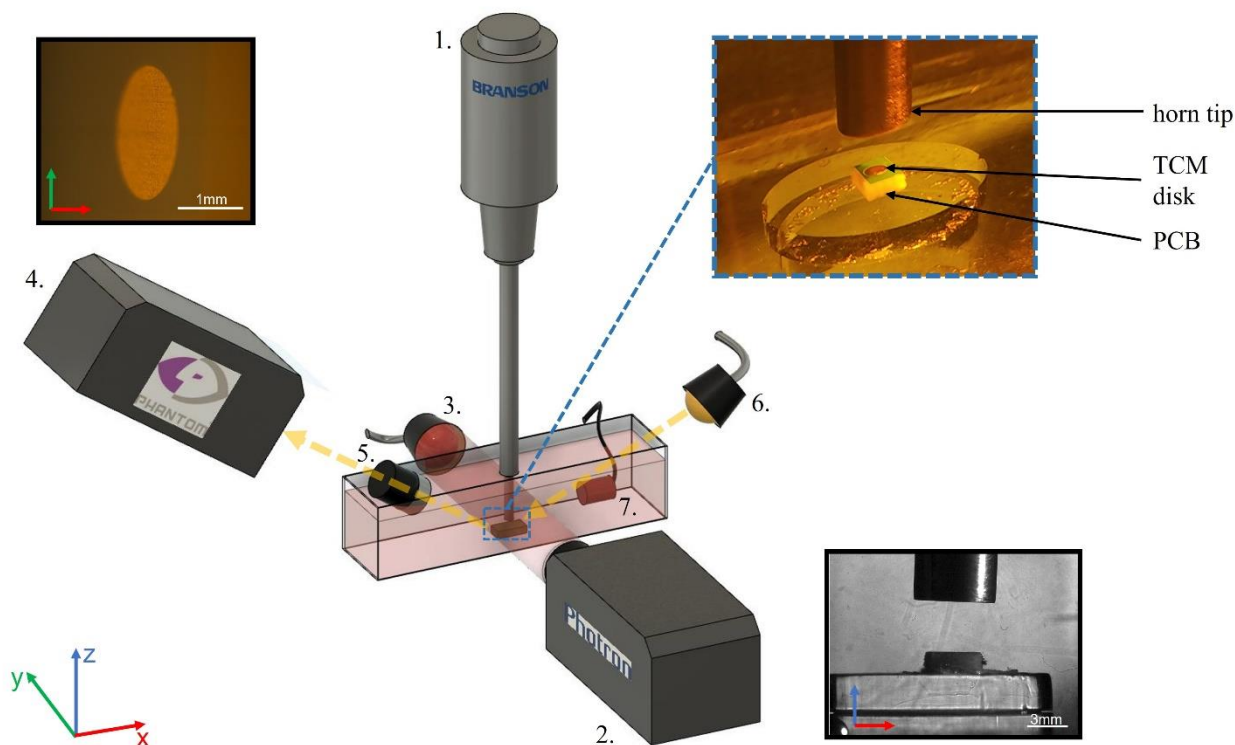


Fig. 6.2: Schematic representation of the experimental setup, featuring the following components: 1. The sonotrode, the tip of which was aligned to a PCB section (inset top-right) within a custom-made tank filled with DES. 2. Photron high-speed camera used to study cavitation development in the vicinity of the tip, with pulsed laser illumination provided via a collimator lens, 3, with FOV depicted (inset bottom-right). 4. Phantom high-speed camera for direct observation of the TCM disk, with objective lens 5, and white light illumination, 6. Typical FOV as depicted (inset top-left). Acoustic detection of cavitation activity was undertaken with a swPCD, denoted by, 7.

### 6.2.5 Shadowgraphic high-speed imaging

HSI of the cavitation activity in the vicinity of the sonotrode tip was undertaken with a Fastcam SA-Z 2100 K (Photron, UK) (*component 2*, fig. 6.2). Illumination was provided via synchronous 10 ns laser pulses at 640 nm (CAVILUX Smart, Cavitar, Finland), coupled to a liquid light guide and a collimating lens (*component 3*, fig. 6.2). In addition to setting the effective temporal resolution (the duration of frame capture), this illumination configuration facilitates shadowgraphic HSI such that bubble-collapse shockwaves may be directly imaged, via refractive index variations imposed by the pressure transient of the propagating shockwave [24-26, 55]. Imaging was undertaken through a macro-lens (Milvus 100 mm f/2M, Zeiss, Oberkochen, Germany), over  $1024 \times 758$  pixels, providing a spatial resolution of  $39 \mu\text{mpixel}^{-1}$ , with the field-of-view (FOV) as shown in fig. 6.2 (inset, bottom-right). Imaging was obtained at 8 kfps over a duration of approximately 11 s.

### 6.2.6 Dual-perspective high-speed imaging

A Phantom V710 (Vision Research, New Jersey USA, *component 4*, fig. 6.2) high-speed camera was used to directly observe the TCM-disk surface during sonication. Imaging from this perspective was undertaken at 1 kfps, through a long working distance  $5\times$  microscope objective lens (0.14 NA Mitutoyo, Japan) (*component 5*, fig. 6.2), dipped into the DES at an angle of  $\sim 40^\circ$  above the horizontal. This was necessary to observe the disk beneath the sonotrode tip. Illumination was provided by a 150 W halogen lamp, coupled to a liquid light guide and a collimating lens (Thorlabs, UK) (*component 6*, fig. 6.2). The FOV from this angled imaging perspective is shown in fig. 6.2 (inset top-left), where the gold layer of the TCM-disk, fig. 6.1 (b) provides the reflective surface, with a line focus across the y-direction such that the proximal and distal edges of the disk are slightly out of focus.

## 6.2.7 Microscopy and profilometry

PCB samples were removed after each minute of accumulated 10 s sonications, washed in deionised water and scanned with an Alicona Infinite Focus G4 3D surface profilometer (Bruker-Alicona, Graz Austria). Surface microscopy and profilometry was obtained through a 5× lens (Bruker-Alicona) for every sample, with additional higher magnification (20×) profilometry obtained for regions of notable delamination. 2D surface microscopy across each sample at 1-minute intervals allowed quantification of delamination evolution over time via a bespoke imaging thresholding macro in ImageJ (National Institute of Health, Wisconsin USA), described below.

### 6.2.7.1 Microscope image processing

The purpose of the image processing of the surface microscopy data was to segment the TCM layer from the backing PCB substrate. Fig. 6.3 highlights the thresholding step of the macro to perform this operation.

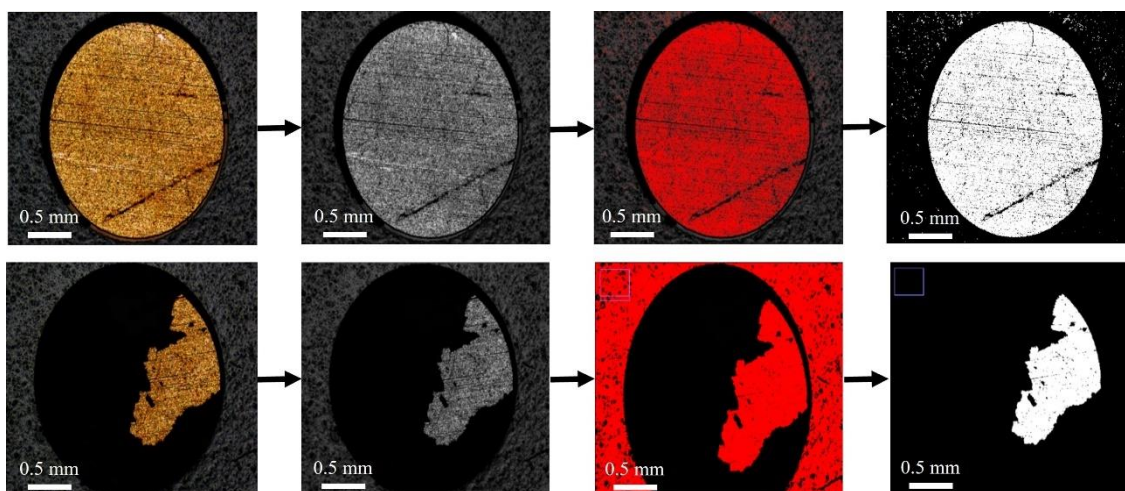


*Fig. 6.3: Image thresholding operation to segment the TCM from the PCB substrate in ImageJ.*

The first operation was to convert the surface microscopy image from its original bitmap colour format to an 8bit greyscale image for subsequent image thresholding. Briefly, image thresholding can be described as the process of converting an image  $I$  into a binary image  $B$  using a threshold grey level  $t$  [206]:

$$B(x, y) = \begin{cases} 1 & \text{if } I(x, y) \geq t, \\ 0 & \text{otherwise.} \end{cases} \quad (6.1)$$

as detailed by fig. 6.3 and equation 6.1, a particular pixel intensity value, or grey level ( $t$ ), is given as the threshold value. All pixels greater than or less than this value are given either a maximum (255) or minimum (0) value, which are presented as white and black in the final image of fig. 6.3, respectively [207]. Thus, the image is converted to binary containing only two pixel values. As the TCM has a different pixel intensity to the PCB substrate, it can be easily segmented.

Following the initial thresholding, a series of morphological operations were performed to refine the image and remove small regions of noise and improve the image segmentation. Firstly, a despeckle was applied to remove small regions of noise in the image, presented as minute white regions sporadically spread across the image. Finally, a closing operation was performed. The purpose of the closing operation is to dilate and then erode the image. In real terms, this has the effect of merging almost connected objects and eroding them slightly to give a more detailed contour of the image. This gives the best representation of the original surface microscopy with the TCM fully separated.

This process was applied to all surface microscope images, allowing for a quantitative analysis of the rate of TCM delamination to be performed in §6.3.2.

### **6.2.8 Data collection**

Sonications were initiated manually from the control console of the sonotrode, at defined input powers. The remaining instrumentation was synchronised via electronic triggering controlled from a signal generator (DG4102, Rigol Technologies, Beijing China). For TCM-delamination, Photron and Phantom HSI were synchronised to record the entire 10 s sonications with both cameras triggered immediately before the initiation of sonication. A total of five PCB samples were analysed at each input power, for a total, accumulated sonication time of 5 minutes.

### 6.3 Results

The results below are organised as follows: §6.3.1 presents the characterisation of the cavitation behaviour in DES, with  $V_{RMS}$  of the swPCD detections plotted as a function of input power plot across the range available with the sonotrode. The data underpinning this plot are described and represented in chapter 5. Fig. 6.4 guided selection of two input powers for taking forward to the overview of TCM-delamination performance, §6.3.2, and HSI of delamination events, §6.3.3.

§6.3.2 presents the 2D microscopy and 3D profilometry observations of the delamination of five PCB samples, at 1-minute interval throughout the 5-minute total sonication time, as an overview of the delamination performance at each of the selected input powers.

In §6.3.3, dual-perspective HSI of several key TCM-delamination events at each selected input power is presented. Comparison between the cavitation observed at two input powers is made, facilitating mechanistic interpretation of the delamination performance.

#### 6.3.1 Characterisation of cavitation activity in DES

Fig. 6.4 is a plot of  $V_{RMS}$  versus input power for cavitation generated in Ethaline-DES, with each data point representing an average of five sonications, at each input power sampled. Representative data and a full explanation of the plot is previously reported in chapter 5. Briefly, however,  $V_{RMS}$  of the filtered cavitation emission signal is taken as representative of the average shockwave content within the signal generated during a sonication. It has previously been published that, for sonications in water,  $V_{RMS}$  has a non-linear dependence on input power. Moreover, it was suggested that the structure of a  $V_{RMS}$  versus input power plot can therefore be used as a simple guide to selecting the optimal input power, for any sonochemical application mediated by cavitation bubble collapses [55].

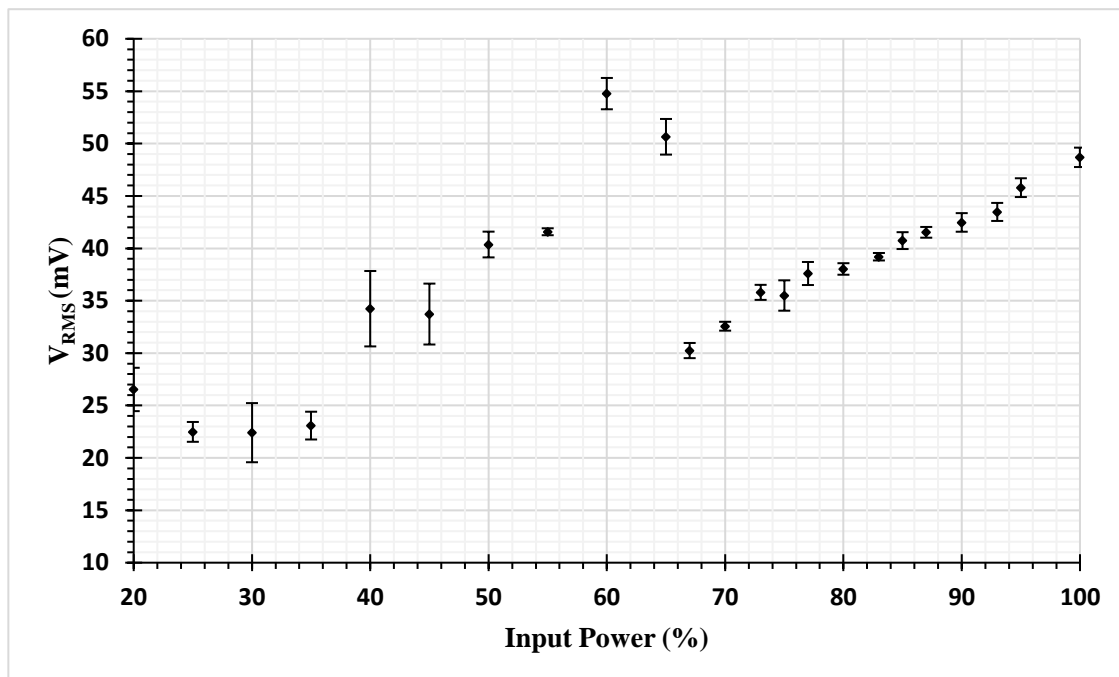


Fig. 6.4: Mean  $V_{RMS}$  from five 400 ms sonications at each input power, of the signal detected by the swPCD during sonications in DES.

The results shown in fig. 6.4 indicates that a sonication in DES at 60% input power generates almost double the shockwave content that is generated during a sonication at 70% input power. As described in chapter 5, this is because a 70% input power sonication generates cavitation that is transitioning between orders of subharmonic response (specifically,  $f_0/m$ , where  $m$  increases through positive integer values, with increasing power). The cavitation at such a transitioning power (or tip-vibration amplitude), does not oscillate and collapse as smoothly as that at the lower power, generating irregular and intermittent shockwave emissions, which is reflected in the lower  $V_{RMS}$  at the higher power.

The results described in chapter 5 also suggest that distinctive cavitation structures develop at different powers. Notably, at 60% input power, a bulbous bubble structure extends though the DES, as has been previously reported for sonotrode sonications in high viscosity liquids [195] and is sustained for most of a 10 s sonication. In contrast, at the higher powers of 70% and 90%, although a bulbous structure develops earlier in the sonication, it also recedes back

into a conical structure in contact with the tip (reminiscent of sonotrode cavitation in lower viscosity liquids, such as water), more rapidly at the higher powers.

In the TCM delamination results below, we demonstrate, for the first time, the effectiveness of using this characterisation approach to selecting optimal input powers. Specifically, observations were conducted at 60% and 90% input powers, such that the difference between the input powers may be taken as significant, and the delamination performance at each power is assessed.

### **6.3.2 Overview of TCM- delamination performance at 60% and 90% input powers**

In this section, surface microscopy and profilometry of the TCM-disk, taken at 1-minute intervals throughout the total accumulated sonication time of 5 minutes, at each of the input powers identified in the previous section, are reported. Specifically, each PCB sample was exposed to six 10 s sonications (to facilitate dual-perspective HSI of the cavitation activity during the entire sonication and any delamination events that occurred, observations from which are reported in Results §6.3.3, below), removed for microscopical and profilometry examination, then returned to the DES tank for a further six 10 s sonications. The dataset consists of five PCB samples each at 60% and 90% input power, with a further five samples sonicated continuously for 5 minutes in DES, as a baseline delamination assessment for the effective 10 s pulsing required to capture the HSI at each power. In addition to the dual-perspective HSI of delamination mechanisms (*Results* section 6.3.3), we seek to assess the utility of characterising the cavitation in DES for identifying effective powers at which to administer sonications.

Figs. 6.5 and 6.6 are Alicona surface microscopy images of the TCM-disk at 60% and 90% input powers, respectively. The metal layer profile of fig. 1 (b) indicates it is the gold layer that is visible, as the top reflective surface.

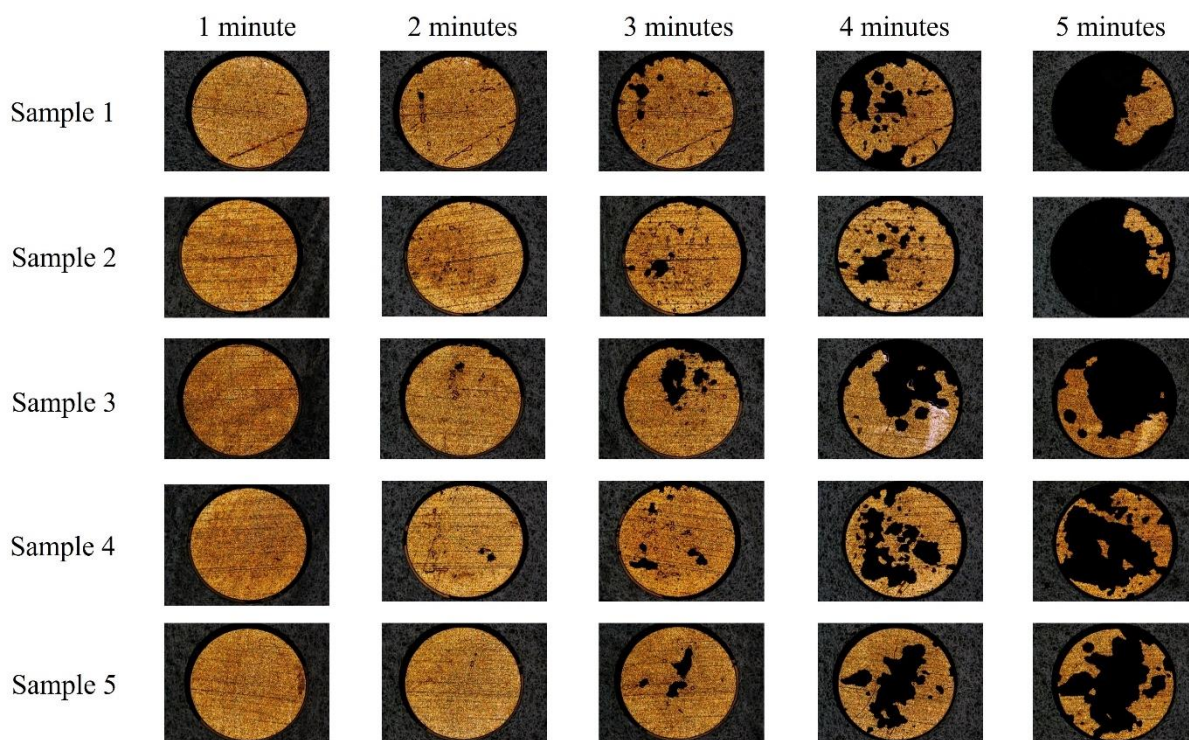


*Fig. 6.5: Surface microscopy of TCM-disks from five PCB samples, taken at one-minute intervals (after  $6 \times 10$  s sonications), over a total sonication of five minutes ( $30 \times 10$  s sonications) at 60% input power, demonstrating the accumulated delamination. Scale is provided by the 2mm  $\varnothing$  disk.*

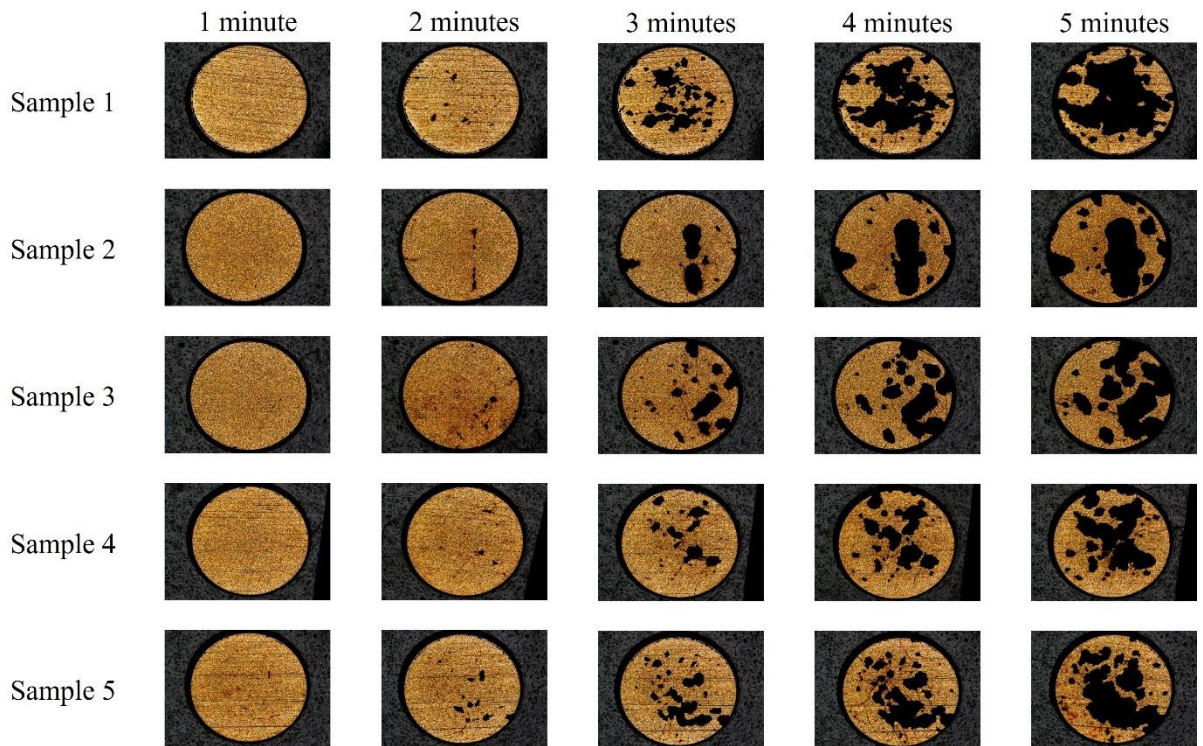


*Fig. 6.6: Surface microscopy of TCM-disks from five PCB samples, taken at one-minute intervals (after  $6 \times 10$  s sonications), over a total sonication of five minutes ( $30 \times 10$  s sonications) at 90% input power, demonstrating the accumulated delamination. Scale is provided by the 2mm  $\varnothing$  disk.*

Both figs. 6.5 and 6.6 indicate negligible (observable) delamination over the first minute of sonication. Even sample 1, which features a pre-existing score feature, which may be expected to provide a discontinuity on the surface and act to nucleate and promote cavitation activity, does not show any sign of early delamination during the first minute of sonications. We note low levels of apparent TCM delamination after the first minute of sonication in fig. 6.7, which quantifies the average percentage of TCM removal for all samples at each power, at each 1-minute sonication intervals. The  $\sim 2\%$  TCM removal is at least in part attributable to thresholding applied during implementation of the ImageJ macro. By the end of the second minute of 10 s sonications, however, most samples at both input powers exhibit some form of initial delamination feature, typically an almost circular hole or pit, approximately 40-50  $\mu\text{m}$  in diameter. Fig. 6.7 confirms that there are a few more of these features at the higher input power of 90%. After the third minute of sonication, samples are

either exhibiting many more of these features, or the features formed during previous sonications have been significantly widened. During the last two minutes of sonication, individual holes continue to widen and merge. The main finding, however, is that after the fifth minute, the percentage of TCM removal is  $68 \pm 13$  at 60% input power, comparing to  $40 \pm 10$  at 90% power. Fig 6.7 presents TCM removal as a function of time, during each minute of sonication acoustic emissions were monitored and consistent shockwave periodicity was observed during sonications at each given power, shown previously in Chapter 5.

Fig. 6.7 also includes percentage TCM removal for a continuous 5-minute sonication at the two input powers (without accompanying HSI or, evidently, minute-by-minute surface microscopy). TCM delamination is reduced for continuous sonication at both powers, notably so for 90% input power, with only  $10 \pm 3\%$  removal.

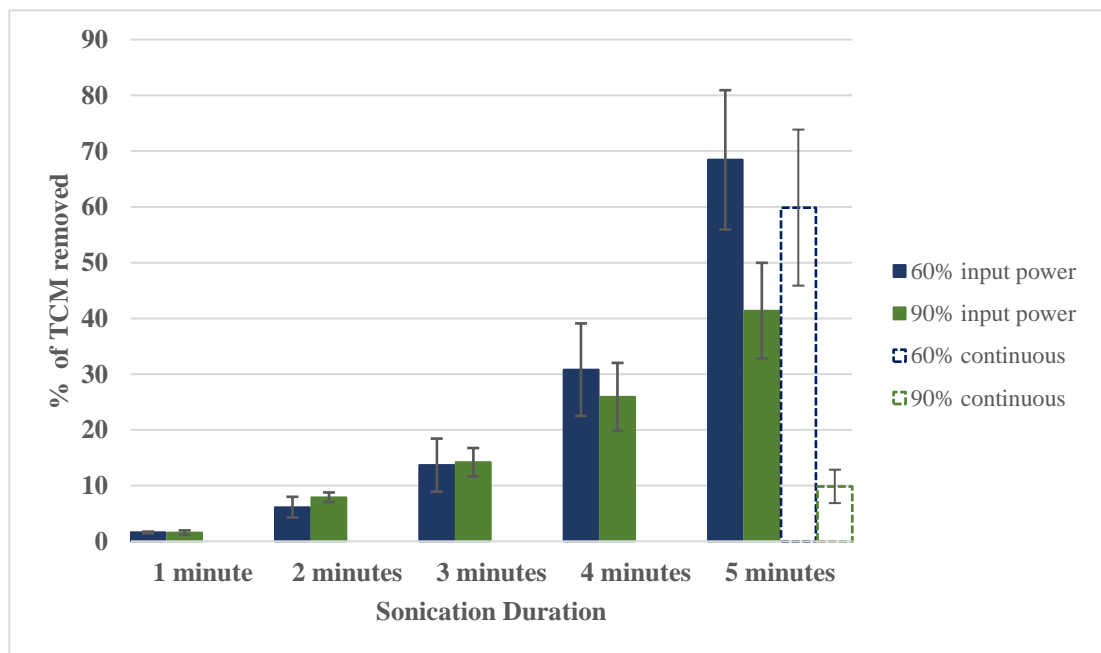


Fig. 6.7: histogram of percentage TCM removal vs sonication time presented as an average of the 5 samples ( $\pm$  standard deviation) at 60% input power (blue) and 90% input power (orange). Average delamination for samples continuously sonicated for 5 minutes are also presented (dashed).

To further investigate and characterise the removal features, profilometry was conducted on every sample while it was mounted on the microscope, between 1-minute sonications. Fig. 6.8 displays profilometry data at various sonication intervals, and at both input powers.

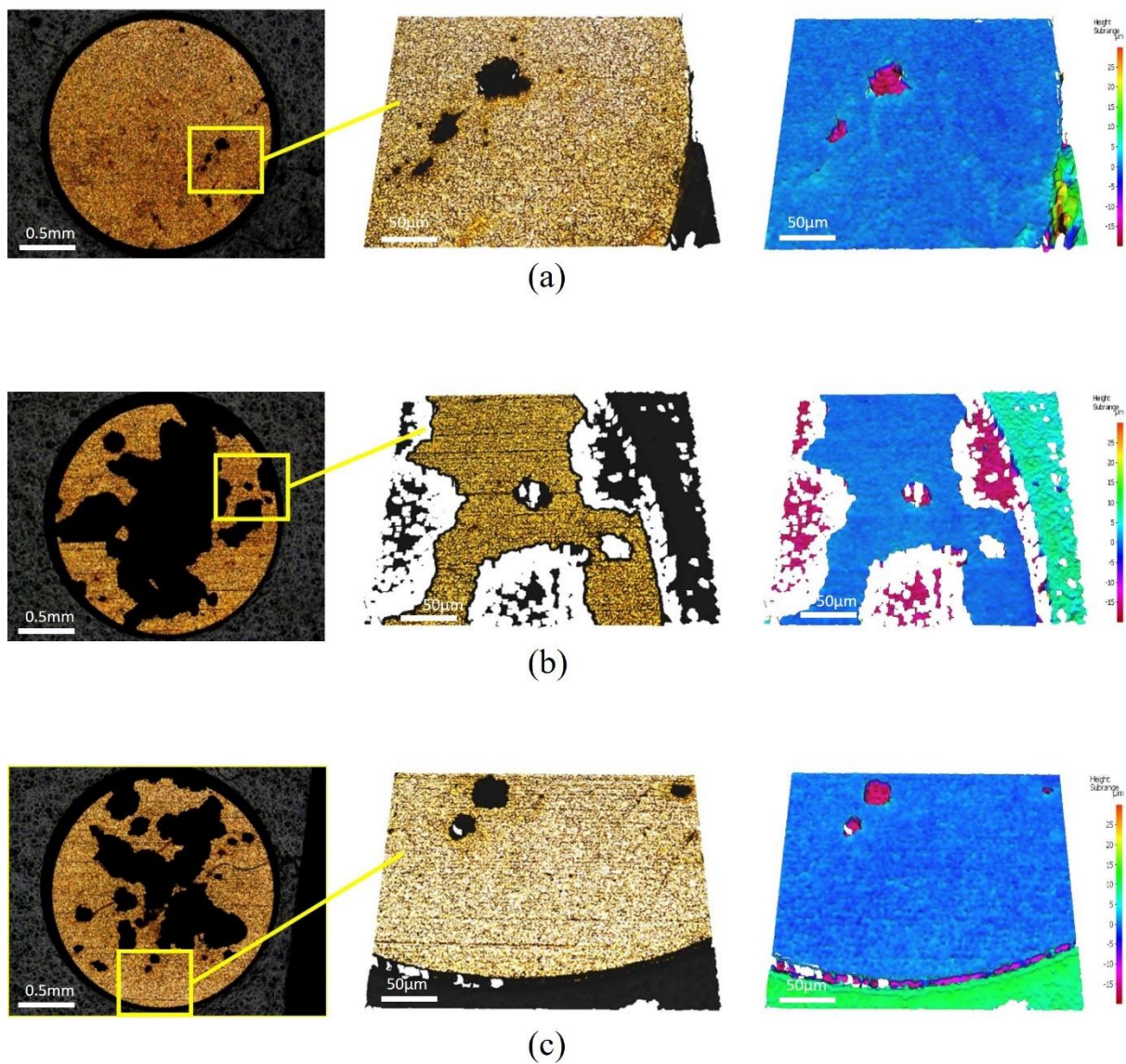


Fig. 6.8: Profilometry of removal features on the TCM-disk at 20 $\times$  magnification for (a) sample 3, after the 2<sup>nd</sup> minute of sonication at 90% power, (b) sample 5 after the 5<sup>th</sup> minute of sonication at 60% power and (c) sample 4 after the 5<sup>th</sup> minute of sonication at 90% power.

All removal features investigated during this study had a depth of  $\sim 18 \mu\text{m}$ , indicating complete removal of the TCM layers. We did not observe any evidence of layer-by-layer removal, including around the edges of the features.

### 6.3.3 Dual-perspective HSI of TCM-delamination

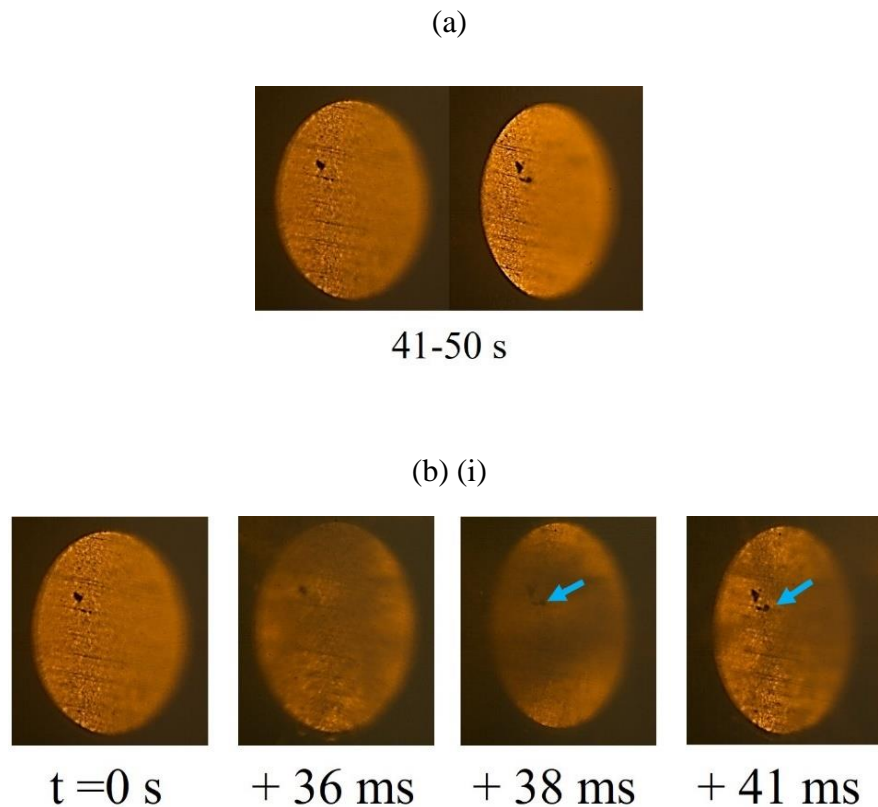
This *Results* section presents combination Phantom and Photron imaging of specific delamination events on single samples, captured by both cameras, at 60 and 90% input power. It should be noted that these observations have been selected from an extensive HSI dataset of many delamination events, recorded throughout the course of this study. The observations presented were chosen as being representative of delamination events for each power, and stage, of the sonication, as stated – and with TCM removal observable from both HSI perspectives. Moreover, the evolution of cavitation structures, observed from the Photron HSI perspective, are typical of that which occurred at each power, and stage, of the sonications.

HSI results figures are presented as follows, taking Fig. 6.9 as an example: (a) presents single frame captures of the TCM-disk taken with the Phantom camera *before* and *after* a 10 s sonication, in this case the 41-50 s sonication of sample 4, during the 2<sup>nd</sup> minute, at 60% input power. The overall delamination morphology from the surface microscopy data of figs 6.6 and 6.6 can be cross-referenced to the Phantom *before* and *after* captures, for any given sample at each stage of sonication at either power, throughout the HSI figures presented below.

Fig. 6.9 (b) (i) are frames extracted from the Phantom high-speed sequence captured during the sonication, here showing the appearance of the hole features typical of the earliest observed delamination events, for all PCB samples. For all frames extracted from a HSI sequence (both Phantom and Photron),  $t = 0 \text{ s}$  refers to the start of that specific 10 s

sonication, with all other timings given relative to that. The cavitation activity between the sonotrode tip and PCB surface can somewhat obscure the disk imaging from this perspective (at 36 and 38 ms of fig. 6.9 (b) (i)), although the development of delamination is often still apparent.

Fig 6.9. (b) (ii) are frames extracted from the Photron imaging sequence, corresponding to the sampled Phantom imaging of fig. 6.9 (b) (i), showing the specific cavitation activity around key moments of delamination. The right-hand side of many objects in the Photron imaging, including bubbles and the sonotrode tip, are brighter due to the continuous white light illumination for the Phantom imaging perspective, fig. 6.2, which is reflected into the Photron imaging perspective.



(b) (ii)

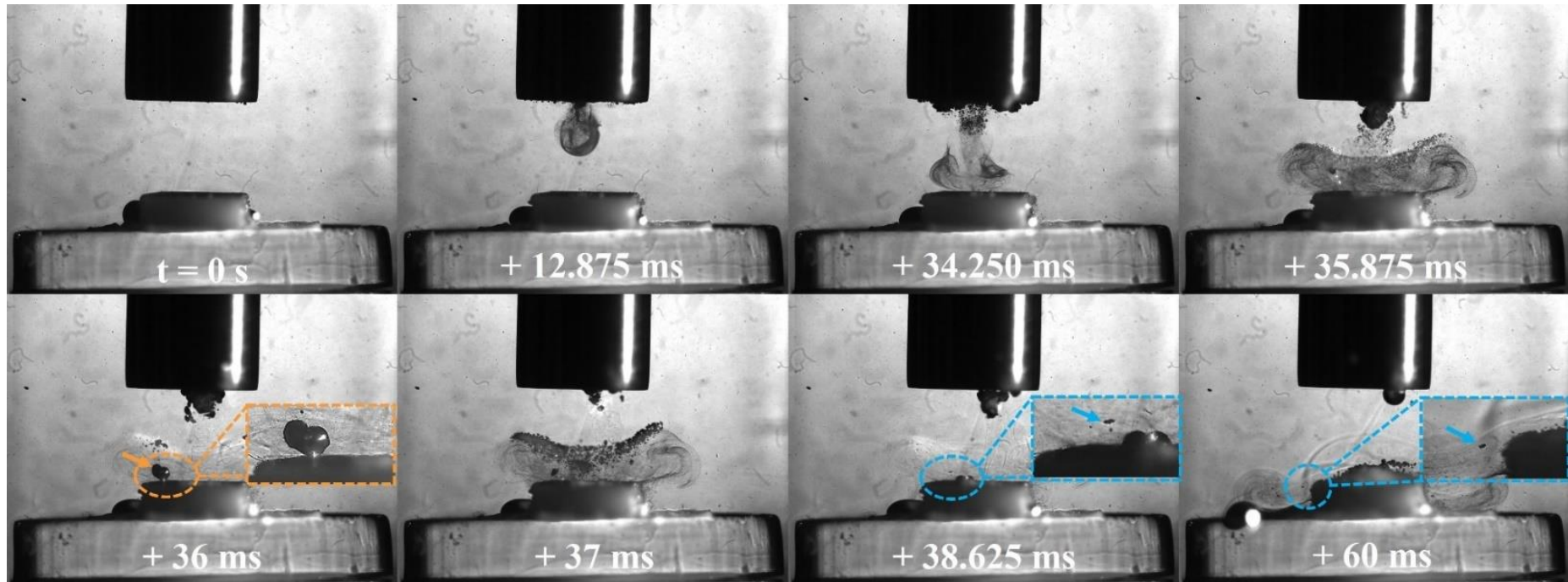


Fig. 6.9: (a) Single before and after images of an early stage TCM delamination event from the Phantom camera perspective, occurring during the 41-50 s sonication of the 2<sup>nd</sup> minute at 60% input power, for sample 4. (b) Combination (i) Phantom and (ii) Photron frames from an HSI sequence of specific delamination events during the 41-50 s sonication. A jetting bubble at 36 ms (arrowed orange and zoomed inset) dislodges a TCM fragment (arrowed blue within the zoomed insets at 38.625 and 60 ms). Scale provided by (i) the 2 mm  $\varnothing$  TCM disk, (ii) the 6.4 mm  $\varnothing$  tip.

Chapter 6: A mechanistic study identifying improved technology critical metal delamination from printed circuit boards at lower power sonications in a deep eutectic solvent.

Fig. 6.9 (a) demonstrates that a small individual hole was inflicted onto the TCM-disk, during the 41-50 s sonication,  $\sim 100 \mu\text{m}$  from a similar looking feature from a previous sonication. This HSI sequence indicates this second hole occurs  $\sim 36$  ms into this 10 s sonication and is observable at 41 ms, through the cavitation activity. The Photron imaging of fig. 6.9 (b) (ii) captures a bubble exhibiting an involution (arrowed orange at 36 ms), indicative of jet-formation which would be expected in such close vicinity to a rigid surface, under acoustic driving [14, 32]. Subsequent images from the sequence capture a small fragment of material (which can be distinguished from the bubbles because it does not oscillate under the ultrasonic driving, arrowed blue within the zoomed insets, throughout) originating from the region of the TCM-disk that was impacted by the bubble-jet, around 36 ms. Acoustic streaming under the tip of the sonotrode, which is often revealed by vortex-like structures in the bubble mist acts to propel the TCM fragment away from the centre of the disk and over the edge of the PCB section, at 60 ms.

Fig. 6.10 is representative dual perspective HSI taken during the 5<sup>th</sup> minute of sonication of sample 2, at 60% input power. It contains a significant amount of data – and is representative of much more – necessary to adequately represent the main events occurring within the complex cavitating environment, over an extended time. In the following text, only the salient features are highlighted.

As is clear from fig. 6.5, the fifth minute of sonications at 60 % input power caused widespread delamination for all samples. Fig. 6.10 (a) demonstrates TCM delamination from sample 2 totalling an area  $\approx 0.79 \text{ mm}^2$  ( $\sim 25\%$  of the total TCM disk area) occurred during the 11-20 s sonication, of the fifth minute, with less than 20% of the TCM disk remaining after the 31-40 s sonication.

Fig. 6.10 (b) (i), (c) (i) and (d) (i) are frames extracted from the Phantom high-speed sequence capturing three distinct delamination events that occurred during this minute of

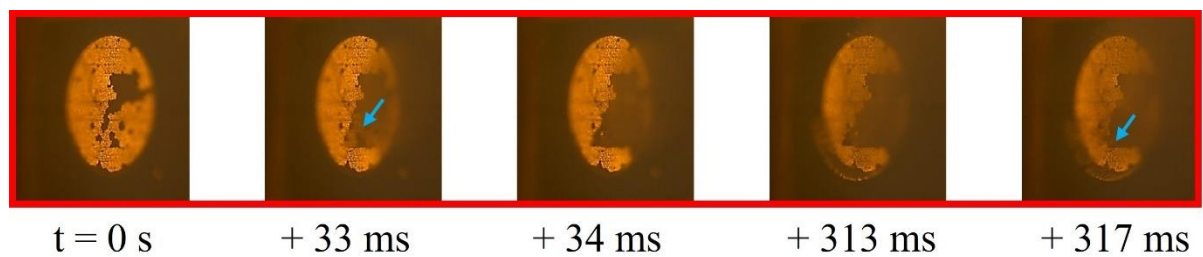
Chapter 6: A mechanistic study identifying improved technology critical metal delamination from printed circuit boards at lower power sonications in a deep eutectic solvent.

accumulated sonications. It is the corresponding Photron imaging of figs 6.10 (b) (ii), (c) (ii) and (d) (ii), however, that capture the key features for the cavitation at 60% input powers, distinguishing it from that at 90% (presented below, fig. 6.11). Specifically, a sustained, tightly packed and vigorously cavitating cluster of cavitation bubbles, is shown to remain in contact with the PCB surface throughout all 10 s sonications at 60% (this also occurred later in the sonication represented by fig. 6.9). Another interesting feature is the bubble filaments of the bulbous structure, that curve downwards from the edges and sides of the sonotrode tip, toward the PCB sample. This bulbous structure has been reported previously for sonications in highly viscous fluids [94, 195, 196] and also features in the cavitation characterisation in DES results, of chapter 5. For the TCM delamination observations of fig. 6.9, the curving bubble filaments appear to feed the cavitation cluster that persists on the PCB surface, throughout sonications at 60% input power.

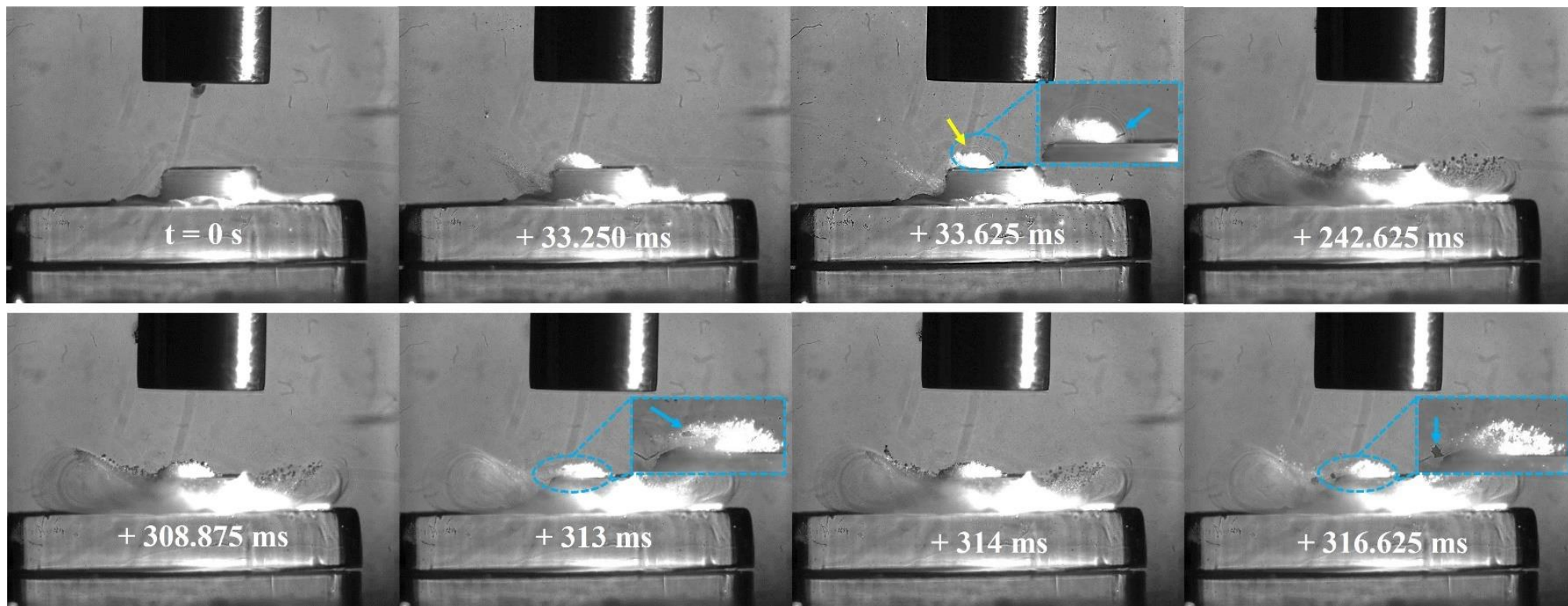
(a)



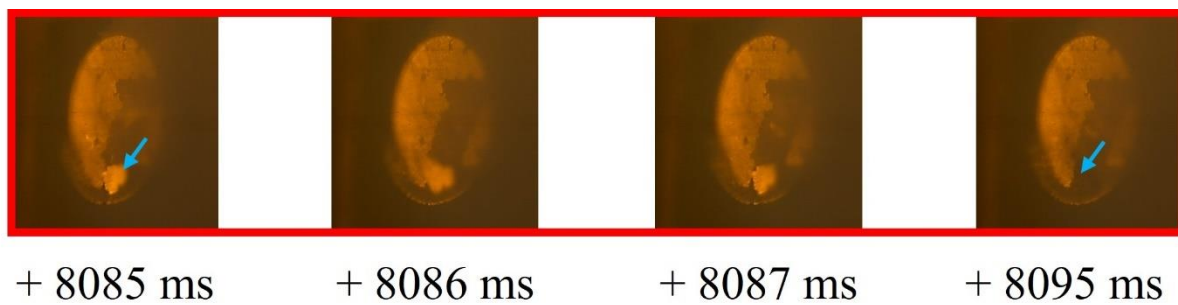
(b) (i) 11-20s



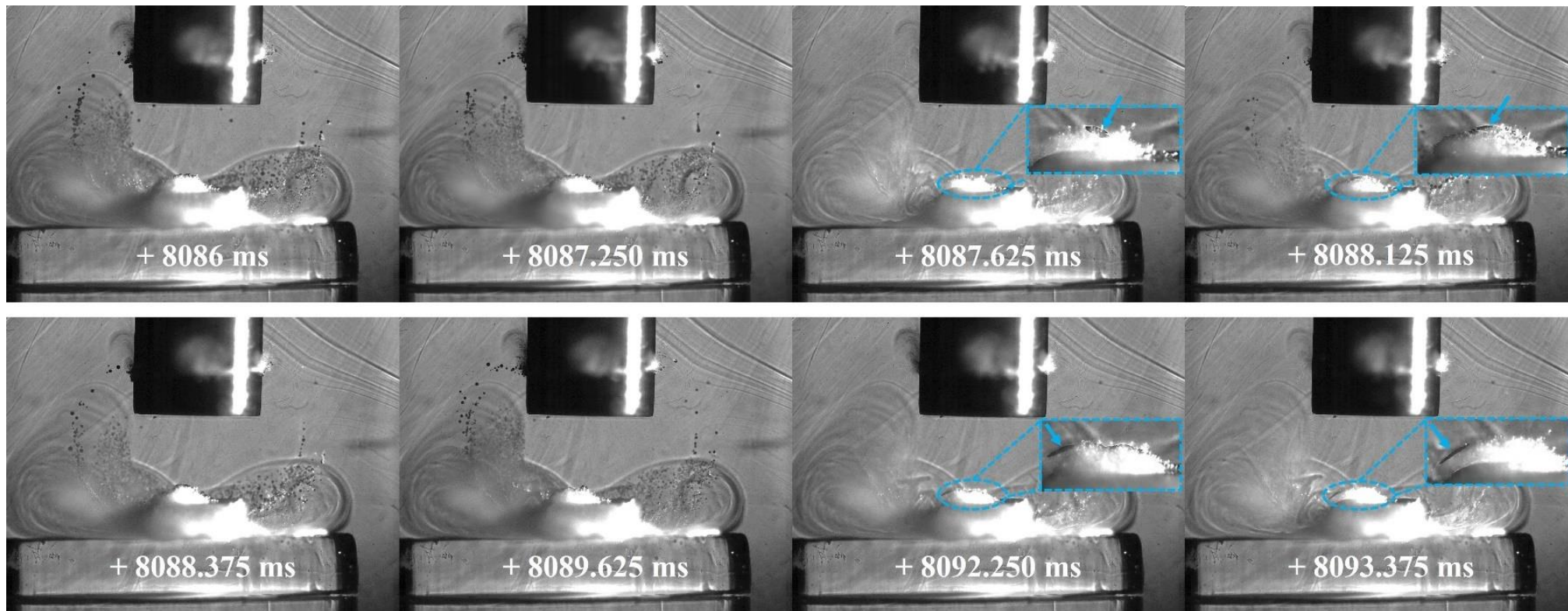
(b) (ii)



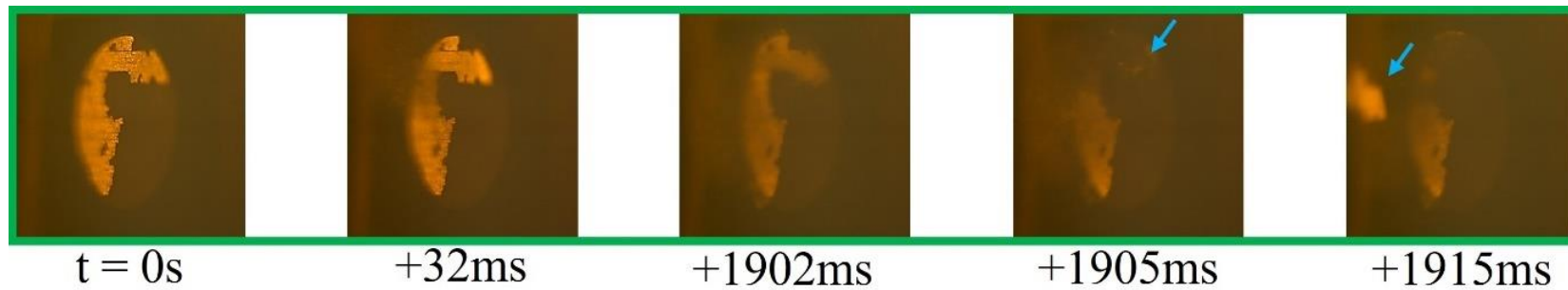
(c) (i) 11-20 s



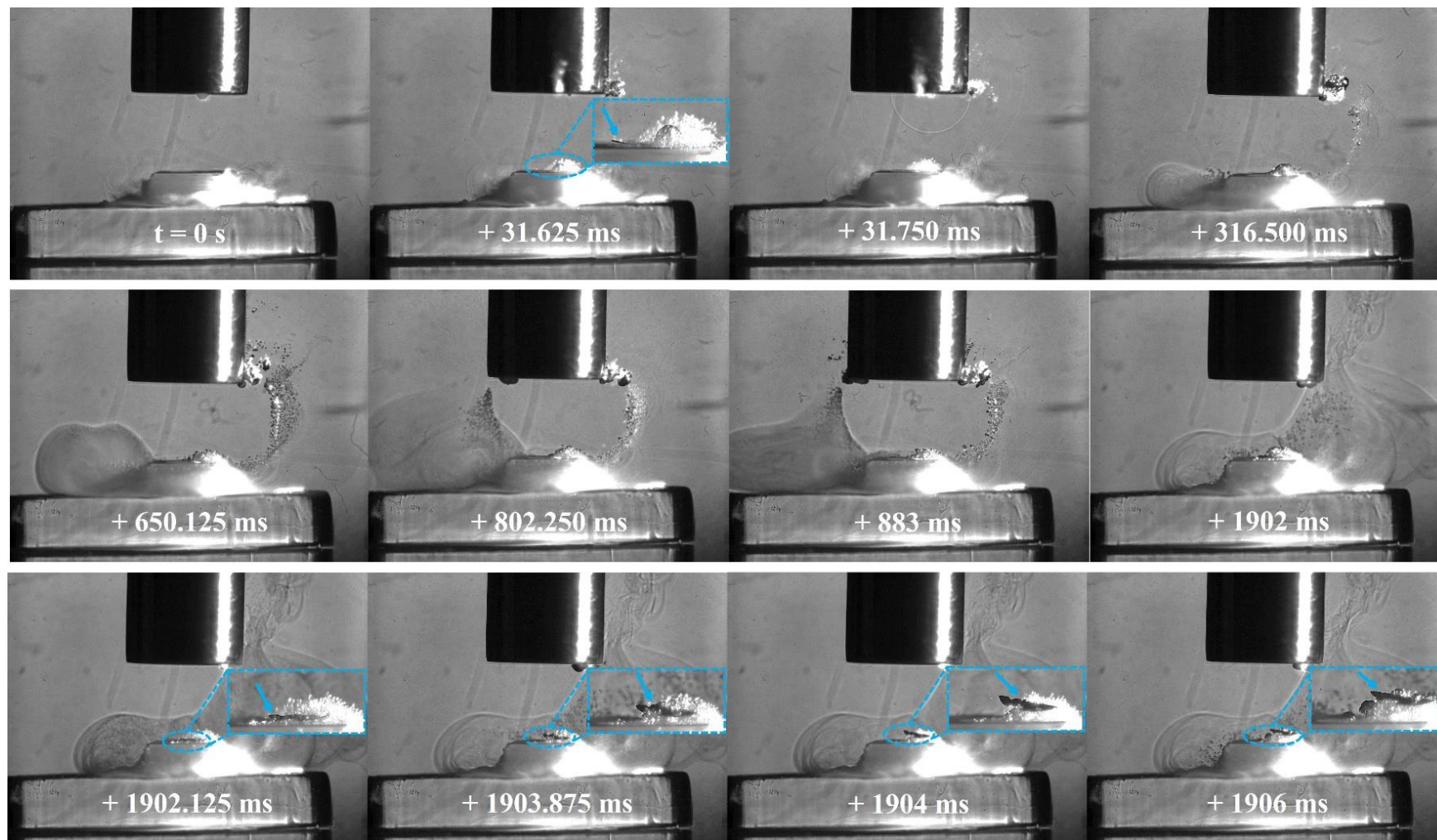
(c) (ii)



(d) (i) 31-40 s



(d) (ii)



Chapter 6: A mechanistic study identifying improved technology critical metal delamination from printed circuit boards at lower power sonications in a deep eutectic solvent.

*Fig. 6.10: (a) Single images of the TCM disk from the Phantom camera perspective, before and after each of the 10 s sonications, from the fifth minute at 60% input power for sample 2. (b)-(d) Combination (i) Phantom and (ii) Photron frames from HSI sequences, of specific delamination events at different points during the sonication. Bubble collapse shockwaves are arrowed yellow, TCM fragments within zoomed insets arrowed blue, throughout the Photron imaging. Scale provided by (i) the 2 mm  $\varnothing$  TCM disk, (ii) the 6.4 mm  $\varnothing$  tip.*

Fig. 6.10 (b) (i) demonstrates delamination of a small single TCM fragment, occurring during the initial 317 ms of the 11-20 s sonication (red box, Fig. 6.10 (a)). At 33 ms, a fragment of TCM is prised upwards from the PCB, although not fully delaminated. Fig. 6.10 (b) (ii) of the corresponding Photron HSI sequence show the TCM fragment emerging from the persistent cavitation cluster at the PCB surface at 313 ms. Bubble collapse shockwaves (arrowed yellow throughout), such as at 33.625 ms, indicate that the surface cluster is cavitating vigorously.

Fig 6.10. (c) are dual perspective HSI from later in the same 10 s sonication, with a further TCM delamination event occurring shortly after 8 s into the sonication (i). Fig. 6.10 (c) (ii) demonstrates that the cluster at the PCB surface has been sustained throughout the sonication. The imaging from both perspectives again strongly suggest a gradual prising of a much larger TCM fragment than that in fig. 6.10 (b) earlier in the sonication, from the surface of the PCB over several ms, before full delamination to removal is apparent, in the Phantom imaging between 8087 and 8089 ms, and in the Photron imaging at 8092.250 ms.

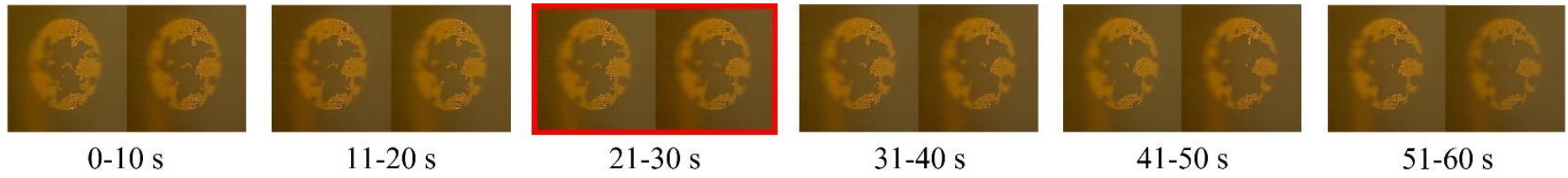
Fig. 6.10 (d) highlights another significant TCM removal event from sample 2 at 60% input power during the 31-40 s sonication of the fifth minute. Additional Photron imaging is included in Fig 6.10 (d) (ii) to demonstrate that the prising and delamination of a large TCM fragment can take some time to fully separate from the PCB substrate. The Phantom imaging of fig. 6.10 (d) (i) suggests the prising of this fragment (approximately 20% the total TCM-

Chapter 6: A mechanistic study identifying improved technology critical metal delamination from printed circuit boards at lower power sonications in a deep eutectic solvent.

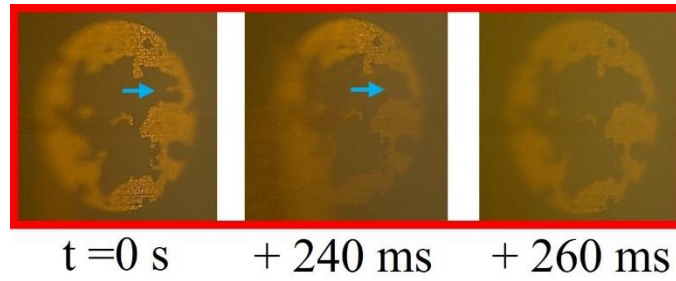
disk area) starts at 32 ms, with the Photron imaging of fig. 6.10 (d) (ii) confirming the surface cluster formed on the PCB around this time. For almost 2 s, the fragment (still attached to the substrate) is ‘jostled’ by the cavitation. The fragment is finally liberated at ~1902 ms, with the removal process well captured by the Photron imaging of fig. 6.10 (d) (ii), from 1902-1906 ms.

Fig. 6.11 (a) presents single frame captures from the Phantom camera of delamination of the TCM-disk at 90% input power over the fifth minute of sonication, on sample 1. Fig. 6.11 (b) presents early (i) Phantom and (ii) Photron image sequences extracted from the 21-30 s sonication, corresponding to TCM delamination. Fig. 6.11 (c) and (d) present frames extracted from the Photron HSI sequence depicting the evolution of the cavitation development beyond the first second of sonication and, in particular, highlight the differences for the cavitation that develops during sonications at 60% input power, Fig. 6.10.

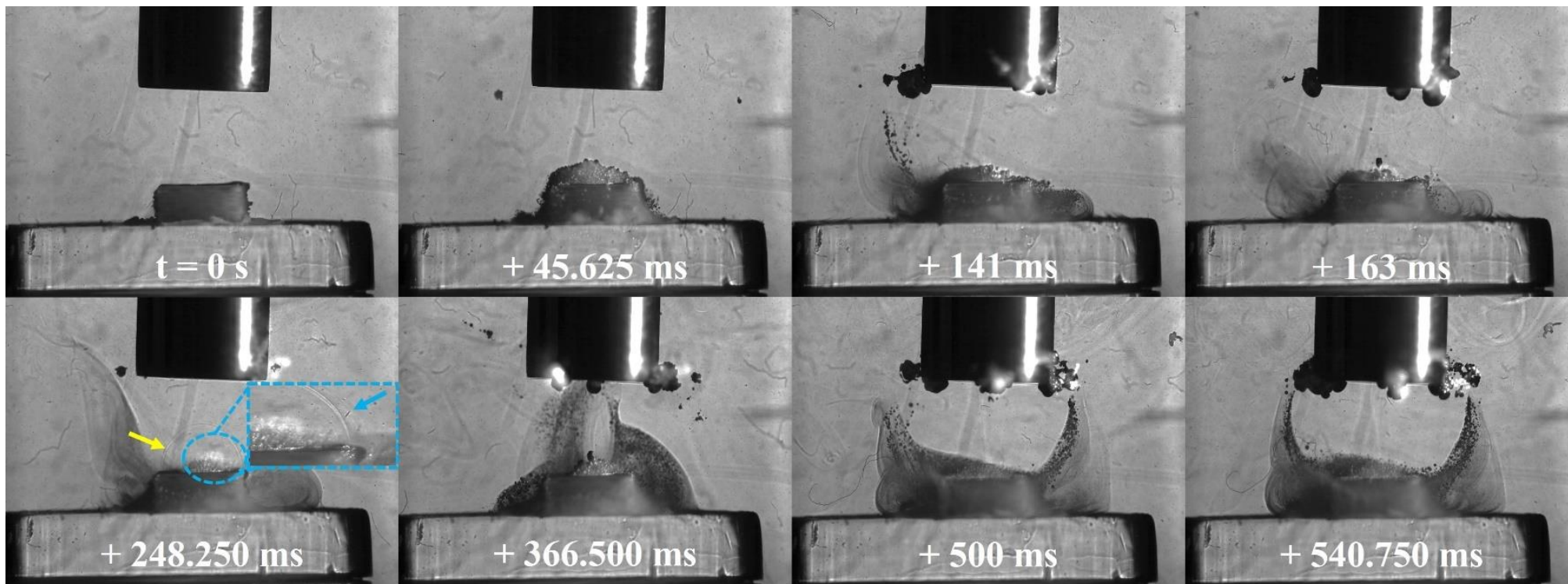
(a)



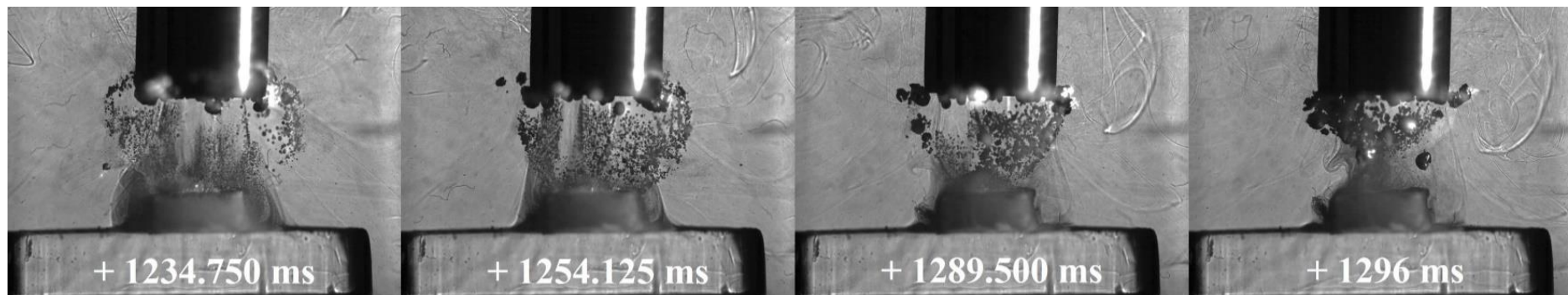
(b) (i)



(b) (ii)



(c)



(d)

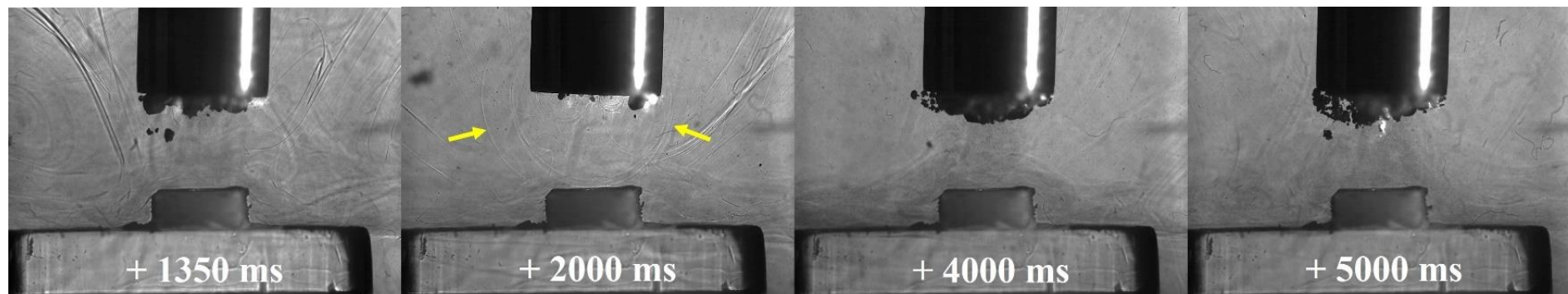


*Fig. 6.11: (a) Single frame captures of the TCM disk from the Phantom camera perspective, before and after each of the 10 s sonications, from the fifth minute at 90% input power, for sample 1. (b) (i) Phantom frames from a HSI sequence, of specific delamination events during the 21-30 s sonication. (b) (ii) corresponding Photron frames for the HSI sequence of specific delamination event detected by the Phantom. (c) Change in the cavitation structure after ~ 1.2 s, with the bubble activity receding from the PCB over 60 ms. (d) complete transformation of the cavitation activity after the first ~ 1.3 s, beyond which a primary cluster close to the sonotrode tip dominates for the remainder of sonication duration. Bubble collapse shockwaves are arrowed yellow, TCM fragments within zoomed inset arrowed blue, throughout the Photron imaging. Scale provided by (i) the 2 mm  $\varnothing$  TCM disk, (ii) the 6.4 mm  $\varnothing$  tip.*

Fig. 6.11 (a) demonstrates that the full extent of delamination during the fifth minute of sonication is lower than that at 60% power, with delamination primarily involving very small fragments of TCM and enlargement of previous pits, observed in the 21-30 s sonication, fig. 6.11 (b) (i). No large fragments, comparable to those observed at 60% power, were observed at 90% power. Fig. 6.11 (b) (ii) represents the cavitation development for first 540 ms. Over this duration, the cavitation is similar to that observed throughout the 60% power sonications, with bubble filaments streaming towards the PCB surface and a large bubble cluster directly on the bubble surface. Larger bubble clusters can also be observed attached to the horn tip. At 248.250 ms a small fragment of TCM is shown removed from the PCB surface, Fig. 6.11 (b) (ii), zoomed inset, visible as the bubble cloud is undergoing a collapse phase, evident by the bubble collapse shockwave and corresponding to the observed delamination from the Phantom perspective (b) (i). Fig. 6.11 (c) demonstrates the recession of the bubble activity back towards the sonotrode tip, with individual bubble clusters appearing larger in size, and more densely compacted, than earlier in the sonication, and at

Chapter 6: A mechanistic study identifying improved technology critical metal delamination from printed circuit boards at lower power sonications in a deep eutectic solvent. comparable time in a sonication at 60% power, fig. 6.10 (d) (ii). Beyond ~1350ms the bulbous cavitation structure and direct bubble/PCB contact has been entirely removed, and the sonication is reminiscent of a single tightly packed bubble cloud oscillating at the horn tip, with smaller satellite clouds detached from the main bubble cluster, fig. 6.11 (d). This behaviour is equivalent to that observed in the acoustic characterisation in DES (chapter 6). We note that no TCM delamination is observed beyond the first ~1 s of sonication at 90% power during any of the 1-minute intervals, suggesting that the lack of direct bubble/surface contact inhibits delamination.

## 6.4 Discussion

Recycling of e-waste is an existing and rapidly growing problem for today's consumerist society. In addition to TCM delamination from PCBs, this includes reclamation of precious and technology critical metals from aged photovoltaics and thermoelectric generators [201, 208]. Here, we present the first study investigating the mechanisms that underpin ultrasonically enhanced TCM delamination from PCBs, mediated by cavitation activity in a DES that is chemically tailored to target copper.

The main finding, from the ultrasonics perspective, is that sonications at a lower power are more effective than those at a higher power. The dual perspective HSI observations indicate that this occurs because the lower, 60% input power, develops a bulbous cavitation structure which sustains an active cavitation cluster, maintaining contact with the surface of the PCB throughout the duration of a sonication. At the higher 90% input power, this cavitation structure recedes back to the sonotrode tip earlier in the sonication – likely due to changes in liquid properties, including viscosity – removing the cavitation from the PCB surface and protecting it from any significant enhancement of delamination, for the majority of the sonication.

The bulbous bubble structure that determines these effects has been reported previously for sonotrode sonications in viscous liquids. *Thiemann et al* and *Eddingsaas & Suslick* [195, 196] reported very similar cavitation structures, via sonoluminescence observations in sulphuric acid, with the former also highlighting bubble jetting for the cavitation behaviour at the extremities of the bubble cloud. This investigation suggests that this jetting activity is significant for initial pitting of the TCM disk, creating nucleation sites through which the surface cluster generated and sustained, optimally during sonications at 60%, can penetrate. The latter study describes a bulbous globe of luminescence below the sonotrode tip, which receded to a cone shaped structure in contact with the tip, with increased acoustic intensity [195, 196], in agreement with our observations at the higher input power of 90%, producing

Chapter 6: A mechanistic study identifying improved technology critical metal delamination from printed circuit boards at lower power sonications in a deep eutectic solvent. less effective cavitation for TCM-delamination. *Tzarakis et al* also reported a similar structure via HSI of cavitation in glycerine along with a circulating pattern of symmetrical vortices, such as that observed in this study, via the bubble mist generated in the DES [94]. Generally, the formation of the bulbous structure in liquids of higher viscosity, rather than the better-known conical structure directly beneath the tip in less viscous liquids (including water), appears to be poorly understood, and is worthy of future investigation including via simulation and modelling.

The selection of the two input powers for delamination observations was guided by a detailed characterisation of cavitation in DES, across the range of powers available, fig. 6.4 and chapter 5, based on acoustic detection of the cavitation emission signal. Specifically, the structure of the  $V_{\text{RMS}}$  versus input power plot indicates a much higher bubble collapse shockwave content (with most sonochemical applications recognised as mediated by bubble collapses), for cavitation in DES at an input power of 60%, compared to any higher input power. The results of the acoustic characterisation suggest that this is due to cavitation oscillating cleanly and regularly in response to the tip-oscillation [55] and could also be related to the sustained bulbous structure formed in the DES at this power. It is noted that the detailed acoustic emissions discussed in Chapter 5 dictated the selection of input powers used in this chapter. Here, acoustic emissions detected by the swPCD were used primarily for real time monitoring of the shockwave periodicity at the given input power.

*Rivera et al* have previously demonstrated the utility of using DESs to separate TCMs from PCB substrate in silent/passive immersion conditions, noting major limitations in etch rate associated with mass transport limitations due to the viscosity of the liquid [112]. Here, through the addition of power ultrasound-generated cavitation, we have demonstrated removal of TCMs from the PCB substrate over 30 times faster.

Chapter 6: A mechanistic study identifying improved technology critical metal delamination from printed circuit boards at lower power sonications in a deep eutectic solvent.

Guided by the characterisation of cavitation in DES, *Results* section 6.3.1, we further demonstrate that sonications of the PCB samples at a lower power of 60% resulted in a greater than 27% removal of TCM compared to higher power (90%) sonications.

We also note, however, that ultrasonically enhanced TCM delamination is not a continuous process. Rather, metal layers are removed in sections, observed in this study as initial pitting removing small fragments, with larger fragments delaminated later into sonication. As such, continuous etch rates are not suited for reporting ultrasonically enhanced delamination. Notably, the most significant delamination from the samples observed here occurred during the fifth minute of the sonications at 60% input powers.

The DES targets and solubilises the copper layer, via oxidation in the presence of  $\text{FeCl}_3$ , and the HSI indicates the most effective cavitation for TCM delamination occurs directly on the PCB surface. The redox chemistry of the iron catalyst can occur on the whole of the gold surface and electrons are removed from the copper layer leading to localised copper corrosion. The cavitating bubble clusters penetrate the space created by the rapid copper solubilisation, beneath the gold/nickel layers, undercutting and prising fragments of TCM from the PCB substrate. The surface microscopy and profilometry further suggest that all TCM layers are removed from the PCB substrate, with little remaining residual copper layer observed between sonications. Further processing of delaminated material would therefore be required for subsequent separation of TCM layers, once delaminated from the PCB.

Generally, for sonochemical applications, parameter optimisation is a significant challenge, with a large parameter-space available for exploration (non-exhaustively: transducer source, configuration, frequency and power of operation, and pulsing protocols). Here, we have demonstrated that cavitation characterisation for optimisation within any liquid in terms of power consumption, nominally with any source, may be easily assessed, via determining the level of shockwave content within the emission signal. We speculate that this should also apply to identifying the optimal protocols for pulsed sonications, specifically; bubble

Chapter 6: A mechanistic study identifying improved technology critical metal delamination from printed circuit boards at lower power sonications in a deep eutectic solvent. collapse shock wave content as measured by  $V_{RMS}$ , could be used to determine the most efficient temporal administration of acoustic power, as well as the most effective power of sonication for a given liquid, generally.

## **6.5 Conclusion and Future Investigations**

Future work will involve assessing the effect of varying temperature of the DES during sonication. Altering temperature will have some effect on cavitation activity as well as relevant liquid properties such as viscosity [112]. We observed a reduced effectiveness of the process at both powers, when samples are continuously sonicated for 5 minutes, as opposed to in 10 s intervals, used here to accommodate the dual-perspective HSI. A full exploration of pulsing, including optimal duty cycle, pulse duration and pulse interval could significantly improve the delamination efficiency, both in terms of power consumption and speed of process.

## Conclusions

This thesis presents an investigation into the characterisation of cavitation generated by high-power sonotrodes in viscous deep eutectic solvents for the purpose of process optimisation of recovering technology critical materials from electronic waste.

The sonotrode is amongst the most common industrial sources of high-power ultrasound. Despite this, efforts to characterise its performance in terms of cavitation output are limited. Through combined acoustic emission monitoring and HSI, it has been shown that the primary bubble cluster generated at the tip of the horn collapses subharmonically at  $f_0/m$  with the integer value  $m$  increasing as input power to the sonotrode increases. In water, transitional power amplitudes are identified for which  $m$  is indistinct. At these transitional power amplitudes, cavitation intensity is reduced despite the increase in input power. The mean time average shock wave content,  $V_{RMS}$ , measured with an in-house manufactured swPCD reveals a local minimum value at these amplitudes, generated due to inefficient periodicity of bubble collapse. This observation is of relevance to a number of industrial applications, where optimal sonochemical yield is desired.

Whilst the majority of study of cavitation is performed in water, there is a growing interest in the application of high-power ultrasound to different liquids. DESs are a class of ionic liquids with the ability to be tailored for selective recovery of metals from electronic waste. DESs have the distinct advantage over traditional recovery techniques, including significantly lower temperature requirements, avoidance of toxic reagents and reduced water consumption. DESs are cheap to manufacture from readily available constituents and can be adapted for selectivity of target metals. However, their direct utility is limited by their high viscosity, which results in slow dissolution kinetics. Recovery of metals requires immersion in DESs for several hours with the process limited by mass transport. The addition of power ultrasonics for mechanical and chemical acceleration of the process is seen as a promising

approach to overcoming the current limitations associated with ionometallurgy. However, little study into the effect of cavitation in high viscosity liquids has been performed, with no studies characterising cavitation activity over the range of powers available to most commercially available sonotrodes. Cavitation characterisation in water and three commonly reported DESs was performed over the full range of powers available to two commercially available sonotrodes for the purpose of developing a method of optimising cavitation output in each liquid. HSI and monitoring of acoustic emissions generated during sonications indicated very different cavitation dynamics in the DESs compared to water, particularly at lower powers. Cavitation in DESs was characterised with the generation of a wide reaching bulbous cavitating structure which exhibited inertial cavitation features such as bubble-collapse shockwaves and jetting throughout the complex structure. At higher powers, this bulbous structure was observed to recede back to the sonotrode tip, where cavitation dynamics more closely resemble that observed in water. Local minima in the cavitation output, quantified by  $V_{RMS}$  were attributed to the observed transitional powers and bubble dynamic phenomena.

The observations from the extensive cavitation characterisation in each liquid identified potentially optimal sonication parameters for sonochemical applications. This study provided the first ever mechanistic study of cavitation-enhanced technology critical metal delamination from PCBs. Through dual-perspective HSI, synchronous observation of delamination of the technology critical metals on the surface of the PCBs was combined with monitoring of the detailed cavitation dynamics responsible for delamination. Results demonstrated that bubble jetting was influential for initial pitting of the PCB surface, generating nucleation sites for further cavitation and chemical etching of the exposed copper layer. Rapid copper solubilisation and generation of nucleation sites allows for cavitating bubbles to penetrate the space created, whereby further cavitation dynamics such as microstreaming and bubble-collapse shockwaves aid in complete delamination of the metals

from the PCB surface, further aided by acoustic streaming generated by the sonotrode. Through these mechanisms, an over thirty-fold increase in delamination rate is achieved compared to passive etching. Furthermore, for this experimental configuration, sonication at 60% power was identified to improve delamination by over 27%. This is attributed to the generation of a greater reaching bulbous cavitating structure and regular periodicity of bubble collapse as shown during the cavitation characterisation in each liquid. The results highlighted the utility of high-power ultrasound as a technology capable of process enhancement. This first mechanistic study of the cavitation generated in these high viscosity DESs highlights the importance of full characterisation of the cavitation generated in any ultrasonic system for optimal processing.

In this thesis, acoustic emissions are detected by an in-house manufactured swPCD, designed for sensitivity to bubble-collapse shockwaves. Detailed characterisation and comparison of the swPCD against a commercially available CaviSensor demonstrated that cavitation detectors can be readily and cheaply manufactured. The swPCD used in this study exhibited improved sensitivity over the bandwidth required for cavitation monitoring and, importantly, could be incorporated with HSI.

Global electronic waste generation is projected to exceed 75 Mt by 2030. In addition to the significant environmental and health impacts associated with this quantity of waste generation, there is also an economic benefit to improving recycling of these waste streams. The UK alone produced electronic waste to the value of \$148M in 2019, much of which is lost due to poor recycling techniques. This study presents evidence that high-power ultrasound, in combination with DESs, has potential to become a tool for green recycling of electronic waste. The results presented in this thesis demonstrate a proof of concept. For industrial relevance, scalability of the processing used in this thesis must be considered. This is likely to come, in part, through further parameter optimisation studies investigating the effects of tip/sample distance, immersion depth, temperature, oxidising agent concentration

as well as ultrasonic parameters such as frequency, pulsing and duty cycle. Nonetheless, simple characterisation of the effects of parameter optimisation on cavitation activity should be performed via the use of cavitation detection. Further investigation of integrated systems that incorporate flow and alternative transducer designs could also aid in the development of an industrially scalable system that can efficiently process the growing quantity of electronic waste.

This thesis concludes with an extended future work and spinout activities chapter. This chapter introduces additional waste streams that demonstrate present and future potential for ionometallurgy enhanced by high-power ultrasound-induced cavitation. Lithium-ion batteries and photovoltaics are promising sources of technology critical materials and early research contributions are summarised following a review of the literature. Finally, two spinout activities beyond the primary scope of this thesis but contributing to cavitation research are summarised.

## **7 Future work and spinout activities**

### **7.1 Ultrasonically enhanced processing and recycling of additional technology critical materials**

#### **7.1.1 Lithium-ion battery recycling**

Lithium-ion batteries (LiBs) are already widely used in portable electronics such as laptops, mobile phones and video cameras [209]. Nowadays, LiBs are perhaps more commonly associated with electric vehicle batteries. The transport sector is amongst the most rapidly expanding sources of environmental emissions worldwide [210] contributing over a quarter of all global greenhouse gas emissions. Resultingly, large-scale decarbonisation of the automotive industry has become high priority across much of the globe. To achieve this, electrification of the transport sector is seen as a promising solution to reduce airborne emissions, leading to eventual de-carbonisation [211]. Electric vehicles (EVs) are widely regarded as the future of the transport industry with the number of EVs on the road increasing exponentially. In the UK alone, in 2017, 15000 new EVs were registered. This number is estimated to be between 84000 and 500000 by 2025 [212]. Across the EU, this figure is speculated to be around 7 million by 2025 [213, 214]. Given that the main power source of EVs is the LiB, intuitively, the quantity of LiBs and, more importantly, waste LiBs will also rise. Taking the 15000 new EVs registered in the UK in 2017, with an estimated average weight of 250 kg [215], the resultant unprocessed pack waste at the end of the EVs life span would equate to approximately 3750 tonnes. Given the aforementioned growth in EVs, the quantity of waste LiB in the future becomes staggering, with the need for industrially scalable, environmentally friendly recycling methods clear.

Recycling of LiBs is very much in its infancy, with an estimated 95% of LiBs ending up in landfill in 2016 [216] and only 5% of LiBs being recycled in the EU in 2019 [217]. Clearly,

LiB recycling remains a challenge, particularly due to the complex structure. LiBs are composed of a varying series of small cells which are combined to make a module which, in turn, are combined to make a battery pack. Fig. 7.1 highlights different battery cell types and their organisation into the overall hierarchical structure.

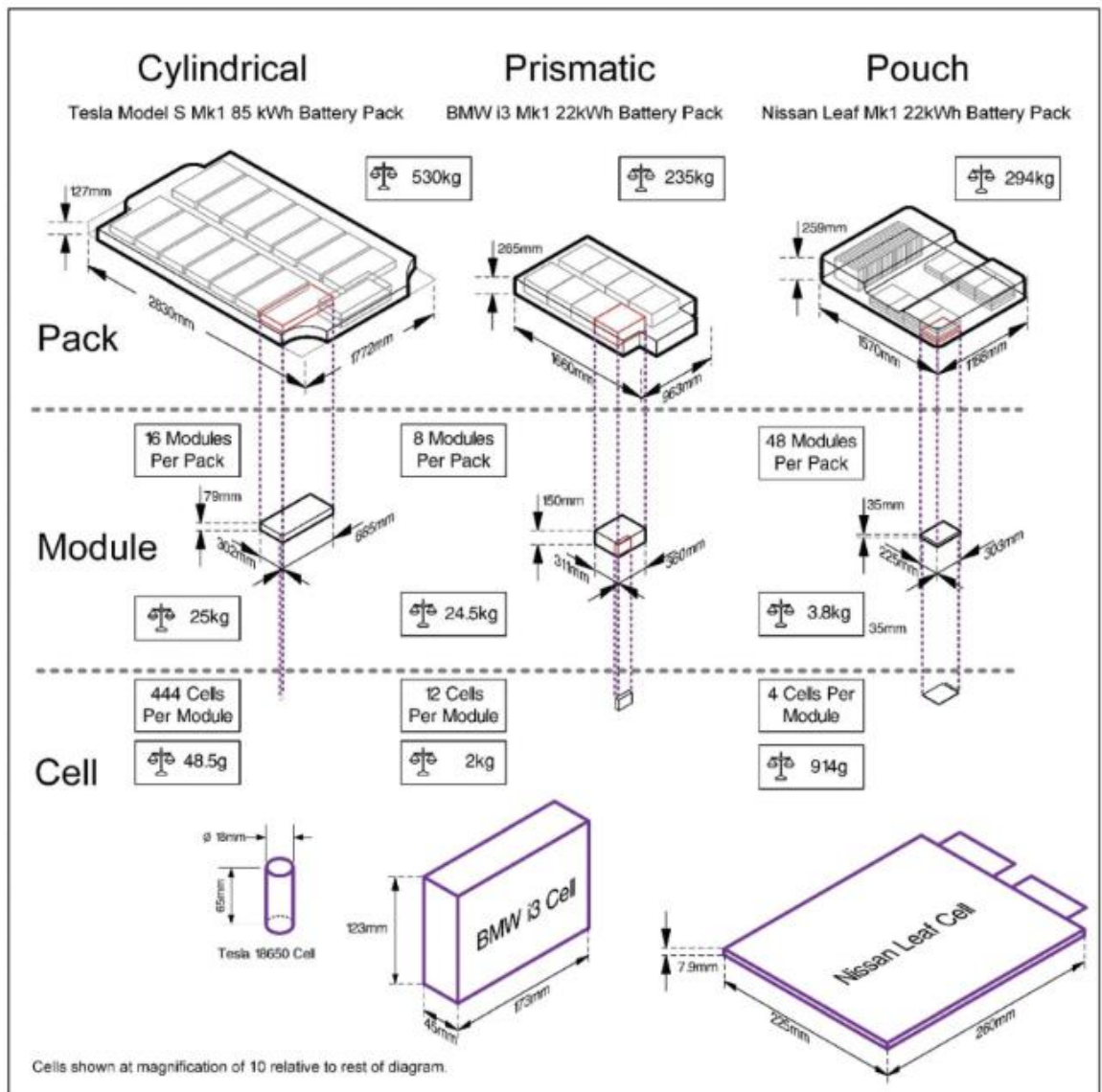


Fig. 7.1: Battery cell types and their arrangement into modules and packs. Taken from [223].

The LiB cell itself is a complex structure comprised of several components and materials, summarised in table 7.1, below.

Table 7.1: Cell materials in a typical LiB. Adapted from [223].

Cell component	Materials	Composition/wt%	Cost%
Cathode active material	Layered structures e.g. $\text{LiCoO}_2$ (LCO)/ $\text{Li}(\text{Ni}_x\text{Mn}_y\text{Co}_{1-x-y})\text{O}_2$ (NMC)	22-25	65-70
Cathode foil	Al	4-5	1
Anode active material	Graphite, hard carbon, lithium titanate, silicon-based materials	24-26	8-9
Anode foil	Cu	3	2
Binder	PVdF, PTFE, PVA, CVC	2-3	8-9
Electrolyte	Mixtures of ethylene carbonate (EC)/propylene carbonate (PC)/dimethyl carbonate (DMC) + additives e.g. fluoroethylene carbonate (FEC)	10-12	1
Conductive additive	Acetylene black (AB)	1	0.1
Conductive salt	$\text{LiPF}_6$	1.5	2
Separator	Polyethylene (PE)/polypropylene (PP)	4-5	4
Cell case	Metal or Laminate	4-6	4

The data in table 7.1 summarises the typically found materials in a LiB. As can be observed, there is variation in chemistry between those made by, for example, one manufacturer to the next. Most commonly though, the anode electrode active material is typically composed of (carbon) graphite. The cathode electrode active material is often more variable, with some form of Lithium metal oxide (such as  $\text{LiCoO}_2$  and  $\text{LiMn}_2\text{O}_4$ ) historically used. Although developments of new materials (table 7.1) has introduced different variations in recent years. In summary, however, the cathode is a combination of lithium, with ratios of nickel, manganese and cobalt [218]. A basic schematic of the LiB cell is demonstrated in fig. 7.2.

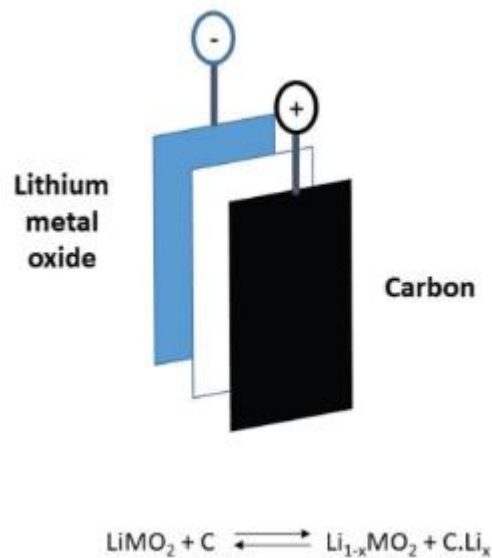


*Fig. 7.2: Basic schematic of a LiB. Taken from [223].*

The electrodes in LiBs have a layered structure of composite film, up to 200  $\mu\text{m}$  thick, containing active materials, polymeric binder and conductive additives, which are sandwiched either side of a metallic foil [219]. The metallic foil acts as a current collector and is typically copper foil for the anode and aluminium foil for the cathode [219], with each foil coated on both sides by the respective active materials described and summarised in table 7.1.

Perhaps the largest driver of LiB recycling arises from the need for ethical sourcing of the constituent materials found within the cells. Graphite, lithium, cobalt and nickel are all designated as ‘strategic elements’ and ‘critical materials’ by the UK, EU and US both due to their global scarcity and resource security from geopolitical factors [217]. As such, effort to recycle complete EV battery packs down to their constituent materials is crucial. As figure 7.1 highlighted, a complete EV battery pack is comprised of thousands of cells. The process of taking these complete packs down to individual cells for recycling involves individual opening and disassembly. This physical separation is labour intensive and slow, hence most current recycling approaches start with comminution (crushing). Comminution is not desirable from an environmental perspective as it requires additional processing steps, more energy and more processing chemicals [220].

Following all physical separation techniques, material extraction process may be utilised to separate the constituents of the LiB cell from each other by breaking down the binder. The three methods of extraction include: direct recycling, whereby the electrode coatings are relithiated and reincorporated into a new cell, pyrometallurgy, and hydrometallurgy [214]. A general recycling process schematic is presented in fig. 7.3.

Pyrometallurgy is one of the most widespread metal recycling technologies used. The process involves placing the LiB cells into a high-temperature furnace and melting to produce an alloy of the most valuable metals [214]. The resulting alloy typically contains quantities of copper, nickel and cobalt which are then separated via hydrometallurgy. The remaining LiB constituents are either burned (graphite) or not recovered (aluminium and lithium) [214]. The major advantage of pyrometallurgy is the ability to process whole cells or modules without the need for extensive pre-recycling processing [215].

Hydrometallurgy involves dissolving the electrode materials in acids and separating the constituent metals using solvent extraction. In terms of metal reclamation, copper is reclaimed from the anode, and nickel, cobalt and lithium from the cathode [217]. The hydrometallurgical process produces a “black mass” of constituents comprising the active materials from each electrode, which requires material separation separately. Typically, materials other than the metal oxide are not recovered, leading to high volumes of waste. As such, hydrometallurgy is very cost intensive, with the need to minimise superfluous material subjected to the process as much as possible [217].



Fig. 7.3: Generalised recycling loop of LiB battery modules with products presented in blue and processes presented in orange. Ultrasonic delamination and selective separation in DES are highlighted red as the most relevant processes reviewed for optimisation in the subsequent section. Adapted from [214, 215, 218, 220].

A common drawback of both techniques is their environmental impact. Pyrometallurgy drawbacks also include the production of toxic gases which must be captured, high energy costs to heat the process, and limited number of materials reclaimed [215]. Hydrometallurgy involves leaching with strong acids such as HCl, HNO<sub>3</sub> and H<sub>2</sub>SO<sub>4</sub> which are hazardous. The large volumes of solvent required, and the cost of neutralisation are major drawbacks of this process [215]. Other sources of concern, particularly for scalability, revolve around the slow delamination time (hours) and high temperatures required (60 – 100 °C) [215], which is not conducive with industrial scalability.

To combat some of the drawbacks previously outlined, *Li et al* [209] demonstrated efficiency in separating the active material from spent LiB electrodes using a combined recovery process. A 40 kHz, 100 W ultrasonic cleaning bath was used. Anode and cathode material was sonicated with the aim of separating LiCoO<sub>2</sub> from the aluminium foils and graphite from the copper foils, respectively. The authors demonstrated that electrode separation was enhanced in the cleaning bath compared to simply agitating the samples, with a greater than 90% removal efficiency of electrode materials from the aluminium foil with 15 minutes of sonication at room temperature in water [209]. Following the delamination treatment, the recovered electrode material was, however, subjected to acid-leaching for 4 hours for further separation. The authors claimed that the ultrasonic washing stage of the process reduced both environmental and economical impact by removing the necessity for initial pyrometallurgical and hydrometallurgical process, to separate the conductive metal layers from the electrode active materials.

More recently, other studies have demonstrated the utility of low power ultrasound for the delamination process [221, 222], however they are all characterised by the slow rate of delamination (5 to 90 minutes, depending on pre-treatment of the electrode) [219]. In order to overcome this, *Lei et al* [219] demonstrated the use of a 20 kHz, 1250 W sonotrode operating through a 20 mm-Ø tip. The authors demonstrated that, with high power

sonications, the adhesive bond between the active layer of the electrode and the current collector was broken within 0.5 s, directly under the sonotrode. Through high-speed imaging at 20 kfps, the authors postulated that the acoustic cavitation generated beneath the sonotrode was crucial in the early delamination of the material layers. Furthermore, it was observed that the delamination of the cathode layers was increased by the addition of a small volume fraction of Ethylene Glycol, as a wetting agent, to the sodium hydroxide solution used for delamination [219].

Further down the recycling loop (fig. 8.2), *Thompson et al* [218] demonstrated the use of Deep Eutectic Solvents (DESs) for the separation of nickel and cobalt from LiBs. Here, replacement of the end-stage strong acids used in traditional hydrometallurgical processes was incorporated. As with PCB delamination outlined previously in Chapter 6, the advantage of using DESs for this application involve greater selectivity than traditional acids, less aqueous waste and avoiding emission of harmful gases. Due to the variability in cathode active material composition and chemistry (outlined previously in table 7.1), the selectivity offered by DESs offers an attractive alternative to strong acid leaching. The authors demonstrated separation of materials in this system after leaching times in the order of hours. Interestingly, they suggested the use of ultrasound as a method of initially separating the active material from the electrodes before separating the materials from the black mass.

This chapter section summarises the initial experimental procedures adopted in collaboration with Dr Chunhong Lei (author of above, [219]) investigating the cavitation at the sonotrode tip for rapid delamination of LiB electrodes. Future collaborative work to be carried out is discussed, with a timescale for experimentation and dissemination.

## 7.1.2 Materials and methods

### LiB electrode preparation

The LiB cells were obtained and prepared by Dr Chunhong Lei at the University of Leicester. The LiB electrodes were sourced from Nissan Leaf batteries, with varying levels of usage history and cathode chemistry. For this preliminary investigation, LiB cathode sheets were used and these sheets were composed of 25  $\mu\text{m}$  thick aluminium foil collector, coated on both sides with 100  $\mu\text{m}$  thick active material containing a mixture of lithium manganese oxide and lithium nickel manganese cobalt oxide (NMC) powder with carbon black conductive additive and PVdF binder [219]. The cathode sheets were cut into squares approximately 30 mm  $\times$  30 mm, fig. 7.4.

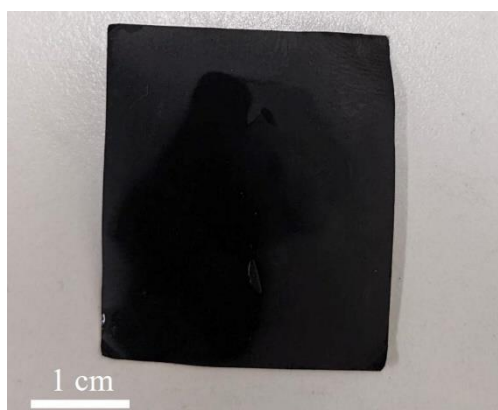


*Fig. 7.4: LiB cathode sheet prepared for sonication.*

## Experimental setup

A commercial ultrasonic system (Branson Sonics, 1.25DCXa20-V) was used for this investigation. This sonotrode operates at 20 kHz and a maximum power of 1250 W, through a 20 mm-Ø tip.

General experimental setup is approximately equivalent to that described in Chapter 5, fig. 5.1, with notable differences described below.

High-speed imaging of the cavitation activity at the vicinity of the sonotrode tip was undertaken with the same Fastcam SA-Z 2100K (Photron, UK), as described in previous chapters, imaging through the same macro lens as described in Chapters 5 and 6 at a frame rate of 20 kfps. The camera was slightly angled on a tripod for optimal imaging of the LiB surface beneath the sonotrode. Illumination was provided by the 150 W halogen lamp (Thorlabs, UK), described in Chapter 3, §3.5.2, coupled to a liquid light guide and collimating lens.

All sonications were performed in water at varied tip heights ranging from 1.5 mm to 10 mm (estimated from the HSI). Sonications and HSI were initiated manually for a total of 3 s. Clearly, water as a solvent has distinct environmental advantages over traditionally used strong acids, with further advantages of lower viscosity.

### 7.1.3 Results

#### Observation of LiB delamination

Fig. 7.5 is representative HSI frames capturing the initial fragmentation and delamination of the cathode material early in a sonication at a tip height of 3 mm operating at 30% input power. The enlarged sonotrode tip diameter coupled with relatively small tip height created a small FOV for observation of all the cavitation activity.

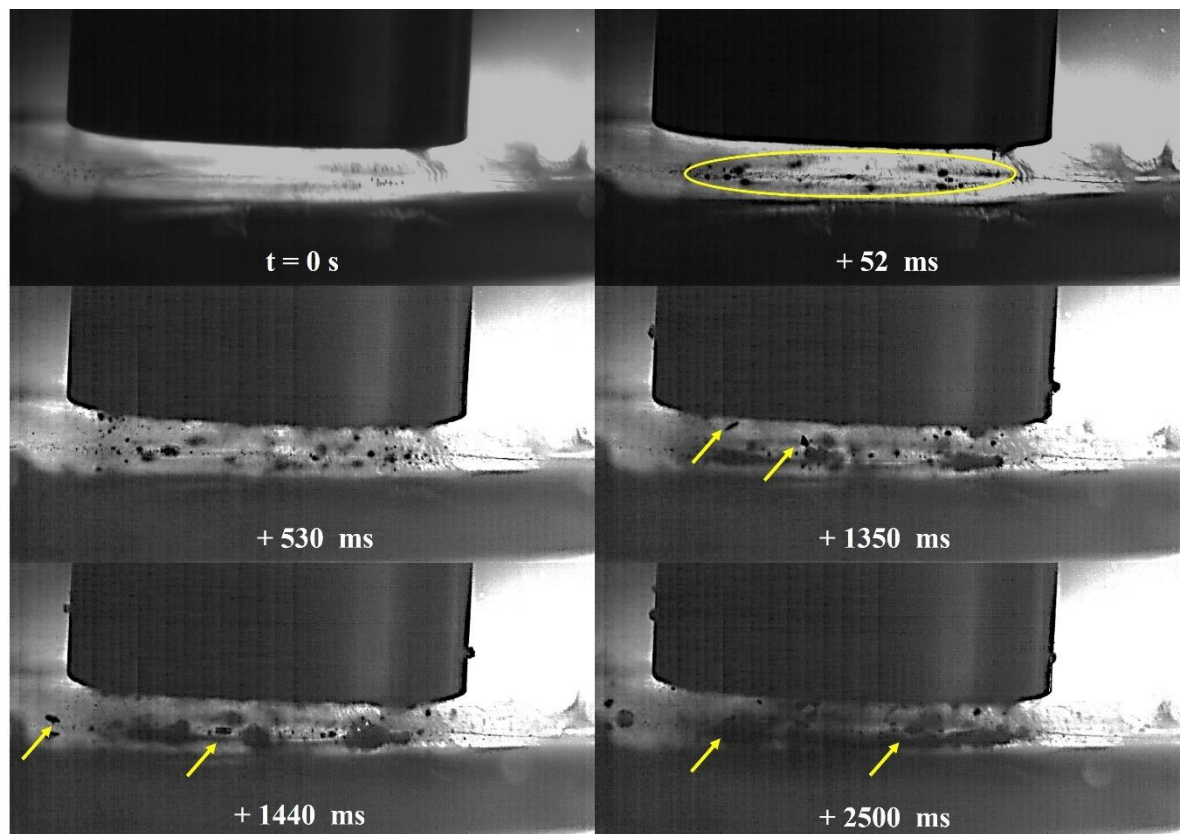


*Fig. 7.5: Representative HSI frames capturing cathode material delamination. A concentric ring of bubbles forms upon sonication initiation (circled yellow) with subsequent fragmentation of the cathode material arrowed yellow. Scale is provided by the 20 mm- $\emptyset$  tip.*

Shortly after sonication initiation, a concentric ring of bubbles form on the surface around the perimeter of the tip diameter. These bubbles oscillate and translate across the surface of the cathode with no observed delamination. Owing to the size of the sonotrode tip, full vibrational tip oscillation is not achieved until over half a second into the sonication. Here, a cloud of bubbles can be observed translating down from the sonotrode tip (fig, 7.5, + 530 ms) in a structure reminiscent of the conical CBS typically reported in sonications in water, 500 – 800 ms later cathode material fragmentation is observed, with cavitating bubbles translating to and attacking fragmented sections, further aiding delamination.

Fig. 7.6 demonstrates the before/after of a cathode sheet sonicated for 3 s. As can be observed, almost the entire region of cathode material directly under the sonotrode tip is delaminated, leaving the aluminium foil visible.



*Fig. 7.6: Cathode sheet before sonication (left) and after 3 s sonication at 30% input power and a tip height of 3 mm (right).*

#### 7.1.4 Discussion and future work:

Investigations into the ultrasonically enhanced delamination cathode LiB material are in the preliminary stage. HSI of the cavitation at the sonotrode tip has provided insight into potentially optimal tip heights, with heights exceeding 5 mm resulting in no delamination within the first 3 s of sonication. A key observation made by *Lei et al [219]* was the role of wetting agents to enhance delamination.

Future work, scheduled for November 2023, in collaboration with Dr Chunhong Lei and the University of Glasgow will firstly seek to investigate the addition of quantities of Ethylene Glycol and Glycerol. As the authors noted these as potentially promising wetting agents when added in, small quantities, to water. The future investigations will involve the combination of HSI and, importantly, acoustic detection using the swPCD previously discussed and used throughout this thesis – a version of which has been distributed to the University of Leicester for preliminary testing. The HSI will additionally be synchronised with the pulsed laser illumination described and utilised throughout this thesis, allowing for greater image quality as well as detection of bubble-collapse shockwaves. Furthermore, imaging at higher frame rates will be possible, providing greater temporal resolution for elucidating cavitation dynamics. The addition of small granular particles to the cavitating fluids to act as nucleation sites and enhance abrasive contact is also under preliminary investigation. The target for this work is a journal submission by the end of 2023.

## 7.1.5 Photovoltaic recycling

### Components of a PV

Photovoltaics (PVs) or solar modules convert energy from sunlight into electricity without the need for a rotor, engine or gears and have gained significant popularity and demand as an alternative source of energy generation [223]. PVs can be classified into three categories: first-generation, second-generation, and third-generation [224]. First-generation PV modules contain crystalline silicon (c-Si), which may be monocrystalline, polycrystalline or ribbon sheets. Second-generation PV modules include thin-film amorphous silicon (a-Si), cadmium telluride (CdTe), multi-junction cells, copper indium gallium diselenide (CIGS), and copper indium diselenide (CIS). Third-generation PV modules using perovskite, passivated emitter and rear cells (PERC), dye-sensitized cells and organic PV cells, are under current development [223-225]. Currently, the majority of production consists of c-Si solar cells (first-generation) accounting for approximately 80% [223] to 93% of total production [226].

First-generation c-Si PV modules typically consist of tempered glass, encapsulated film composed of ethylene vinyl acetate (EVA), the solar cell, PVdF backing sheet, metal frame and a junction box (Fig. 7.7 (a)). Within the PV module, the key structure is the solar cell. This consists mainly of silicon wafer with a silicon nitride anti-reflective coating as the semiconductor material, along with an aluminium frame and silver electrodes [201, 227] (fig. 7.7 (b)). Typically, the solar cell electrodes are silver on the upper side and aluminium (and silver) electrodes on the rear side. The solar cells are connected to the remaining module with copper wires, often coated in lead [228].

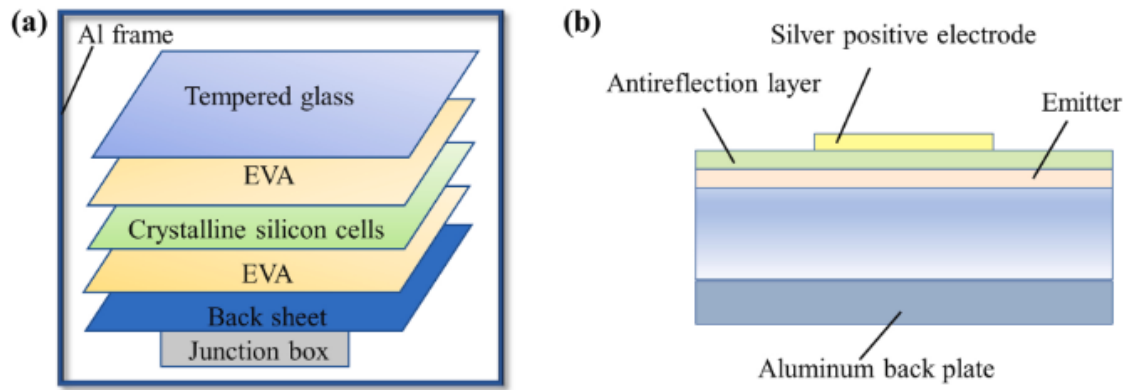
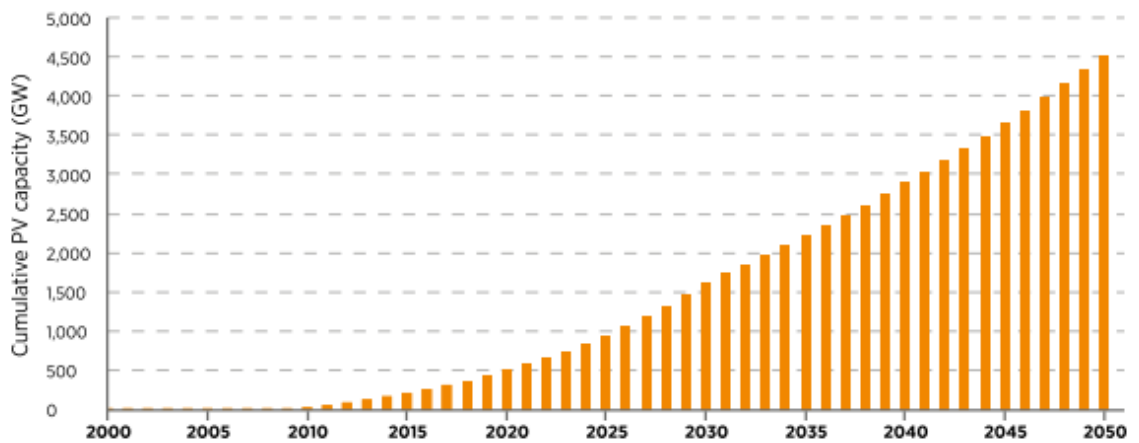


Fig. 7.7: Schematic representation of (a) a first-generation c-Si PV module and (b) the solar cell layer within the module. Taken from [232].

## PV deployment growth

The amount of installed PV capacity has been growing rapidly from less than 13 Gigawatts (GW) in the early 2000s to almost 200 GW by 2014 [229]. With the push for transition from traditional fossil fuels to renewable energy, the growth in PV deployment worldwide is set to exponentially grow, reaching 1600 GW by 2030 and over 4500 GW by 2050, fig. 7.8 [230]. Although contributing a small amount to global power output (2%) in 2017, PV were forecasted to lead renewable electricity capacity growth over the following five years [224].



*Fig. 7.8: Projected growth of PV capacity from 2000 to 2050, based on International Renewable Energy Agency (IRENA) interpolation of annual growth rate. Taken from [235].*

## PV waste

As global PV deployment grows, the amount of waste from spent PVs grows accordingly. Given that the lifespan of PV modules is quoted as being between 20 years [223] and 30 years [201, 231], the vast majority of first-generation PV modules installed in the 1990s are reaching their end of life stage [232]. Approximately 75 tonnes of PV module waste is produced for every 1 MW installed [233]. Following the growth in PV installation, fig. 7.9 forecasts the cumulative PV module waste over the next 30 years. PV waste will approach 80 mega tonnes (Mt) by 2050. This is double the total amount of worldwide e-waste in 2018 [233].

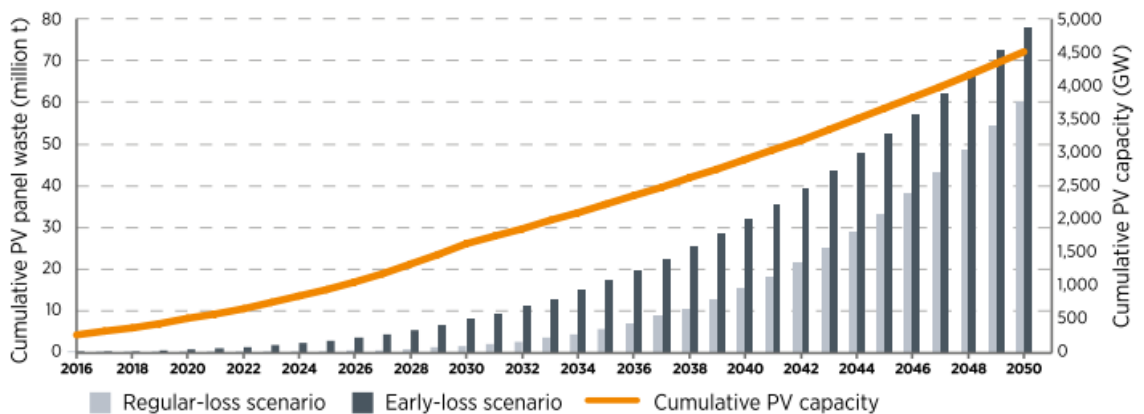


*Fig. 7.9: Projected increase in cumulative PV module waste, based on International Renewable Energy Agency (IRENA) estimates, projecting both a regular-loss and early-loss scenario. Taken from [230].*

Research into the health and environmental safety of PV modules is relatively scarce, despite the fact that PVs contain potentially harmful chemicals such as cadmium and lead [224], which can leach into soil and consequently pollute the environment [223]. *Nover et al* [234] demonstrated leaching of metals such as aluminium, copper, nickel and lead over long-term leaching in aqueous-based solutions, over a one year duration. *Tammaro et al* [235] observed the release of hazardous metals (lead, cadmium, chromium and nickel) in both first-generation c-Si and second generation thin-film PVs following leaching in pure water. The authors noted that quantities of these metals were observed to be above the legal EU threshold for drinking water, as well as for discharge in soil. The authors noted that less than 3% of all samples tested did not exceed any limits for metal leaching. Furthermore, based on the number of end-of-life PVs by 2050, the authors estimated that up to 30 tonnes of lead and 2.9 tonnes of cadmium could be releasable from PVs, respectively [235]. A review by *Kwak et al* [224] surveyed over 80 scientific studies and collation of the data presented clear harm from waste PV materials both to the ecosystem and human health.

PV module waste largely remains under the classification of general waste, worldwide. Hence, regulations and control over their end-of-life disposal and treatment remain limited. In the EU, however, PV waste is classified under waste electrical and electronic equipment (WEEE). Accordingly, to comply with EU regulations, a minimum of 75% must be recovered and a minimum of 65% must be recycled [201, 230]. Furthermore, it is the burden of the principal producers of the PV modules to fulfil responsibilities with regards to: finance (producers are liable through a financial guarantee to cover the cost of collection and recycling of products likely to be used by private households); reporting (producers must report on modules sold, taken back, and forwarded for treatment); and information (producers are accountable for labelling modules in accordance with the WEEE directive for recycling them) [230]. With the forecasted increase in PV waste over the coming years,

further regulations and a drive to development of sustainable, cost effective and green recycling is inevitably required.

### **PV recycling**

Recycling not only aids in prevention of the negative impact to the environment from improper handling of PV waste, it helps in avoidance of shortages of the crucial constituent materials needed for PV production [236]. Recycling programmes have been established for two of the major types of PV modules (CdTe and ,most commonly, c-Si), the first of which recovers glass and the semiconductor elements for reuse in CdTe synthesis, the second only recovers the aluminium frame and glass [236]. It has also been reported that, with current recycling technologies, the cost to recycle end of life PV modules greatly exceeds the cost of landfill, where most of the PV critical elements end up [232]. Currently, around 10% of worldwide end of life PV modules are recycled [227]. This is despite the European Environment Agency claiming that 95% of PV waste has the potential to be recycled [231].

With the cumulative value of the material components in recyclable PV modules predicted exceed \$15 billion by 2050 [227], it is clear that development of recycling processes that can extract these materials is of significant interest. It is estimated that the 2030 end of life PV modules will contain almost 2 Mt of glass, over 0.5 Mt of aluminium, over 0.1 Mt of silicon, over 16000 tonnes of copper and 1000 tonnes of silver [227]. Of this material, the most valuable are silicon and silver [228].

Several studies have investigated the extraction of precious materials from spent PV modules. Each study differs in exact processing, particularly with regard to which materials they are aiming to recover, hence which exact chemistry of leaching solvent is utilised. The process of PV recycling is generalised below in fig. 7.10.

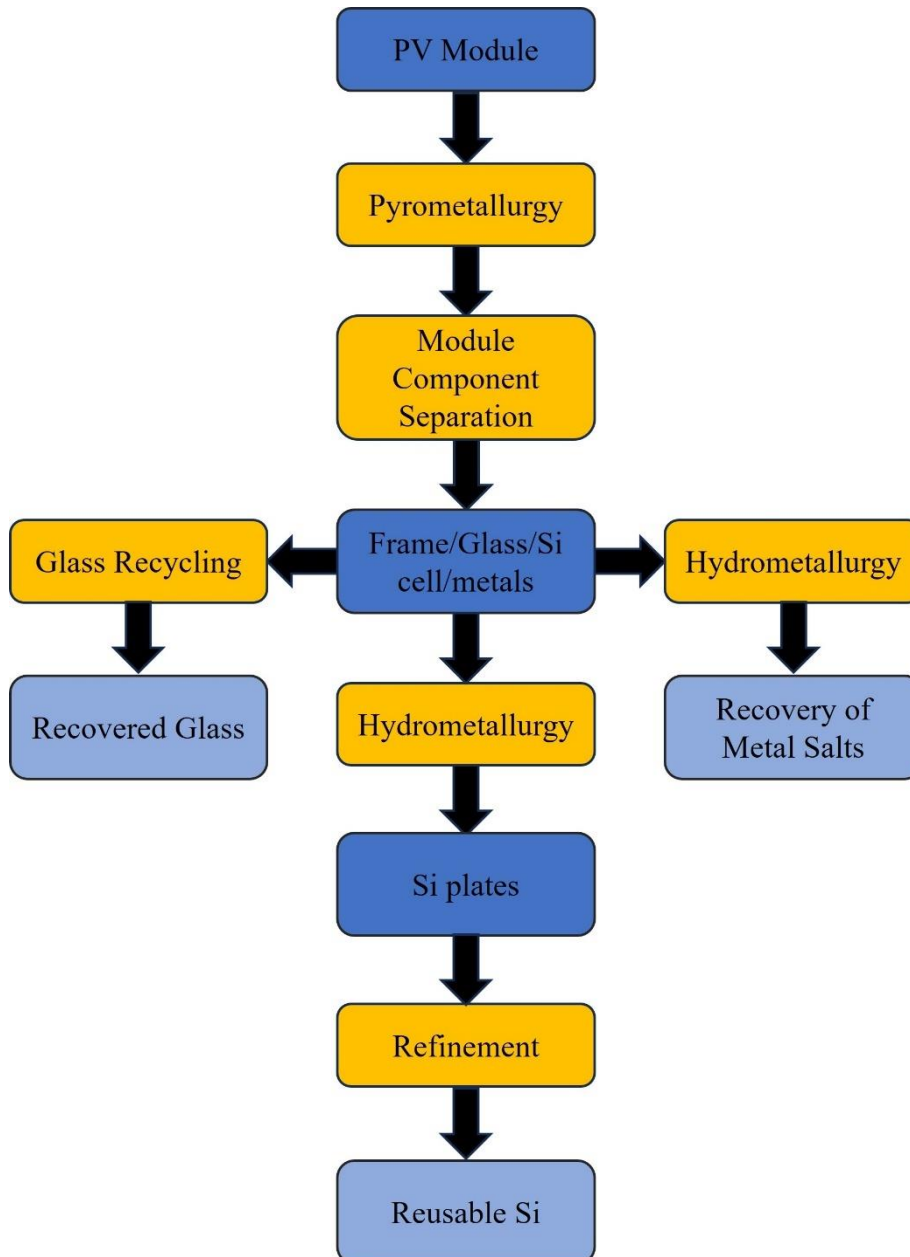


*Fig. 7.10: Generalised recycling loop of PV modules with products presented in blue and processes presented in orange. Specific chemical etching processes are simplified to broadly “hydrometallurgy”. Adapted from [201, 223, 237-239].*

Often, whole PV modules are subjected to initial removal of the EVA resin layer (fig. 7.7), typically by pyrolysis or chemical etching in a strong acid. Following thermal treatment, constituents of the PV module can be separated for their own respective recovery. Often, detailing of this initial module separation are not included in the reporting of valuable material recovery from the PV cell itself – where most effort is focused [223, 238]. Table 7.2 summarises typical methods of PV cell recycling to date and the materials gathered.

Table 7.2: Summary of experimental work on PV recycling

Authors	Process	Materials Recovered
Frisson et al, 2000 [240]	<ul style="list-style-type: none"> <li>• Pyrolysis in furnace</li> <li>• Chemical etching in strong acid mixture</li> <li>• Chemical etching in strong base</li> </ul>	<ul style="list-style-type: none"> <li>• Silicon</li> </ul>
Klugmann-Radziemska and Ostrowski, 2010 [239]	<ul style="list-style-type: none"> <li>• Chemical etching in strong base to remove Al metal</li> <li>• Chemical etching in a mixture of strong acids for removal of Ag and coatings</li> </ul>	<ul style="list-style-type: none"> <li>• Silicon</li> </ul>
Kang et al, 2012 [241]	<ul style="list-style-type: none"> <li>• Recovery of glass using organic solvents</li> <li>• Thermal decomposition for removal of adhesive and recover Si</li> </ul>	<ul style="list-style-type: none"> <li>• Glass</li> <li>• Silicon</li> </ul>
Wang et al, 2012 [242]	<ul style="list-style-type: none"> <li>• Pyrometallurgy for thermal delamination</li> <li>• Acid etching to remove tin-lead coating</li> </ul>	<ul style="list-style-type: none"> <li>• Glass</li> <li>• Silicon</li> <li>• Copper</li> </ul>
Yi et al, 2014 [238]	<ul style="list-style-type: none"> <li>• Leaching in nitric acid then sodium hydroxide</li> <li>• Pyrometallurgy to scavenge metal impurities</li> </ul>	<ul style="list-style-type: none"> <li>• Silicon</li> </ul>
Dias et al, 2016 [223]	<ul style="list-style-type: none"> <li>• Pyrolysis</li> <li>• Sequential leaching in strong acid and sodium chloride in an ultrasonic bath for silver salt recovery</li> </ul>	<ul style="list-style-type: none"> <li>• Silver</li> </ul>
Jung et al, 2016 [228]	<ul style="list-style-type: none"> <li>• Pyrolysis</li> <li>• Precipitation</li> <li>• Sequential leaching in nitric acid under agitation, leaching in phosphoric acid, sodium hydroxide and organic chemicals</li> <li>• Electrolytic refinement</li> </ul>	<ul style="list-style-type: none"> <li>• Silicon</li> <li>• Copper</li> <li>• Silver</li> <li>• Aluminium</li> <li>• Lead</li> </ul>
Rahman et al, 2021 [226]	<ul style="list-style-type: none"> <li>• Pyrolysis</li> <li>• Chemical etching in potassium hydroxide</li> <li>• Ball milling</li> </ul>	<ul style="list-style-type: none"> <li>• Silicon for re-incorporation into anode material for LiBs</li> </ul>
Luo et al, 2021 [227]	<ul style="list-style-type: none"> <li>• Pyrolysis</li> <li>• Chemical leaching in nitric acid</li> <li>• Ultrasonic cleaning to remove adhesive layer</li> <li>• Precipitation in acid and alkaline leaching solutions</li> </ul>	<ul style="list-style-type: none"> <li>• Silicon</li> <li>• Silver</li> <li>• Aluminium</li> <li>• Lead</li> </ul>

From an economic perspective, recovery of pure silicon from end of life PVs is the major priority. This is primarily due to its cost and shortage [239]. Silicon accounts for approximately 0.76 kg/module and about half the cost of the module [226]. With the increasing demand for silicon in technological industries, the demand for recovery silicon at a quality sufficient for re-use is increasing. This demand is reflected in the literature, with most studies focused on recovery of silicon exclusively.

Silver represents the next-most valuable material present in PVs and is crucial in green energy technologies due to its high electrical conductivity [243]. Approximately half of all silver ever mined has gone to industrial uses and ended up on landfills [243] and industrial silver usage operates at a deficit with respect to silver mining. In 2010, 28000 tonnes of silver was used, which was 6000 tonnes more than was mined [243]. This deficit is balanced by recycling and drawing silver from ground stocks.

Silver demand is only expected to increase, with green energy applications representing the most rapidly growing area for silver demand [243]. Silver is one of the most process-critical raw materials for PV manufacturing, accounting for over 7% of all silver manufacturing in 2014 [229] and predicted to rise to 20% by 2028 [229]. Furthermore, it is forecasted that, by 2024, silver manufacturing demand will exceed that both by silver mining and recycling [229]. To combat the future supply issues, a three-pronged end of life management plan has been developed for PVs: Firstly, silver consumption is to be reduced with an eventual goal to replacement with a substitute material – likely copper [243]; secondly, PVs exhibiting early failure are to be repaired and resold; finally, recycling processes are to be implemented at greater scale [230].

Clearly, demand for improved recycling of silver supplies is imperative to keep up with the demands of a green technology-focused society. As such, recent research in PV recycling has incorporated the recovery of precious metals (particularly silver), table. 7.2. However, these methods possess a common and important problem. The major downside to currently

investigated recycling techniques revolves around the leaching agents use in the hydrometallurgy stages of the recycling processes. The most commonly used agents include nitric acid and hydrofluoric acid which are highly toxic and require extensive and costly treatment and disposal measures. [227, 239]. The common use of pyrometallurgy as an initial step in module decomposition also produces toxic gases which require extensive management. Moreover, the recovered material is often of a relatively low purity compared to the raw materials [227].

To combat these issues, *Zante et al [201]* demonstrated the use of deep eutectic solvents (DESs) and brines as a selective and environmentally friendlier alternative solution for etching of PV cells for silver and aluminium recovery. The PV cells used in this study were the same presented in the materials and methods and results sections, below, and were donated by the University of Glasgow. In a two-step leaching process, the authors reported the ability to selectively etch aluminium and silver using water, and a brine consisting of  $\text{ChCl} : 4\text{H}_2\text{O}$ , respectively. With the addition of an iron (III) chloride redox catalyst at a concentration of  $0.5 \text{ M/dm}^3$ , complete recovery of aluminium was reported after 1 minute when the PV was sonicated in a 150W, 37 kHz ultrasonic cleaning bath. Complete removal of silver was reported after 10 minutes.

This chapter summarises the initial investigation into the use of high-power ultrasonics as a means of enhancing the rate of silver delamination from PV cells. The results of this initial study were presented as evidence for the accepted grant proposal – A proactive Approach to the Recovery and Recycling of Photovoltaic Modules (APOLLO) funded by the European Commission: Programme – Horizon Europe Framework Programme, Topic – Recycling end of life PV modules (HORIZON-CL5-2022-D3-03-09).

The aims of the topic are as follows:

- Demonstrate efficient, low-cost, emerging recycling technologies for PV modules/products.
- Increase recyclability and minimise the environmental impact of PV technology.
- Introduce new business models and open new markets in PV recycling.
- Reduce dependency on primary raw materials through the circular use of resources, sustainable products and innovation.
- Strengthen domestic sourcing of raw materials in the EU.

### 7.1.6 Materials and methods

#### PV samples

The PV cells were composed of 100  $\mu\text{m}$  thick silicon wafer, coated with a  $< 100$  nm silicon nitride anti-reflective layer on the front side (fig. 7.11 (a)) and a 20  $\mu\text{m}$  thick aluminium layer on back side (fig. 7.11 (b)). Both sides contain silver electrode strips in the form of thin lines interspersed between thicker silver busbars. The height of the silver busbars was approximately 20  $\mu\text{m}$ . The whole PV cells were diced, using a diamond-tipped glass cutter, into sections approximately 2 cm  $\times$  2cm which contained at least one whole silver busbar.

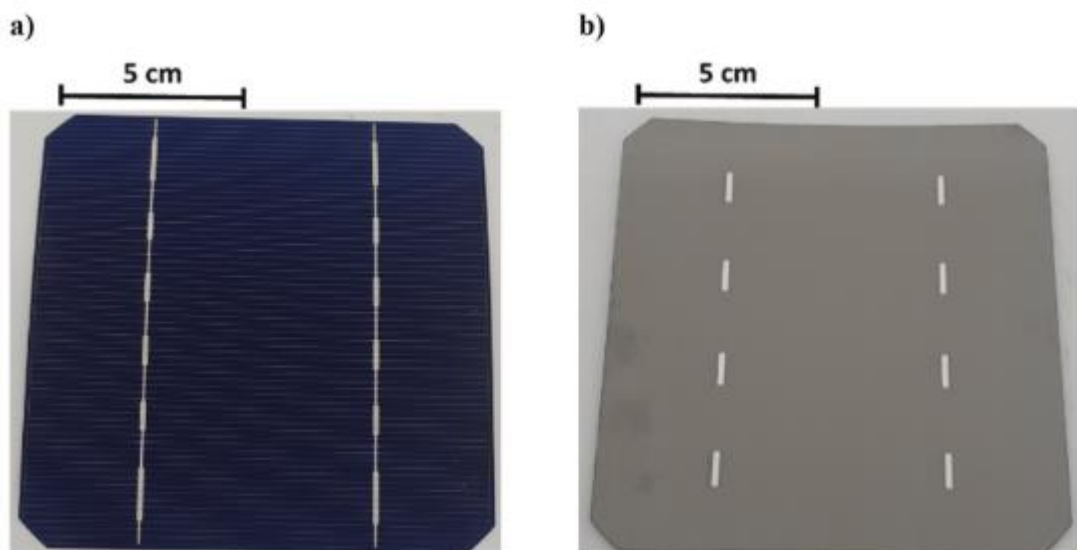


*Fig. 7.11: photograph of whole PV cell from (a) front side and (b) back side. Taken from [206].*

## Solvent preparation

The solution used was a brine, rather than a DES, and was utilised as opposed to Ethaline due to initial studies at the University of Leicester department of Chemistry suggesting its advantage of greater silver etching speed.

The brine used was a mixture of choline chloride (ChCl) and water in a 1:4 molar ratio. The brine was mixed at 60°C with a magnetic stirrer until a clear homogenous liquid was formed. A redox catalyst of anhydrous iron (III) chloride ( $\text{FeCl}_3$ ) was added at a ratio of 0.5 M/dm<sup>3</sup>. This concentration equivalent to that used by *Zante et al* [201] and was able to achieve optimal chemical stimulation whilst maintaining adequate opacity of the liquid to facilitate HIS.

## Experimental setup

The same Branson sonotrode used in Chapters 5 & 6 was utilised for this study. To recap, this was a 450 W, 20 kHz sonotrode operating through a 6.4 mm-Ø tip.

High-speed imaging of the cavitation activity at the vicinity of the sonotrode tip was undertaken with the same Fastcam SA-Z 2100K (Photron, UK), as described in previous chapters, imaging through the same macro lens as described in Chapters 5 and 6 at a frame rate of 20 kfps. Illumination was provided by a 150 W halogen lamp (Thorlabs, UK) coupled to a liquid light guide and collimating lens.

Sonications were performed at a tip height of 10 mm (estimated from the HSI). Sonications and HSI were initiated manually for a total of 10 s. A total of five samples were analysed at a single input power of 80%.

## **Microscopy and profilometry**

2D surface microscopy of the samples after a 30 s sonication were gathered using a Motic AE2000MET inverted microscope through a  $10\times$  lens, connected to a 3MP camera (Moticam S3) for immediate delamination identification.

For total delamination measurement over the full sonication investigation. PV samples were removed after two minutes of accumulated 10 s sonications, washed in deionised water and scanned with an Alicona Infinite Focus G4 3D surface profilometer (Bruker-Alicona, Graz Austria). Surface microscopy and profilometry was obtained through a  $5\times$  lens (Bruker-Alicona) for every sample. 2D surface microscopy of samples before and after sonication allowed for quantification of delamination via a bespoke imaging thresholding macro in ImageJ (National Institute of Health, Wisconsin USA).

## 7.1.7 Results

### High-speed observation of silver delamination

Fig. 7.12 is representative frames from a HSI sequence capturing delamination of small silver fragments at the start of sonication of the second minute for sample 1.

At the onset of sonication, cavitating bubbles impact upon the surface. Shortly after, apparent small fragments (observable as the brightest spots, reflecting the light from the illumination source) are displaced from the cavitation region below the sonotrode tip. After 300 ms, the busbar appears to exhibit removal of some surface silver.

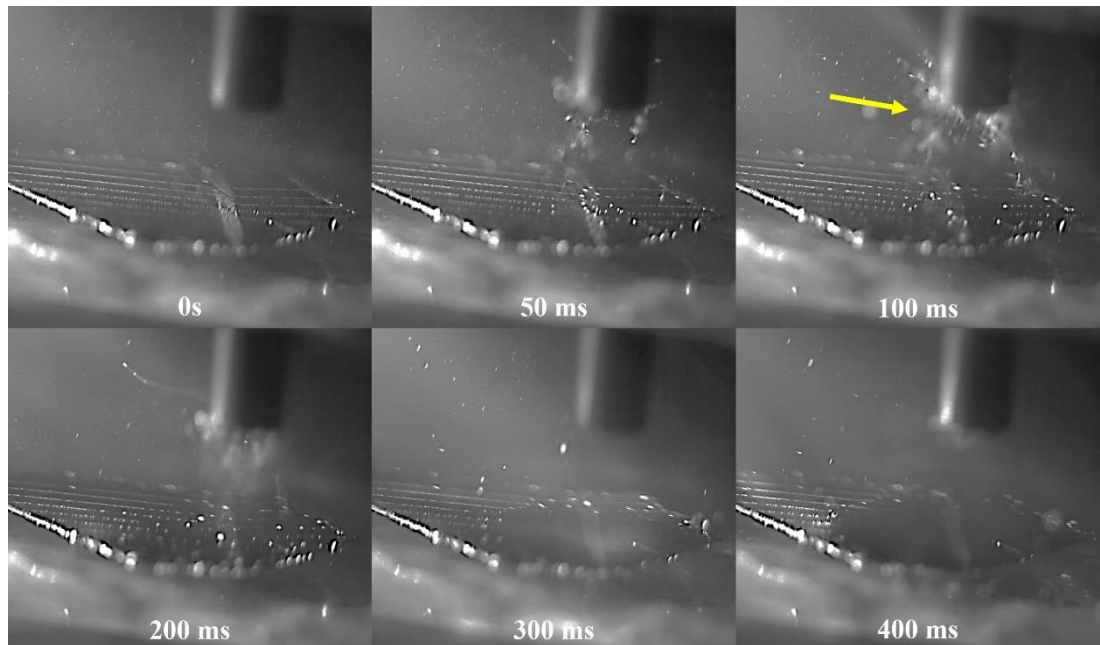


*Fig. 7.12: Extracted frames from a HSI sequence of etching of a silver busbar on the PV sample over initial 400 ms, cavitation activity at the sonotrode tip arrowed yellow. Scale provided by the 6.4 mm- $\varnothing$  sonotrode tip.*

### Overview of initial silver delamination on PVs after sonication

The results in fig. 7.13 present 2D surface microscopy of the PV section under sonication in fig. 7.12 after 30 s of sonication. The initial delamination behaviour manifests as pitting across the surface of the silver busbar. These pits range from 30 – 60  $\mu\text{m}$  in diameter and appear to be caused by the direct jetting and cavitation on the surface of the PV cell.

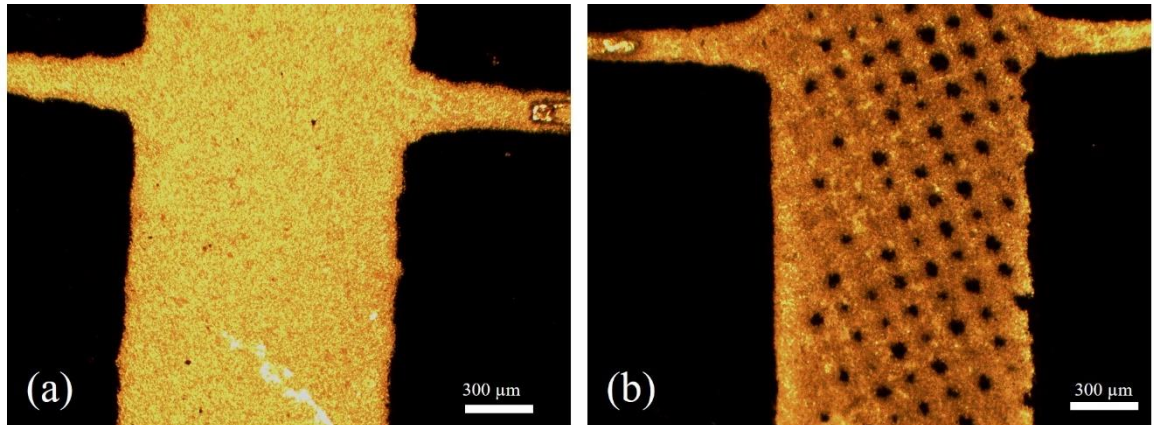


*Fig. 7.13: Surface 2D microscopy of the silver busbar after 30 s of sonication, characterised by pitting of the silver busbar.*

### Delamination over full two-minute sonication

The results in fig. 7.14 present 3D (a) and 2D surface (b) microscopy of a section within the silver busbar taken after the two-minute sonications of sample 1. Total silver delamination over the entire length of the silver busbar was difficult to quantify due to the size of the busbar and the limited resolution of the microscopy. Hence, delamination over representative sections equivalent to the spacing between the parallel silver lines, perpendicular to the main busbar was investigated. This length was 2 mm.

After two minutes of sonication, over 80% of the silver has been delaminated from PV. The region of delamination is directly related to the zone of cavitation, limited to the diameter of the tip. Average delamination of the silver sections after 2 minutes of sonication across the five samples analysed was  $83 \pm 12\%$

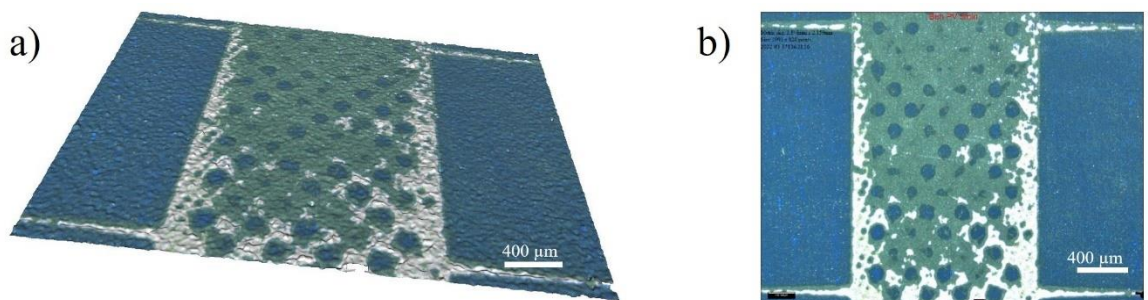


*Fig. 7.14: (a) 3D microscopy of the PV cell after sonication for two minutes for sample 1. (b) 2D surface microscopy of the PC cell after sonication for two minutes for sample 1.*

### 7.1.8 Discussion and future work

The preliminary investigation into the utility of high-power ultrasonics as a means to delaminate silver from spent PVs was conducted. Results suggest that the cavitation generated at the tip of the sonotrode aids in delamination of silver at the focus of the cavitation. Initial delamination appears to be generated in the form of pitting of the silver surface from direct bubble/surface interaction through jetting. Following the initial weakening or opening of nucleation sites, it appears that larger areas of silver are delaminated over the duration of the sonication. Although apparent fragments of silver are shown in the HSI of fig. 7.14, the majority of silver would be expected to be dissolved in the etching solution and recovered via dilution and filtration in a secondary process. Thus, the addition of ultrasound is also likely aiding in delamination rate by increasing mass transport effects around the region of the sonotrode tip.

However, as the cavitation is highly localised under a sonotrode, this rate enhancement is only localised to the region under the sonotrode tip. *Zante et al* demonstrated that, although ultrasound enhanced the rate of aluminium recycling, the use of ultrasound for silver etching was less beneficial [201]. Although silver etching was enhanced via the application of ultrasound in a cleaning bath, it was not significantly faster than stirring the liquid. With the low quantity of silver (around 5 mg) on the PV cell, the etch rate is relatively comparable using both methods, with the ultrasonic cleaning bath producing around a 15% greater silver etching speed. It should be noted that the use of the ultrasonic cleaning bath is likely not the most efficient system for this work owing to its volume relative to the PV cell and a more targeted source of cavitation would likely enhance the delamination in a similar fashion to that observed for PCBs and LiBs. Furthermore, the use of ultrasound allows for the removal of external heating sources that require much more energy to operate. Ultrasound at room temperature was shown to leach 100% of the aluminium from PVs compared to just 17% when stirring [201]. This increase is associated to the greater leaching kinetics achieved by

the ultrasound at least in part due to the cavitation on the surface. When stirring, to achieve the same effect as with ultrasonics, heating to over 50 °C is required. Additionally, with the use of any ultrasonic source, inherent heating will occur due to energy dissipation into the liquid.

A major issue observed through this preliminary investigation was the fragmentation of the PV cells under the sonotrode. Given that the PV cells are in the order of 100 µm thick, the pressures generated by the sonotrodes resulted in the shattering of several of the PV samples. Where this may not be an issue for overall silver etching (given that the PV surfaces will still be exposed to the etching solution), it will limit the effectiveness of the cavitation. From this investigation, although the utility of a high-power sonotrode was demonstrated for silver delamination from PVs, it is noted that future work for development of an optimised system PV etching is required. Research within CavLab is currently under development for a flow-based system comprising a series of concentric tube transducers. Early results indicate strong cavitation capable of material processing.

Further optimisation is needed with respect to the etchant used in this study. Compared to the cost of leaching with nitric acid, the cost of the choline chloride brine used in this study is  $8 \times$  greater, due to the high quantity of choline chloride [201]. Although *Zante et al* proposed an alternative to choline chloride that was also able fully etch silver from the PV, crucially at a lower cost than conventional acid-based processes [201].

At present, due to the low silver content within the PV cells (0.26 wt%, \$2.1 per kg) and the low value of aluminium (\$0.3 per kg), the recovery of metals from these PV cells is not an economically attractive process [201]. However, the leaching process adopted in this and the *Zante et al* study has potential to be made auto-catalytic which would greatly bring down the cost associated with oxidising agent quantities required, additionally reuse of the solvents over several cycles is viable. Furthermore, no optimisation with respect to the ultrasonic parameters have been performed. Through investigation into target-specific

ultrasonic sources, a cost-effective process for extraction of the precious metals from PVs may yet become viable. With the volume of PV waste set to exponentially rise, development of green, efficient recycling methods to handle demand is of significant interest.

## 7.2 Using ultrasound to increase metal dissolution and prevent passivation using concentrated ionic fluid.

### 7.2.1 Introduction

Electrodeposition and dissolution of metals is typically diffusion limited and this controls the dissolution rates and surface morphology. The electrolyte can also result in the passivation<sup>7</sup> of some metals where mass transport is slow. The rate of mass transport (of the electrolyte) to the electrode surface can be increased by the addition of motion. For example, using a rotating disc electrode, the rotating working electrode introduces a localised flux, allowing for enhanced mixing and removal of insoluble passivating layers [244]. The rate of rotation offers some control of the electrolyte flux of the process [245]. Further increases to mass transport can be achieved with the addition of laminar and turbulent flow [246]. Furthermore, electrochemical modification using jets has demonstrated utility for both electrodeposition and micromachining [247, 248]. This has led to the enhancement of localised etching on surfaces which are useful for micromachining.

The use of ultrasound as a means to introduce forced convection into electrochemical reactions has recently gained interest [249]. With acoustic streaming and cavitation-associated phenomena such as jetting and bubble-collapse shockwaves thought to be the driving force behind this [250]. Acoustic streaming generates mixing within the bulk electrolyte, leading to a reduction of the diffusion layer at the electrode surface [251] which can be tailored by alterations such as input power of the ultrasonic driving [252] and separation distance between ultrasound source and electrode [38].

Most electrochemical studies of forced convection have focused on electrodeposition due to its importance in electroplating [253]. However, electrodisolution is an important process for electropolishing and refining. Furthermore, the majority of electrochemical studies are

---

<sup>7</sup> Passivation refers to the altering or coating of a material (often metal) surface to make it unreactive.

carried out in aqueous solution. However, an increase in research into DESs and ionic liquids has been observed due to their ability for tuning specific redox chemistries [146]. The drawback of DESs remain the relatively high viscosities, which are known to limit the rates of electrochemical processes [200, 254]. Some limited study into electrodeposition in DESs has been performed [255] which demonstrated a 200-fold increase in deposition rate when compared to silent electrodeposition. Thus, the principal objective of this study was to demonstrate the utility of high-power ultrasound on the enhancement of electrodisolution of copper and nickel in a DES electrolyte.

## 7.2.2 Materials and methods

### DES preparation

The DES solution used was Ethaline, prepared and stored in the same manner as described in Chapter 3, §3.1.

### Anodic linear sweep voltammetry

Anodic linear sweep voltammetry (LSV) experiments were performed at 20 °C, using a Metrohm Autolab PGStat302N potentiostat, operated by the corresponding Nova 2.1 software. A three-electrode setup was adopted, consisting of a 1.25 mm-Ø hooked copper or nickel disk working electrode; a copper or nickel wire reference electrode (corresponding to the working electrode); and an IrO<sub>2</sub> coated Ti mesh as counter electrode. LSV measurements were recorded at scan rates between 10 and 100 mV.s<sup>-1</sup>.

### Experimental setup

The electrode surface was positioned approximately 4 mm below the tip of the Sonics sonotrode. To summarise – operating at 20 kHz, 500 W with data collected over 1 s sonications. HSI was collected at a frame rate of 80 kfps by the same Photron Fastcam and laser illumination configuration used throughout this thesis. This setup is the same as that used in previous chapters, with respect to sonotrode/sample positioning and Photron high-speed camera orientation, see for example Chapter 5, fig. 5.1.

### 7.2.3 Results and discussion

This results and discussion section presents an overview of the principal results and conclusions generated in this study. With a particular focus on the experimental data collected by the author at the University of Glasgow. Key results necessary to outline the purpose and outcomes of this study are presented.

#### Linear sweep voltammetry

A brief overview of linear sweep voltammetry (LSV) is given in Appendix D.

The electro-dissolution of the two investigated metal electrodes – copper and nickel – under both silent and sonicated conditions in Ethaline are presented in fig. 8.1.

Briefly, the results manifest and can be interpreted as follows: under silent conditions, the copper surface undergoes a passivation process due to the formation of insoluble copper species. While nickel oxidation shows a slower formation of a passivating layer, likely from the formation of nickel species, before dropping off completely, suggesting a more solid non-conductive layer has formed [254]. Under sonication, the LSVs do not exhibit a decrease in current from passivation of the electrode surface. The current density for copper and nickel has increased from  $\sim 20 \text{ mA.cm}^{-2}$  to  $\sim 270 \text{ mA.cm}^{-2}$  and from  $\sim 10 \text{ mA.cm}^{-2}$  to  $\sim 300 \text{ mA.cm}^{-2}$ , respectively at an overpotential of 1.4 V. this equates to a 14 and 30-fold increase, respectively. The results from fig. 8.1 can determine that sonication provides a clear increase in mass transport to and from the electrode surface, reducing the surface concentration and ensuring the layer close to the electrode does not become super-saturated with metal ions.

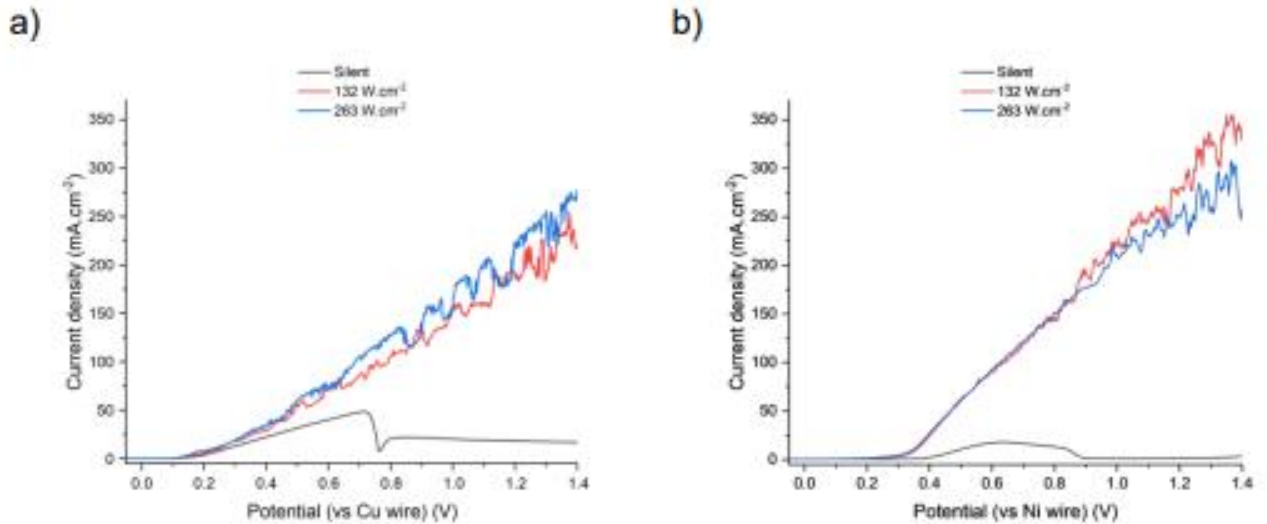


Fig. 7.15:(a) LSV of copper electrode in Ethaline run in silent and ultrasonic conditions. (b) LSV of nickel electrode in Ethaline run in silent and ultrasonic conditions. Taken from [261].

### High-speed observations

Simultaneous HSI of the cavitation activity generated at the electrode surface during the LSV measurements were recorded in order to relate the improved LSV results generated by sonication to the real-time observations during measurement.

Fig. 8.2 presents frames extracted from a 1 s sonication on the copper electrode comparing to the LSV data of fig. 8.1 (a), showing specific cavitation activity and development of acoustic streaming during the sonication. The sonication initiation is followed by a downwards stream of bubbles from the centre of the sonotrode tip. This bubble cloud collides with the electrode surface and forms a densely packed bubble vortex (observed at 12.66 ms), with corresponding acoustic streaming forcing fluid down and outwards from the centre of the electrode [14, 202]. The addition of microstreaming (fluid circulation in the vicinity of bubbles, generating turbulence and improving mixing [14] from bubble clouds facilitates sustained flow away from the electrode surface which results in increased mass transport throughout the sonication. Additional cavitation-related phenomena such as bubble-collapse

shockwaves and jetting further enhance the process and are believed to be the source of the current density spikes in the LSV data of fig. 8.1 [178]. However, further study of the relationship between the frequency of these spikes and the cavitation activity is required. Fig. 8.1 (a) appears to present a series of ‘dips’ that could be related to periodic emissions. Addition of acoustic detection, matched with identification of the frequency of occurrence of these dips in the LSV (which will require comparable sweep rates) could further elucidate the relationship between the sonication and LSV spikes. Bubble-collapse shockwaves, originating from violently collapsing bubble clouds near the sonotrode tip (arrowed yellow, fig. 8.2) were previously reported as important for material delamination [58]. Jetting, which occurs when a bubble deflates and collapses asymmetrically in proximity to a rigid surface, is observed (inset at 28.01 ms) from single bubbles within a millimetre of the electrode layer. In fig. 8.2, the non-spherical bubble has involuted from the bulk-Ethaline side, indicative of a thin column of liquid that rapidly traverses the gas phase, to impact the electrode surface. This jetting has previously been shown to cause micron-sized surface erosion, or pitting, and removal of passivating layers [204, 256] as well as being key for metal delamination from printed circuit boards [257]. As the sonication develops, the bubble cloud continues to expand, with a greater density of smaller bubbles occupying the region between sonotrode tip and electrode. This cloud is sustained, with smaller bubble sub-clusters directly impacting the electrode surface throughout the sonication.

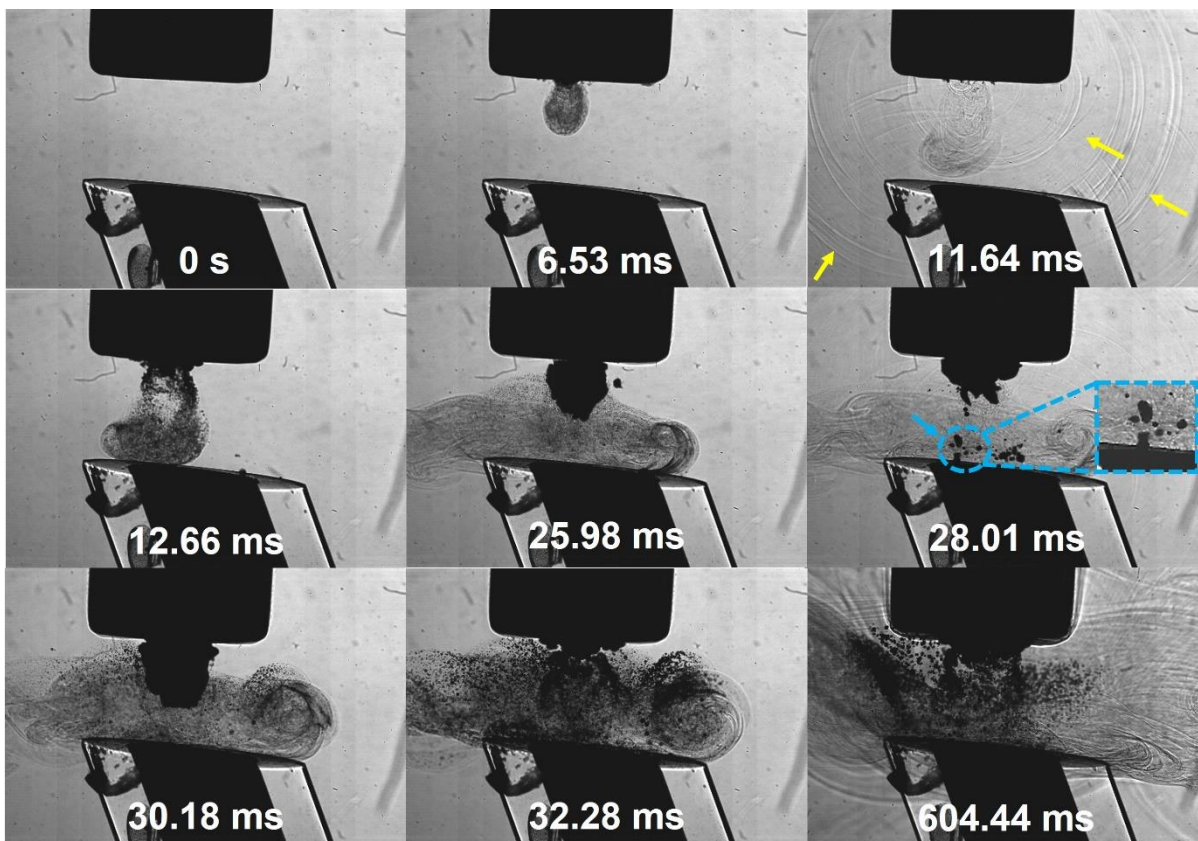


Fig. 7.16: High-speed imaging sequence of cavitation onset and development at the electrode surface. Bubble-collapse shockwaves are arrowed yellow and jetting bubbles on electrode surface arrowed blue. Scale provided by the 6 mm- $\varnothing$  tip. Taken from [258].

## 7.2.4 Conclusions

The addition of high-power ultrasound to the electrodisolution of copper and nickel in Ethaline was investigated in this study. Under silent conditions, both copper and nickel LSVs indicate the formation of a passivating layer, causing extensive reduction in the current density and mass transport rate. Conversely, under sonication, there is no indication of passivation. The application of ultrasound increases mass transport of normally passivating species away from the active surface by the presence of acoustic streaming and cavitation mediated effects such as microstreaming. Further effects such as bubble-collapse shockwaves and jetting are, at least in part, responsible for erosion of passivating layers and pitting on the electrode surface.

## 7.3 Mass and heat transfer in bubble driven by audible sound

### 7.3.1 Introduction

During bubble collapse the contents of the bubble are highly compressed, resulting in transient high interior pressure and temperature [14]. Under these conditions, the gas molecules contained within the bubble decompose into a set of unstable, reactive compounds. These compounds then recombine to form new molecules following complicated chemical reactions, which offer potential for a number of applications in the development of chemical species. Thus, easily controlling and replicating the collapse process is of interest.

Subjecting the bubble to sound pressure is a well-established method for forcing a gas bubble to undergo repeated spherically symmetrical oscillations. The nature of these oscillations, and correspondingly the extent and nature of the chemistry within, vary depending on bubble size, drive amplitude and drive frequency. With frequency being the main focus of this study. Very few studies have been conducted in the audible frequency range (below 20 kHz). In 1936, shortly after the first reported empirical investigations into the chemical effects of ultrasound [259], *Flosdorf et al* [260] experimentally investigated the effect of audible frequency sound on various oxidation processes. Despite the authors detecting sonically activated chemical activity well below 20 kHz, research within the audible frequency range did not expand. It is much easier to operate at a laboratory-based level at higher frequencies due to the associated wavelength at higher frequencies allowing experimentation in much smaller volumes of liquid. Nonetheless, *Mason* [41] argued that one strong future avenue for the advancement of sonochemistry is the expansion into lower frequency ranges, where these larger wavelengths invite interesting possibilities with regards to industrial scalability. Only very recently, have studies into the audible frequency range generated any attention. *Pandit et al* [261] reported on the chemical and physical effects of cavitation by modelling of single

cavitating bubble dynamics, with results investigating a sweep of input frequencies starting at 5 kHz, using a reduced-order model to perform the large parametric sweep of parameters.

Models based on the solution of the full set of equations governing the dynamics of the considered phenomenon are computationally demanding to perform. Hence, reduced-order models offer a time efficient solution. However, reduced-order models must only be implemented within their range of validity. Such a range can be established by either comparison with appropriate experimental data or the full set of governing equations, the numerical solution to which is referred to as the direct numerical solution (DNS).

The principal objective of this study was the development of a new and accurate model which incorporates heat and mass transfer within the bubble, valid for collapsing bubbles. The accurate simulation of both effects is fundamental to understanding and simulating the resultant chemistry within the bubble. Importantly, the implementation of these models to the audible frequency range was performed.

### **Model summary**

In total, three mathematical models were presented and compared against one another, and against the experimental observations<sup>8</sup>. Of these models, a new hybrid model (HM) was developed with the rationale that the HM was a reduced-order model, aimed at simplifying the traditionally complex bubble modelling equations. Furthermore, the HM was compared to a traditionally used reduced-order model.

Firstly, a form of the advection-diffusion equation [262] is retained and solved for implementation into the advection-diffusion model (ADM). This is a highly computationally intensive model but would be expected to generate the most accurate results, through proper treatment for both heat and mass transfer in the gas phase. Secondly, a reduced order method

---

<sup>8</sup> Note – all mathematical modelling was performed by first author Davide Masiello and supervisory team

called the boundary-layer model (BLM) is employed. This reduced-order model has previously been utilised for modelling of mass and heat transfer [261, 263, 264]. However, its lack of validity at low frequencies leaves the necessity for further investigation into its accuracy in the audible range. Finally, the HM was developed combines aspects of the previously mentioned models.

The mathematical modelling considered the presence of a single spherical bubble of a given radius, at rest and completely surrounded by a liquid of infinite extent, free from boundaries. The bubble was assumed to contain a mixture of non-condensable gases and the vapour of the surrounding liquid. The results generated in this study were only over one acoustic cycle.

### 7.3.2 Materials and methods

A schematic representation of the experimental set-up is shown in Fig. 8.3. The system is composed of a Shimadzu HPV-X2 high-speed camera (Shimadzu, Kyoto Japan), imaging at a temporal resolution of  $2 \times 10^6$  fps over a duration of  $128\mu\text{s}$ ; a MonoZoom 7 objective lens (Leica microsystems, Wetzlar Germany); a levitation cell (where the bubble is formed and kept stable); a 17.885kHz Langevin transducer; and a synchronous (to frame capture) 10ns pulsed laser at 640nm (CAVILUX Smart UHS, Cavitar, Tampere Finland), coupled to a liquid light guide and collimating lens to facilitate shadowgraphic imaging for back illumination [24].

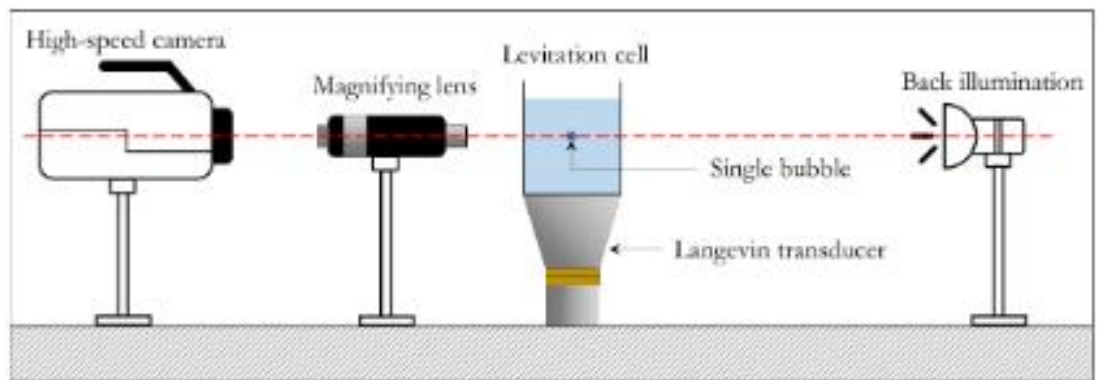


Fig. 7.17: Schematic representation of the experimental apparatus setup. Taken from [267].

The levitation cell is cubic in shape and made out of a 2 mm thick polycarbonate sheet, which is sufficiently transparent to allow high speed imaging and robust enough to resist the acoustic vibrations. Other shapes that have been used for levitation cells are spherical and cylindrical shapes [39, 265]. At the vessel fill depth of around 83mm, a standing wave develops due to reflection of the transmitted acoustic wave from the water surface. The acoustic standing field is established by the Langevin transducer, bonded to the bottom of the vessel using araldite, driven at 17.885 kHz with a sinusoidal wave generated by a standard digital function generator (FeelTech, Zhengzhou China), passed through a 250V piezo-amplifier (with a voltage gain of 20 V/V).

The experimental procedure is as follows. A water droplet is dropped from a height into the levitation cell, which is filled with degassed water. The droplet impact with the water surface entrains air creating a few bubbles, the largest of which will rise back to the surface. The smaller bubbles instead migrate to the acoustic pressure antinode positioned at the centre of the cell [266], where they finally merge into a single bubble which is stable against further translational motion, due to the tweezing effect of the acoustic standing wave. Once the bubble is formed, high-speed images of its oscillations are taken which is aligned in plane of the centre of the cell.

This process does not guarantee a strict reproducibility of the bubble size. Experimental apparatuses for the production of single micro-bubbles of reproducible sizes have been proposed before [21, 53, 73], and are demonstrated in this thesis (Chapter 4) but they rely on laser-induced nucleation to generate their bubbles with their set up being fairly complex. Thus, the primary authors adopted this acoustic method of single bubble generation. The trial-and-error procedure required for the bubble formation in the apparatus used in this work proved to be sufficiently good to obtain satisfactory results, nonetheless.

The camera field of view was calibrated using a probe of known diameter, thus allowing for determination of the spatial resolution. Then, each high-speed frame in the imaging sequence was processed as summarised in fig. 8.4. The camera takes grayscale images (fig. 8.4 (a)), which are then converted to binary images by replacing the pixels in the original image with luminescence greater than a certain normalised threshold with the value 0 (black) and replacing all other pixels with the value 1 (white) (fig. 8.4 (b)). The binary image is then processed with a boundary tracing algorithm to find the relative coordinates of the gas-liquid interface. The algorithm (who's specific generation and properties were kept to the primary author) requires the specification of a starting point on the interface. Since the bubble is stable to translation, its central point is the same throughout the image sequence. The set of coordinates locating the interface pixels is generated (fig. 8.4 (c)) and it is used to perform a count of the pixels included in the bubble, which yields the bubble area and radius.

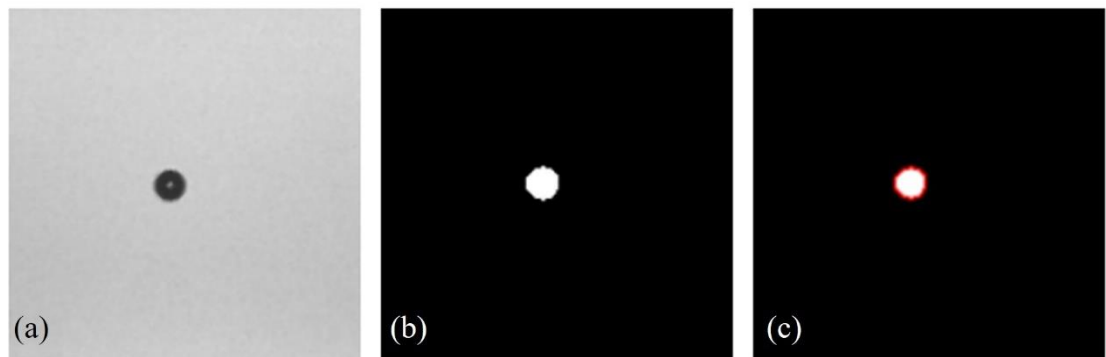


*Fig. 7.18: Representation of (a) original grayscale image, (b) thresholding operation to segment bubble and (c) detected bubble boundary. Taken from [267].*

Bubbles formed with the technique described can be very stable and survive for several hours, even when collapsing inertially at higher driving pressure amplitudes. However, it was also observed that after several tens of minutes, shape instabilities can arise producing non-spherical bubble shapes together with the associated phenomenon of bubble ‘dancing’, which is a widely studied area in itself (see, for example, [267-270]). Here, we only consider the high-speed imaging sequences taken shortly after the bubble formation in order to ensure that the bubble is still spherical, which is one of the main model assumptions.

### 7.3.3 Results and Discussion from experimental validation

This results and discussion section presents an overview of the final comparison between the experimental observations obtained and the mathematical modelling generated. Only the experimental observations were generated at the University of Glasgow and were the main focus of this authors interest.

The HSI sequence presented in fig. 8.5 was used as the experimental dataset to which the mathematical models generated in this study were compared. Here, a BCSW is observed at  $0 \mu\text{s}$  with subsequent oscillation and growth to a maximum radius at around  $52 \mu\text{s}$ , followed by subsequent collapse at  $56 \mu\text{s}$ , equivalent to one period of oscillation.

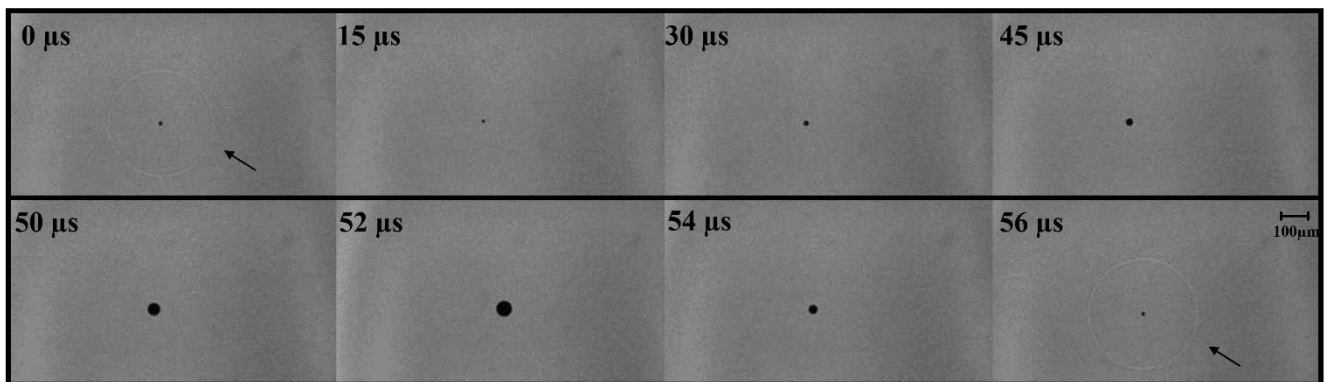


*Fig. 7.19: Representative frames from a high-speed shadowgraphic sequence at 4 V, captured at 2 Mfps, over one cycle of bubble oscillation.  $t = 0 \mu\text{s}$  is defined by the frame closest to the moment of the first bubble collapse captured, confirmed by the emission of a shockwave (arrowed). The successive collapse at  $56 \mu\text{s}$  corresponds to the period of the driving acoustic field. Taken from [262].*

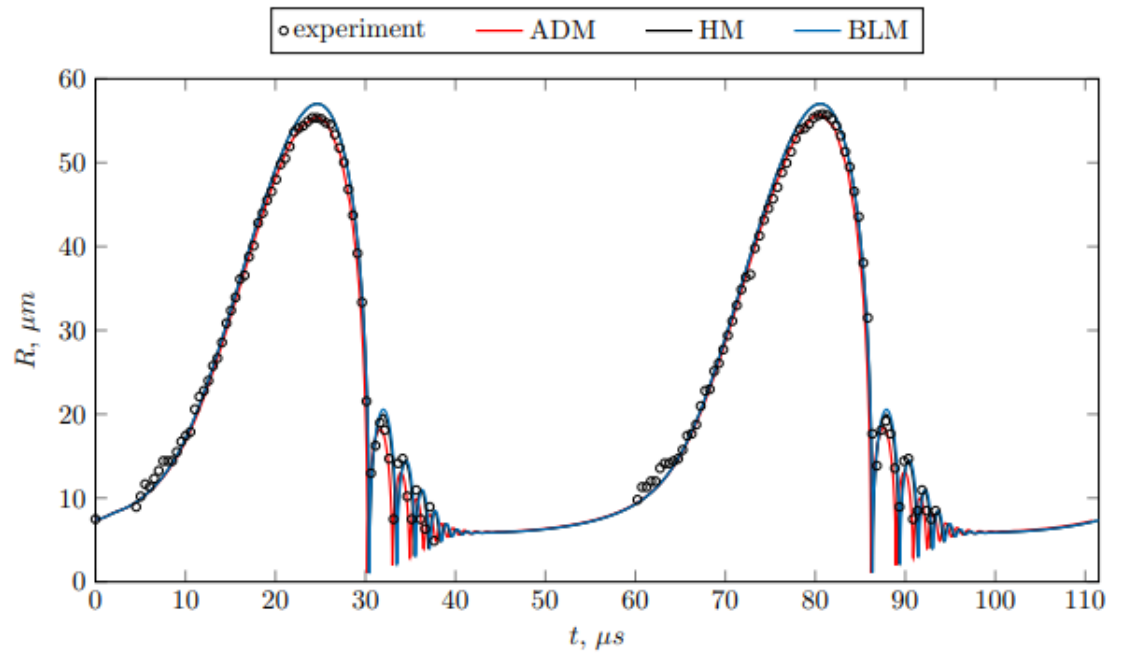


Fig. 7.20: Comparison between experimental data and simulated models at drive frequency,  $f_0 = 17.885$  kHz and  $R_0 = 7.5$   $\mu\text{m}$ . Experimental data taken from dataset represented in fig. 8.5. Taken from [262].

As can be observed in fig. 8.6, the oscillating bubble undergoes an initial expansion to a maximum radius size of approximately 55  $\mu\text{m}$ , followed by a collapse which produces a shockwave (fig. 8.5). Following initial collapse, the bubble undergoes a series of rebounds before the cycle repeats. At this input voltage (4.0 mV), the bubble collapses every cycle ( $T_0 = 56$   $\mu\text{s}$ ).

The most accurate (and most complex) was the ADM, with the precise fitting of this model to the experimental data suggesting the theoretical arguments proposed in the paper are valid and correct. The HM predicted a slightly larger maximum radius during the initial expansion with corresponding rebounds presented slightly out of phase relative to the experimental and ADM results. The BLM produced a similar trend, with respect to over-estimation of radius and presentation out of phase, with the magnitude of each slightly greater than the HM. The over estimation of maximum bubble radius was attributed to the BLM over-estimating the boundary-layer thickness, thus over-predicting the amount of water trapped in the bubble

during collapse [262]. However, each of the three models present an reasonably good prediction of the bubble dynamics. The results presented reinforced the motivation to expand bubble modelling to the audible end of the frequency spectrum, with generation of new models perhaps more appropriate for modelling at the lower end of the frequency spectrum, which may gain even more interest in the future.

#### **7.3.4 Limitations and future work**

A common main model assumption is the spherical nature of the bubble. Whilst this is apparent in fig. 8.5 and all data used for modelling comparison in this study, non-spherical oscillations are developed. Fig. 8.7 demonstrates the shape oscillation of the collapsing bubble during one acoustic cycle at input voltages below that used in the results of this study, where bubble-collapse shockwaves from a spherically symmetrical bubble were observed. Stable cavitating bubbles exhibiting shape oscillations are of potential interest. *Secker et al* [271] have demonstrated the utility of low amplitude pressure fields on the generation of small bubble pulsations for the removal of biofilms from skin wound models. The authors were able to tune the sound field to stimulate the bubble walls into a rippling effect which was observed on the surface of tissue and detectable by scattering of high frequency noise [271]. Furthermore, *Coussios & Roy* [272] concluded that shape oscillations arising during stable cavitation provided enhanced drug delivery and thrombolysis [272].

Multi-modal shape oscillations have been observed from acoustically driven microbubbles [269, 270, 273] with mathematical modelling investigating their nature. The temporal evolution of different mode shapes developed has been attributed to nonlinear mode coupling. Generally, the initial spherical oscillation becomes unstable with increased driving amplitude, leading to shape oscillations.

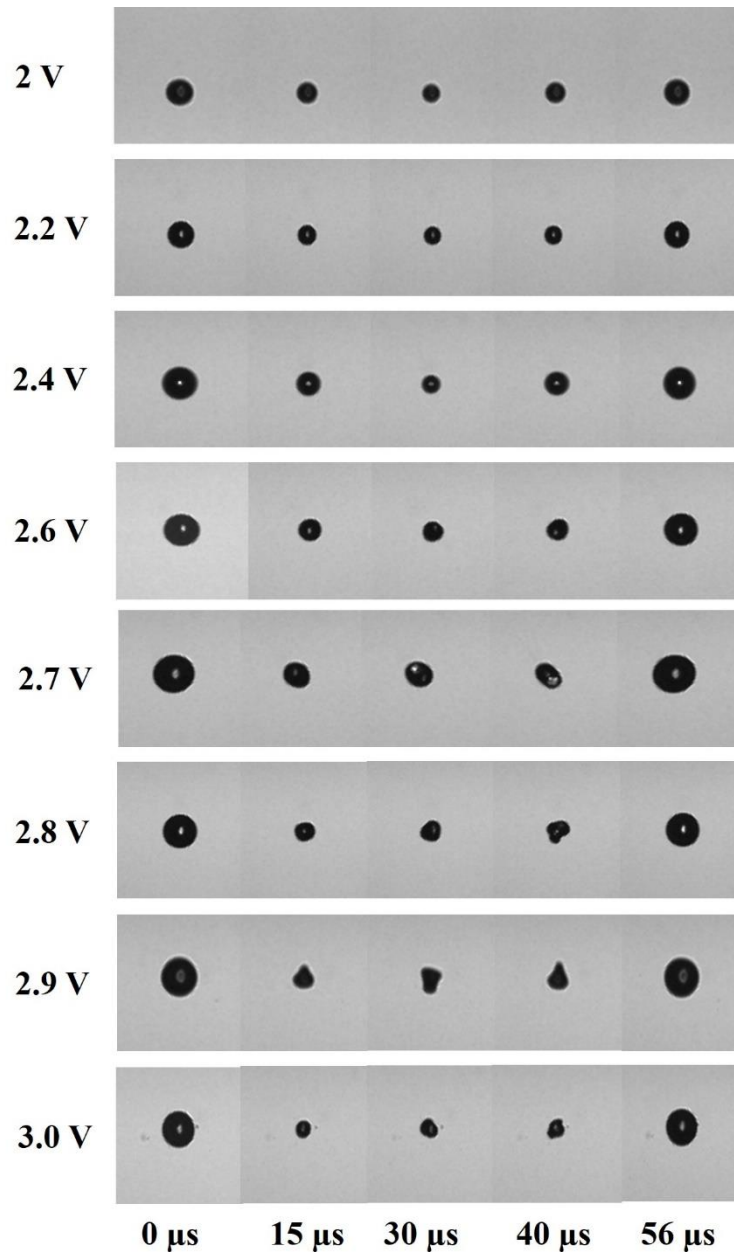


*Fig. 7.21: Single bubble shape oscillations observed over one acoustic cycle at a range of input voltages. Image sequences recorded at 1 Mfps.*

Fig. 8.7 demonstrates the generation of shape modes of the single microbubble as a function of amplitude. These shape oscillations are reminiscent of others observed over a range of altering powers with laser-induced bubbles [269, 270]. Bubble oscillation appears spherically symmetrical at low input voltages. At around 2.6 mV, the bubble appears to deform slightly, noticeable at 40 μs. Further increasing voltage results in a variety of mode shapes characterised by elongation of the bubble (2.7 V at 40 μs) and an almost pyramidal

structure developing (2.9 V at 40  $\mu$ s) reminiscent of jetting and counter-jetting observed from microbubbles under focused ultrasound at 220 kHz [274].

Characterisation of the input parameters associated with generation of these mode shapes could be of particular interest to, for example, ultrasound contrast agents [269] or acoustic cleaning, whereby tuning bubble mode oscillation can enhance liquid microcirculation close to the bubble wall [37, 271] and, crucially, mitigate the negative effects of inertial cavitation such as pitting.

Clearly, the utility in better understanding the generation of particular mode shapes as a function of bubble size, frequency and input power is advantageous. Mathematical modelling of such behaviour may often be adequate, but given the complex nature of these models, coupled with the need for certain assumptions, experimental validation and observations is required. Hence there is rationale for experimental observations, coupled with acoustic measurement via a needle hydrophone, to investigate non-spherically oscillating bubble dynamics below the onset of inertial cavitation.

## Appendix A

### Previous research within CavLab

The cavitation laboratory (CavLab) is dedicated to the study of cavitation generated by a range of ultrasonic transducers and laser sources. With the fundamental tools of these studies being combined high-speed imaging and acoustic detection. Traditionally, CavLab research has been motivated by medical applications of cavitation, involving focused ultrasound on microbubbles or for the understanding of fundamental bubble-collapse phenomena [24, 26, 73]. Recently, however, the industrial applications of ultrasound-induced cavitation have been adopted for CavLab research, both in-house and collaboratively [55, 58]. The investigations carried out in this thesis are predominantly industrially focused. Nevertheless, previous research within CavLab has guided this thesis with key research findings summarised below.

### **An analysis of the acoustic cavitation noise spectrum: The role of periodic shock waves**

*Song, Johansen & Prentice. J Acoust Soc Am. 2016.*

Studying the role of periodic shockwaves (PSWs) generated from bubble collapse is central to understanding the acoustic emission spectrum observed during cavitation. Through the use of laser nucleation<sup>9</sup> [85], a single cavitation bubble/cavitation cloud was placed at the focus of a high-intensity focused ultrasound (HIFU) transducer operating at 692 kHz, at varying pressure amplitudes. Acoustic measurements were detected by a 0.2 mm PVdF needle hydrophone (Precision Acoustics, Dorchester, UK) calibrated over a bandwidth of 125 kHz to 20 MHz. Fig. A.1 (a) and (b) demonstrates the acoustic data, after filtering of the  $f_0$  drive signal and the corresponding emission spectrum, respectively. Experimental data here was generated at an amplitude of  $1.63 \pm 0.12$  MPa. Defined spikes can clearly be

---

<sup>9</sup> Induction of a cavitating bubble using a laser setup is used and described in this thesis in Chapter 5.

observed every second acoustic cycle (fig. A.1 (a)), this is referred to as period-doubling, whereby the inertia of the host medium prevents collapse for every compressive phase of the driving signal [26].

Analysis of the experimental acoustic data was coupled with the generation of a ‘synthetic cavitation signal and spectrum’ [26, 73, 275]. The spectral model confirmed that the spectral features exhibited in the experimental results (fig. A.1 (b)) could be easily attributed to the PSWs, fig. A.1 (c) and (d). Effectively, it was demonstrated that PSWs observed here at double the period of the drive signal ( $2T_0$ ) result in the raising of spectral peaks at integer values of  $f_0/2$ , observed in fig. A.1 (b) as peaks at  $nf_0/2$  for all  $n$ . This was also confirmed at a higher driving amplitude, which elevated the nonlinear response of the bubbles such that the cloud collapsed at  $3T_0$  (or  $f_0/3$ ). Here, spectral features were exhibited at  $nf_0/3$  for all  $n$  [73]. This finding has also been confirmed for cavitating contrast agent microbubbles using the same HIFU transducer [26] and elevated nonlinear response as a function of input power has been documented under a high power sonotrode in water [55].

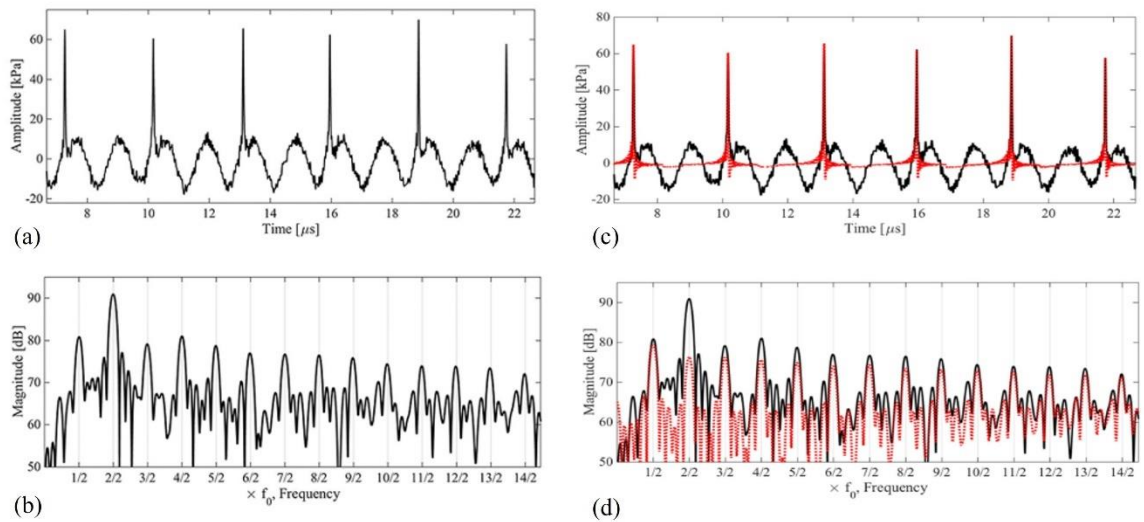


*Fig. A.1: (a) Experimentally detected acoustic emissions from a single cavitating bubble after subtraction of a controlled exposure where no bubble was nucleated. (b) corresponding acoustic emissions spectrum from (a). (c) Synthetic PSW signal (red) overlaid to the experimentally detected signal. (d) Synthetic PSW spectrum overlaid to the experimentally measured emission spectrum. Taken from [73].*

**Performance characterisation of a passive cavitation detector optimised for subharmonic periodic shock waves from acoustic cavitation in MHz and sub-MHz ultrasound.**

*Johansen, Song and Prentice. Ultrasonics Sonochemistry. 2018.*

Understanding of the contributions of PSWs to the cavitation emission spectra led to the development and testing of a swPCD, designed for broadband sensitivity across lower frequency components and high frequency noise.

Objective testing of the swPCD at increment construction stages was undertaken relative to laser-induced BCSWs (equivalent to that reported in Chapter 4) with the final design experimentally compared to a commercially available device, the Y-107 (Sonic Concepts Inc, WA, USA). Manufacturer-supplied information describes this device as a 0.2 mm thick piezo-polymer stack with a high acoustic impedance ( $> 4 \text{ MRayl}$ ) backing. The Y107 has a reported bandwidth of 10 kHz – 15 MHz and is designed to fit within a 20 mm central hole of a HIFU transducer. As such, the design of the original swPCD geometry was equivalent to that of the Y107, with a 15 mm- $\emptyset$  active material front disk. Fig. A.2 demonstrates the final swPCD design.

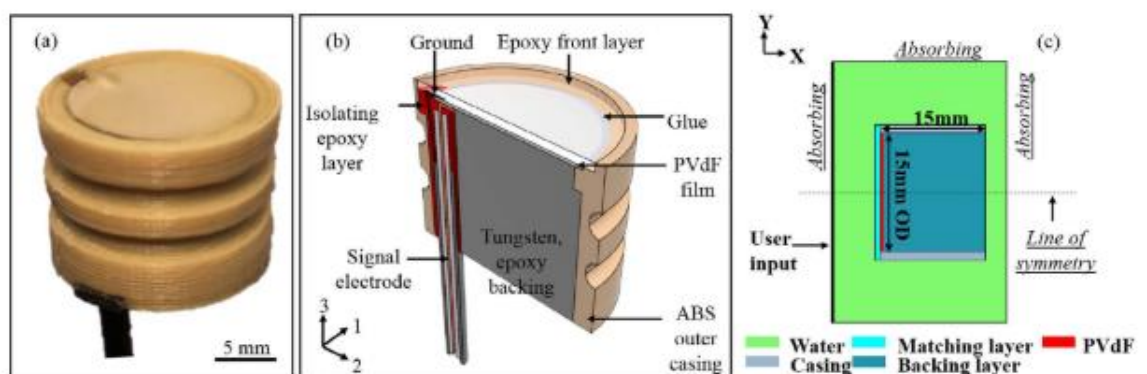


*Fig. A.2: (a) Final swPCD, (b) schematic cross section of the swPCD, and (c) schematic of FEM geometry used to guide swPCD construction. Taken from [69].*

The swPCD design and performance characterisation was simulated using a commercially available finite element method (FEM) software (PZFlex, Glasgow, UK) (now OnScale) for optimisation of the matching and backing layers of the sensor.

The active material of the swPCD was PVdF (as used for the Y-107) of 110  $\mu\text{m}$  thickness, chosen for its sensitivity bandwidth covering the frequencies of interest [25]. The rationale for the range of frequencies of principal interest for shockwave detection were, in part, guided by the results of *Johansen et al* [25].

**Deconvolution of acoustically detected bubble-collapse shock waves.** *Johansen et al, 2017.*

Briefly, in this paper the authors demonstrated the detection of shockwaves emitted by the collapse of a laser-induced bubble (methodology described in chapter 4) using a PVdF needle hydrophone calibrated for magnitude and phase from 125 kHz to 20 MHz, with simulated bubble collapse and shockwave profiles generated for comparison to hydrophone measurements. Through presentation of full waveform deconvolution with complex sensitivity over the calibrated bandwidth of the sensor, it can be observed that the shockwaves exhibited broadband frequency response, with lower end frequencies (below 5 MHz) exhibiting greater power magnitude (fig. A.3).

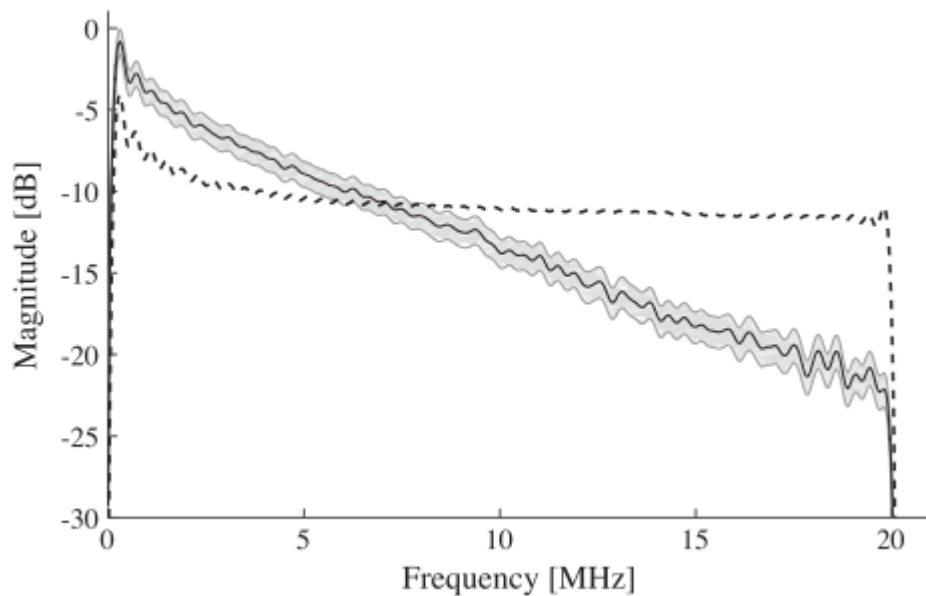


Fig. A.3: Frequency spectra of deconvolved bubble-collapse signal (black and grey envelope) and simulated shock (black dash) Taken from [25].

The swPCD was tuned in FEM by altering the matching and backing layers either side of the active material.

Backing layers act to tune the characteristics of the active material, promoting narrow- or broadband features [276-278]. Three impedance backing layers were tested, as follows: low impedance (air – 0.000425 MRayl), no impedance difference (water – 1500 MRayl) and high impedance (tungsten-loaded epoxy – 9.99 MRayl). The high impedance backing layer was selected due to its improved bandwidth. When the backing layer is of greater acoustic impedance to the active material, then quarter wavelength resonance behaviour is exhibited [279]. This shifts the resonance frequency down, towards the low components in PSWs which are observed to be greater magnitude, fig. A.4.

Matching layers act to increase the transmission coefficient around resonance [276]. A single matching layer to target the subharmonic features in the cavitation spectrum was added to the swPCD, at a quarter wavelength thickness [280]. The exact matching layer material was decided based upon equation A1, which predicts optimal matching layer acoustic impedance ( $Z_{ml}$ ) based on the acoustic impedance of the active material ( $Z_a$ ) and the load ( $Z_l$ ).

$$Z_{ml} = \sqrt{Z_l Z_a} \quad (\text{A1})$$

The final swPCD design was compared to the Y-107 with laser induced single BCSWs and bubble clouds nucleated at the focus of a 220 kHz HIFU transducer both indicating better performance than the Y-107 at frequencies of interest. The swPCD exhibited a  $\sim 30$  dB higher signal to noise ratio (SNR) at  $f_0/2$  and greater sensitivity up to approximately 3 MHz, exhibited in fig. A.4.

The authors noted that the design of the swPCD sacrifices temporal resolution for improved sensitivity. Furthermore, the large active area of the swPCD would result in relatively poor directivity, with the concluding remarks that design should be tailored to experimental requirements for its deployment.

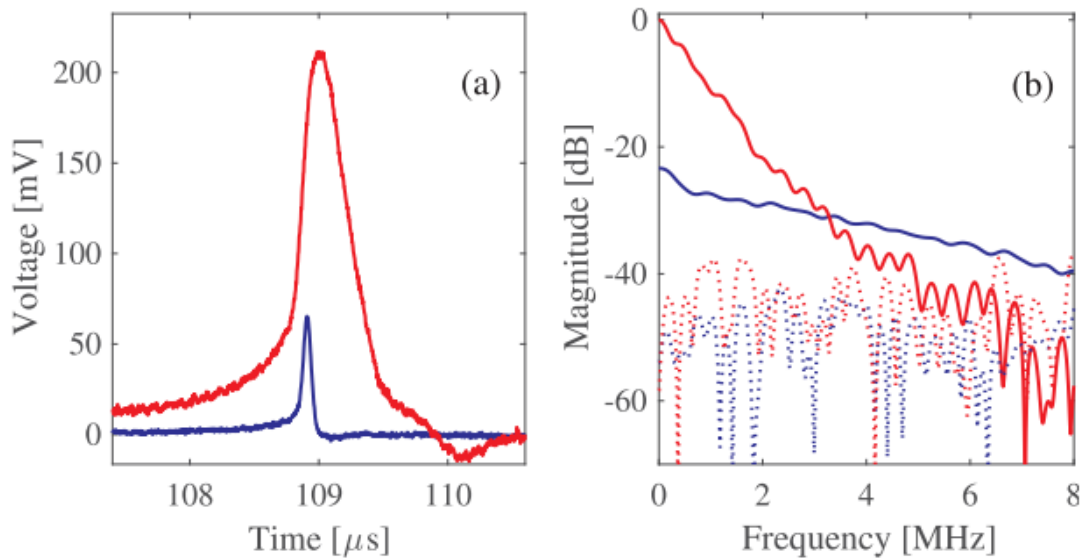


Fig. A.4: (a) Voltage trace comparing final swPCD (red) and Y-107 (blue) for detection of a BCSW. (b) spectra of shockwaves where stapled data represent the noise floor. Taken from [69].

## Appendix B

### Principal MATLAB filtering code

Main filtering protocol steps, as discussed in Chapter 3, §3.9 are displayed below.

```

%% load data

close all
clear all

load('filename.mat');

t = time;
y = data;
L = length(data);
dt = t(2,1)-t(1,1);

fs = 1/dt;
f0 = 20e3;
y = y * 1000; % converting to mV

Fcut1 = f1; %lower frequency threshold
Fcut2 = 4e6; %upper frequency threshold

%% low-pass filter at 10 MHz to remove high frequency noise

h_lpf = fir1(2^9, 10e6/(fs/2));
slpf1 = convn(y, h_lpf, 'same');

FS = fs;

%% high-pass filter at 50 Hz to remove line noise

h_hpf = fir1(2^9, 50/(fs/2), 'high');
slpf1y = convn(slpf1, h_hpf, 'same');

%% high-pass filter at f0 Hz to remove line noise

h_hpf = fir1(2^9, f0/(fs/2), 'high');
slpf1y = convn(slpf1, h_hpf, 'same');

%% bandpass filter across range of swPCD sensitivity
h_bpf = fir1(2^9, [Fcut1 Fcut2]/(FS/2), 'bandpass');
sig1 = convn(slpf1y, h_bpf, 'same');

```

```

%% Plot filtered signal
figure ()
plot(t*1e6,sig1,'r','LineWidth',1.5);
grid on;
set (gca, 'FontName', 'Times New Roman');
set (gca, 'FontSize', 10);
set(gca,'FontWeight','bold');
xlabel('time (\mus)');
ylabel('Voltage (mV)');
title('Filtered time domain data');

%% Frequency Spectrum of signal

[SLPF1 w1] = freqz(sig.*blackman(length(rms(sig))),1,2^21,fs);
figure('unit','normalized','position',[0.1 0.1 0.8 0.8]);
subplot(2,1,1); hold on;
plot(w1/1e6,db(abs(SLPF1)/max(abs(SLPF1))),'LineWidth',1);
grid on;
xlabel('Frequency(MHz)');
ylabel('Magnitude(dB)');
title('Frequency response of acoustic emission');

```

## Appendix C

### C.1 Characterisation of cavitation activity in CaDES and Reline

#### C.1.1 Bubble cluster shockwave periodicity at selected input powers in CaDES

The results in CaDES, below, are presented in the same format as water and Ethaline, in the main text of Chapter 5, with three key input powers of 55, 70 and 80% showcased. Again, justification for the selection of these input powers is provided by the shockwave content in the emission signal over all powers.

Fig. C.1 is swPCD data over (a) a 200 ms duration and (b) 2 ms duration at an input power of 55% in CaDES. Fig. C.1 (c) presents sample HSI extracted from the image sequence, corresponding to the green box of (b).

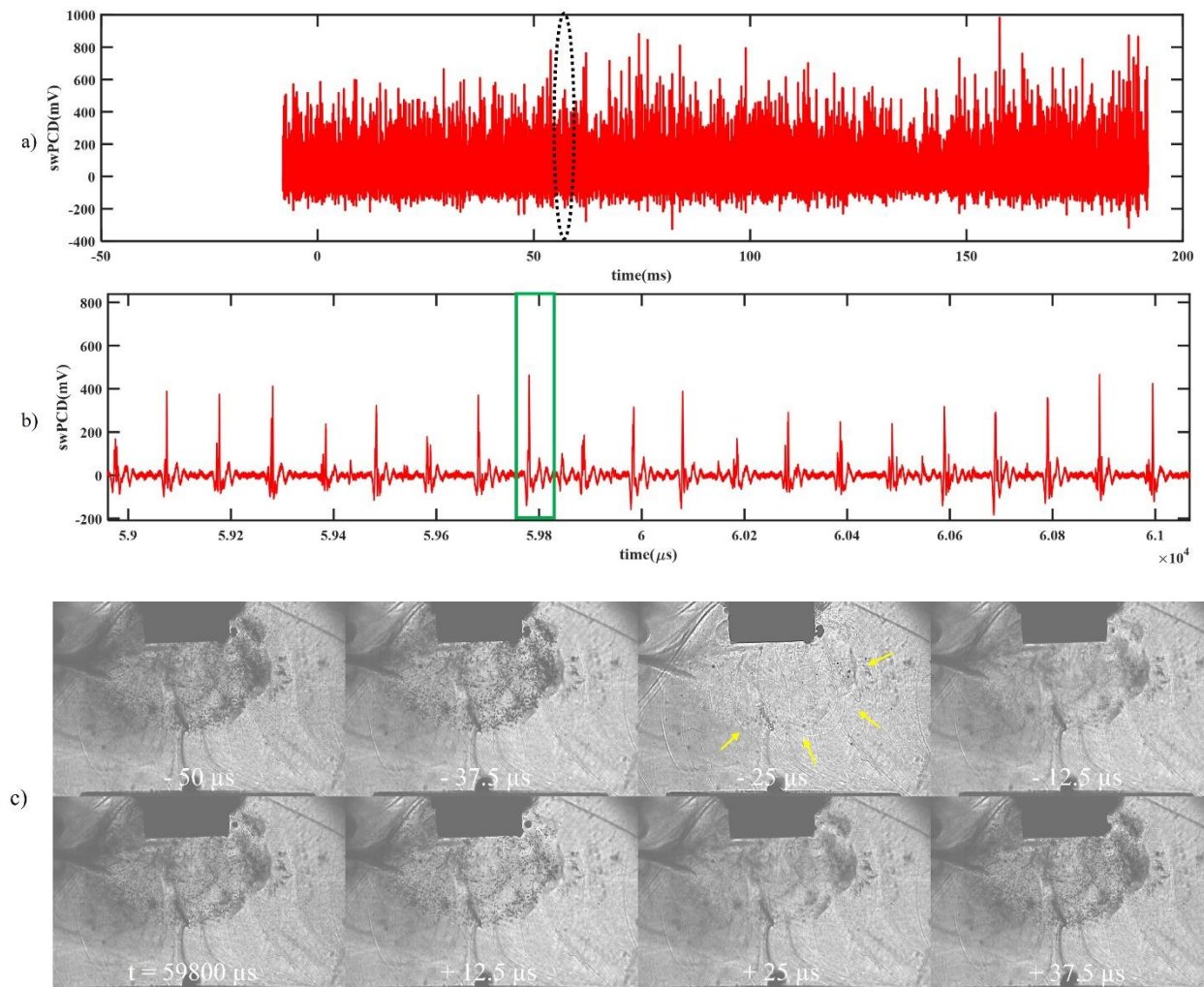


*Fig. C.1: swPCD data over (a) 200 ms and (b) 2 ms identified by the dashed oval, sampled approximately 4 s into the sonication at 55% input power in CaDES. Sample HSI extracted from the image sequence, corresponding to the green box of (b). Bubble collapse shockwaves are arrowed in yellow.*

Fig. C.1 reveals primary cluster collapse and shockwave detection at  $2T_0$  with single non-collapsing deflations between each detected shockwave, similar to that observed in water at lower powers (Main text, fig. 5.4). The difference between CaDES and water being the sonotrode power, giving an associated increase in average shockwave amplitude ( $\sim 400$  mV). The periodicity of shockwaves was similar at powers adjacent to 55%, with correspondingly lower and higher shockwave amplitudes, respectively. The bubble cluster dynamics and structure are notably different in CaDES, with a characteristic bulbous cloud extending over a large volume beneath the sonotrode tip. Bubble collapse shockwaves appear to originate from all around this cavitating sphere, fig. C.1 (c).

Fig. C.2 presents data, in the same format, at 70% input power.

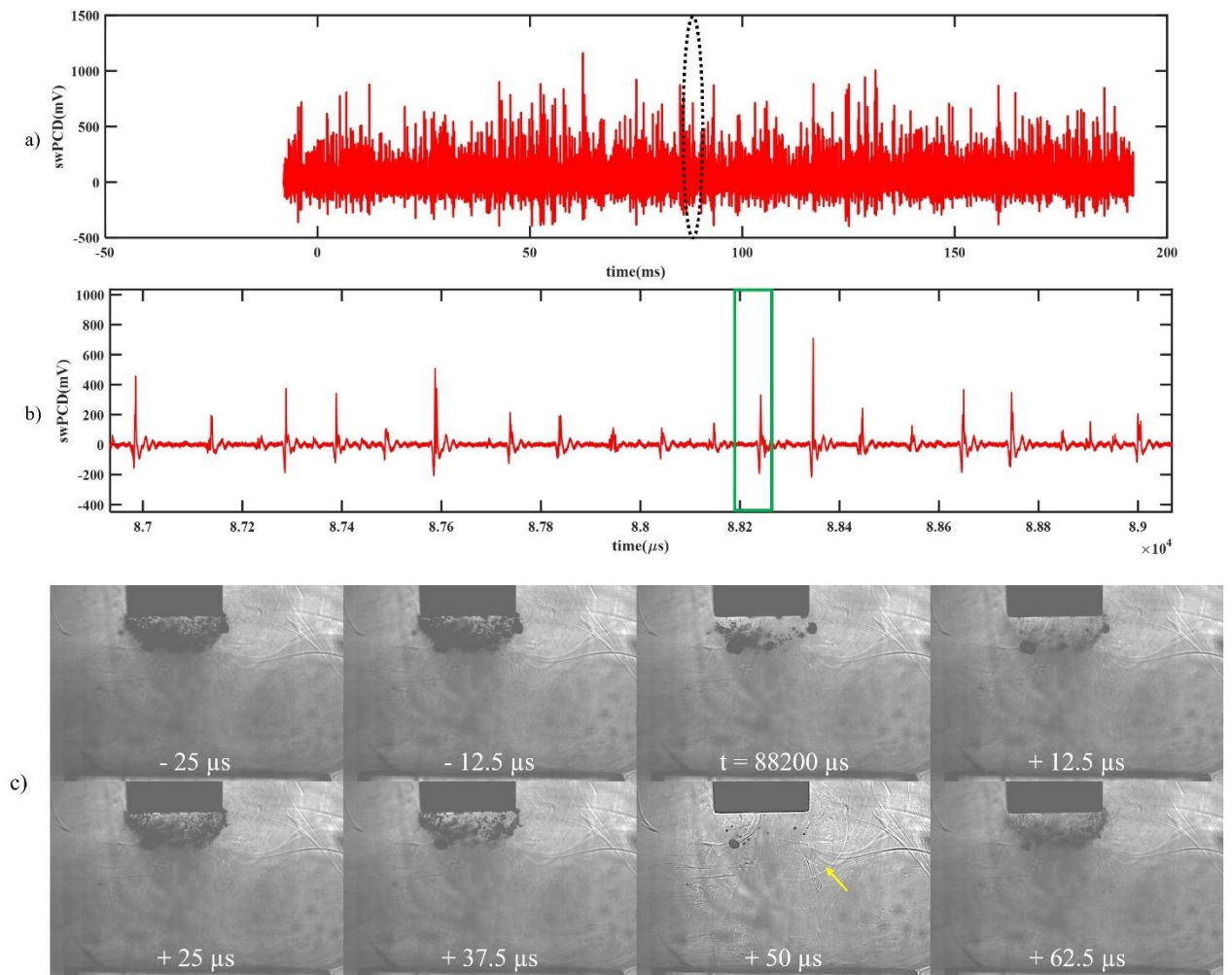


Fig. C.2: swPCD data over (a) 200 ms and (b) 2 ms identified by the dashed oval, sampled approximately 4 s into the sonication at 70% input power in CaDES. Sample HSI extracted from the image sequence, corresponding to the green box of (b). Bubble collapse shockwaves are arrowed in yellow.

Fig. C.2 (a) appears sparser in peaks than fig. C.1, with fig. C.2 (b) revealing a combination of shockwaves mostly oscillating at periods of  $2T_0$  and  $3T_0$  as well as lower amplitude, barely detectable, peaks between  $8.76 \times 10^4$  and  $8.82 \times 10^4$   $\mu\text{s}$ . Additionally, the bulbous cavitating cloud appears smaller in diameter, receding closer to the sonotrode tip.

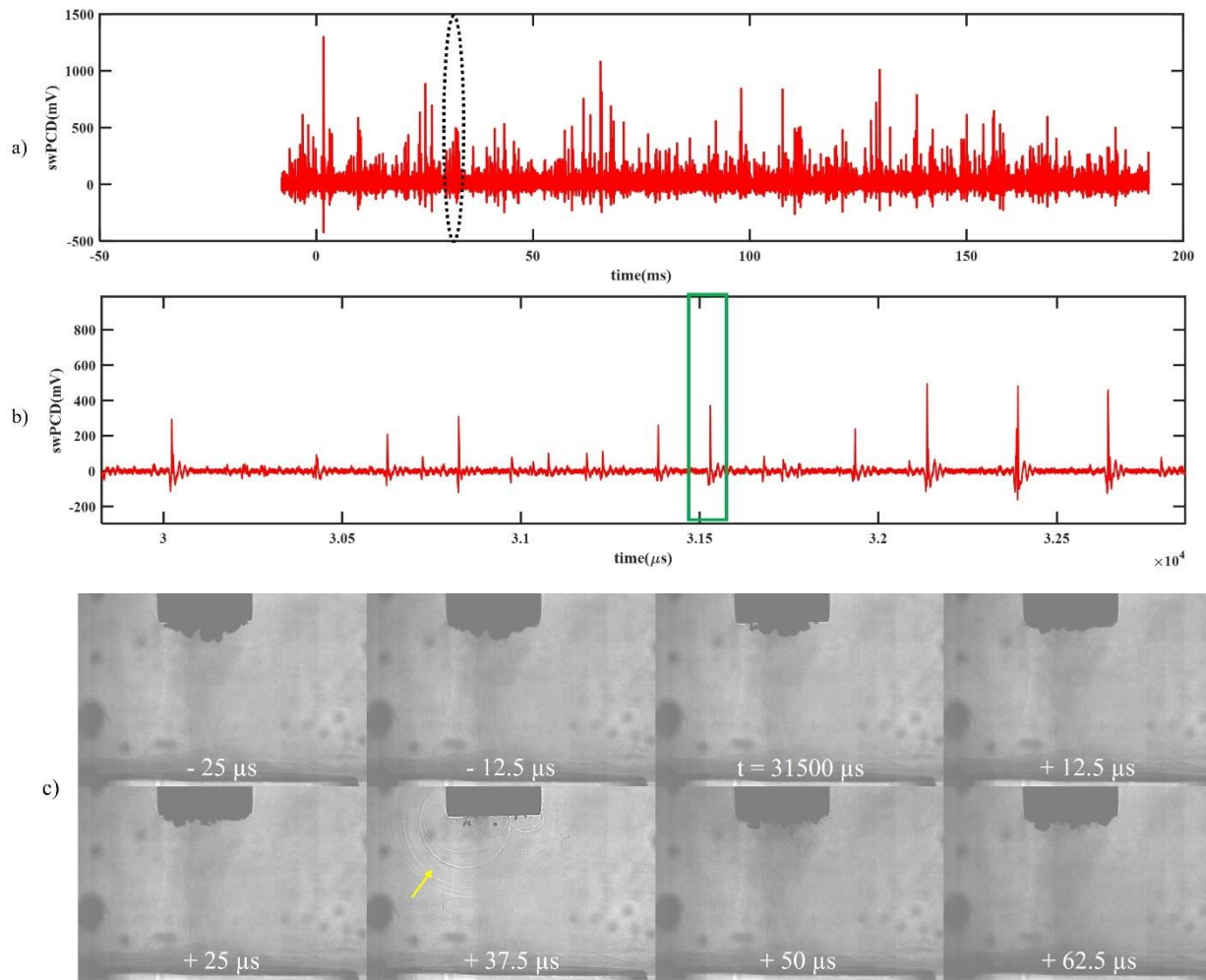
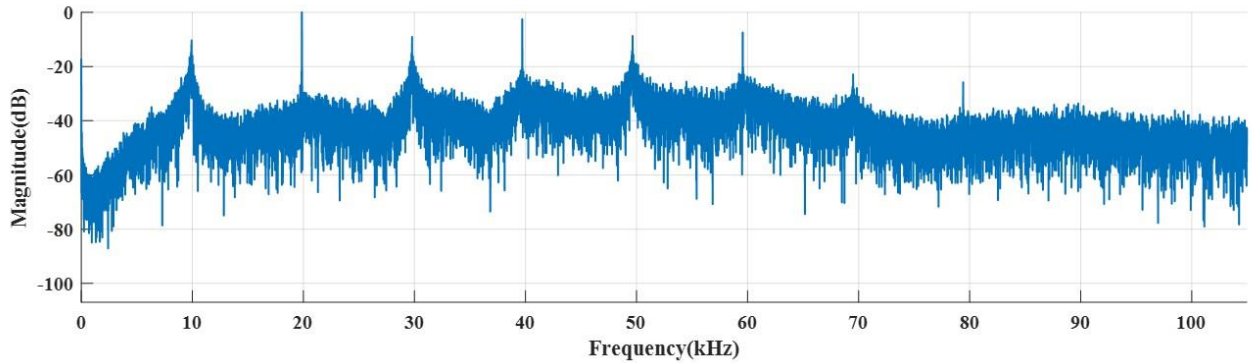


Fig. C.3: swPCD data over (a) 200 ms and (b) 2 ms identified by the dashed oval, sampled approximately 4 s into the sonication at 80% input power in CaDES. Sample HSI extracted from the image sequence, corresponding to the green box of (b). Bubble collapse shockwaves are arrowed in yellow.

Fig. C.3 (a) appears even more sparse in shockwave peaks. This is more apparent in (b) where we observe extended regions on non-collapsing deflations from  $3 - 3.15 \times 10^4 \mu\text{s}$ . Additionally, shockwave periodicity appears to be mostly oscillating at  $4T_0$ , with presence of 2 and  $3T_0$ . This increase in oscillation period is as expected, as previously established in water. At this higher power, the cavitating cloud has entirely receded back to the sonotrode tip with the cavitation more reminiscent of a single cloud akin to sonication in water. Few satellite clusters form, likely due to the viscous forces in the fluid.

### C.1.2 Cavitation emission noise spectra at selected input powers in CaDES

Fig. C.4 – C.6 present the acoustic emission spectra corresponding to the time domain emission signals detected in CaDES, above. Presented in the same format as for water and Ethaline in the main text, Chapter 5.



*Fig. C.4: Cavitation emission noise spectra for the sampled 200 ms section of signal presented previously in CaDES at 55% input power.*

The emission spectra at 55% input power in CaDES presents clear peaks with  $m = 2$  at  $nf_0/2$ , for all  $n$ . These peaks are raised by the defined  $2T_0$  periodicity of the shockwaves at this input power.

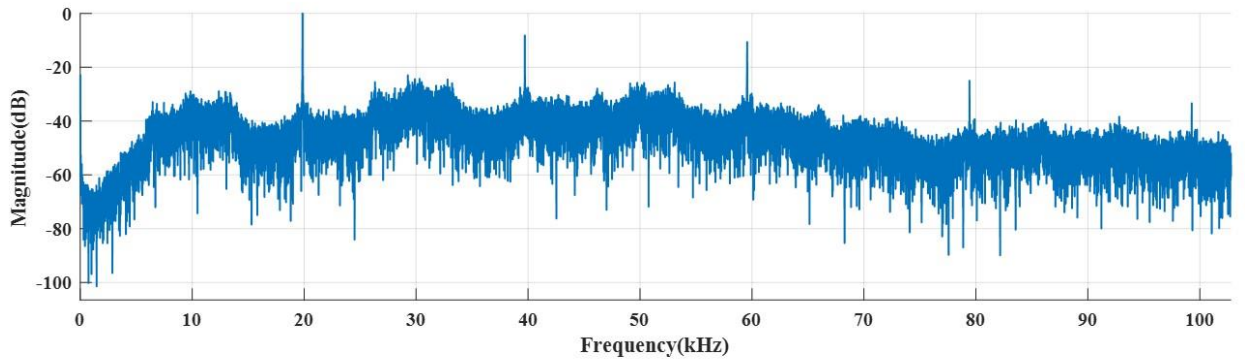


Fig. C.5: Cavitation emission noise spectra for the sampled 200 ms section of signal presented previously in CaDES at 70% input power.

At 70% input power, the emission spectra presents very minor peaks at  $m = 2$  and  $m = 3$ , at  $nf_0/m$ , for all  $n$ . The lack of definition of the peaks at this power is related to the emission signal containing a variation of  $2T_0$  and  $3T_0$  shockwaves, in the same manor that transitional amplitudes were identified in water.

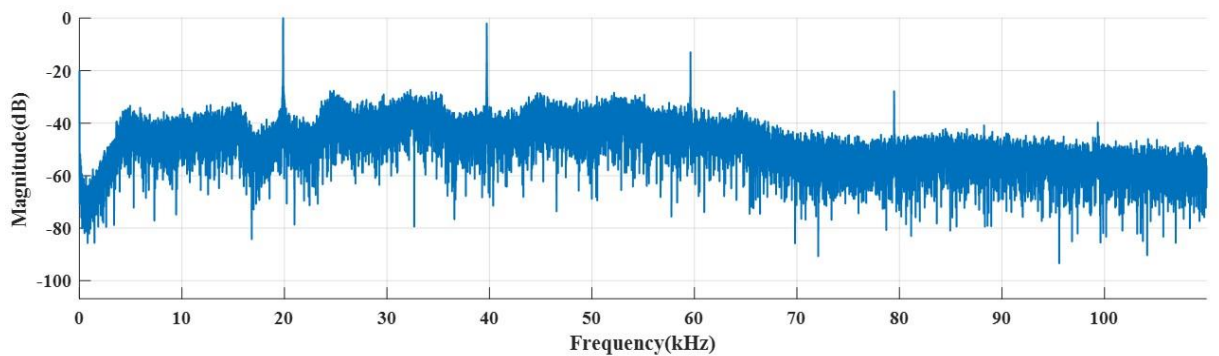


Fig. C.6: Cavitation emission noise spectra for the sampled 200 ms section of signal presented previously in CaDES at 80% input power.

At 80% power there is little definition in the subharmonic spectrum, with barely apparent low amplitude broad peaks visible at  $nf_0/4$  for all  $n$ . Although, for  $n > 60$  kHz, peaks are not apparent above the spectral floor. This is both attributed to the shockwave amplitude variance at 80% power associated to the transitional nature of this power and the result of higher powers producing more multi-fronted shockwaves, as explained previously for water.

Both of these phenomena manifest in broadening of the spectral peaks and redistribution to broadband noise, raising the spectral floor.

### C.1.3 Shockwave content with the emission signal over all measured input powers in CaDES

As previously presented for water and Ethaline in the main text, this results section presents swPCD data at 17 input powers ranging between 20 – 100%. The cavitation emission signals collected from five 400 ms sonication are presented at appropriate interval powers.

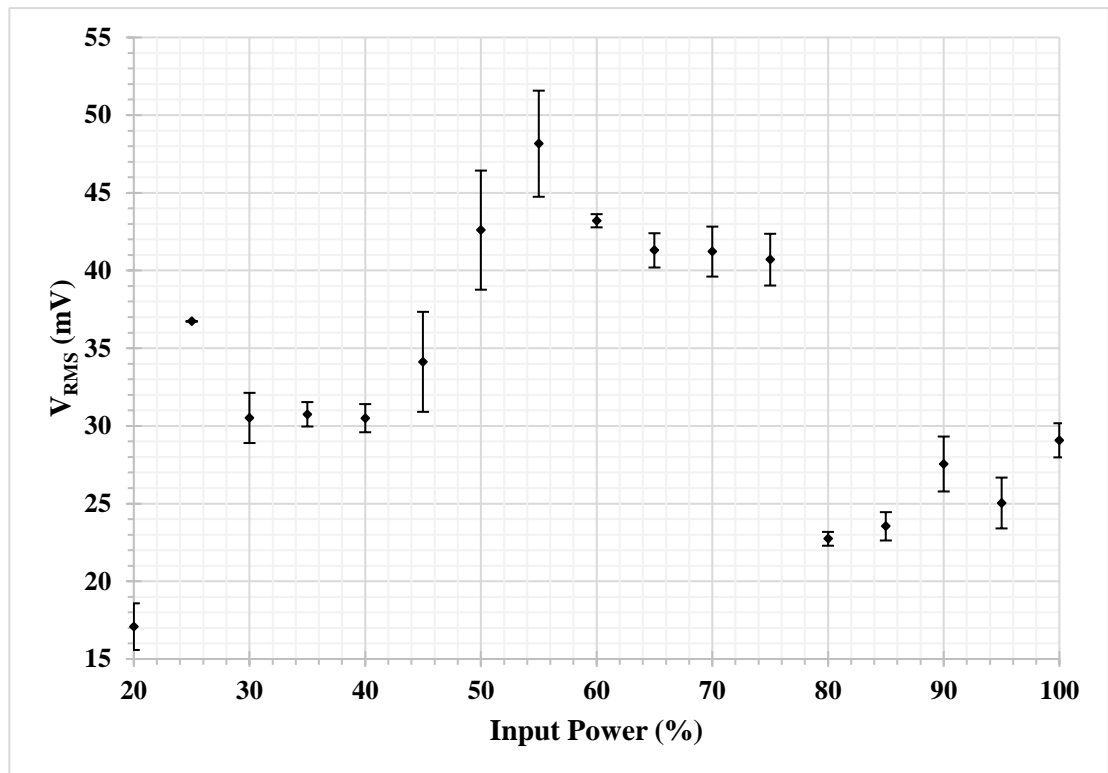


Fig. C.7: Mean  $\pm$  standard deviation  $V_{RMS}$  over five 400 ms sonications at each input power over a seventeen-input power range in CaDES.

Fig. C.7 presents a uniquely different  $V_{RMS}$  plot to that of water and similar to that of Ethaline. Here, a general increase is observed until a maximum at 55% input power, which was shown to be the power of most uniform (or in synch) bubble-cluster oscillation, with periodicity of  $2T_0$ . Beyond 55%, a short drop in cavitation emission is detected, associated with the transitional nature of this power. However, beyond 75% we observe a large drop (over 40%)

in  $V_{RMS}$ . This is associated with the greater increased drop in shockwave content detected in the acoustic emissions, associated with vastly increased durations of non-shocking activity.

### C.1.4 Bubble cluster shockwave periodicity at selected input powers in Reline

The results in Reline, below, are presented in the same format as the previous fluids with three key input powers of 30, 45 and 80% showcased. Again, justification for the selection of these input powers is provided by the shockwave content in the emission signal over all powers.

Fig. C.8 is swPCD data over (a) a 200 ms duration and (b) 2 ms duration collected in accordance with §6.2.4 at an input power of 30% in Reline. Fig. C.8 (c) presents sample HSI extracted from the image sequence, corresponding to the green box of (b).

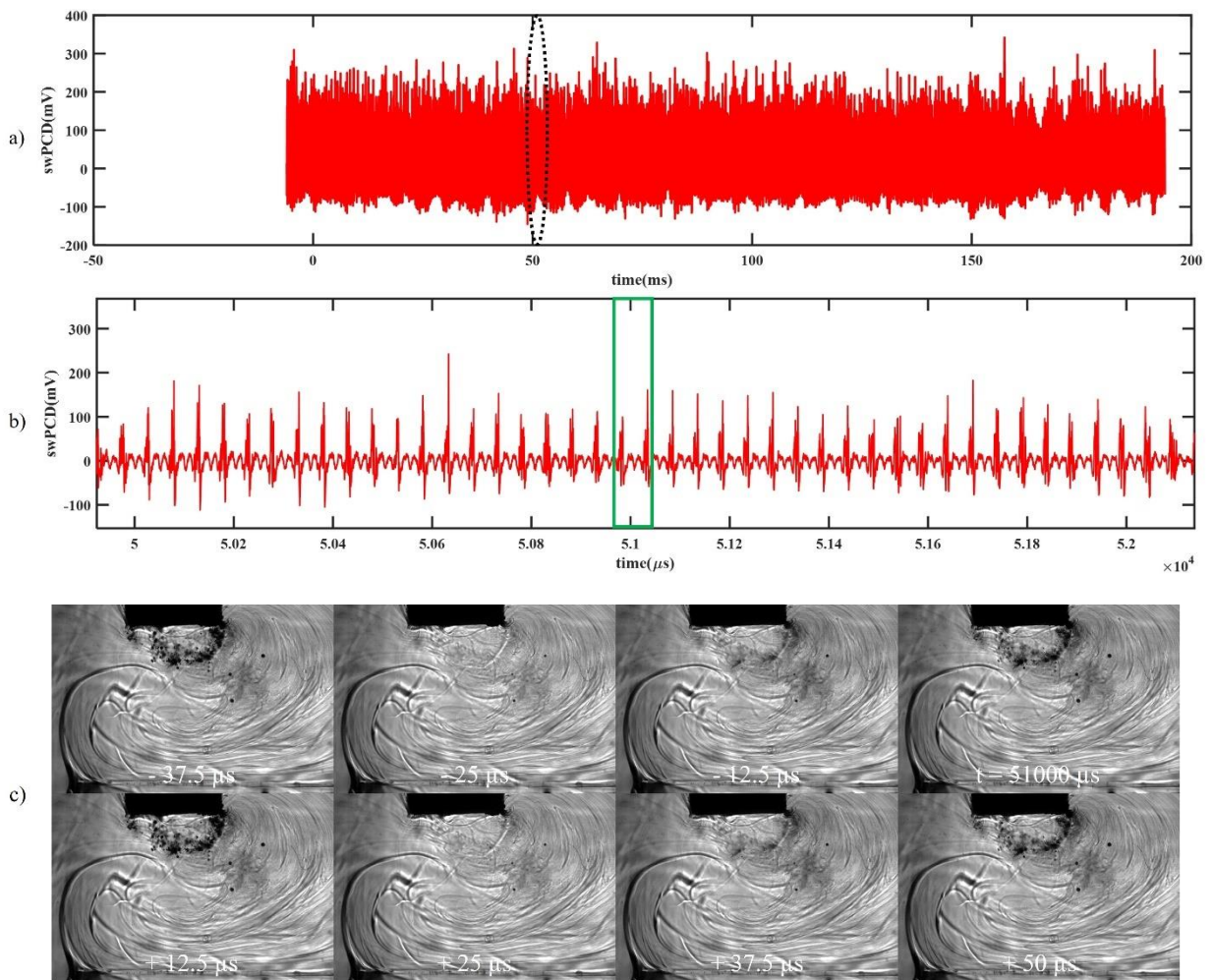


*Fig. C.8: swPCD data over (a) 200 ms and (b) 2 ms identified by the dashed oval, sampled approximately 4 s into the sonication at 30% input power in Reline. Sample HSI extracted from the image sequence, corresponding to the green box of (b).*

Fig. C.8 reveals primary cluster collapse and shockwave detection at  $T_0$ . Here, bubble collapse shockwaves are detected, but every cycle with no partial deflation between collapses. At this power, average shockwave amplitude is relatively low ( $\sim 120$  mV). Here, the periodic shockwaves do not appear to propagate far, as they are expected to lose energy in this highly viscous fluid [95]. *Khavari et al* noted a poorer capture of shockwaves in their high-speed imaging in glycerol due to rapid energy loss of shockwaves [95], here we observe a similar effect on shockwave detection in Reline. We observe the negative pressure peaks appear larger in magnitude (relative to the positive peaks), this has been hypothesised as a consequence of the reduced number and volume of bubbly activity resulting in lower scattering or attenuating of the pressure signal as it propagates through the media [81].

Fig. C.9 presents the equivalent emission signal in Reline at 45% input power.

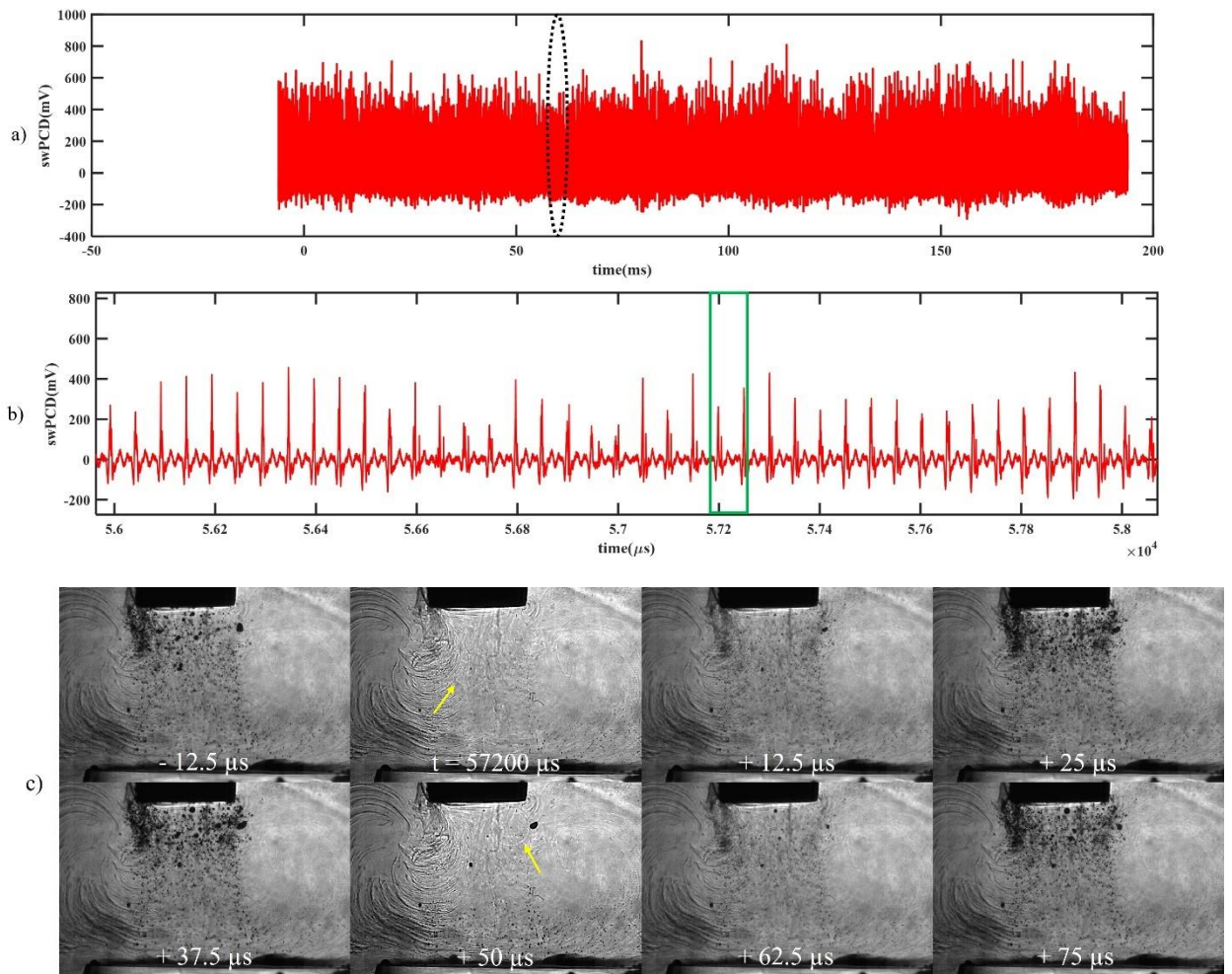


Fig. C.9: swPCD data over (a) 200 ms and (b) 2 ms identified by the dashed oval, sampled approximately 4 s into the sonication at 45% input power in Reline. Sample HSI extracted from the image sequence, corresponding to the green box of (b). Bubble collapse shockwaves are arrowed in yellow.

Again, at 55% power in Reline the emission signal is entirely dominated by  $T_0$  shockwaves. Here, shockwave amplitude is approximately double that at 30% power. Fig. C.9 (c) highlights a greater overall volume of cavitation region. Here, the greater displacement achieved by the horn allows for generation of an extended cavitation zone in the viscous medium producing a larger cavitation cloud.

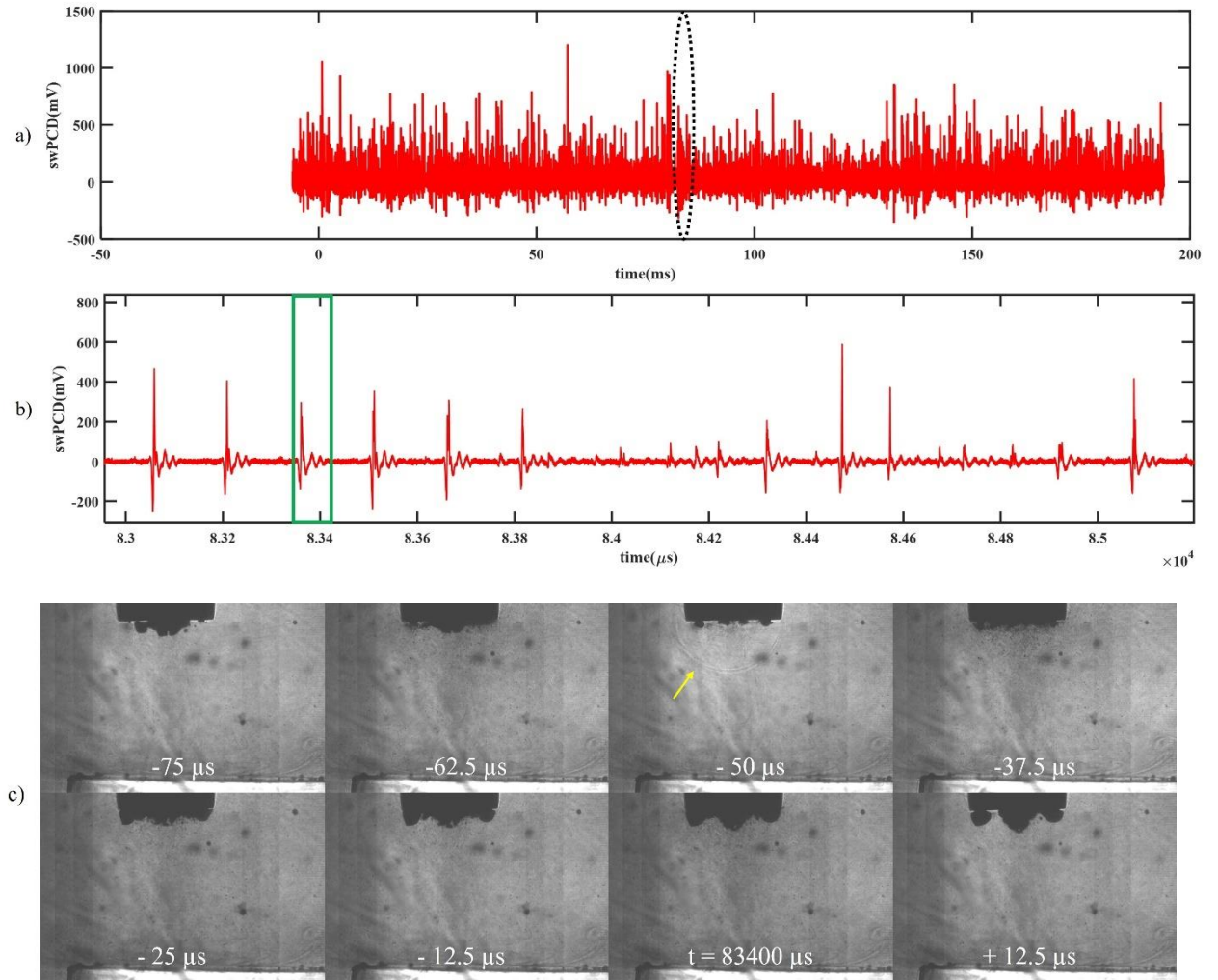
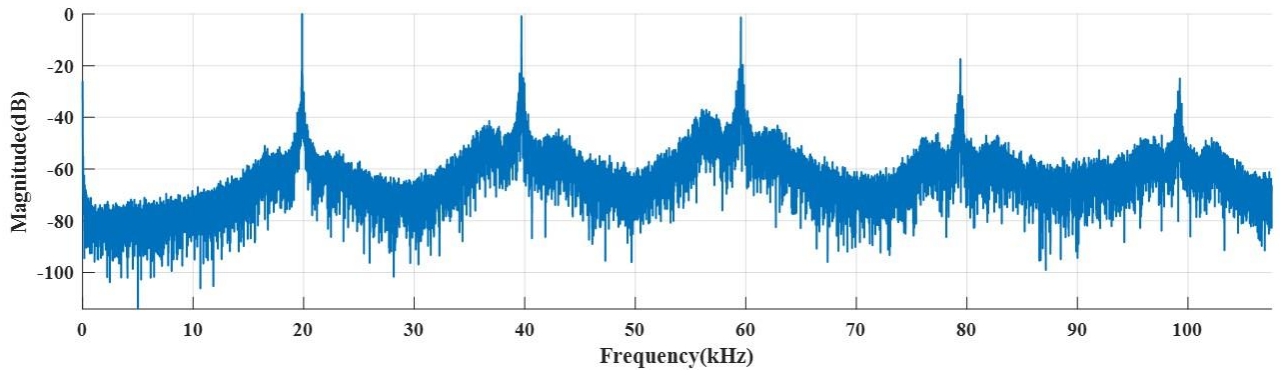


Fig. C.10: swPCD data over (a) 200 ms and (b) 2 ms identified by the dashed oval, sampled approximately 4 s into the sonication at 80% input power in Reline. Sample HSI extracted from the image sequence, corresponding to the green box of (b). Bubble collapse shockwaves are arrowed in yellow.

As input power is increased to 80% there is a clear difference in the emission data, presented in fig. C.10. Here, periodic emissions at  $2T_0$  and  $3T_0$  are observed in between extended regions of non-collapse. Again, average shockwave amplitude is increased however this is balanced with the increased spacing between detected shockwaves. Here, we observe a much smaller cavitation zone with fewer satellite clusters and individual bubbles, again thought to be contributing to a slightly greater negative phase on the shockwaves due to reduced attenuation and scattering.

### C.1.5 Cavitation emission noise spectra at selected input powers in Reline

Figs. C.11 – C.13 present the acoustic emission spectra corresponding to the time domain emission signals detected in Reline, above. Presented in the same format as for the previous media.



*Fig. C.11: Cavitation emission noise spectra for the sampled 200 ms section of signal presented previously in Reline at 30% input power.*

The emission spectra for Reline at 30% comprises only  $nf_0$  peaks, for all  $n$ . This is a consequence of the purely  $T_0$  shockwaves detected in the acoustic emission signal. Similar results were reported in glycerol under sonication with a sonotrode at 24 kHz, with the reason for the purely fundamental peaks (and suppression of subharmonics) being the weakening of shockwaves as they propagate through the bubbly viscous media [94, 95]. The  $nf_0$  peaks could be enhanced by contribution from the direct field and associated harmonics. However, the high-speed imaging (despite being poorer at this low power) does indicate the contribution from periodic shockwaves. It is also possible that the spectra is contributed to by stable oscillating bubbles further enhancing the fundamental peak and associated harmonics.

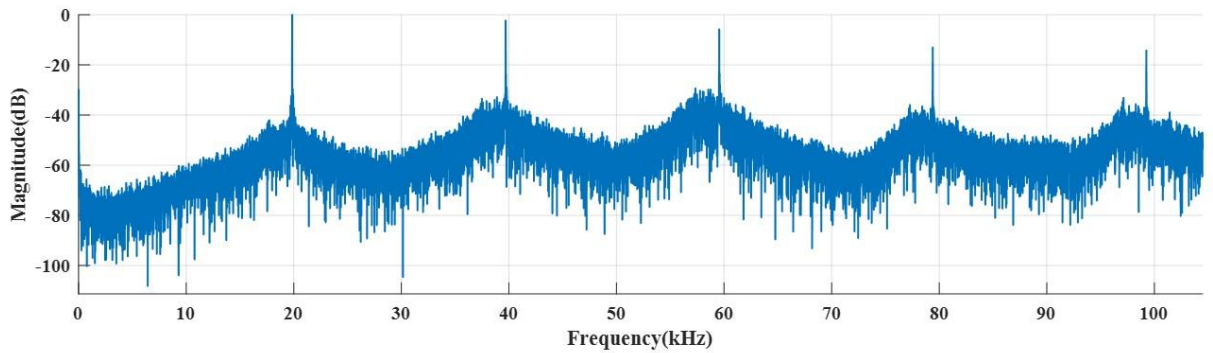


Fig. C.12: Cavitation emission noise spectra for the sampled 200 ms section of signal presented previously in Reline at 45% input power.

Given the close similarity in acoustic emissions, it is perhaps no surprise that the spectra at 45% power is almost identical to that of 30%. There is a minor increase in the spectral floor in between peaks and a slightly reduced amplitude level of the harmonic peaks. This is likely due to increased bubble activity and size of cavitation zone scattering and attenuating the signal. Furthermore, increased bubble activity will also increase variability in shockwave amplitude, contributing to redistribution of the power at spectral peaks to the noise floor (as previously discussed).

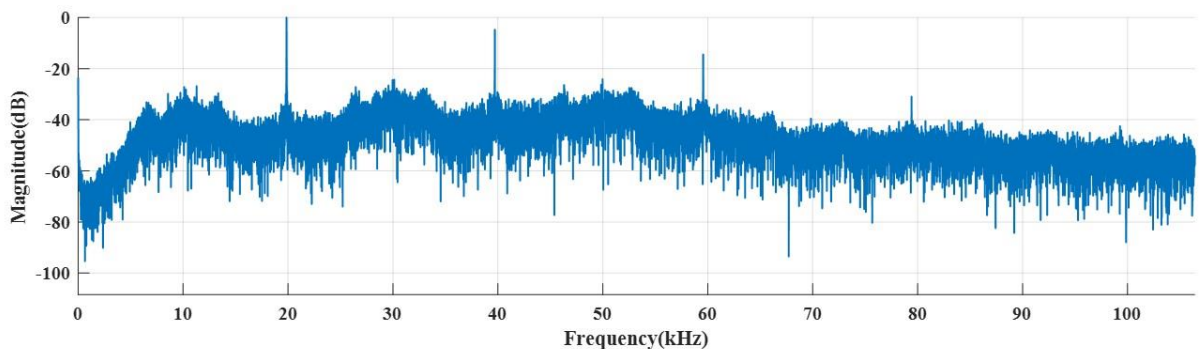


Fig. C.13: Cavitation emission noise spectra for the sampled 200 ms section of signal presented previously in Reline at 80% input power.

At 80% power, the contribution from  $nf_0$  is reduced, with an increase in low amplitude, broad subharmonic peaks at  $nf_0/m$  for  $m = 2$  and  $m = 3$ . Furthermore, the large shockwave amplitude variance and transitional nature of the shockwave periodicity results in increasing the noise floor, as previously observed for both other fluids.

### C.1.6 Shockwave content with the emission signal over all measured input powers in Reline

This results section presents swPCD data at 17 input powers ranging between 20 – 100%. The cavitation emission signals collected from five 400 ms sonication are presented at appropriate interval powers, as displayed for the previous solutions.

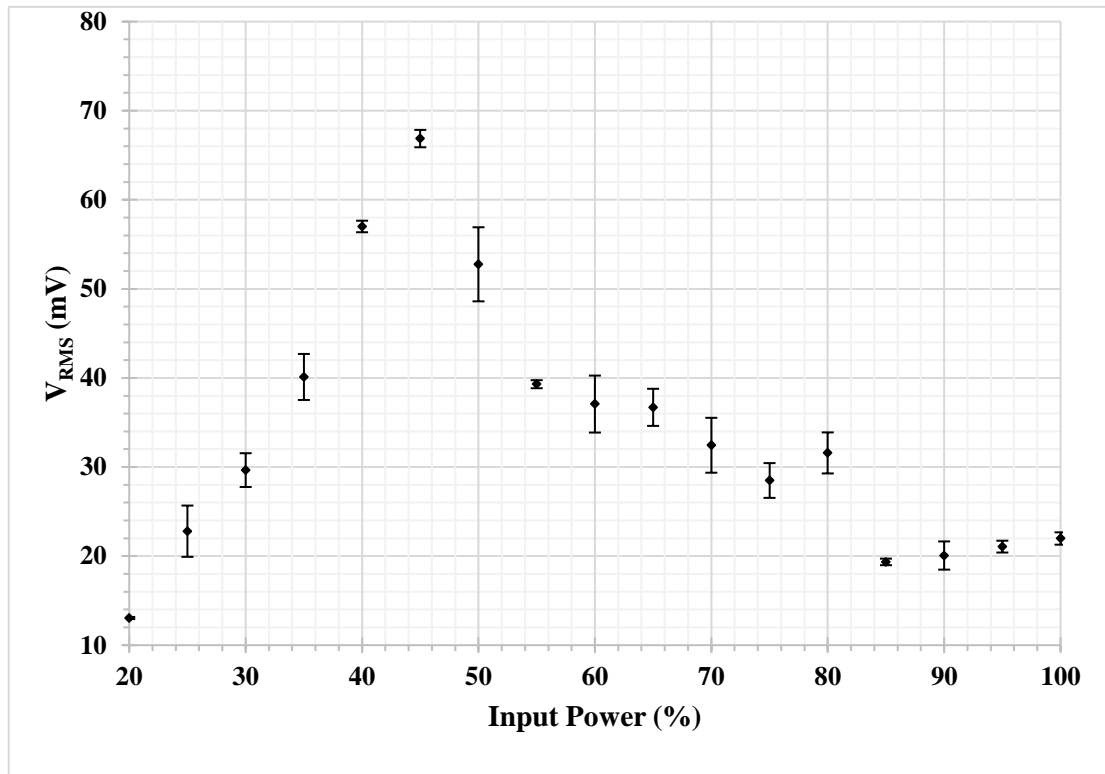


Fig. C.14: Mean  $\pm$  standard deviation  $V_{RMS}$  over five 400 ms sonications at each input power over a seventeen-input power range in Reline.

Fig. C.14 demonstrates an almost linear increase in  $V_{RMS}$  until 45% input power. Here, this increase is related to a purely increased shockwave amplitude associated with the increase in vibrational amplitude and input power of the sonotrode. Until 45% power, the period of shockwave oscillation has been shown to be exclusively  $T_0$ . Beyond 45% the oscillation period of the associated cavitation transitions, with the presence of multiple periodic intervals. Interestingly, at the higher powers (above 80%) very low shockwave intensity is observed. This is comparable to the CaDES displayed previously. Here, the Reline oscillation (varying between  $m = 2$  and  $m = 3$ ) appears to lag behind that of CaDES at the

same power range (varying between  $m = 3$  and  $m = 4$ ) which in turn lags behind that of water at the same power range. This behaviour is possibly associated with the much greater viscosity of reline dampening the oscillations of the primary bubble cluster, inhibiting the transition to higher order subharmonics. Furthermore, the  $V_{RMS}$  drop is less instantaneous in Reline, again probably associated with the greater viscosity dampening the shift to higher-order oscillations.

## Appendix D

### Basic Principles of Linear Sweep Voltammetry

Linear sweep voltammetry (LSV) involves the linear sweeping of potential (voltage) between a working and reference electrode [281]. The result is to plot the current response at the working electrode as a function of this voltage sweep.

As the voltage is swept through the potential range, a current begins to flow and eventually reaches a peak before dropping off. This behaviour is explained by considering the influence of voltage on the equilibrium established at the electrode surface. The following example, taken from [282] considers the reduction of iron (III) to iron (II). An equilibrium is established at the electrode surface and governed by the Nernst equation [283], equation D1.

$$E = E^0 + \frac{RT}{nF} \ln \frac{[Ox]}{[Red]} \quad (D1)$$

where  $E$  is the applied electrode potential difference and  $E_0$  is the standard electrode potential.  $R$  is the universal gas constant and  $T$  is the temperature in Kelvin.  $n$  is the number of electrons transferred in the reaction and  $F$  is the Faraday constant.  $Ox$  and  $Red$  refer to the oxidised and reduced forms of a species, respectively.

The Nernst equation is used to determine the direction in which a redox reaction will occur [282-284] by determining the relationship between concentration and voltage. As the voltage is swept from  $V_1$  to  $V_2$ , the equilibrium position switches from no conversion to full conversion of the reactant at the electrode surface. The exact profile of the resulting voltammogram can be rationalised by consideration of the voltage and mass transport effects. As the voltage is initially swept from  $V_1$  the equilibrium at the surface begins to alter and current begins to flow:

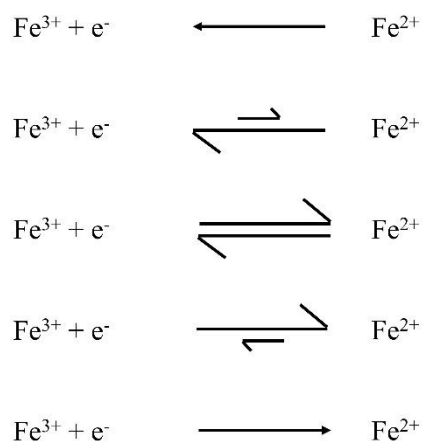


*Fig. D.1: Equilibrium relationship considering the reduction of Iron (III) to Iron (II) during LSV sweep. Adapted from [282].*

The current increases as the voltage is swept from  $V_1$  to  $V_2$ , occurring due to the fact that the equilibrium position is shifted further to the right-hand side (fig. D.1), thus converting more reactant. This converted reactant forms at the electrode surface and, at a point in the voltage sweep, the development of this so-called diffusion layer above the electrode surface has sufficiently passivated the surface such that the flux of reactant to the electrode is not fast enough, i.e., the rate of diffusion is slower. Beyond this point, the current begins to drop off. An example of a typical LSV curve in silent conditions is presented in fig. D.2, below.

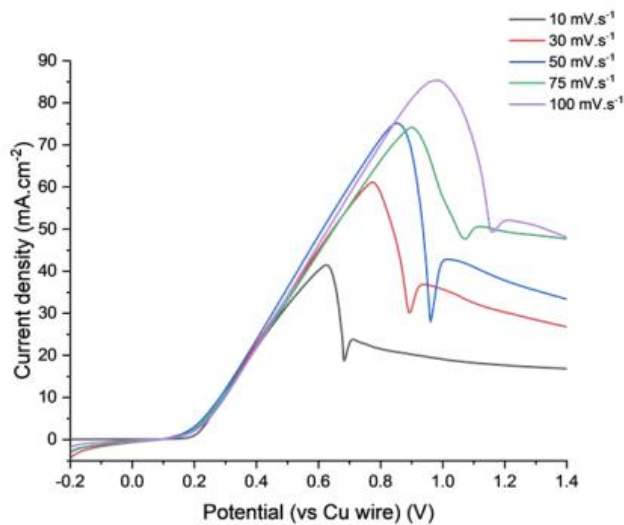


Fig. D.2: LSV for copper run in Ethaline in silent conditions at increasing sweep rates.

Taken from [258]

Another key consideration for LSV is scan rate. Although a measure of current as a function of voltage, the rate of scan will influence the measurement, particularly with respect to magnitude. This is easily rationalised as, clearly, the LSV will take longer to record at slower scan rates. The longer the duration required, the greater extent of growth of the passivating diffusion layer. Consequently, the flux from the electrode will be correspondingly slower. As the current is proportional to the flux towards the electrode, the magnitude of the LSV curve will be reduced.

## Bibliography

- [1] E. Stavropoulos-Vasilakis, N. Kyriazis, H. Jadidbonab, P. Koukouvinis, and M. Gavaises, "Review of Numerical Methodologies for Modeling Cavitation," in *Cavitation and Bubble Dynamics*, 2021, pp. 1-35.
- [2] J. Franc and J. Pierre, *Fundamentals of Cavitation* (Fluid Mechanics and its Application). Kluwer Academic Publishers, 2005.
- [3] M. Ashokkumar, *Handbook of Ultrasonics and Sonochemistry*. 2016.
- [4] W. Lauterborn and R. Mettin, "Acoustic cavitation," in *Power Ultrasonics*, 2015, pp. 37-78.
- [5] K. A. Mørch, "Reflections on cavitation nuclei in water," *Physics of Fluids*, vol. 19, 2007, doi: 10.1063/1.2747210.
- [6] J. Thornycroft and S. W. Barnaby, "Torpedo Boat Destroyers," *Proc. Inst. Civil Engineers.*, vol. 12, no. 51, 1895.
- [7] L. Rayleigh, "VIII. On the pressure developed in a liquid during the collapse of a spherical cavity," *Philosophical Magazine Series 1*, vol. 34, pp. 94-98, 1917.
- [8] S. K. Bhangu and M. Ashokkumar, "Theory of Sonochemistry," *Top Curr Chem (Cham)*, vol. 374, no. 4, p. 56, Aug 2016, doi: 10.1007/s41061-016-0054-y.
- [9] M. Ashokkumar, *Ultrasonic Synthesis of Functional Materials*. SpringerBriefs in Molecular Science, 2016.
- [10] M. Minnaert, "On musical air-bubbles and the sounds of running water," *The London, Edinburgh, and Dublin Philosophical Magazine and Journal of Science*, vol. 16, no. 104, pp. 235-248, 1933, doi: 10.1080/14786443309462277.
- [11] Z. Izadifar, P. Babyn, and D. Chapman, "Ultrasound Cavitation/Microbubble Detection and Medical Applications," *Journal of Medical and Biological Engineering*, vol. 39, no. 3, pp. 259-276, 2018, doi: 10.1007/s40846-018-0391-0.
- [12] N. Vyas *et al.*, "Which Parameters Affect Biofilm Removal with Acoustic Cavitation? A Review," *Ultrasound Med Biol*, vol. 45, no. 5, pp. 1044-1055, May 2019, doi: 10.1016/j.ultrasmedbio.2019.01.002.
- [13] J. L. Luque-García and M. D. Luque de Castro, "Ultrasound: a powerful tool for leaching," *TrAC Trends in Analytical Chemistry*, vol. 22, no. 1, pp. 41-47, 2003, doi: 10.1016/s0165-9936(03)00102-x.
- [14] M. Lamminen, "Mechanisms and factors influencing the ultrasonic cleaning of particle-fouled ceramic membranes," *Journal of Membrane Science*, vol. 237, no. 1-2, pp. 213-223, 2004, doi: 10.1016/j.memsci.2004.02.031.

- [15] D. J. Flannigan and K. S. Suslick, "Plasma formation and temperature measurement during single-bubble cavitation," *Nature*, vol. 434, no. 7029, pp. 50-2, Mar 3 2005, doi: 10.1038/nature03400.
- [16] K. S. Suslick, "Sonoluminescence and Sonochemistry," in *Encyclopedia of Physical Science and Technology*, R. A. Meyers Ed.: Elsevir Academic Press, 2001.
- [17] L. H. Thompson and L. K. Doraiswamy, "Sonochemistry: Science and Engineering," *Ind. Eng. Chem. Res.*, vol. 38, pp. 1215-1249, 1999.
- [18] C. A. Wakeford, R. Blackburn, and P. D. Lickiss, "Effect of ionic strength on the acoustic generation of nitrite, nitrate and hydrogen peroxide," *Ultrason Sonochem*, no. 6, pp. 141-148, 1998.
- [19] C. C. Church and E. L. Carstensen, "'Stable' Inertial Cavitation," *Ultrasound Med Biol*, vol. 27, no. 10, pp. 1435–1437, 2001.
- [20] L. van Wijngaarden, "Mechanics of collapsing cavitation bubbles," *Ultrason Sonochem*, vol. 29, pp. 524-7, Mar 2016, doi: 10.1016/j.ultsonch.2015.04.006.
- [21] F. Reuter and R. Mettin, "Mechanisms of single bubble cleaning," *Ultrason Sonochem*, vol. 29, pp. 550-62, Mar 2016, doi: 10.1016/j.ultsonch.2015.06.017.
- [22] B. Verhaagen and D. Fernandez Rivas, "Measuring cavitation and its cleaning effect," *Ultrason Sonochem*, vol. 29, pp. 619-28, Mar 2016, doi: 10.1016/j.ultsonch.2015.03.009.
- [23] A. Vogel, S. Busch, and U. Parlitz, "Shock wave emission and cavitation bubble generation by picosecond and nanosecond optical breakdown in water," *The Journal of the Acoustical Society of America*, vol. 100, no. 1, pp. 148-165, 1996, doi: 10.1121/1.415878.
- [24] K. Johnston *et al.*, "Periodic shock-emission from acoustically driven cavitation clouds: a source of the subharmonic signal," *Ultrasonics*, vol. 54, no. 8, pp. 2151-8, Dec 2014, doi: 10.1016/j.ultras.2014.06.011.
- [25] K. Johansen, J. H. Song, K. Johnston, and P. Prentice, "Deconvolution of acoustically detected bubble-collapse shock waves," *Ultrasonics*, vol. 73, pp. 144-153, Jan 2017, doi: 10.1016/j.ultras.2016.09.007.
- [26] J. H. Song, A. Moldovan, and P. Prentice, "Non-linear Acoustic Emissions from Therapeutically Driven Contrast Agent Microbubbles," *Ultrasound Med Biol*, vol. 45, no. 8, pp. 2188-2204, Aug 2019, doi: 10.1016/j.ultrasmedbio.2019.04.005.
- [27] T. Yamamoto, S.-i. Hatanaka, and S. V. Komarov, "Fragmentation of cavitation bubble in ultrasound field under small pressure amplitude," *Ultrasonics Sonochemistry*, vol. 58, 2019, doi: 10.1016/j.ultsonch.2019.104684.

- [28] A. B. Sieber, D. B. Preso, and M. Farhat, "Cavitation bubble dynamics and microjet atomization near tissue-mimicking materials," *Physics of Fluids*, vol. 35, no. 2, 2023, doi: 10.1063/5.0136577.
- [29] S. Aghapour Aktij, A. Taghipour, A. Rahimpour, A. Mollahosseini, and A. Tiraferri, "A critical review on ultrasonic-assisted fouling control and cleaning of fouled membranes," *Ultrasonics*, vol. 108, p. 106228, Dec 2020, doi: 10.1016/j.ultras.2020.106228.
- [30] N. S. Yusof, B. Babgi, Y. Alghamdi, M. Aksu, J. Madhavan, and M. Ashokkumar, "Physical and chemical effects of acoustic cavitation in selected ultrasonic cleaning applications," *Ultrason Sonochem*, vol. 29, pp. 568-76, Mar 2016, doi: 10.1016/j.ultsonch.2015.06.013.
- [31] L. Bai, P. Wu, H. Liu, J. Yan, C. Su, and C. Li, "Rod-shaped cavitation bubble structure in ultrasonic field," *Ultrason Sonochem*, vol. 44, pp. 184-195, Jun 2018, doi: 10.1016/j.ultsonch.2018.02.030.
- [32] A. Thiemann, T. Nowak, R. Mettin, F. Holsteyns, and A. Lippert, "Characterization of an acoustic cavitation bubble structure at 230 kHz," *Ultrason Sonochem*, vol. 18, no. 2, pp. 595-600, Mar 2011, doi: 10.1016/j.ultsonch.2010.10.004.
- [33] R. Mettin, S. Luther, C.-D. Ohl, and W. Lauterborn, "Acoustic cavitation structures and simulations by a particle model," *Ultrason Sonochem*, vol. 6, pp. 25-29, 1999.
- [34] K.-m. Quan, "The Bjerknes forces and acoustic radiation energy," in *Energy Aspects of Acoustic Cavitation and Sonochemistry*, 2022, pp. 99-109.
- [35] S. Luther, R. Mettin, P. Koch, and S. Lauterborn, "Observation of acoustic cavitation bubbles at 2250 frames per second," *Ultrason Sonochem*, vol. 8, pp. 159-162, 2001.
- [36] J.-L. Laborde, C. Bouyer, J.-P. Caltagirone, and A. Gkard, "Acoustic bubble cavitation at low frequencies," *Ultrasonics*, vol. 36, pp. 589-594, 1998.
- [37] T. G. Leighton, *The Acoustic Bubble*. Academic Press, 1994.
- [38] R. Ramachandran and R. Saraswathi, "Sonochemical studies on mass transport in some standard redox systems," *Russian Journal of Electrochemistry*, vol. 47, no. 1, pp. 15-25, 2011, doi: 10.1134/s1023193511010149.
- [39] T. J. Matula, R. A. Roy, P. D. Mourad, W. B. McNamara, 3rd, and K. S. Suslick, "Comparison of multibubble and single-bubble sonoluminescence spectra," *Phys Rev Lett*, vol. 75, no. 13, pp. 2602-2605, Sep 25 1995, doi: 10.1103/PhysRevLett.75.2602.
- [40] T. J. Mason and J. P. Lorimer, *Applied Sonochemistry: The Uses of Power Ultrasound in Chemistry and Processing*. Wiley-VCH, 2002.

- [41] T. J. Mason, "Sonochemistry: current uses and future prospects in the chemical and processing industries," *The Royal Society*, no. 357, pp. 355–369, 1999.
- [42] T. J. Mason, J. P. Lorimer, and D. M. Bates, "Quantifying sonochemistry: casting some light on a 'black art'," *Ultrasonics*, vol. 30, no. 1, 1992.
- [43] L. Azar, "Principles and Quantitative Measurements of Cavitation," in *Handbook for Critical Cleaning*, vol. 2, B. Kanegsberg and E. Kanegsberg Eds., 2nd ed. Boca Raton, FL.: CRC Press, 2011.
- [44] G. Mark *et al.*, "OH-radical formation by ultrasound in aqueous solution – Part II: Terephthalate and Fricke dosimetry and the influence of various conditions on the sonolytic yield," *Ultrason Sonochem*, vol. 5, pp. 41-52, 1998.
- [45] A. Weissler, "Formation of Hydrogen Peroxide by Ultrasonic Waves: Free Radicals," *J. Am. Chem. Soc.*, vol. 81, no. 5, pp. 1077–1081, 1958.
- [46] K. R. Morison and C. A. Hutchinson, "Limitations of the Weissler reaction as a model reaction for measuring the efficiency of hydrodynamic cavitation," *Ultrason Sonochem*, vol. 16, no. 1, pp. 176-83, Jan 2009, doi: 10.1016/j.ultsonch.2008.07.001.
- [47] D. B. Rajamma, S. Anandan, N. S. M. Yusof, B. G. Pollet, and M. Ashokkumar, "Sonochemical dosimetry: A comparative study of Weissler, Fricke and terephthalic acid methods," *Ultrason Sonochem*, vol. 72, p. 105413, Apr 2021, doi: 10.1016/j.ultsonch.2020.105413.
- [48] M. Hodnett and P. Prentice, "Measurement techniques in power ultrasonics," in *Power Ultrasonics*, 2023, pp. 131-146.
- [49] S. Koda, T. Kimura, T. Kondo, and H. Mitome, "A standard method to calibrate sonochemical efficiency of an individual reaction system," *Ultrason Sonochem*, vol. 10, no. 3, pp. 149-56, May 2003, doi: 10.1016/S1350-4177(03)00084-1.
- [50] S.-I. Hatanaka, K. Yasui, T. Kozuka, T. Tuziuti, and H. Mitome, "Influence of bubble clustering on multibubble sonoluminescence," *Ultrasonics*, vol. 40, pp. 655-660, 2002.
- [51] M. Versluis, "High-speed imaging in fluids," *Experiments in Fluids*, vol. 54, no. 2, 2013, doi: 10.1007/s00348-013-1458-x.
- [52] R. Castrejón-García, J. R. Castrejón-Pita, G. D. Martín, and I. M. Hutchings, "The shadowgraph imaging technique and its modern application to fluid jets and drops," *Revista Mexicana de Física*, vol. 57, 3, pp. 266-275, 2011.
- [53] S. Deguchi, S. Takahashi, S. Tanimura, and H. Hiraki, "Producing single microbubbles with controlled size using microfiber," *Advances in Bioscience and Biotechnology*, vol. 02, no. 05, pp. 385-390, 2011, doi: 10.4236/abb.2011.25056.

- [54] D. Kröninger, K. Köhler, T. Kurz, and W. Lauterborn, "Particle tracking velocimetry of the flow field around a collapsing cavitation bubble," *Experiments in Fluids*, vol. 48, no. 3, pp. 395-408, 2009, doi: 10.1007/s00348-009-0743-1.
- [55] L. Yusuf, M. D. Symes, and P. Prentice, "Characterising the cavitation activity generated by an ultrasonic horn at varying tip-vibration amplitudes," *Ultrason Sonochem*, vol. 70, p. 105273, Jan 2021, doi: 10.1016/j.ultsonch.2020.105273.
- [56] C. J. Vian, P. R. Birkin, and T. G. Leighton, "Cluster Collapse in a Cylindrical Cell: Correlating Multibubble Sonoluminescence, Acoustic Pressure, and Erosion," *J. Phys. Chem.*, vol. 114, pp. 16416–16425, 2010.
- [57] D. Krefting, R. Mettin, and W. Lauterborn, "High-speed observation of acoustic cavitation erosion in multibubble systems," *Ultrasonics Sonochemistry*, vol. 11, no. 3-4, pp. 119-123, 2004, doi: 10.1016/j.ultsonch.2004.01.006.
- [58] J. A. Morton *et al.*, "New insights into sono-exfoliation mechanisms of graphite: In situ high-speed imaging studies and acoustic measurements," *Materials Today*, vol. 49, pp. 10-22, 2021, doi: 10.1016/j.mattod.2021.05.005.
- [59] A. Priyadarshi *et al.*, "In-situ observations and acoustic measurements upon fragmentation of free-floating intermetallics under ultrasonic cavitation in water," *Ultrason Sonochem*, vol. 80, p. 105820, Dec 2021, doi: 10.1016/j.ultsonch.2021.105820.
- [60] F. Reuter, S. Lauterborn, R. Mettin, and W. Lauterborn, "Membrane cleaning with ultrasonically driven bubbles," *Ultrason Sonochem*, vol. 37, pp. 542-560, Jul 2017, doi: 10.1016/j.ultsonch.2016.12.012.
- [61] K. V. Jenderka and C. Koch, "Investigation of spatial distribution of sound field parameters in ultrasound cleaning baths under the influence of cavitation," *Ultrasonics*, vol. 44 Suppl 1, pp. e401-6, Dec 22 2006, doi: 10.1016/j.ultras.2006.05.042.
- [62] M. Juschke and C. Koch, "Model processes and cavitation indicators for a quantitative description of an ultrasonic cleaning vessel: Part I: experimental results," *Ultrason Sonochem*, vol. 19, no. 4, pp. 787-95, Jul 2012, doi: 10.1016/j.ultsonch.2011.12.020.
- [63] F. J. Fuchs, "Ultrasonic cleaning and washing of surfaces," in *Power Ultrasonics*, 2015, pp. 577-609.
- [64] P. de Sternberg Stojalowski, "Process Challenge Devices for cleaning evaluation and how to go about them," *journal of the institute of decontamination sciences*, vol. 23, no. 2, 2019.

- [65] P. Bonnin, "Why measure protein quantity when looking for contamination?," *Journal of the institute of decontamination sciences*, vol. 23, no. 2, 2019.
- [66] *BS EN 61161:2013: Ultrasonics. Power Measurement. Radiation Force Balances and Performance Requirements*, B. S. Institute, 2013.
- [67] M. Ashokkumar, M. Hodnett, B. Zeqiri, F. Grieser, and G. J. Price, "Acoustic Emission Spectra from 515 kHz Cavitation in Aqueous Solutions Containing Surface-Active Solutes," *J. AM. CHEM. SOC.*, vol. 129, pp. 2250-2258, 2007.
- [68] M. Hodnett, R. Chow, and B. Zeqiri, "High-frequency acoustic emissions generated by a 20 kHz sonochemical horn processor detected using a novel broadband acoustic sensor: a preliminary study," *Ultrason Sonochem*, vol. 11, no. 6, pp. 441-54, Sep 2004, doi: 10.1016/j.ultsonch.2003.09.002.
- [69] P. Wu, X. Wang, W. Lin, and L. Bai, "Acoustic characterization of cavitation intensity: A review," *Ultrason Sonochem*, vol. 82, p. 105878, Jan 2022, doi: 10.1016/j.ultsonch.2021.105878.
- [70] *Ultrasonics - Measurement of cavitation noise in ultrasonic baths and ultrasonic reactors*, International, Electrotechnical, and Commission, Geneva, Switzerland., 2019.
- [71] P. Wu, L. Bai, W. Lin, and X. Wang, "Mechanism and dynamics of hydrodynamic-acoustic cavitation (HAC)," *Ultrason Sonochem*, vol. 49, pp. 89-96, Dec 2018, doi: 10.1016/j.ultsonch.2018.07.021.
- [72] C. Wang and S. Lin, "The nonlinear standing wave inside the space of liquid," *Science China Physics, Mechanics and Astronomy*, vol. 53, no. 3, pp. 496-503, 2010, doi: 10.1007/s11433-010-0105-2.
- [73] J. H. Song, K. Johansen, and P. Prentice, "An analysis of the acoustic cavitation noise spectrum: The role of periodic shock waves," *J Acoust Soc Am*, vol. 140, no. 4, p. 2494, Oct 2016, doi: 10.1121/1.4964633.
- [74] A. M. Hurrell and S. Rajagopal, "The Practicalities of Obtaining and Using Hydrophone Calibration Data to Derive Pressure Waveforms," *IEEE Trans Ultrason Ferroelectr Freq Control*, vol. 64, no. 1, pp. 126-140, Jan 2017, doi: 10.1109/TUFFC.2016.2594770.
- [75] K. Johansen, J. H. Song, and P. Prentice, "Performance characterisation of a passive cavitation detector optimised for subharmonic periodic shock waves from acoustic cavitation in MHz and sub-MHz ultrasound," *Ultrason Sonochem*, vol. 43, pp. 146-155, May 2018, doi: 10.1016/j.ultsonch.2018.01.007.

- [76] E. A. Brujan, T. Ikeda, and Y. Matsumoto, "Shock wave emission from a cloud of bubbles," *Soft Matter*, vol. 8, no. 21, 2012, doi: 10.1039/c2sm25379h.
- [77] C. M. Schoellhammer *et al.*, "Ultrasound-mediated gastrointestinal drug delivery," *Sci Transl Med*, vol. 7, no. 310, p. 310ra168, Oct 21 2015, doi: 10.1126/scitranslmed.aaa5937.
- [78] S. Datta *et al.*, "Correlation of cavitation with ultrasound enhancement of thrombolysis," *Ultrasound Med Biol*, vol. 32, no. 8, pp. 1–1267, 2006.
- [79] K. L. Tan and S. H. Yeo, "Bubble dynamics and cavitation intensity in milli-scale channels under an ultrasonic horn," *Ultrason Sonochem*, vol. 58, p. 104666, Nov 2019, doi: 10.1016/j.ultsonch.2019.104666.
- [80] I. Tzanakis, M. Hodnett, G. S. B. Lebon, N. Dezhkunov, and D. G. Eskin, "Calibration and performance assessment of an innovative high-temperature cavimeter," *Sensors and Actuators A: Physical*, vol. 240, pp. 57-69, 2016, doi: 10.1016/j.sna.2016.01.024.
- [81] A. Žnidarčič, R. Mettin, C. Cairós, and M. Dular, "Attached cavitation at a small diameter ultrasonic horn tip," *Physics of Fluids*, vol. 26, no. 2, 2014, doi: 10.1063/1.4866270.
- [82] B. Zeqiri, M. Hodnett, and A. J. Carroll, "Studies of a novel sensor for assessing the spatial distribution of cavitation activity within ultrasonic cleaning vessels," *Ultrasonics*, vol. 44, no. 1, pp. 73-82, Jan 2006, doi: 10.1016/j.ultras.2005.08.004.
- [83] B. Zeqiri, P. N. Gelat, M. Hodnett, and N. D. Lee, "A novel sensor for monitoring acoustic cavitation. Part I Concept theory and prototype development," *IEEE UFFC*, vol. 50, no. 10, 2003.
- [84] A. Sabraoui, C. Inserra, B. Gilles, J. C. Bera, and J. L. Mestas, "Feedback loop process to control acoustic cavitation," *Ultrason Sonochem*, vol. 18, no. 2, pp. 589-94, Mar 2011, doi: 10.1016/j.ultsonch.2010.07.011.
- [85] B. Gerold, S. Kotopoulis, C. McDougall, D. McGloin, M. Postema, and P. Prentice, "Laser-nucleated acoustic cavitation in focused ultrasound," *Rev Sci Instrum*, vol. 82, no. 4, p. 044902, Apr 2011, doi: 10.1063/1.3579499.
- [86] W. Lauterborn and E. Cramer, "Subharmonic Route to Chaos Observed in Acoustics," *Physical Review Letters*, vol. 47, no. 20, pp. 1445-1448, 1981, doi: 10.1103/PhysRevLett.47.1445.
- [87] B. Zeqiri, N. D. Lee, M. Hodnett, and P. N. Gelat, "A novel sensor for monitoring acoustic cavitation. Part II Prototype performance evaluation," *IEEE UFFC*, vol. 50, no. 10, 2003.

- [88] N. Vyas, Q. X. Wang, K. A. Manmi, R. L. Sammons, S. A. Kuehne, and A. D. Walmsley, "How does ultrasonic cavitation remove dental bacterial biofilm?," *Ultrason Sonochem*, vol. 67, p. 105112, Oct 2020, doi: 10.1016/j.ultsonch.2020.105112.
- [89] M. R. Hasan, C. A. Che Abdullah, M. Nor Afizah, M. S. Mohd Ghazali, and M. A. Noranizan, "Efficacy of ultrasonic cleaning on cockle shells," *Journal of Food Engineering*, vol. 352, 2023, doi: 10.1016/j.jfoodeng.2023.111523.
- [90] X. Zhu, T. J. Mason, F. Chemat, M. Ashokkumar, and B. K. Tiwari, "Power ultrasonics for food processing," in *Power Ultrasonics*, 2023, pp. 701-720.
- [91] P. de Sternberg Stojalowski. *Features of WD and the optimal cycle*. (2020).
- [92] F. J. Fuchs and J. D. Kramlick, "Ultrasonic cleaning," in *Power Ultrasonics*, 2023, pp. 455-471.
- [93] D. Y. Hoo *et al.*, "Ultrasonic cavitation: An effective cleaner and greener intensification technology in the extraction and surface modification of nanocellulose," *Ultrason Sonochem*, vol. 90, p. 106176, Nov 2022, doi: 10.1016/j.ultsonch.2022.106176.
- [94] I. Tzanakis, G. S. Lebon, D. G. Eskin, and K. A. Pericleous, "Characterizing the cavitation development and acoustic spectrum in various liquids," *Ultrason Sonochem*, vol. 34, pp. 651-662, Jan 2017, doi: 10.1016/j.ultsonch.2016.06.034.
- [95] M. Khavari *et al.*, "Cavitation-induced shock wave behaviour in different liquids," *Ultrason Sonochem*, vol. 94, p. 106328, Mar 2023, doi: 10.1016/j.ultsonch.2023.106328.
- [96] B. Sanderson, "Applied sonochemistry—the uses of power ultrasound in chemistry and processing. By Timothy J Mason and John P Lorimer, Wiley-VCH Verlag, Weinheim, 2002, 303 pp, ISBN 3-527-30205-0," *Journal of Chemical Technology & Biotechnology*, vol. 79, no. 2, pp. 207-208, 2004, doi: 10.1002/jctb.957.
- [97] J. Du and F. Chen, "Cavitation dynamics and flow aggressiveness in ultrasonic cavitation erosion," *International Journal of Mechanical Sciences*, vol. 204, 2021, doi: 10.1016/j.ijmecsci.2021.106545.
- [98] P. R. Birkin, D. G. Offen, C. J. Vian, and T. G. Leighton, "Multiple observations of cavitation cluster dynamics close to an ultrasonic horn tip," *J Acoust Soc Am*, vol. 130, no. 5, pp. 3379-88, Nov 2011, doi: 10.1121/1.3650536.
- [99] A. Moussatov, C. Granger, and B. Dubus, "Cone-like bubble formation in ultrasonic cavitation field," *Ultrason Sonochem*, vol. 10, no. 4-5, pp. 191-5, Jul 2003, doi: 10.1016/S1350-4177(02)00152-9.

- [100] L. Bai, W. Xu, J. Deng, C. Li, D. Xu, and Y. Gao, "Generation and control of acoustic cavitation structure," *Ultrason Sonochem*, vol. 21, no. 5, pp. 1696-706, Sep 2014, doi: 10.1016/j.ultsonch.2014.02.027.
- [101] G. Kozmus, J. Zevnik, M. Hocevar, M. Dular, and M. Petkovsek, "Characterization of cavitation under ultrasonic horn tip - Proposition of an acoustic cavitation parameter," *Ultrason Sonochem*, vol. 89, p. 106159, Sep 2022, doi: 10.1016/j.ultsonch.2022.106159.
- [102] A. Bampouli *et al.*, "Understanding the ultrasound field of high viscosity mixtures: Experimental and numerical investigation of a lab scale batch reactor," *Ultrason Sonochem*, vol. 97, p. 106444, Jul 2023, doi: 10.1016/j.ultsonch.2023.106444.
- [103] C. P. Baldé, V. Forti, V. Gray, R. Kuehr, and P. Stegmann, "The Global E-waste Monitor – 2017," Bonn/Geneva/Vienna., 2017.
- [104] (2020). *The Global E-waste Monitor 2020: Quantities, flows and the circular economy potential*.
- [105] M. D. Rao, K. K. Singh, C. A. Morrison, and J. B. Love, "Challenges and opportunities in the recovery of gold from electronic waste," *RSC Adv*, vol. 10, no. 8, pp. 4300-4309, Jan 24 2020, doi: 10.1039/c9ra07607g.
- [106] K. Zhang, J. L. Schnoor, and E. Y. Zeng, "E-waste recycling: where does it go from here?," *Environ Sci Technol*, vol. 46, no. 20, pp. 10861-7, Oct 16 2012, doi: 10.1021/es303166s.
- [107] Y. Lu and Z. Xu, "Precious metals recovery from waste printed circuit boards: A review for current status and perspective," *Resources, Conservation and Recycling*, vol. 113, pp. 28-39, 2016, doi: 10.1016/j.resconrec.2016.05.007.
- [108] A. H. Hu, M. Matsumoto, T. C. Kuo, and S. Smith, *Technologies and Eco-innovation towards Sustainability II: Eco Design Assessment and Management*. Singapore: Springer Nature, 2019.
- [109] J. Szalatkiwicz, "Metals Recovery from Artificial Ore in Case of Printed Circuit Boards, Using Plasmatron Plasma Reactor," *Materials (Basel)*, vol. 9, no. 8, Aug 10 2016, doi: 10.3390/ma9080683.
- [110] P. Sivakumar, D. Prabhakaran, and M. Thirumarimurugan, "Optimization Studies on Recovery of Metals from Printed Circuit Board Waste," *Bioinorg Chem Appl*, vol. 2018, p. 1067512, 2018, doi: 10.1155/2018/1067512.

- [111] B. Ghosh, M. K. Ghosh, P. Parhi, P. S. Mukherjee, and B. K. Mishra, "Waste Printed Circuit Boards recycling: an extensive assessment of current status," *Journal of Cleaner Production*, vol. 94, pp. 5-19, 2015, doi: 10.1016/j.jclepro.2015.02.024.
- [112] R. Marin Rivera, G. Zante, J. M. Hartley, K. S. Ryder, and A. P. Abbott, "Catalytic dissolution of metals from printed circuit boards using a calcium chloride-based deep eutectic solvent," *Green Chemistry*, vol. 24, no. 7, pp. 3023-3034, 2022, doi: 10.1039/d1gc04694b.
- [113] S. M. Abdelbasir, C. T. El-Sheltawy, and D. M. Abdo, "Green Processes for Electronic Waste Recycling: A Review," *Journal of Sustainable Metallurgy*, vol. 4, no. 2, pp. 295-311, 2018, doi: 10.1007/s40831-018-0175-3.
- [114] (2003). *Directive 2002/96/EC of the European Parliament and of the Council of 27 January 2003 on waste electrical and electronic equipment (WEEE)*.
- [115] (2012). *Directive 2012/19/EU of the European Parliament and of the Council of 4 July 2012 on waste electrical and electronic equipment (WEEE)*.
- [116] E. Y. Yazici and H. Deveci, "Extraction of metals from waste printed circuit boards (WPCBs) in H<sub>2</sub>SO<sub>4</sub>-CuSO<sub>4</sub>-NaCl solutions," *Hydrometallurgy*, vol. 139, pp. 30-38, 2013, doi: 10.1016/j.hydromet.2013.06.018.
- [117] M. Kaya, "Recovery of metals and nonmetals from electronic waste by physical and chemical recycling processes," *Waste Manag*, vol. 57, pp. 64-90, Nov 2016, doi: 10.1016/j.wasman.2016.08.004.
- [118] R. Jagers, "Decarbonisation: materials and circularity challenges for clean technologies: The role of Critical Raw Materials in reaching net-zero emissions," Royal Society of Chemistry, 2021.
- [119] J. Cui and L. Zhang, "Metallurgical recovery of metals from electronic waste: a review," *J Hazard Mater*, vol. 158, no. 2-3, pp. 228-56, Oct 30 2008, doi: 10.1016/j.jhazmat.2008.02.001.
- [120] S. W. Won, P. Kotte, W. Wei, A. Lim, and Y. S. Yun, "Biosorbents for recovery of precious metals," *Bioresour Technol*, vol. 160, pp. 203-12, May 2014, doi: 10.1016/j.biortech.2014.01.121.
- [121] P. Zhu, Y. Chen, L. Y. Wang, and M. Zhou, "Treatment of waste printed circuit board by green solvent using ionic liquid," *Waste Manag*, vol. 32, no. 10, pp. 1914-8, Oct 2012, doi: 10.1016/j.wasman.2012.05.025.
- [122] P. Zhu, Y. Chen, L. Y. Wang, G. R. Qian, M. Zhou, and J. Zhou, "A novel approach to separation of waste printed circuit boards using dimethyl sulfoxide," *International*

- Journal of Environmental Science and Technology*, vol. 10, no. 1, pp. 175-180, 2012, doi: 10.1007/s13762-012-0124-9.
- [123] M. Goosey and R. Kellner, "A Scoping Study End-of-Life Printed Circuit Boards," The Centre for Sustainable Design, 2002.
- [124] I. Masavetas *et al.*, "Production of Copper Powder from Printed Circuit Boards by Electrodeposition," *Global NEST Journal*, vol. 11, no. 2, pp. 241-247, 2009.
- [125] L. A. Castro and A. H. Martins, "Recovery of tin and copper by recycling of printed circuit boards from obsolete computers," *Brazilian Journal of Chemical Engineering*, vol. 26, no. 4, pp. 649-657, 2009.
- [126] K. Koyama, M. Tanaka, and J.-c. Lee, "Copper Leaching Behavior from Waste Printed Circuit Board in Ammoniacal Alkaline Solution," *Materials Transactions*, vol. 47, no. 7, pp. 1788-1792, 2006, doi: 10.2320/matertrans.47.1788.
- [127] T. Oishi, K. Koyama, S. Alam, M. Tanaka, and J. C. Lee, "Recovery of high purity copper cathode from printed circuit boards using ammoniacal sulfate or chloride solutions," *Hydrometallurgy*, vol. 89, no. 1-2, pp. 82-88, 2007, doi: 10.1016/j.hydromet.2007.05.010.
- [128] A. Isildar, J. van de Vossenberg, E. R. Rene, E. D. van Hullebusch, and P. N. Lens, "Two-step bioleaching of copper and gold from discarded printed circuit boards (PCB)," *Waste Manag*, vol. 57, pp. 149-157, Nov 2016, doi: 10.1016/j.wasman.2015.11.033.
- [129] P. P. Sheng and T. H. Etsell, "Recovery of gold from computer circuit board scrap using aqua regia," *Waste Manag Res*, vol. 25, no. 4, pp. 380-3, Aug 2007, doi: 10.1177/0734242X07076946.
- [130] S. Udayakumar, M. I. B. A. Razak, and S. Ismail, "Recovering valuable metals from Waste Printed Circuit Boards (WPCB): A short review," *Materials Today: Proceedings*, vol. 66, pp. 3062-3070, 2022, doi: 10.1016/j.matpr.2022.07.364.
- [131] Z. Wu, W. Yuan, J. Li, X. Wang, L. Liu, and J. Wang, "A critical review on the recycling of copper and precious metals from waste printed circuit boards using hydrometallurgy," *Frontiers of Environmental Science & Engineering*, vol. 11, no. 5, 2017, doi: 10.1007/s11783-017-0995-6.
- [132] E. Hsu, K. Barmak, A. C. West, and A.-H. A. Park, "Advancements in the treatment and processing of electronic waste with sustainability: a review of metal extraction and recovery technologies," *Green Chemistry*, vol. 21, no. 5, pp. 919-936, 2019, doi: 10.1039/c8gc03688h.

- [133] A. Chaurasia, K. K. Singh, and T. R. Mankhand, "Extraction of Tin and Copper by Acid Leaching of PCBs," *International Journal of Metallurgical Engineering*, vol. 2, no. 2, pp. 243-248, 2013, doi: 10.5923/j.ijmee.20130202.17.
- [134] I. Birloaga, I. De Michelis, F. Ferella, M. Buzatu, and F. Veglio, "Study on the influence of various factors in the hydrometallurgical processing of waste printed circuit boards for copper and gold recovery," *Waste Manag*, vol. 33, no. 4, pp. 935-41, Apr 2013, doi: 10.1016/j.wasman.2013.01.003.
- [135] I. Birloaga, V. Coman, B. Kopacek, and F. Veglio, "An advanced study on the hydrometallurgical processing of waste computer printed circuit boards to extract their valuable content of metals," *Waste Manag*, vol. 34, no. 12, pp. 2581-6, Dec 2014, doi: 10.1016/j.wasman.2014.08.028.
- [136] M. K. Jha, J.-C. Lee, A. Kumari, P. K. Choubey, V. Kumar, and J. Jeong, "Pressure Leaching of Metals from Waste Printed Circuit Boards using Sulfuric Acid," *JOM*, vol. 63, no. 8, pp. 29-32, 2011.
- [137] A. D. Bas, H. Deveci, and E. Y. Yazici, "Treatment of manufacturing scrap TV boards by nitric acid leaching," *Separation and Purification Technology*, vol. 130, pp. 151-159, 2014, doi: 10.1016/j.seppur.2014.04.008.
- [138] M. Kumar, J.-c. Lee, M.-S. Kim, J. Jeong, and K. Yoo, "LEACHING OF METALS FROM WASTE PRINTED CIRCUIT BOARDS (WPCBs) USING SULFURIC AND NITRIC ACIDS," *Environmental Engineering and Management Journal*, vol. 13, no. 10, pp. 2601-2607, 2014, doi: 10.30638/eemj.2014.290.
- [139] A. Ashiq, J. Kulkarni, and M. Vithanage, "Hydrometallurgical Recovery of Metals From E-waste," in *Electronic Waste Management and Treatment Technology*, 2019, pp. 225-246.
- [140] A. Akcil, C. Erust, C. S. Gahan, M. Ozgun, M. Sahin, and A. Tuncuk, "Precious metal recovery from waste printed circuit boards using cyanide and non-cyanide lixivants--A review," *Waste Manag*, vol. 45, pp. 258-71, Nov 2015, doi: 10.1016/j.wasman.2015.01.017.
- [141] G. Liu, D. Pan, Y. Wu, H. Yuan, L. Yu, and W. Wang, "An integrated and sustainable hydrometallurgical process for enrichment of precious metals and selective separation of copper, zinc, and lead from a roasted sand," *Waste Manag*, vol. 132, pp. 133-141, Aug 1 2021, doi: 10.1016/j.wasman.2021.07.020.
- [142] L. Zhang and Z. Xu, "A review of current progress of recycling technologies for metals from waste electrical and electronic equipment," *Journal of Cleaner Production*, vol. 127, pp. 19-36, 2016, doi: 10.1016/j.jclepro.2016.04.004.

- [143] S. Ilyas, J.-c. Lee, and R.-a. Chi, "Bioleaching of metals from electronic scrap and its potential for commercial exploitation," *Hydrometallurgy*, vol. 131-132, pp. 138-143, 2013, doi: 10.1016/j.hydromet.2012.11.010.
- [144] M. A. Faramarzi, M. Stagars, E. Pensini, W. Krebs, and H. Brandl, "Metal solubilization from metal-containing solid materials by cyanogenic *Chromobacterium violaceum*," *J Biotechnol*, vol. 113, no. 1-3, pp. 321-6, Sep 30 2004, doi: 10.1016/j.jbiotec.2004.03.031.
- [145] A. Abbott, D. Boothby, G. Capper, D. L. Davies, and R. Rasheed, "Deep Eutectic Solvents Formed between Choline Chloride and Carboxylic Acids: Versatile Alternatives to Ionic Liquids," *J. AM. CHEM. SOC.*, vol. 126, pp. 9142-9147, 2004.
- [146] A. P. Abbott, "Deep eutectic solvents and their application in electrochemistry," *Current Opinion in Green and Sustainable Chemistry*, vol. 36, 2022, doi: 10.1016/j.cogsc.2022.100649.
- [147] M. A. R. Martins, S. P. Pinho, and J. A. P. Coutinho, "Insights into the Nature of Eutectic and Deep Eutectic Mixtures," *Journal of Solution Chemistry*, vol. 48, no. 7, pp. 962-982, 2018, doi: 10.1007/s10953-018-0793-1.
- [148] Z. Yuan, H. Liu, W. F. Yong, Q. She, and J. Esteban, "Status and advances of deep eutectic solvents for metal separation and recovery," *Green Chemistry*, vol. 24, no. 5, pp. 1895-1929, 2022, doi: 10.1039/d1gc03851f.
- [149] E. L. Smith, A. P. Abbott, and K. S. Ryder, "Deep eutectic solvents (DESs) and their applications," *Chem Rev*, vol. 114, no. 21, pp. 11060-82, Nov 12 2014, doi: 10.1021/cr300162p.
- [150] B. B. Hansen *et al.*, "Deep Eutectic Solvents: A Review of Fundamentals and Applications," *Chem Rev*, vol. 121, no. 3, pp. 1232-1285, Feb 10 2021, doi: 10.1021/acs.chemrev.0c00385.
- [151] T. El Achkar, H. Greige-Gerges, and S. Fourmentin, "Basics and properties of deep eutectic solvents: a review," *Environmental Chemistry Letters*, vol. 19, no. 4, pp. 3397-3408, 2021, doi: 10.1007/s10311-021-01225-8.
- [152] E. F. S. Authority, "Scientific Opinion on safety and efficacy of choline chloride as a feed additive for all animal species," *EFSA Journal*, vol. 9, no. 9, 2011, doi: 10.2903/j.efsa.2011.2353.
- [153] A. Abbott, G. Capper, D. L. Davies, K. J. McKenzie, and S. U. Obi, "Solubility of Metal Oxides in Deep Eutectic Solvents Based on Choline Chloride," *Journal of Chemical & Engineering Data*, vol. 51, pp. 1280-1282, 2006.

- [154] A. P. Abbott, G. Capper, D. L. Davies, R. K. Rasheed, and V. Tambyrajah, "Novel solvent properties of choline chloride/urea mixtures," *Chem Commun (Camb)*, no. 1, pp. 70-1, Jan 7 2003, doi: 10.1039/b210714g.
- [155] K. A. Omar and R. Sadeghi, "Physicochemical properties of deep eutectic solvents: A review," *Journal of Molecular Liquids*, vol. 360, 2022, doi: 10.1016/j.molliq.2022.119524.
- [156] A. P. Abbott, G. Capper, D. L. Davies, and R. K. Rasheed, "Ionic liquid analogues formed from hydrated metal salts," *Chemistry*, vol. 10, no. 15, pp. 3769-74, Aug 6 2004, doi: 10.1002/chem.200400127.
- [157] S. P. Ijardar, V. Singh, and R. L. Gardas, "Revisiting the Physicochemical Properties and Applications of Deep Eutectic Solvents," *Molecules*, vol. 27, no. 4, Feb 17 2022, doi: 10.3390/molecules27041368.
- [158] A. Abbott, G. Capper, D. L. Davies, and R. Rasheed, "Ionic Liquids Based upon Metal Halide/Substituted Quaternary Ammonium Salt Mixtures," *Inorg. Chem.*, vol. 43, p. 3447-3452, 2004.
- [159] A. P. Abbott, G. Capper, and S. Gray, "Design of improved deep eutectic solvents using hole theory," *Chemphyschem*, vol. 7, no. 4, pp. 803-6, Apr 10 2006, doi: 10.1002/cphc.200500489.
- [160] C. D'Agostino, R. C. Harris, A. P. Abbott, L. F. Gladden, and M. D. Mantle, "Molecular motion and ion diffusion in choline chloride based deep eutectic solvents studied by <sup>1</sup>H pulsed field gradient NMR spectroscopy," *Phys Chem Chem Phys*, vol. 13, no. 48, pp. 21383-91, Dec 28 2011, doi: 10.1039/c1cp22554e.
- [161] Y. Dai, G. J. Witkamp, R. Verpoorte, and Y. H. Choi, "Tailoring properties of natural deep eutectic solvents with water to facilitate their applications," *Food Chem*, vol. 187, pp. 14-9, Nov 15 2015, doi: 10.1016/j.foodchem.2015.03.123.
- [162] H. G. Morrison, C. C. Sun, and S. Neervannan, "Characterization of thermal behavior of deep eutectic solvents and their potential as drug solubilization vehicles," *Int J Pharm*, vol. 378, no. 1-2, pp. 136-9, Aug 13 2009, doi: 10.1016/j.ijpharm.2009.05.039.
- [163] F. S. Oliveira, A. B. Pereiro, L. P. N. Rebelo, and I. M. Marrucho, "Deep eutectic solvents as extraction media for azeotropic mixtures," *Green Chemistry*, vol. 15, no. 5, 2013, doi: 10.1039/c3gc37030e.
- [164] K. H. Kim, A. Eudes, K. Jeong, C. G. Yoo, C. S. Kim, and A. Ragauskas, "Integration of renewable deep eutectic solvents with engineered biomass to achieve a closed-

- loop biorefinery," *Proc Natl Acad Sci U S A*, vol. 116, no. 28, pp. 13816-13824, Jul 9 2019, doi: 10.1073/pnas.1904636116.
- [165] M. Manolova, R. Böck, I. Scharf, T. Mehner, and T. Lampke, "Electrodeposition of Pd alloys from choline chloride/urea deep eutectic solvents," *Journal of Alloys and Compounds*, vol. 855, 2021, doi: 10.1016/j.jallcom.2020.157462.
- [166] A. P. Abbott, G. Frisch, and K. S. Ryder, "Electroplating Using Ionic Liquids," *Annual Review of Materials Research*, vol. 43, no. 1, pp. 335-358, 2013, doi: 10.1146/annurev-matsci-071312-121640.
- [167] A. Y. M. Al-Murshedi, A. Al-Yasari, H. F. Alesary, and H. K. Ismail, "Electrochemical fabrication of cobalt films in a choline chloride–ethylene glycol deep eutectic solvent containing water," *Chemical Papers*, vol. 74, no. 2, pp. 699-709, 2019, doi: 10.1007/s11696-019-01025-z.
- [168] A. P. Abbott, A. Ballantyne, R. C. Harris, J. A. Juma, K. S. Ryder, and G. Forrest, "A Comparative Study of Nickel Electrodeposition Using Deep Eutectic Solvents and Aqueous Solutions," *Electrochimica Acta*, vol. 176, pp. 718-726, 2015, doi: 10.1016/j.electacta.2015.07.051.
- [169] Y. H. You, C. D. Gu, X. L. Wang, and J. P. Tu, "Electrodeposition of Ni–Co alloys from a deep eutectic solvent," *Surface and Coatings Technology*, vol. 206, no. 17, pp. 3632-3638, 2012, doi: 10.1016/j.surfcoat.2012.03.001.
- [170] C. Gu and J. Tu, "One-step fabrication of nanostructured Ni film with lotus effect from deep eutectic solvent," *Langmuir*, vol. 27, no. 16, pp. 10132-40, Aug 16 2011, doi: 10.1021/la200778a.
- [171] J. C. Malaquias, M. Steichen, M. Thomassey, and P. J. Dale, "Electrodeposition of Cu–In alloys from a choline chloride based deep eutectic solvent for photovoltaic applications," *Electrochimica Acta*, vol. 103, pp. 15-22, 2013, doi: 10.1016/j.electacta.2013.04.068.
- [172] A. P. Abbott, G. Capper, K. J. McKenzie, and K. S. Ryder, "Electrodeposition of zinc–tin alloys from deep eutectic solvents based on choline chloride," *Journal of Electroanalytical Chemistry*, vol. 599, no. 2, pp. 288-294, 2007, doi: 10.1016/j.jelechem.2006.04.024.
- [173] S. Ghosh and S. Roy, "Electrochemical copper deposition from an ethaline–CuCl<sub>2</sub>·2H<sub>2</sub>O DES," *Surface and Coatings Technology*, vol. 238, pp. 165-173, 2014, doi: 10.1016/j.surfcoat.2013.10.069.

- [174] A. P. Abbott, G. Capper, K. J. McKenzie, A. Glidle, and K. S. Ryder, "Electropolishing of stainless steels in a choline chloride based ionic liquid: an electrochemical study with surface characterisation using SEM and atomic force microscopy," *Phys Chem Chem Phys*, vol. 8, no. 36, pp. 4214-21, Sep 28 2006, doi: 10.1039/b607763n.
- [175] A. P. Abbott, R. C. Harris, F. Holyoak, G. Frisch, J. Hartley, and G. R. T. Jenkin, "Electrocatalytic recovery of elements from complex mixtures using deep eutectic solvents," *Green Chemistry*, vol. 17, no. 4, pp. 2172-2179, 2015, doi: 10.1039/c4gc02246g.
- [176] G. R. T. Jenkin *et al.*, "The application of deep eutectic solvent ionic liquids for environmentally-friendly dissolution and recovery of precious metals," *Minerals Engineering*, vol. 87, pp. 18-24, 2016, doi: 10.1016/j.mineng.2015.09.026.
- [177] J. M. Hartley, J. Allen, J. Meierl, A. Schmidt, I. Krossing, and A. P. Abbott, "Calcium chloride-based systems for metal electrodeposition," *Electrochimica Acta*, vol. 402, 2022, doi: 10.1016/j.electacta.2021.139560.
- [178] M.-L. Doche, A. Mandroyan, M. Mourad-Mahmoud, V. Moutarlier, and J.-Y. Hihn, "An ultrasonic-assisted process for copper recovery in a des solvent: Leaching and re-deposition," *Chemical Engineering and Processing: Process Intensification*, vol. 121, pp. 90-96, 2017, doi: 10.1016/j.cep.2017.08.006.
- [179] K. M. Swamy and K. L. Narayana, "Intensification of leaching process by dual-frequency ultrasound," *Ultrason Sonochem*, vol. 8, pp. 341-346, 2001.
- [180] R. Marin Rivera *et al.*, "Ultra-fast extraction of metals from a printed circuit board using high power ultrasound in a calcium chloride-based deep eutectic solvent," *RSC Sustainability [under review]*, 2023.
- [181] C. S. Desilets, J. D. Fraser, and G. S. Kino, "The design of efficient broad-band piezoelectric transducers," *IEEE TRANSACTIONS ON SONICS AND ULTRASONICS*, vol. 25, no. 3, pp. 115-125, 1978.
- [182] T. L. Szabo, *Diagnostic Ultrasound Imaging: Inside Out*. Elsevier Academic Press, 2004.
- [183] P. Acoustics. "PVdF." online. <https://www.acoustics.co.uk/product/pvdf/> (accessed 07, 2023).
- [184] R. Oshana, "Overview of DSP Algorithms," in *DSP for Embedded and Real-Time Systems*, 2012, pp. 113-131.

- [185] E. Digital Signal Processing Committee IEEE Acoustics Speech and Signal Processing Society, "Programs for Digital Signal Processing Digital Signal Processing Committee IEEE Acoustics Speech and Signal Processing Society," *IEEE TRANSACTIONS ON SYSTEMS, MAN, AND CYBERNETICS*, vol. 11, no. 7, 1981.
- [186] N. P. Laboratory. *Cavitation Sensor User Notes v7*, 2022.
- [187] G. Sinibaldi *et al.*, "Laser induced cavitation: Plasma generation and breakdown shockwave," *Physics of Fluids*, vol. 31, no. 10, 2019, doi: 10.1063/1.5119794.
- [188] S. E. Rigby, A. Tyas, T. Bennett, S. D. Clarke, and S. D. Fay, "The Negative Phase of the Blast Load," *International Journal of Protective Structures*, vol. 5, no. 1, 2014.
- [189] Y. Zhou, "Reduction of Bubble Cavitation by Modifying the Diffraction Wave from a Lithotripter Aperture," *Journal of Endourology*, vol. 26, no. 8, pp. 1075-1084, 2012, doi: 10.1089/end.2011.0671.
- [190] S. Azmi, M. F. Koudahi, and E. Frackowiak, "Reline deep eutectic solvent as a green electrolyte for electrochemical energy storage applications," *Energy & Environmental Science*, vol. 15, no. 3, pp. 1156-1171, 2022, doi: 10.1039/d1ee02920g.
- [191] A. Yadav and S. Pandey, "Densities and Viscosities of (Choline Chloride + Urea) Deep Eutectic Solvent and Its Aqueous Mixtures in the Temperature Range 293.15 K to 363.15 K," *Journal of Chemical & Engineering Data*, vol. 59, no. 7, pp. 2221-2229, 2014, doi: 10.1021/je5001796.
- [192] L. Yusuf, "Optimising acoustic cavitation for industrial application," PhD, James Watt School of Engineering, University of Glasgow, 2022.
- [193] T. Yamashita and K. Ando, "Low-intensity ultrasound induced cavitation and streaming in oxygen-supersaturated water: Role of cavitation bubbles as physical cleaning agents," *Ultrason Sonochem*, vol. 52, pp. 268-279, Apr 2019, doi: 10.1016/j.ultsonch.2018.11.025.
- [194] C. J. B. Vian, P. R. Birkin, and T. G. Leighton, "Cluster Collapse in a Cylindrical Cell: Correlating Multibubble Sonoluminescence, Acoustic Pressure, and Erosion," *J. Phys. Chem.*, vol. 114, pp. 16416-16425, 2010.
- [195] N. C. Eddingsaas and K. S. Suslick, "Evidence for a Plasma Core during Multibubble Sonoluminescence in Sulfuric Acid," *J. AM. CHEM. SOC.*, vol. 129, pp. 3838-3839, 2007.

- [196] A. Thiemann, F. Holsteyns, C. Cairos, and R. Mettin, "Sonoluminescence and dynamics of cavitation bubble populations in sulfuric acid," *Ultrason Sonochem*, vol. 34, pp. 663-676, Jan 2017, doi: 10.1016/j.ultsonch.2016.06.013.
- [197] Hielscher and Ultrasonics. "Cavitation Erosion Testing." <https://www.hielscher.com/cavitation-erosion-testing.htm> (accessed 09/2023).
- [198] Y. Fang, T. Yamamoto, and S. Komarov, "Cavitation and acoustic streaming generated by different sonotrode tips," *Ultrason Sonochem*, vol. 48, pp. 79-87, Nov 2018, doi: 10.1016/j.ultsonch.2018.05.011.
- [199] H. A. Sabzkoochi and G. Kolliopoulos, "Green Zero-Waste Metal Extraction and Recycling from Printed Circuit Boards," presented at the International Conference on Raw Materials and Circular Economy, 2021.
- [200] J. M. Hartley *et al.*, "Tailoring lixiviant properties to optimise selectivity in E-waste recycling," *RSC Sustainability*, vol. 1, no. 1, pp. 107-116, 2023, doi: 10.1039/d2su00038e.
- [201] G. Zante, R. Marin Rivera, J. M. Hartley, and A. P. Abbott, "Efficient recycling of metals from solar cells using catalytic etchants," *Journal of Cleaner Production*, vol. 370, 2022, doi: 10.1016/j.jclepro.2022.133552.
- [202] J. Jordens, B. Bamps, B. Gielen, L. Braeken, and T. Van Gerven, "The effects of ultrasound on micromixing," *Ultrason Sonochem*, vol. 32, pp. 68-78, Sep 2016, doi: 10.1016/j.ultsonch.2016.02.020.
- [203] N. Masuda, A. Maruyama, T. Eguchi, T. Hirakawa, and Y. Murakami, "Influence of Microbubbles on Free Radical Generation by Ultrasound in Aqueous Solution: Dependence of Ultrasound Frequency," *J Phys Chem B*, vol. 119, no. 40, pp. 12887-93, Oct 8 2015, doi: 10.1021/acs.jpcc.5b05707.
- [204] R. M. Santos, D. François, G. Mertens, J. Elsen, and T. Van Gerven, "Ultrasound-intensified mineral carbonation," *Applied Thermal Engineering*, vol. 57, no. 1-2, pp. 154-163, 2013, doi: 10.1016/j.applthermaleng.2012.03.035.
- [205] A. Mandroyan, M. Mourad-Mahmoud, M. L. Doche, and J. Y. Hihn, "Effects of ultrasound and temperature on copper electro reduction in Deep Eutectic Solvents (DES)," *Ultrason Sonochem*, vol. 21, no. 6, pp. 2010-9, Nov 2014, doi: 10.1016/j.ultsonch.2014.02.019.
- [206] H. B. Mitchell, *Image Fusion: Theories, Techniques and Applications*. Springer, 2010.

- [207] V. Rajinikanth, N. Sri Madhava Raja, and N. Dey, "A Beginner's Guide to Multilevel Image Thresholding," in *Intelligent Signal Processing and Data Analysis*, N. Dey Ed.: CRC Press, 2021.
- [208] G. Zante and M. Boltoeva, "Review on Hydrometallurgical Recovery of Metals with Deep Eutectic Solvents," *Sustainable Chemistry*, vol. 1, no. 3, pp. 238-255, 2020, doi: 10.3390/suschem1030016.
- [209] J. Li, P. Shi, Z. Wang, Y. Chen, and C. C. Chang, "A combined recovery process of metals in spent lithium-ion batteries," *Chemosphere*, vol. 77, no. 8, pp. 1132-6, Nov 2009, doi: 10.1016/j.chemosphere.2009.08.040.
- [210] R. Sims *et al.*, "Transport," in *Climate Change 2014: Mitigation of Climate Change. Contribution of Working Group III to the Fifth Assessment Report of the Intergovernmental Panel on Climate Change*: Cambridge University Press, 2014, pp. 1-30.
- [211] G. Hill, O. Heidrich, F. Creutzig, and P. Blythe, "The role of electric vehicles in near-term mitigation pathways and achieving the UK's carbon budget," *Applied Energy*, vol. 251, 2019, doi: 10.1016/j.apenergy.2019.04.107.
- [212] J.-P. Skeete, P. Wells, X. Dong, O. Heidrich, and G. Harper, "Beyond the Event horizon: Battery waste, recycling, and sustainability in the United Kingdom electric vehicle transition," *Energy Research & Social Science*, vol. 69, 2020, doi: 10.1016/j.erss.2020.101581.
- [213] N. Hill and J. Bates, "Europe's Clean Mobility Outlook: Scenarios for the EU LightDuty Vehicle fleet, Associated Energy Needs and emissions, 2020-2050," in "No. Ricardo/ED11522," Ricardo Energy & Environment, Ricardo Energy & Environment, 2018.
- [214] R. Sommerville, P. Zhu, M. A. Rajaeifar, O. Heidrich, V. Goodship, and E. Kendrick, "A qualitative assessment of lithium ion battery recycling processes," *Resources, Conservation and Recycling*, vol. 165, 2021, doi: 10.1016/j.resconrec.2020.105219.
- [215] G. Harper *et al.*, "Recycling lithium-ion batteries from electric vehicles," *Nature*, vol. 575, no. 7781, pp. 75-86, Nov 2019, doi: 10.1038/s41586-019-1682-5.
- [216] J. Heelan *et al.*, "Current and Prospective Li-Ion Battery Recycling and Recovery Processes," *Jom*, vol. 68, no. 10, pp. 2632-2638, 2016, doi: 10.1007/s11837-016-1994-y.

- [217] R. Sommerville, J. Shaw-Stewart, V. Goodship, N. Rowson, and E. Kendrick, "A review of physical processes used in the safe recycling of lithium ion batteries," *Sustainable Materials and Technologies*, vol. 25, 2020, doi: 10.1016/j.susmat.2020.e00197.
- [218] D. L. Thompson, I. M. Pateli, C. Lei, A. Jarvis, A. P. Abbott, and J. M. Hartley, "Separation of nickel from cobalt and manganese in lithium ion batteries using deep eutectic solvents," *Green Chemistry*, vol. 24, no. 12, pp. 4877-4886, 2022, doi: 10.1039/d2gc00606e.
- [219] C. Lei *et al.*, "Lithium ion battery recycling using high-intensity ultrasonication," *Green Chemistry*, vol. 23, no. 13, pp. 4710-4715, 2021, doi: 10.1039/d1gc01623g.
- [220] D. L. Thompson *et al.*, "The importance of design in lithium ion battery recycling – a critical review," *Green Chemistry*, vol. 22, no. 22, pp. 7585-7603, 2020, doi: 10.1039/d0gc02745f.
- [221] J. Marshall, D. Gastol, R. Sommerville, B. Middleton, V. Goodship, and E. Kendrick, "Disassembly of Li Ion Cells—Characterization and Safety Considerations of a Recycling Scheme," *Metals*, vol. 10, no. 6, 2020, doi: 10.3390/met10060773.
- [222] L. P. He, S. Y. Sun, X. F. Song, and J. G. Yu, "Recovery of cathode materials and Al from spent lithium-ion batteries by ultrasonic cleaning," *Waste Manag*, vol. 46, pp. 523-8, Dec 2015, doi: 10.1016/j.wasman.2015.08.035.
- [223] P. Dias, S. Javimczik, M. Benevit, H. Veit, and A. M. Bernardes, "Recycling WEEE: Extraction and concentration of silver from waste crystalline silicon photovoltaic modules," *Waste Manag*, vol. 57, pp. 220-225, Nov 2016, doi: 10.1016/j.wasman.2016.03.016.
- [224] J. I. Kwak, S. H. Nam, L. Kim, and Y. J. An, "Potential environmental risk of solar cells: Current knowledge and future challenges," *J Hazard Mater*, vol. 392, p. 122297, Jun 15 2020, doi: 10.1016/j.jhazmat.2020.122297.
- [225] G. Panthi, R. Bajagain, Y.-J. An, and S.-W. Jeong, "Leaching potential of chemical species from real perovskite and silicon solar cells," *Process Safety and Environmental Protection*, vol. 149, pp. 115-122, 2021, doi: 10.1016/j.psep.2020.10.035.
- [226] M. M. Rahman *et al.*, "End-of-Life Photovoltaic Recycled Silicon: A Sustainable Circular Materials Source for Electronic Industries," *Advanced Energy and Sustainability Research*, vol. 2, no. 11, 2021, doi: 10.1002/aesr.202100081.

- [227] M. Luo *et al.*, "A comprehensive hydrometallurgical recycling approach for the environmental impact mitigation of EoL solar cells," *Journal of Environmental Chemical Engineering*, vol. 9, no. 6, 2021, doi: 10.1016/j.jece.2021.106830.
- [228] B. Jung, J. Park, D. Seo, and N. Park, "Sustainable System for Raw-Metal Recovery from Crystalline Silicon Solar Panels: From Noble-Metal Extraction to Lead Removal," *ACS Sustainable Chemistry & Engineering*, vol. 4, no. 8, pp. 4079-4083, 2016, doi: 10.1021/acssuschemeng.6b00894.
- [229] W. Li and T. Adachi, "Evaluation of long-term silver supply shortage for c-Si PV under different technological scenarios," *Natural Resource Modeling*, vol. 32, no. 1, 2018, doi: 10.1111/nrm.12176.
- [230] IRENA. (2016). *IRENA T12-06:2016, End of Life Management: Solar Photovoltaic Panels*.
- [231] European Union. (2021). *Emerging waste streams: Opportunities and challenges of the clean-energy transition from a circular economy perspective*.
- [232] P. Nain and A. Kumar, "Initial metal contents and leaching rate constants of metals leached from end-of-life solar photovoltaic waste: An integrative literature review and analysis," *Renewable and Sustainable Energy Reviews*, vol. 119, 2020, doi: 10.1016/j.rser.2019.109592.
- [233] D. Mulvaney, R. M. Richards, M. D. Bazilian, E. Hensley, G. Clough, and S. Sridhar, "Progress towards a circular economy in materials to decarbonize electricity and mobility," *Renewable and Sustainable Energy Reviews*, vol. 137, 2021, doi: 10.1016/j.rser.2020.110604.
- [234] J. Nover, R. Zapf-Gottwick, C. Feifel, M. Koch, J. W. Metzger, and J. H. Werner, "Long-term leaching of photovoltaic modules," *Japanese Journal of Applied Physics*, vol. 56, no. 8S2, 2017, doi: 10.7567/jjap.56.08md02.
- [235] M. Tamaro, A. Salluzzo, J. Rimauro, S. Schiavo, and S. Manzo, "Experimental investigation to evaluate the potential environmental hazards of photovoltaic panels," *J Hazard Mater*, vol. 306, pp. 395-405, Apr 5 2016, doi: 10.1016/j.jhazmat.2015.12.018.
- [236] C. Sener and V. Fthenakis, "Energy policy and financing options to achieve solar energy grid penetration targets: Accounting for external costs," *Renewable and Sustainable Energy Reviews*, vol. 32, pp. 854-868, 2014, doi: 10.1016/j.rser.2014.01.030.

- [237] Z. Zhang *et al.*, "Optimization of indium recovery from waste crystalline silicon heterojunction solar cells by acid leaching," *Solar Energy Materials and Solar Cells*, vol. 230, 2021, doi: 10.1016/j.solmat.2021.111218.
- [238] Y. K. Yi, H. S. Kim, T. Tran, S. K. Hong, and M. J. Kim, "Recovering valuable metals from recycled photovoltaic modules," *J Air Waste Manag Assoc*, vol. 64, no. 7, pp. 797-807, Jul 2014, doi: 10.1080/10962247.2014.891540.
- [239] E. Klugmann-Radziemska and P. Ostrowski, "Chemical treatment of crystalline silicon solar cells as a method of recovering pure silicon from photovoltaic modules," *Renewable Energy*, vol. 35, no. 8, pp. 1751-1759, 2010, doi: 10.1016/j.renene.2009.11.031.
- [240] L. Frisson *et al.*, "Recent Improvements in Industrial PV Module Recycling," in *Sixteenth European Photovoltaic Solar Energy Conference*, 2020, pp. 2160-2163.
- [241] S. Kang, S. Yoo, J. Lee, B. Boo, and H. Ryu, "Experimental investigations for recycling of silicon and glass from waste photovoltaic modules," *Renewable Energy*, vol. 47, pp. 152-159, 2012, doi: 10.1016/j.renene.2012.04.030.
- [242] T.-Y. Wang, J.-C. Hsiao, and C.-H. Du, "Recycling of Materials from Silicon Base Solar Cell Module," in *Proceedings of the 38th IEEE Photovoltaic Specialists Conference*, 2012, pp. 2355-2358.
- [243] L. Grandell and A. Thorenz, "Silver supply risk analysis for the solar sector," *Renewable Energy*, vol. 69, pp. 157-165, 2014, doi: 10.1016/j.renene.2014.03.032.
- [244] F. Yang *et al.*, "Electrochemical corrosion mechanisms of nickel-aluminium bronze with different nickel contents using the rotating disc electrode," *Corrosion Science*, vol. 157, pp. 438-449, 2019, doi: 10.1016/j.corsci.2019.06.018.
- [245] C. Deslouis, B. Tribollet, M. Duprat, and F. Moran, "Transient Mass Transfer at a Coated Rotating Disk Electrode: Diffusion and Electrohydrodynamical Impedances," *J. Electrochem. Soc.*, vol. 134, 1987.
- [246] F. B. Leitz and I. Marincic, "Enhanced mass transfer in electrochemical cells using turbulence promoters," *Journal of Applied Electrochemistry*, vol. 7, pp. 473-484, 1977.
- [247] A. Speidel, J. Mitchell-Smith, I. Bisterov, and A. T. Clare, "The importance of microstructure in electrochemical jet processing," *Journal of Materials Processing Technology*, vol. 262, pp. 459-470, 2018, doi: 10.1016/j.jmatprotec.2018.07.022.

- [248] J. Mitchell-Smith, A. Speidel, and A. T. Clare, "Advancing electrochemical jet methods through manipulation of the angle of address," *Journal of Materials Processing Technology*, vol. 255, pp. 364-372, 2018, doi: 10.1016/j.jmatprotec.2017.12.026.
- [249] J. Klima, "Application of ultrasound in electrochemistry. An overview of mechanisms and design of experimental arrangement," *Ultrasonics*, vol. 51, no. 2, pp. 202-9, Feb 2011, doi: 10.1016/j.ultras.2010.08.004.
- [250] R. G. Compton, J. C. Eklund, F. Marken, T. O. Rebbitt, R. P. Akkermans, and D. N. Waller, "Dual activation: coupling ultrasound to electrochemistry-an overview," *Electrochimica Acta*, vol. 42, no. 19, pp. 2919-2927, 1997.
- [251] R. G. Compton, J. C. Eklund, S. D. Page, T. J. Mason, and D. J. Walton, "Voltammetry in the presence of ultrasound: mass transport effects," *Journal of Applied Electrochemistry*, pp. 775-784, 1996.
- [252] F. Marken, J. C. Eklund, and R. G. Compton, "Voltammetry in the presence of ultrasound: can ultrasound modify heterogeneous electron transfer kinetics?," *Journal of Electroanalytical Chemistry*, vol. 395, pp. 335-339, 1995.
- [253] R. G. Compton and M. E. Hyde, "How ultrasound influences the electrodeposition of metals," *Journal of Electroanalytical Chemistry*, vol. 531, pp. 19-24, 2001.
- [254] A. P. Abbott, G. Frisch, J. Hartley, W. O. Karim, and K. S. Ryder, "Anodic dissolution of metals in ionic liquids," *Progress in Natural Science: Materials International*, vol. 25, no. 6, pp. 595-602, 2015, doi: 10.1016/j.pnsc.2015.11.005.
- [255] B. G. Pollet, J.-Y. Hihn, and T. J. Mason, "Sono-electrodeposition (20 and 850kHz) of copper in aqueous and deep eutectic solvents," *Electrochimica Acta*, vol. 53, no. 12, pp. 4248-4256, 2008, doi: 10.1016/j.electacta.2007.12.059.
- [256] R. M. Wagterveld, L. Boels, M. J. Mayer, and G. J. Witkamp, "Visualization of acoustic cavitation effects on suspended calcite crystals," *Ultrason Sonochem*, vol. 18, no. 1, pp. 216-25, Jan 2011, doi: 10.1016/j.ultsonch.2010.05.006.
- [257] B. Jacobson *et al.*, "A mechanistic study identifying improved technology critical metal delamination from printed circuit boards at lower power sonications in a deep eutectic solvent," *Ultrason Sonochem*, vol. 101, p. 106701, Dec 2023, doi: 10.1016/j.ultsonch.2023.106701.
- [258] C. E. Elgar *et al.*, "Using ultrasound to increase metal dissolution and prevent passivation using concentrated ionic fluid.," *Ultrason Sonochem*, vol. [Preprint - Under Review], 2023.

- [259] W. T. Richards and L. A. L., "THE CHEMICAL EFFECTS OF HIGH FREQUENCY SOUND WAVES I. A PRELIMINARY SURVEY The chemical effects of high frequency sound waves I. A preliminary Survey," *Journal of the American Chemical Society*, vol. 112, 1927.
- [260] E. W. Flosdorf, L. A. Chambers, and W. M. Malisoff, "Sonic Activation in Chemical Systems: Oxidations at Audible Frequencies," *Journal of the American Chemical Society*, vol. 58, no. 7, 1936.
- [261] A. V. Pandit, V. P. Sarvothaman, and V. V. Ranade, "Estimation of chemical and physical effects of cavitation by analysis of cavitating single bubble dynamics," *Ultrason Sonochem*, vol. 77, p. 105677, Sep 2021, doi: 10.1016/j.ultsonch.2021.105677.
- [262] D. Masiello *et al.*, "Mass and heat transfer in audible sound driven bubbles," *The Royal Society Proceedings A* vol. [Not yet published], 2023.
- [263] R. Toegel, B. Gompf, R. Pecha, and D. Lohse, "Does Water Vapor Prevent Upscaling Sonoluminescence?," *Physical Review Letters*, vol. 85, no. 15, pp. 3165-3168, 2000.
- [264] A. Dehane, S. Merouani, O. Hamdaoui, and A. Alghyamah, "A complete analysis of the effects of transfer phenomenons and reaction heats on sono-hydrogen production from reacting bubbles: Impact of ambient bubble size," *International Journal of Hydrogen Energy*, vol. 46, no. 36, pp. 18767-18779, 2021, doi: 10.1016/j.ijhydene.2021.03.069.
- [265] K. S. Suslick, N. C. Eddingsaas, D. J. Flannigan, S. D. Hopkins, and H. Xu, "The Chemical History of a Bubble," *Acc Chem Res*, vol. 51, no. 9, pp. 2169-2178, Sep 18 2018, doi: 10.1021/acs.accounts.8b00088.
- [266] Z. C. Feng and L. G. Leal, "Nonlinear bubble dynamics," *Annu. Rev. Fluid. Mech.*, no. 29, p. 201, 1997.
- [267] T. B. Benjamin and A. T. Ellis, "Self-propulsion of asymmetrically vibrating bubbles," *Journal of Fluid Mechanics*, vol. 212, no. -1, 2006, doi: 10.1017/s0022112090001860.
- [268] S. J. Shaw, "Nonspherical sub-millimetre resonantly excited bubble oscillations," *Fluid Dynamics Research*, vol. 51, no. 3, 2019, doi: 10.1088/1873-7005/ab1a6d.
- [269] M. Guedra, C. Inserra, C. Mauger, and B. Gilles, "Experimental evidence of nonlinear mode coupling between spherical and nonspherical oscillations of microbubbles," *Phys Rev E*, vol. 94, no. 5-1, p. 053115, Nov 2016, doi: 10.1103/PhysRevE.94.053115.

- [270] M. Guedra, S. Cleve, C. Mauger, P. Blanc-Benon, and C. Inserra, "Dynamics of nonspherical microbubble oscillations above instability threshold," *Phys Rev E*, vol. 96, no. 6-1, p. 063104, Dec 2017, doi: 10.1103/PhysRevE.96.063104.
- [271] T. J. Secker, C. C. Harling, C. Hand, D. Voegeli, C. W. Keevil, and T. G. Leighton, "A proof-of-concept study of the removal of early and late phase biofilm from skin wound models using a liquid acoustic stream," *Int Wound J*, vol. 19, no. 8, pp. 2124-2135, Dec 2022, doi: 10.1111/iwj.13818.
- [272] C. C. Coussios and R. A. Roy, "Applications of Acoustics and Cavitation to Noninvasive Therapy and Drug Delivery," *Annual Review of Fluid Mechanics*, vol. 40, no. 1, pp. 395-420, 2008, doi: 10.1146/annurev.fluid.40.111406.102116.
- [273] A. Eshraghi, S. Bhattacharya, L. K. Rajendran, H. Gomez, and P. P. Vlachos<sup>1</sup>, "The role of absorbed energy on oscillation mode of an air bubble in a cavitation-induced acoustic field," *Pre-Print article available at <http://dx.doi.org/10.2139/ssrn.4100217>*, 2022.
- [274] S. Cleve, C. Inserra, and P. Prentice, "Contrast Agent Microbubble Jetting during Initial Interaction with 200-kHz Focused Ultrasound," *Ultrasound Med Biol*, vol. 45, no. 11, pp. 3075-3080, Nov 2019, doi: 10.1016/j.ultrasmedbio.2019.08.005.
- [275] J. Eisner and R. Mettin, "Synthetic acoustic spectra of ultrasonic cavitation emissions," presented at the DAGA, Darmstadt, 2012.
- [276] C. S. Desilets, "The design of efficient broad-band piezoelectric transducers," *IEEE TRANSACTIONS ON SONICS AND ULTRASONICS*, vol. 25, no. 3, 1978.
- [277] T. M. Reeder and D. K. Winslow, "Characteristics of Microwave Acoustic Transducers for Volume Wave Excitation," *IEEE Transactions on Microwave Theory and Techniques*, vol. 17, no. 11, 1969.
- [278] G. Kossoff, "The Effects of Backing and Matching on the Performance of Piezoelectric Ceramic Transducers," *IEEE TRANSACTIONS ON SONICS AND ULTRASONICS*, vol. 13, no. 1, 1966.
- [279] B. Fay, G. Ludwig, C. Lankjaer, and L. P. A., "Frequency Response of PVdF Needle-Type Hydrophones," *Ultrasound Med Biol*, vol. 20, no. 4, pp. 361-366, 1994.
- [280] T. L. Szabo, "Transducers," in *Diagnostic Ultrasound Imaging: Inside Out*, 2014, pp. 121-165.
- [281] R. D. A. A. Rajapaksha, U. Hashim, S. C. B. Gopinath, N. A. Parmin, and C. A. N. Fernando, "Nanoparticles in electrochemical bioanalytical analysis," in *Nanoparticles in Analytical and Medical Devices*, 2021, pp. 83-112.

- [282] Department, of, Chemical, Engineering, and, and Biotechnology. "Linear Sweep and Cyclic Voltametry: The Principles." University of Cambridge. <https://www.ceb.cam.ac.uk/research/groups/rg-eme/Edu/linear-sweep-and-cyclic-voltametry-the-principles> (accessed 08, 2023).
- [283] V. Fourmond and C. Léger, "An introduction to electrochemical methods for the functional analysis of metalloproteins," in *Practical Approaches to Biological Inorganic Chemistry*, 2020, pp. 325-373.
- [284] N. Elgrishi, K. J. Rountree, B. D. McCarthy, E. S. Rountree, T. T. Eisenhart, and J. L. Dempsey, "A Practical Beginner's Guide to Cyclic Voltammetry," *Journal of Chemical Education*, vol. 95, no. 2, pp. 197-206, 2017, doi: 10.1021/acs.jchemed.7b00361.